Department of Physics and Astronomy
University College London
University of London

Atoms, Ions and Molecules in Intense Ultrafast Laser Fields.

Joseph Wood

Submitted in partial fulfilment of the requirements
for the degree of Doctor of Philosophy
at University College London

May 2009

I, Joseph Wood, confirm that the work presented in this thesis is my own. Where information has been derived from other sources, I confirm that this has been indicated in the thesis.

. . . . . .

Joseph Wood

Abstract

The dynamics of atoms and hydrogen molecules in ultrafast intense laser pulses are studied experimentally using time of flight mass spectroscopy and fast ion beam techniques. The content of the study can be split naturally into two parts; the first dealing with the interaction of noble gas atoms and ions with laser pulses of between 40 and 50 fs in duration and around 20 mJ of energy per pulse, the second dealing with a time-resolved investigation of the nuclear dynamics of hydrogen molecules and their corresponding molecular ions with laser pulses of approximately 10 fs duration and an energy per pulse of 50 μJ.

Within the first section of the study the technique of Intensity Selective Scanning with Effective Intensity Matching (ISS-EIM) has been used to observe Multi Electron Tunnelling Ionisation (METI) for the first time. These experiments were conducted with laser pulses focussed on neutral targets of argon and krypton.

Also within the first section, the recombination of ionised electrons with their residual atomic cores has been observed for the first time in the atomic channel. This recombination occurs in the metastable ion population of singly charged ion beams of krypton and argon, provided by a fast ion beam apparatus.

In the second section of the study, a pump-probe technique is employed using few cycle laser pulses to initiate (pump) and then image (probe) the nuclear dynamics of hydrogenic molecules and their molecular ions. In the ions, vibrational wavepackets have been studied and the phenomena of dephasing and revival observed. Additionally signatures of rotational wavepacket dynamics have been isolated in the neutral molecules. A technique to verify the laser pulse duration at the focus has also been introduced using xenon atoms and the same pump-probe technique.

Acknowledgements

Throughout my studies I have been very fortunate to work with a team of really great people. My main supervisor, Prof Roy Newell, has been incredibly helpful and always offered valuable insight into the physics problems I have encountered.

Dr Will Bryan, initially my second supervisor, has been particularly helpful with the analysis of the experiments described here and a good friend. He has always been willing to help me, even when he'd left University College London (UCL) for pastures new.

Prof Ian Williams, the head of the Queen's University Belfast (QUB) part of the collaboration, has always been very supportive of my work and has been a great person to work with. On his weekly trips to the lab at Rutherford Appleton Laboratory (RAL) the enthusiasm he would bring was contagious.

Gengan, Ian's post doc for the first few years of my time in the group, showed expert experimental hands and could get the ion beam to work superbly. For this alone I am very thankful.

My fellow students, Liz (UCL) and those from QUB (Suresh, Jarlath and Chris) have all become good friends of mine. We spent some long hours together in the laboratory and made a great team. Looking back I remember those late nights, and occasional early mornings, fondly.

In and out of the laboratory everyone has always been open to sharing ideas about the work and willing to help with problems. This made for a stimulating and fun office and laboratory environment. I would like to wish all the best to Liz with her new position in Paris, Chris with his first post doc at QUB and Jarlath and Suresh continued success in their careers at Kansas State University and Heriot Watt University respectfully.

I would also like to thank Dr Ricardo Torres (Imperial College London) for his help in understanding the theory of the rotational wavepacket dynamics and Domhnall and Dr Jim McCann (QUB) for their help with the theory of the vibrational wavepackets, and express my gratitude to all the staff at the CLF, especially Dr Edmond Turcu and the laser control room staff. Without their tireless work, often out of hours, most of the results reported here could not have been obtained. RAL might not have always been one of my favourite places, but the people there are amongst the best anyone could wish to work with.

I also wish to thank my friends and family for the care and support they have shown me. Especially Lindsey, without whom I would have never got through these last few years, she always believed in me and was always there when I needed her.

Finally, I would like to thank the Engineering and Physical Sciences Research Council (EPSRC) and UCL for funding my research as well as the Institute of Physics (IoP), European Science Foundation (ESF) and UCL Graduate School for helping cover the costs of the conferences I've been lucky enough to attend both here in the UK and abroad.

Contents

List of Figures

List of Tables

Chapter 1

Theoretical Review

1.1 Introduction

This thesis considers the physics of hydrogenic molecules, noble gas atoms and their respective ions in intense laser fields. The photon energy involved is typically around one and a half electron volts ($\lambda \approx 800$ nm, $f \approx 3.75 \times 10^{14}$ Hz) and the focused laser intensity ranges from between 1×10^{12} and 1×10^{18} Wcm^{-2}. This places the physics well into the non-linear regime in which non-perturbative effects are fundamental.

Research in the field, both theoretical and experimental, boomed in the sixties when laser technology allowed scientists to realise the high intensities required for non-linear processes to occur in the laboratory. The initial breakthroughs were made by Russian scientists mid-way through the decade with the publishing of the seminal papers by Keldysh [Keldysh, 1965] and Perelomov, Popov and Terent'ev [Perelomov et al., 1966] that have since formed the foundation of the general understanding of the non-linear ionisation of atoms in intense laser fields. Since these breakthroughs, scientists have been attracted from the fields of electron scattering and collision physics into this ever growing and diverse field of physics [Delone and Krainov, 2000]. As well as creating its own *spin-off* fields, such as intense field femtochemistry [Zewail, 1988, Zewail, 2000] and attosecond science [Scrinzi et al., 2006, Marangos, 2006, Villeneuve, 2007], meaning that all in all this area of scientific research is in robust health.

In this chapter details are given of the different and often competing ionisation processes experienced by atoms and molecules in such intense laser fields. Specific importance is given to theories used in the analysis of the experimental data presented here, although where appropriate other ideas and approaches are outlined.

1.2 Ionisation of Atoms

In the non-linear regime there are three main ionisation processes that must be considered, Multi-Photon Ionisation (MPI), Tunnel Ionisation (TI) and Field Ionisation (FI) [Delone and Krainov, 2000]. These processes can occur simultaneously within an atomic system, however, for a given intensity there will tend to be a dominant process. No distinct boundaries exist between the three regimes but a way of differentiating between which mechanism is most likely to dominate the ionisation of a specific atom or ion was deduced by Keldysh in the 1960s [Keldysh, 1965]. Crudely one can think of MPI dominating at moderate to high intensities then as the intensity is increased TI takes over until finally, at very high intensity, FI dominates.

1.2.1 The Keldysh Parameter

In quantum mechanics an adiabatic process occurs in gradually changing conditions allowing the system to adapt its configuration, and subsequently its probability density is modified by the process. I.e. if the system starts in an eigenstate of the initial Hamiltonian, it will end in the corresponding eigenstate of the final Hamiltonian. Conversely a diabatic process involves rapidly changing conditions that prevent the system from adapting its configuration during the process. This causes its probability density to remain unchanged. Typically, there is no eigenstate of the final Hamiltonian with the same functional form as the initial state; and the system ends up in a linear combination of states, which sum to reproduce the initial probability density [Kato, 1950]. An adiabacity parameter attempts to offer a guide to the transition between both regimes and their respective extremes.

In 1965 Keldysh introduced an adiabacity parameter, γ, which relates the tunnelling frequency of the least bound electron, $\omega_{tunneling}$, of a system to the laser frequency, ω_{laser}, see equations 1.1 through to 1.3, where e and m_e are the charge and rest mass of the electron, E corresponds to the amplitude of the electric field and E_{BE} is the binding energy of the least bound electron. I_p is the ionisation potential and U_p is the ponderomotive potential, or the free electron quiver energy in the laser field. In obtaining these relations, the interaction of the electron and the laser field are taken into account exactly, but the Coulomb repulsion between the ionised electron and the atomic residue is neglected.

$$\gamma = \frac{\omega_{laser}}{\omega_{tunneling}} \tag{1.1}$$

$$\gamma = \frac{\omega_{laser}\sqrt{2m_e E_{BE}}}{eE} \tag{1.2}$$

$$\gamma = \sqrt{\frac{I_p}{2U_p}} \tag{1.3}$$

At a given intensity strong enough to distort the potential energy of a system, see figure 1.1(b), and where multiphoton ionisation is possible, an increase in the laser frequency corresponds to a decrease in the duration of a single cycle of the laser field. This limits the time for tunnelling ionisation to occur as the width of the potential barrier fluctuates too quickly and multiphoton ionisation is favoured, see figure 1.1a. If the laser frequency decreases, the opposite is true and tunnel ionisation becomes more likely. If the intensity is increased further so that these distortion are extreme (i.e. free the valence electron), classical field ionisation can occur (figure 1.1(c)).

The Keldysh parameter allows us to quantify these considerations more formally as follows. When $\gamma \gg 1$, MPI dominates as the laser frequency is much greater than the tunneling frequency. When the two frequencies are almost equal, $\gamma \approx 1$, TI dominates. If the laser frequency is much lower than the tunneling frequency, $\gamma \ll 1$, the most prominent mechanism is FI. More recently the second of these conditions has been tightened to $\gamma \ll 0.5$ [Ilkov et al., 1992] in the quasi-static regime. (I.e. the low frequency, high intensity regime which best describes the environment within which the experiments reported here were conducted.) These three ionisation process are illustrated in figure 1.1.

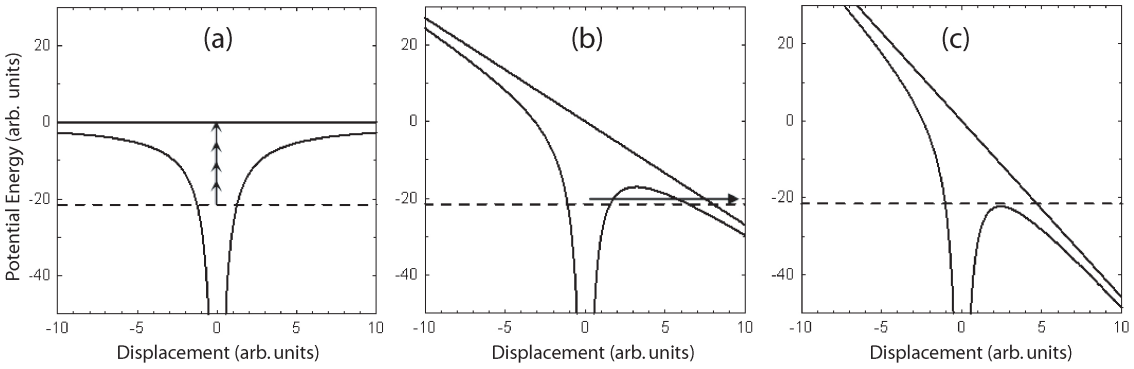

Figure 1.1: A schematic of a generic atomic potential showing the three main ionisation mechanisms in the non-linear regime. (a) Multi photon ionisation (b) Tunnel ionisation. (c) Field ionisation. The dashed lines show the energy of the least bound electron when the E-field equals zero, whilst the top full lines in each panel show the effects of the laser E-field on the atomic potential well. Adapted from [Goodworth, 2002]

1.2.2 Multiphoton Ionisation

In figure 1.1(a) the process of multiphoton ionisation is shown. In this instance (typically $I_{laser}<10^{13}$ Wcm^{-2}) ionisation proceeds via an integral number of single photon transi-

tions, shown by the small vertical arrows on the figure, forming a ladder between the energy level of the electron's pre-ionised state and its final ionised one.

$$\Gamma_n = \sigma_n I_{laser}^n \tag{1.4}$$

The n-photon ionisation rate, Γ_n, at which MPI occurs can be derived using first order perturbation theory to be dependent on the generalised n-photon ionisation cross-section, σ_n, and the laser intensity, I_{laser}, to the power of n (as shown in equation 1.4), where n is the minimum number of photons. Typically σ_n decreases rapidly as n increases. However, given large enough intensities high n-process can be observed, for instance the MPI ionisation of atomic helium up to $n = 22$ was observed as early as 1977 [Lompre et al., 1977]. At the same time many experiments investigated Above Threshold Ionisation (ATI), i.e. [Agostini et al., 1979], where ionisation proceeds with more photons than required, leaving the electron with additional energy.

Clearly to achieve higher ionisation states within the MPI regime, more photons are required. This can be obtained by increasing the laser intensity, which works up until a saturation intensity, I_{SAT}, is reached. Here the MPI rate dies off and MPI ceases to be the dominant ionisation process. The picture is clouded slightly by the fact MPI experiments tend to use focussed laser beams. Such beams have a confocal volume that expands with increasing intensity, which leads to enhanced ionisation yields. This occurs at all intensities but its effects are strongest as I_{SAT} is approached and passed. Subsequently ionisation rates, Γ, beyond I_{SAT} expand as $\mathrm{I}_{laser}^{3/2}$ [Posthumus, 2001] unless the effect of the focussing geometry is excluded, see section 3.3.1 of this thesis and Bryan et al, [Bryan et al., 2006b].

1.2.3 Tunnel Ionisation

Above laser intensities of 10^{13} Wcm^{-2}, the potential well of the system exposed to the laser field is modified to such an extent that the bound electrons of the system can tunnel out of the potential well and ionise the system. This is shown in figure 1.1(b) where the atomic potential has been bent over by the electric field of the laser making the quantum mechanical tunnelling more feasible.

Until very recently the most popular model for TI amongst experimentalists was the semi classical ADK model developed by Ammosov, Delone and Krainov [Ammosov et al., 1986]. More recently this theory has been developed to treat TI in molecules [Tong et al., 2002]. Its basic assumption matches those of earlier TI models [Perelomov et al., 1966] and are complementary to Keldysh's original work [Keldysh, 1965].

Interestingly, the question of whose contribution post-Keldysh should be given the greatest

credit in furthering our understanding of TI is a source of controversy amongst theorotians in Russia [Delone and Krainov, 1998, Popov, 1999], much to the amusement of experimentalists the world over.

$$\Gamma_{static}(E) = \left(\frac{4}{E}\right) exp\left[-\frac{2}{3E}\right] \tag{1.5}$$

$$\Gamma(E) = \sqrt{\frac{3}{\pi E}}\left(\frac{4}{E}\right) exp\left[-\frac{2}{3E}\right] = \sqrt{\frac{3}{\pi E}}\Gamma_{static}(E) \tag{1.6}$$

The ADK formula is based around the ionisation rate of ground state hydrogen atoms in an external field, as given by equation 1.5 [Landau and Lifshitz, 1977], where E is the electric field strength in atomic units. This rate is then averaged over half the optical cycle, to give a quantity representative of ionisation from a laser field, see equation 1.6. The use of such approximations is justified in the low-frequency regime, as the characteristic time of the optical cycle and of an ionisation event are much different (with the time for ionisation being substantially shorter [Brichta et al., 2006]). Finally the treatment has been generalised to treat larger atoms with more complex electronic structures.

$$\Gamma_{ADK} = \sqrt{\frac{3E}{\pi(2I_p)^{\frac{3}{2}}}}\,|C_{n^*,l^*}|^2\, f(l,m) I_p \left(\frac{2(2I_p)^{\frac{3}{2}}}{E}\right)^{\left(\left[\frac{2Z^*}{\sqrt{2I_p}}\right]-|m|-1\right)} exp\left[-\frac{2(2I_p)^{\frac{3}{2}}}{3E}\right] \tag{1.7}$$

Equation 1.7 gives the rate of TI predicted by the ADK model in atomic units (e = m_e = a_0 = $\hbar$ = 1). n, l and m are the traditional quantum numbers; where as n^* and l^* are effective quantum numbers of the atomic residue defined by equations 1.8 and 1.9 respectively, Z is the charge of the residue and E is the electric field strength. As before I_p is the ionisation potential. The quantities *f(l,m)* and $|C_{n*,l*}|^2$ are defined by equations 1.10 and 1.11. Typically $|C_{n*,l*}|^2$ is of the order of two.

$$n^* = n - \delta_q = \frac{Z}{\sqrt{2I_p}} \tag{1.8}$$

$$l^* = n^* - 1 \tag{1.9}$$

$$f(l,m) = \frac{(2l+1)(l+|m|)!}{2^{|m|}(|m|)!(l-|m|)!} \tag{1.10}$$

$$|C_{n^*,l^*}|^2 = \frac{Z^{2n^*}}{n^*\Gamma(n^*+l^*=1)\Gamma(n^*-l^*)} \tag{1.11}$$

More often than not, the probability of ionisation is plotted, rather than the rate. This is

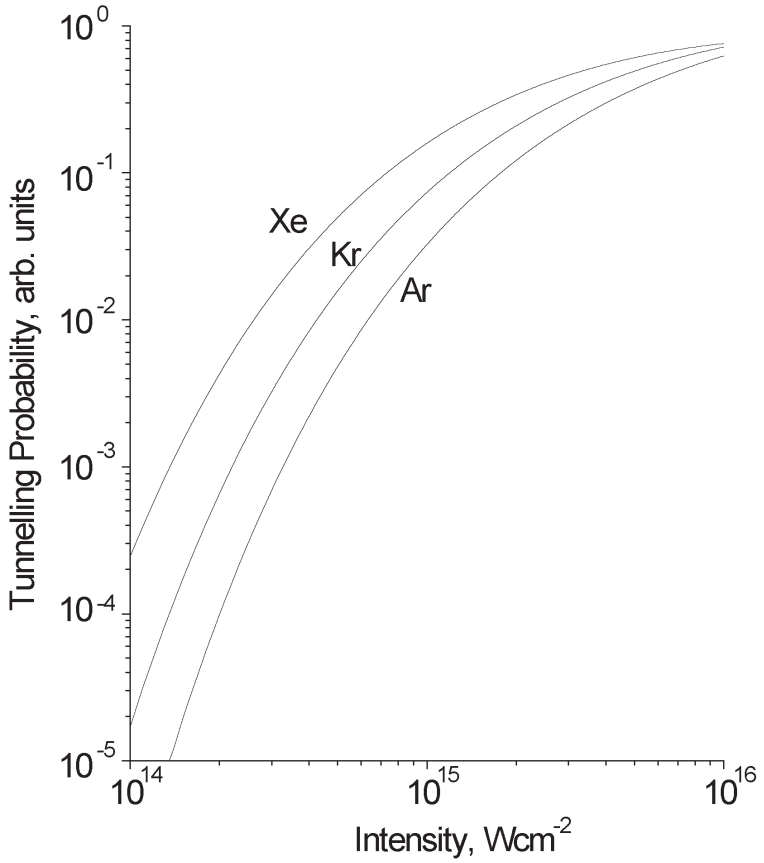

Figure 1.2: Calculated ADK tunnelling probabilities as a function of laser intensity for argon, krypton and xenon.

obtained by equating the ADK rate to the probability per unit time.

The rate of tunnelling from the *m=0* state however, greatly exceeds that of any other state and their collective sum. Consequently, a shortened version of equation 1.7 is often used, see equation1.12, in which w_0 represents the probability of tunnelling ionisation from the m=0 state. All other symbols have the same meaning as before.

$$w_0 = \left(\frac{3e}{\pi}\right)^{\frac{3}{2}} \left(\frac{Z^2}{n^{*\frac{9}{2}}}\right) \left(\frac{4eZ}{n^{*4}E}\right)^{\left(2n^*-\frac{3}{2}\right)} exp\left[-\frac{2Z^3}{3n^{*3}E}\right] \tag{1.12}$$

Figure 1.2 shows calculated probabilities of ionisation as a function of laser intensity for several noble gas atoms. Care must be taken in comparison with experiments, as the energy distribution or focusing geometry must be either included into the theory or, preferentially, removed from the experimental results.

1.2.4 Multi Electron Tunnel Ionisation (METI)

Recently the ADK model has begun to fall out of favour with many researchers. Several extensions and alterations have been made in the last decade, several of which are mentioned in the review by Popov [Popov, 2004], to improve its accuracy and to increase the range of the Keldysh parameter for which it is valid. One of these extensions, Multi Electron Tunnel Ionisation (METI), is described here as it is one of the models used in the analysis of our experiments, see chapter 5.

METI was proposed by Zon [Zon, 1999, Zon, 2000b] as a means of catering for the effects of the residual electrons following an ionisation event and preceding the next. The original ADK model only considers the valence electron, which is sufficient to give good results in many instances. However, Zon proposed that inelastic tunnelling could occur, leaving the parent ion or residual core in an excited state, rather than a ground state configuration. This excitation is thought to take place via *shake up*, a rapid process first proposed by Carlson [Carlson, 1967] and recently found to be important in the multiple ionisation of molecules [Litvinyuk et al., 2005].

The net effects of METI are seen as a reduction in the laser intensity required to ionise subsequent charge states of an ion. These effects are illustrated in figure 1.3 which shows a comparison between METI and the traditional tunnelling theory.

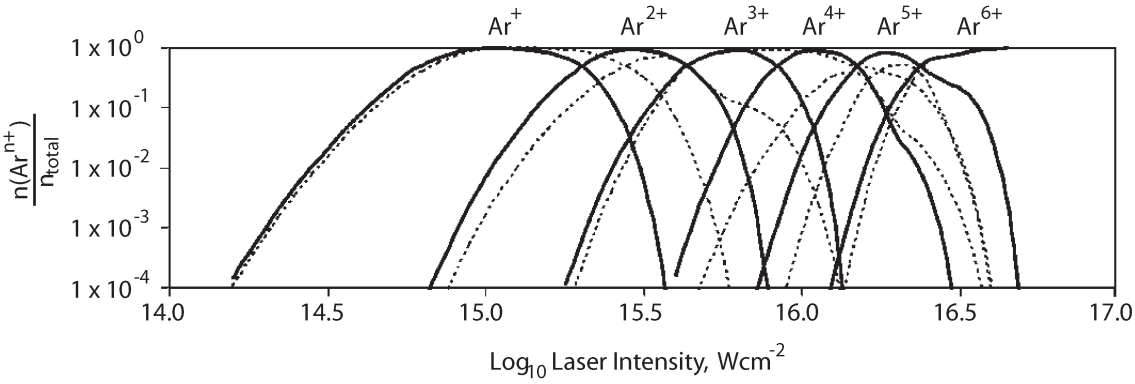

Figure 1.3: A comparison of METI and ADK calculations for the first six charge states of argon. The dotted lines represent the ADK calculations and the solid lines the METI values. Reproduced from [Kornev et al., 2003].

Zon's group has also compared their METI results to experiments [Kornev et al., 2004]. However, this comparison of neon ionisation results [Fittinghoff et al., 1994] only covers two charge states, and is restricted slightly by issues caused by the experimental focussing geometry. A more complete comparison has been obtained by our group [Bryan et al., 2006c] [Bryan et al., 2006d] and is the subject of chapter 5 of this thesis.

1.2.5 Field Ionisation, Barrier Suppression Ionisation and Relativistic Effects

As the laser intensity is increased through the tunnelling regime the potential barrier becomes more narrow and its height reduces. This continues until the electron's bound state energy is equal to the barrier's height as shown in figure 1.1(c) and the electron becomes classically free. This inevitably leads to Field Ionisation (FI), commonly referred to as Barrier Suppression Ionisation (BSI), as the electron leaves the nucleus leaving an ionised core behind.

$$I_{FI}(Wcm^{-2}) = 4 \times 10^9 \frac{I_p(eV)^4}{Z^2} \tag{1.13}$$

Equation 1.13, taken from the topical review by Protopapas [Protopapas et al., 1997], gives the laser intensity at which this ionisation mechanism becomes dominant. Above this value ionisation is said to occur with a probability of unity via FI. For the ground state of hydrogen this limit is reached at 1.4×10^{14} Wcm^{-2}, while for neutral xenon it is reached at the lower intensity of 8.6×10^{13} Wcm^{-2}

Increasing the laser intensity yet further, beyond 10^{18} Wcm^{-2} , relativistic effects become important. This arises as the electrons velocity in the laser field begins to approach the speed of light [Eberly and Sleeper, 1968] and predetermines one to replace the rest mass of the electron by its relativistic mass in any considerations of the physcis at play [Protopapas et al., 1996]. At such extreme intensities the magnetic field of the laser must also be considered [Keitel and Knight, 1995], a variable omitted in all our previous discussions. As these extreme conditions are not realised in our experiment, no further discussion of this interesting area of physics will take place in this document, however readers are directed to the recent review by [Mourou et al., 2006] for more information.

1.2.6 Multiple Ionisation

When working at high intensity, multiple ionisation is often observed in the laser matter interaction. Work in this area has flourished since the first studies of the multiple ionisation with xenon targets by L'Hullier [L'Huillier et al., 1983] in the multiphoton regime. Further multiple ionisation experiments with noble gases followed, with higher laser intensities putting the interactions in the tunnelling ionisation regime [Augst et al., 1989, Augst et al., 1991]. Over the next decade, several groups worldwide (including researchers at UCL), continued documenting noble gas ionisation at laser intensities corresponding to the multiphoton and tunnelling regimes. The most notable of which include work on the multiple ionisation of helium [Walker et al., 1994], krypton and xenon [Talebpour et al., 1997],

neon, argon and xenon [Larochelle et al., 1998].

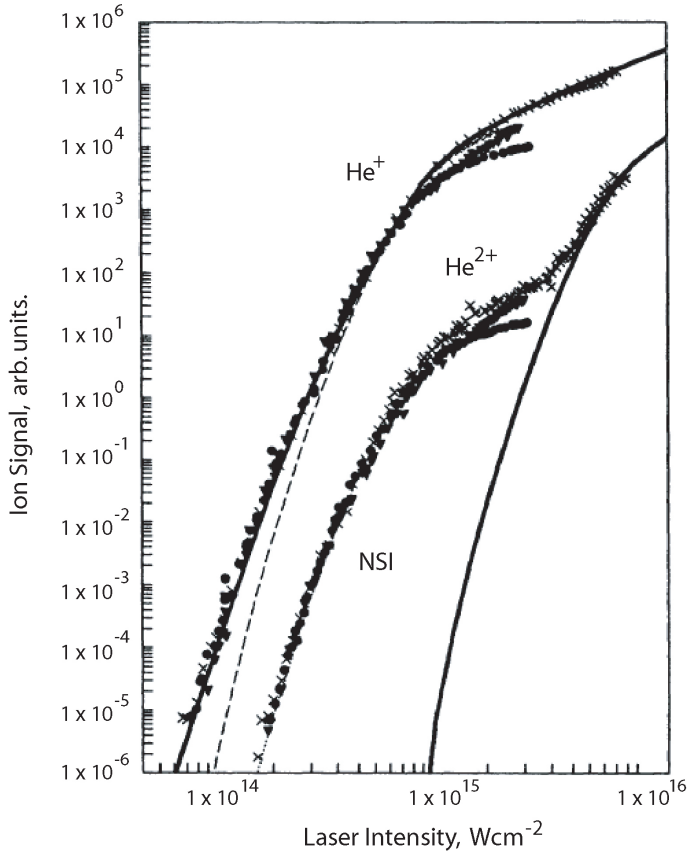

Figure 1.4: Measured ion yields for linearly polarised 100 fs laser pulses at 780 nm. The solid lines represent the results of an SAE model and the dashed curves an AC-tunnelling model. The *knee* structure is the He^{2+}ion yield; is the product of Non-Sequential (NS) ionisation. Figure reproduced from [Walker et al., 1994].

In all these instances the ADK theory (discussed previously) and other Single Active Electron (SAE) models (such as that proposed by Kulander [Kulander et al., 1991]) described the initial ionisation step accurately. However, these theories break down for double and higher ionisation processes. This can be seen in figure 1.4 and suggests that the multiple ionisation of atoms must proceed Non-Sequentially (NS) (see equation 1.15), as well as, or instead of sequentially (see equation 1.14). If only sequential ionisation processes occurred the data should match the corresponding ADK and SAE predictions for all charge states.

$$X \rightarrow X^{+} + e^{-} \rightarrow X^{2+} + 2e^{-} \tag{1.14}$$

$$X \rightarrow X^{2+} + 2e^{-} \tag{1.15}$$

Initially the mechanisms responsible for this deviation from theory were unclear. A problem further clouded by the absence of the distinct NS *knee* in some of the contemporary results [Charalambidis et al., 1997]. (This was later assigned to be due to Charalambidis et al working in the MPI regime rather than the TI regime, where NSI via recollision is expected to be most significant.)

Several mechanisms were suggested, including (i) Shake-off [Fittinghoff et al., 1992], (ii) Collective Tunnelling [Eichmann et al., 2000] and (iii) Recollision [Schafer et al., 1993, Corkum, 1993] to account for the enhanced ion yields observed experimentally. Recently common consensus favours the recollision model.

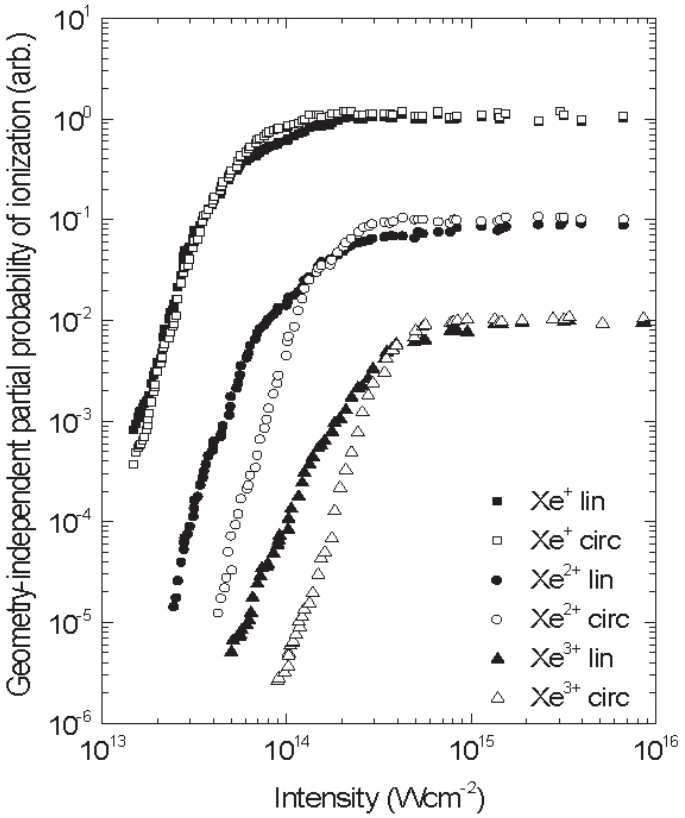

Figure 1.5: Measured ion yields for linear and circular polarised, 55 fs laser pulses at 790 nm. The NSI yield can be seen in the difference between the ionisation probability between the linear and circular results for each ion. Figure reproduced from [Bryan et al., 2006b]

The main reason for this selection is that NSI is most apparent in experiments using linear polarisation, and absent in experimental results from circular polarisation
[Auguste et al., 1992]. Light with a slight degree of ellipticity has been shown to induce NSI. This is not predicted by the simple recollison model and is thought to arise due to spatial dispersion of the wave packet as it evolves in the field [English, 2007, Zettili, 2006]. (Note if modelled classically i.e. without dispersion; the electron in an elliptically polarised

field cannot return to its origin and recollison does not occur [Corkum, 1993].

Very recently recollision has become increasingly important as the source of HHG and attosecond pulses [Kling and Vrakking, 2008]. This importance is signified by the fact that Corkum's paper [Corkum, 1993] has been referenced over a thousand times by other peer reviewed publications. Also further models and processes in atomic ionisation have been developed from the initial ideas of recollision such as RESI Recollision-induced Excitation followed by Subsequent field Ionisation [Rudenko et al., 2004, Zrost et al., 2006].

1.2.7 Correlated Electron Dynamics and High Harmonic Generation (HHG): The Recollison Model

The recollision process responsible for NSI contains three major phases. (1) The tunnel ionisation of the first electron; (2) Its subsequent evolution in the laser field and (3) Its return to the atomic nucleus, resulting in further ionisation. A simple yet powerful model for the mechanics of this process was suggested by Corkum [Corkum, 1993].

In this three step model (illustrated in figure 1.6), the electron follows the process outlined above. The treatment is classical throughout and treats the laser field as a plane wave and the electrons response is governed by Newton's Laws of motion, see equation 1.16 where F is the force exerted on the electron by the laser field *E(t)*, m_e is the electrons mass and e is its charge.

$$F = m_e a(t) = E(t)e \tag{1.16}$$

$$E(t) = E_0 \cos(\omega t + \phi) \tag{1.17}$$

The initial electron tunnels through the barrier and escapes the potential with zero kinetic energy (v(t=0)=0) [Corkum et al., 1989]. From here, the electron follows a path governed by the electric field of the laser. The acceleration, a(t), gained from the laser field is dependent on the field's magnitude, E_0, and its phase, ϕ.

Equations 1.18 through to 1.20 show how the electron's accerlation, a(t), velocity, v(t), and displacement, x(t), from the nucleus can be calculated by combining equations 1.16 and 1.17 and then integrating with respect to time. The constants of integration are found using the boundary conditions of $x = v = 0$, at t=0 [Corkum et al., 1989].

$$a(t) = \frac{eE_0}{m_e} \cos(\omega t + \phi) \tag{1.18}$$

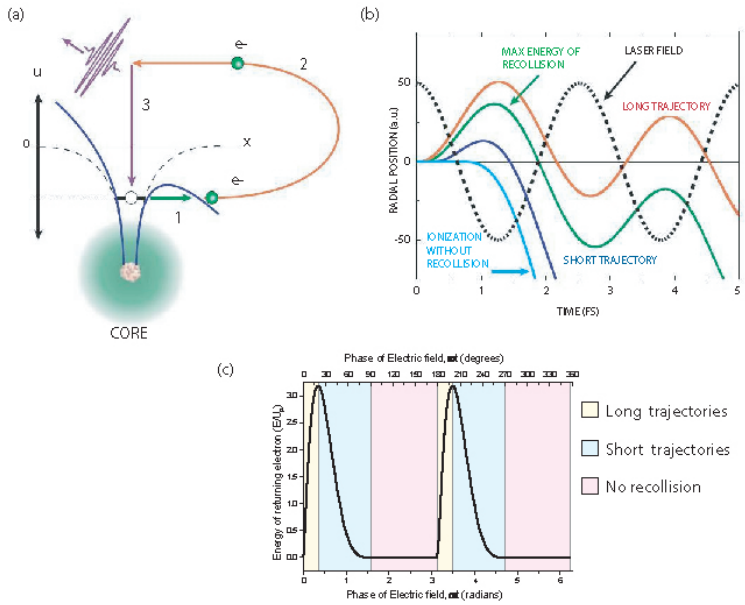

Figure 1.6: The recollision model proposed by Corkum [Corkum, 1993]. Panel (b) shows how electrons released at different phases in the field take either long or short trajectories back to the atomic core. The max kinetic energy of $3.17\mathrm{U}_p$ occurs at a phase, $\phi \approx 17^o$ and coincides with a return of the electron when the electric field amplitude is zero. Trajectories that evolve for longer in the field are referred to as *long trajectories*, whereas those that spend less time in the field are called the *short trajectories*. Panel (c) illustrates how the kinetic energy of the recolliding electron varies with phase. The max kinetic energy is $3.17\mathrm{U}_p$, which occurs at a phase, $\phi \approx 17^o$. In HHG experiments the *long trajectories* are filtered out as they are more dispersed than those from the short ones. This also avoids interference between the energetic electrons, note the degeneracy around $\phi \approx 17^o$ on panel (c). Panels (a) and (b) are reproduced from [Kling and Vrakking, 2008] whereas figure (c) has been calculated using equations 1.16-1.20.

$$v(t) = \frac{eE_0}{m_e\omega}\left[\sin(\omega t+\phi)-\sin(\phi)\right] \tag{1.19}$$

$$x(t) = \frac{eE_0}{m_e\omega^2}\left[-\cos(\omega t+\phi)-\sin(\phi)t+\cos(\phi)\right] \tag{1.20}$$

The acceleration, a(t), gained from the laser field is dependent on the field's magnitude, E_0 and its phase ϕ at the instant of release. For a set field intensity, the maximum kinetic energy with which the electron returns to the core (x=0) is $3.17\,U_p$, which corresponds to emission from the core at a phase $\phi \approx 17^o$.

In this expression U_p, or the ponderomotive potential, corresponds to the average quiver energy picked up by free electron in a laser field. It's defined by equation 1.21 and expressed in practical units in equation 1.22 where I is the laser intensity, and λ is the laser wavelength.

$$U_p = \frac{e^2 E_0^2}{4 m_e \omega^2} \quad (1.21)$$

$$U_p(eV) = 9.33 \times 10^{-14} I(W cm^{-2}) \lambda(\mu m)^2 \quad (1.22)$$

Electrons emitted at the maximum amplitude of the field return with zero kinetic energy. This dependence on ϕ can be seen clearly in figure 1.6(b). Also it's worth noting that not all phases of the electric field allow a return to the core. All these factors contrive to make a phase of $\phi \approx 17^o$ not only the source of the most energetic returning electrons, but also the phase at which return is most likely.

When the electron returns, as well as causing further ionisation photons are often also emitted as a result of recombination. This process is called High Harmonic Generation (HHG), as the emitted photons have frequencies that are multiples of the initial driving field. First observed in the late eighties [McPherson et al., 1987, Ferray et al., 1988], HHG was only understood widely after Corkum's three step model for recollision was published [Corkum, 1993]. As in the case of recollsion, the electron first tunnel ionises. It then undergoes evolution in the field and is driven back to the atomic core. This takes approximately half an optical cycle. On return, the electron recombines with the atomic core releasing its kinetic energy plus the ionisation potential of the core. This process occurs around every half cycle of the optical field and results in the production of odd harmonics of the driving laser field. A cut off in the harmonics energy, $\hbar\omega$, is also observed due to the electron only being able to absorb $3.17 U_p$ of energy along its trajectory. This cut off is defined by equation 1.23 and was found empirically by Krause [Krause et al., 1992] a year before Corkum's influential paper was published. Since which a series of quantum mechanical treatments of the three step model have been published, the most significant being that of Lewenstein et al [Lewenstein et al., 1994] as well as many reviews of HHG, such as that by Eden [Eden, 2004].

$$\hbar\omega = 3.17 U_p + I_p \quad (1.23)$$

Figure 1.7 shows a typical high harmonic spectrum from the interaction of an intense laser beam and a noble gas target. With gas targets, only odd harmonic orders are produced, which is a consequence of the process requiring an odd number of photons due to symmetry considerations (i.e. it must be an electronic dipole allowed transition). Even orders can be produced by using selected solid surfaces and or two colour, two pulse experiments. Also by shaping the driving laser field HHG can be tailored to meet specific criteria (see the recent review by Winterfeldt et al [Winterfeldt et al., 2008] for more details on bespoke HHG experiments).

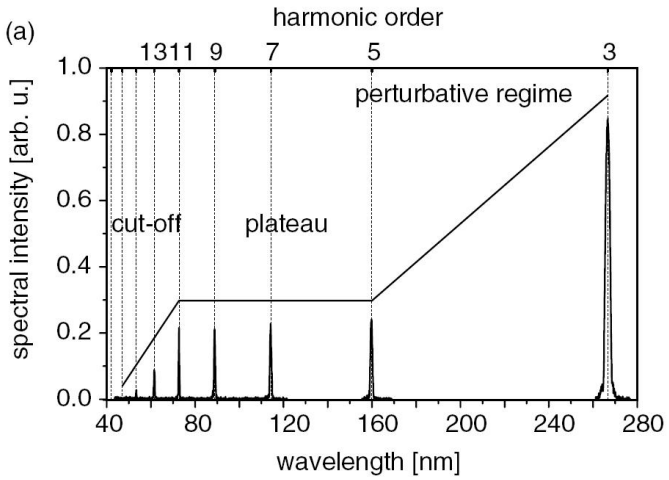

Figure 1.7: A typical high harmonic spectrum. Reproduced from [Pfeifer et al., 2006]. Both the odd order exclusivity and the high harmonic cut off are clearly apparent.

In Corkum's model [Corkum, 1993] the initial ionisation step occurs in the tunnelling regime. This is also the regime, i.e. laser intensity, chosen by scientists conducting HHG experiments. This regime is favoured for NSI, as the recombination of the electron and atomic core is most likely if the system is correlated. This can be viewed by assuming only a fraction of the electron wavefunction tunnels through the barrier in the initial step. This fraction of the wavefunction then evolves in the field before recolliding back with the remaining bound fraction. Due to the high degree of coherence in this process it is far more efficient than a recombination/recollision of an entire electron wavepacket and the atomic core. Hence it is in the low intensity region of the tunnelling regime, that NSI is at its most efficient.

1.2.8 Electron Ion Recombination

In section 1.2.6 the returning electron was assumed to further ionise the atomic core. However, this is only one of a number of outcomes that may result from the electron's return to the nucleus. One of the other possibilities is that instead of ionising the nucleus further, the electron can recombine with its parent. This electron-ion recombination [Hahn, 1997] is a particularly interesting subject having many applications in the physics of the interstellar medium and our own planet's upper atmosphere. As well as recombining with the atomic core or further ionising it, excitation is a third possible outcome of the recollision mechanism.

In this thesis excitation alone shall not be discussed, however, recombination, in which the atomic particle is detected as opposed to the harmonics, will be covered in some detail (see chapter 4), the work in which has resulted in a high profile publication for our research

group [Williams et al., 2007].

1.3 Ionisation of Hydrogen Molecules and Ions

As well as investigating the interaction of atoms with ultrafast high intensity laser pulses, interactions with many simple molecules have been widely studied [Bandrauk, 1993] [Posthumus, 2001, Demtröder, 2006]. In this thesis the experiments have been restricted to hydrogen molecules and their isotopes and ions. There are several reasons for this narrow focus. Firstly, such molecules are of great interest for theoreticians, as they are almost completely solvable requiring relatively few approximations. This family of molecules are also of great interest to the astronomy and astrophysics community due to their high abundances in the interstellar medium and stellar atmospheres. Also, on a more practical level they are easily obtainable, non-corrosive and do not require any restrictive handling arrangements.

When a high intensity laser field interacts with a molecular system, it manipulates the system's eigenstates (as in the case of atoms discussed previously). As before ATI and MPI features are readily observed. However, the extra degrees of freedom, in molecules (vibrational and rotational dynamics about the molecular systems centre of mass), lead to additional high field phenomena not seen in interactions with atomic systems. Also the laser field can cause the fragmentation or dissociation of the molecular system being studied. As well as observing the high electric field molecular dynamics, a degree of control over these dynamics can be shown. This is achieved primarily due to the duration of the ultra short pulses used being of the order, or shorter than, the characteristic time scales of the nuclear dynamics (vibration ≈10 fs, rotation ≈1 ps) within which the control can be realised. All in all this leads to an exciting playground within which to conduct experimental research.

1.3.1 The Potential Surface of H_2^+

In this study the simplest and most theoretically tractable molecules are studied to which the potential energy diagram of H_2^+ is essential. In most instances only the ground electronic state, $1s\sigma_u$, and the repulsive first excited state, $2p\sigma_g$, are considered (see figure 1.9). In all instances the potentials used are from the work of Sharp [Sharp, 1971]. Figure 1.8 shows Sharp's potentials. Only the two lowest states are used, as higher states lie more than 11 eV above these two, and with a photon energy of 1.55 eV (corresponding to λ=800 nm used in the experiments), transition to these states is considered to be negligible.

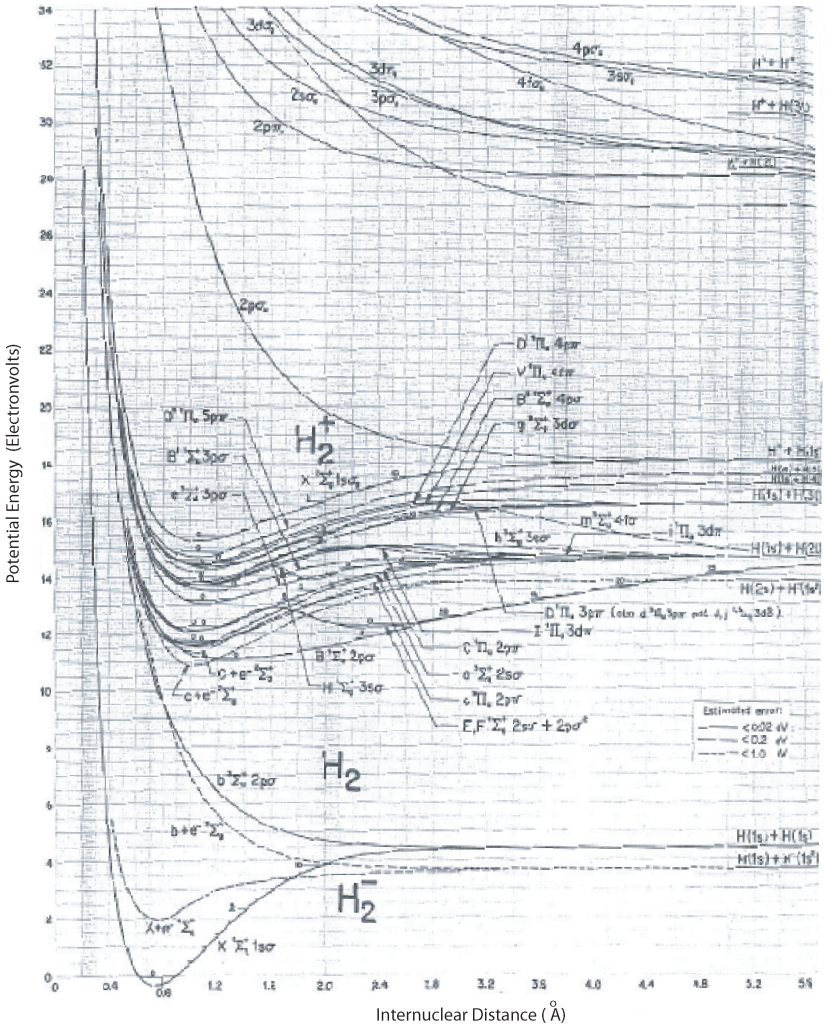

Figure 1.8: Potential Energy Curves of H_2, H_2^+ and H_2^-. Reproduced from [Sharp, 1971].

1.3.2 Dissociative Processes in Hydrogenic Systems

Knowledge of the physics involved in the laser molecule interaction is obtained through the study of the fragmentation process observed. For example, with a target consisting of H_2 molecules we investigate the dynamics through study of the positively charged fragments, H_2^+ and H^+, detected by the spectrometer (see chapters 7 and 8). Typically, the ionisation of the neutral molecule is considered to occur via a fast photoionisation process illustrated in equation 1.24. From this singly charged molecular ion further fragmentation is possible by either Photo-Dissociation (PD) (equation 1.25), or Coulomb Explosion (CE) (equation 1.26). The latter is observed through the detection of fast protons ($E_{kinetic} \gg 3$ eV whilst the signature of the first is the observation of low energy protons ($E_{kinetic} \approx$0-3 eV)

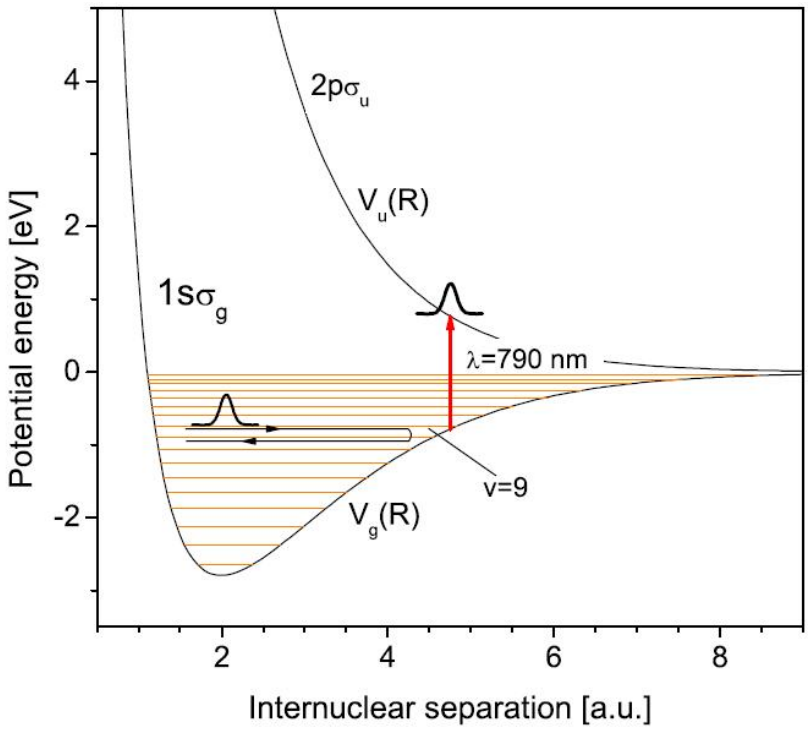

Figure 1.9: The two lowest states of $H_2{}^+$ coupled by a 790 nm photon. The Franck-Condon factor is maximal for the vibrational level, v=9, and an internuclear separation of 4.8 a.u. Reproduced from [Pavičić, 2004].

$$H_2 + n\hbar\omega \rightarrow H_2^+ + e^- \tag{1.24}$$

In each of these equations 1.24-1.26 $n\hbar\omega$ represents the laser beam rather than a set number of photons.

$$H_2^+ + n\hbar\omega \rightarrow H + H^+ \tag{1.25}$$
$$H_2^+ + n\hbar\omega \rightarrow 2H^+ + e^- \tag{1.26}$$

As in the case of atomic ionisation, as the laser intensity increases so the ionisation processes involved change. At low intensity the interaction can be adequately described using perturbation theory, where the dissociation rate is proportional to the laser intensity as given by Fermi's golden rule (see for example [Landau and Lifshitz, 1977]). At higher intensity non-linear processes dominate the ionisation dynamics and a better handle on the physics involved can be gained through the Rabi frequency, ω_R [Bandrauk, 1993], which

is defined in practical units by equation 1.27.

$$\hbar\omega_R(cm^{-1}) \quad = \quad E_0 \cdot d = 1.17 \times 10^{-3}\sqrt{I(Wcm^{-2})}d(a.u.) \tag{1.27}$$

The Rabi frequency measures the strength of the radiative coupling between two given states, ie the 1sσ_u state and the 2pσ_g state of $H_2{}^+$, through use of the appropriate transition dipole moment d. In the case of $H_2{}^+$ these dipole moments were calculated by Bates [Bates, 1951]. At resonance, if the Rabi frequency is much greater than that of a given vibrational level, $\omega_R \gg \omega_v$, then the chance of the electron absorbing a photon is high. If on the other hand $\omega_R \ll \omega_v$, then the chance of an absorption is low.

For the laser pulses used in the experiments the 9^{th} vibration coincides with the one photon resonance between the two states. Correspondingly the v=9 level has the largest transition probability and Franck-Condon factor. This resonance between the 1sσ_u (or V_g) state and the 2pσ_g (or V_u) state, is shown in figure 1.9.

Comprehensive reviews of the ionisation dynamics of H_2 are available from Giusti-Suzor et al. [Giusti-Suzor et al., 1995] and Posthumus [Posthumus, 2004].

1.3.3 The Floquet Picture and Light Induced Potentials (LIPs)

One way of understanding the dissociation processes in $H_2{}^+$ is to use a Floquet method [Bandrauk, 1993, Pavičić, 2004]. This approach is not ideal but offers clear insight into the problem. A better treatment would include the time dependence of the laser field and consider wavepacket propagation methods with direct integration of the Time Dependent Schrödinger Equation (TDSE). Such an approach is not followed here, however, these methods are becoming evermore popular with theorists.

$$H(\mathbf{r}, R, t)\Psi(\mathbf{r}, R, t) \quad = \quad i\hbar\frac{\delta}{\delta t}\Psi(\mathbf{r}, R, t) \tag{1.28}$$

For the $H_2{}^+$ system, perfectly aligned in a linear polarised laser field, the TDSE is given by equation 1.28 where $\mathbf{r}$ denotes the electronic coordinate and R the internuclear separation of the ion's constituent protons. The total Hamiltonian, H($\mathbf{r}$,R,t), comprises the time independent field free Hamiltonian, H_0(r,R), and the interaction term V($\mathbf{r}$,t) as shown in equation 1.29 [Chu, 1981].

$$H(\mathbf{r}, R, t) = H_0(r, R) + V(\mathbf{r}, t) \tag{1.29}$$

The field free Hamltonian defined in equation 1.30 comprises the nuclear kinetic energy, T_R, and the electronic Hamiltonian, H_{elec}, whereas the interaction term (equation 1.31) is the dot product of the dipole moment e$\mathbf{r}$ and the electric field, $\mathbf{E}$(t), defined in equations 1.32-1.33.

$$H_0(\mathbf{r}, R) = T_R + H_{elec}(\mathbf{r}, R) \tag{1.30}$$
$$V(\mathbf{r}, t) = -e\mathbf{r} \cdot \mathbf{E}(t) \tag{1.31}$$
$$\mathbf{E}(t) = \mathbf{e}_z E_0 \cos(\omega t) \tag{1.32}$$
$$V(\mathbf{r}, t) = \frac{eE_0 z}{2} \left(\exp[i\omega t] + \exp[-i\omega t]\right) = V_- \exp[i\omega t] + V_+ \exp[-i\omega t] \tag{1.33}$$

Now the time dependence lies in the interaction term and the Hamiltonian is periodic in time. i.e. H(t) = H(t+T) where T = $2\pi/\omega$. Consequently, using the Floquet Theorem [Shirley, 1965, Chu, 1981], the wavefunction can be written in the form:

$$\Psi(\mathbf{r}, R, t) = \exp\left[\frac{-iEt}{\hbar}\right] F(\mathbf{r}, R, t) \tag{1.34}$$

E is the quasi-energy and F($\mathbf{r}$,R,t) is the Floquet term, which is periodic in time. Rewriting F($\mathbf{r}$,R,t) as a Fourier series, the wavefunction can now be expressed as:

$$\Psi(\mathbf{r}, R, t) = \exp\left[\frac{-iEt}{\hbar}\right] \sum_{n=-\infty}^{n=+\infty} \exp\left[-in\omega t\right] F_n(\mathbf{r}, R). \tag{1.35}$$

This enables the TDSE to be re-written as a set of time independent differential equations, in which neighbouring Fourier components are coupled and F_n($\mathbf{r}$,R) are the wavefunctions, dressed by the phase factors $\exp^{-in\omega t}$. From this expression it can be seen that identical solutions should exist for E, E$\pm\hbar\omega$, E$\pm 2\hbar\omega$, etc.

Writing the wave functions F_n($\mathbf{r}$,R) as Φ_g and Φ_u, (i.e. the wavefunctions of the corresponding electronic states 1sσ_g and 2pσ_u) and by considering the differing symmetries of the two states in question, the resulting differential equations can be written in matrix form and the quasi-energies obtained through diagonalisation. The results of a 2 by 2

matrix diagonalised and with n set to zero yields the following:

$$E \pm (R) \quad = \quad \frac{1}{2} \pm \sqrt{[V_g(R) + \hbar\omega - V_u(R)]^2 + (\hbar\omega_R)^2}, \tag{1.36}$$

the results of which are the adiabatic potential curves $E_-(R)$ and $E_+(R)$, which are illustrated in figure 1.10. As the field-free values of these potentials are those of the V_- and V_+ states plus or minus a photon, the dressed states cross at the resonance shown in figure 1.9. As laser intensity is increased, the crossing becomes an avoided crossing or gap. The width of which opens up proportional to the Rabi frequency (or proportionally to the square root of the intensity).

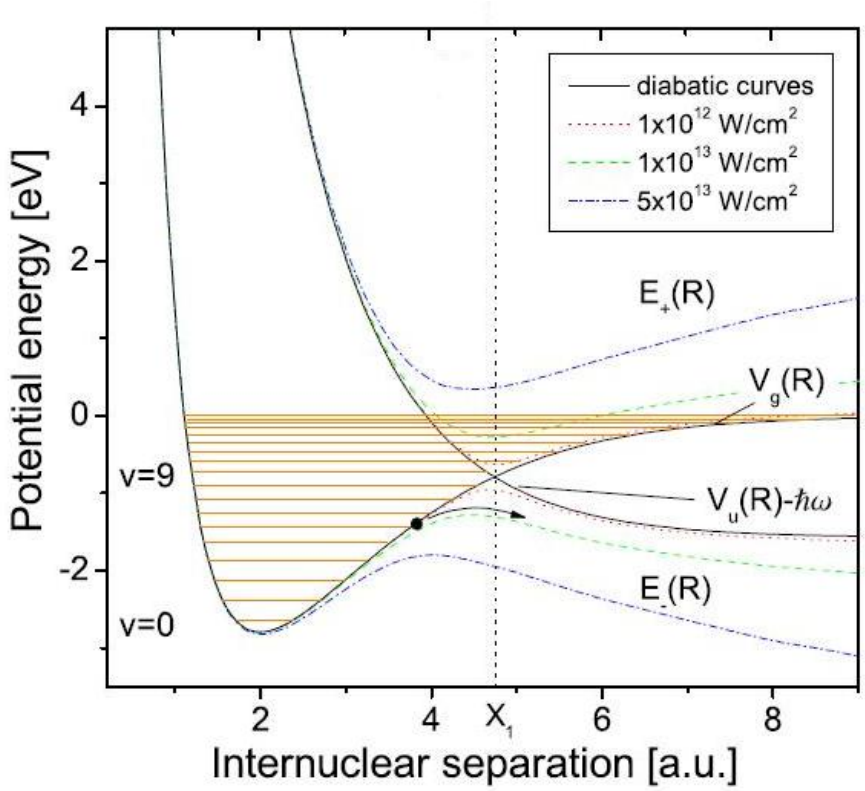

Figure 1.10: Field dressed diabatic and adiabatic potential curves for different intensities. The diabatic curves are obtained by dropping the $2p\sigma_u$ one photon down the y-axis, whereas the adiabatic curves are calculated using equation 1.36.

If the intensity is increased further the one photon gap opens so wide that it ceases to have any meaning. This also coincides with the opening of the so called three photon gap. These processes are illustrated in figure 1.11, where X_1 and X_3 indicate the successive one photon crossings; X_2 shows a three photon crossing. (Note using a 2 by 2 matrix in

the Floquet technique the three photon gap cannot be accurately predicted. Sufficient accuracy was only obtained via diagonalisation of a much larger matrix ≈ 60 by 60.)

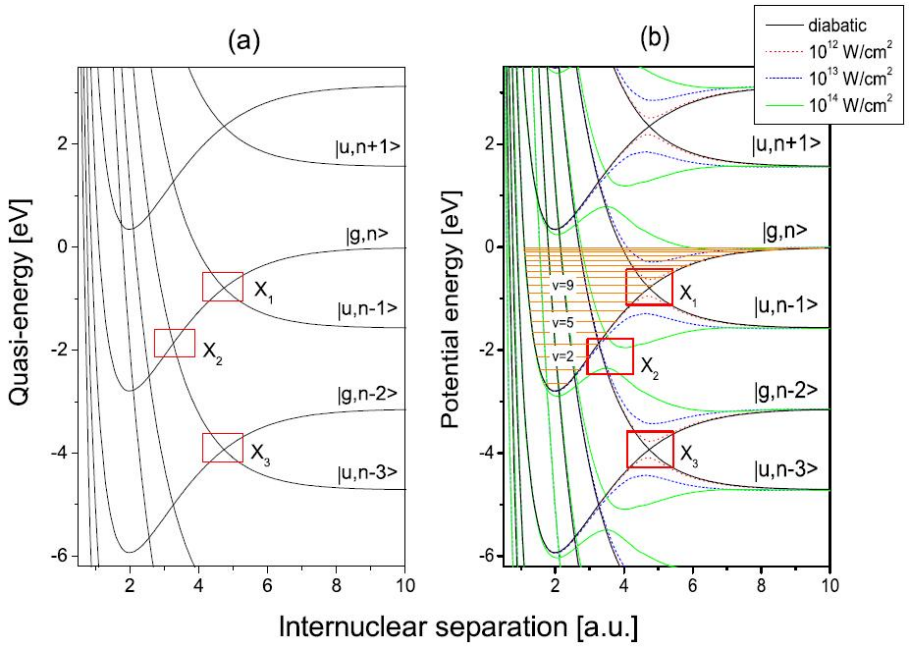

Figure 1.11: The Potential Energy curves of $H_2{}^+$. Panel (a) shows the diabatic curves dressed with 790 nm photons. The curve crossings are labelled. Panel (b) is a repeat of (a) but with the addition of the adiabatic curves generated at three different intensities. Here the the labels X_{1-3} indicate the avoided crossings known as the one (X_1 & X_3) and three (X_2) photon gaps, respectfully. Reproduced from [Pavičić, 2004].

In this model the avoided crossings hold the key to the fragmentation channels. PD can occur via two main mechanisms. The first, labelled one photon ($1\hbar\omega$) dissociation, proceeds when the system moving to larger R reaches the one photon avoided crossing (X_1) and experiences the repulsive potential past the crossing. This leads to the energy of one photon being shared between the particles and is called one photon dissociation.

The second, called two photon ($2\hbar\omega$) dissociation, proceeds similarly but the bound population leaves the potential well at the three photon gap. After this crossing however, the system returns a photon to the field so that the net process involves the release of two photons of energy. There can be no direct two photon process because of the symmetry of the states involved.

The more subtle points of these processes are investigated further in the following sections of this chapter.

1.3.4 Bond Softening

Nearly twenty years ago the mechanism behind one photon disassociation was suggested [Giusti-Suzor et al., 1990] and experimentally observed [Bucksbaum et al., 1990]. Commonly referred to as Bond Softening (BS), the process works in a manner akin to ATI in atoms; Above Threshold Dissociation (ATD). This involves the absorption of a number of photons and then the stimulated emission of all but one of them. The net result of which is for the system to fragment sharing a photon of energy between the nucleons. Subsequently, the observation of low energy protons ($E_{kin} \approx [\hbar\omega]/2$) is the experimental signature of BS.

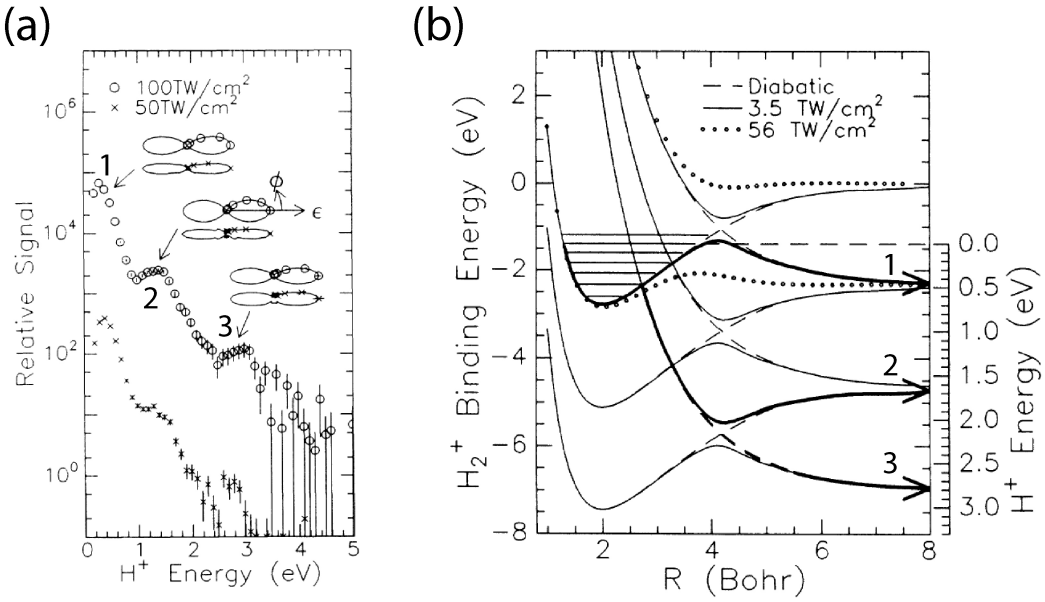

Figure 1.12: Panel (a) shows the energy distribution of protons resulting from the photoionisation of hydrogen. Panel (b) shows dressed potential energy curves for the H_2^+ molecule at three laser intensities calculated using a Floquet method. Labels 1-3 show the one photon, two photon and three photon bond softening routes to fragmentation respectfully. Reproduced from [Bucksbaum et al., 1990]. Note the photon energy here is 2.34 eV, as 532 nm photons were used in the original work.

Assuming the LIP curves (see section 1.3.3 and figure 1.12), obtained from Floquet theory the bond softening process can be seen as a progression through the one photon gap from the bound $1s\sigma_g$ curve to the repulsive $2p\sigma_u$ curve. BS processes involving the net absorption of a more than a single photon are also possible. This is shown clearly in figure 1.12, which illustrates the bond softening process for H_2^+ molecular ions exposed to 100 fs laser pulses at a central wavelength of 532 nm.

1.3.5 Bond Hardening

As well as softening the bond between nuclei, the electric field of an ultrashort laser pulse can also harden it. This Bond Hardening (BH) mechanism occurs when part of the vibrational wavepacket of the system gets trapped in an induced potential well at the peak of the laser pulse. BH was predicted in the early nineties [Giusti-Suzor and Mies, 1992] but was only experimentally verified [Frasinski et al., 1999] seven years later.

The process starts on the leading edge of the pulse, where the vibrational wavepackets around the three photon resonance can cross or exit the bound well through the three photon gap. Now as the laser intensity increases, the width of the one and then three photon gaps increases further, see figure 1.13(a). This leads to the formation of an induced potential well about R=4.5a.u. within which the part of the wavepacket that made the crossing becomes trapped. Past the peak of the pulse, the laser intensity drops and the avoided crossings close; the induced well is inverted, and the trapped wavepacket expelled leading to fragmentation of the internuclear bond, as illustrated in figure 1.13(b).

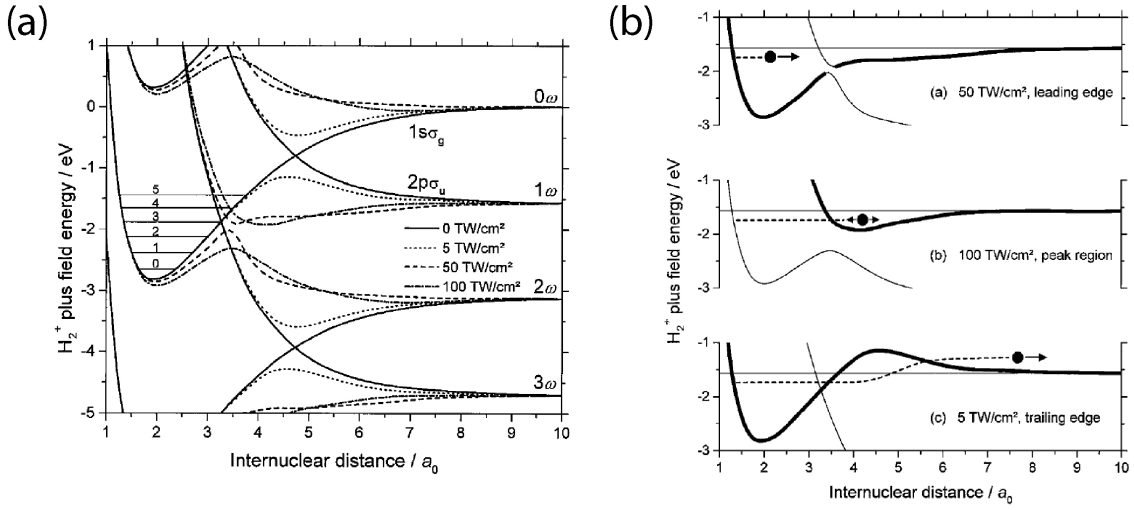

Figure 1.13: Panel (a) shows the dressed potential energy curves for the interaction of the $H_2{}^+$ system with a 790 nm laser field of varying intensity. Panel (b) shows the hardening dynamics for a $H_2{}^+$ system in a 100 TWcm^{-2} laser pulse. On the leading edge of the pulse the vibrational wavepacket crosses the one photon gap. At the peak of the pulse, the width of the one photon gap increases to such an extent that the wavepacket becomes trapped in the induced potential well. Finally, as the pulse leaves the system, the wavepacket is released to large R and the system fragments. Reproduced from [Frasinski et al., 1999].

The experimental signature of bond hardening is a movement of the one photon dissociation signal to lower energy for pulses of increasing duration. This dependence on pulse duration is expected as it is the main determining factor on the lifetime of the induced potential well responsible for the hardening of the molecular bond. Bond hardening is also

thought to be the mechanism behind the counterintuitive alignment [Frasinski et al., 2001] of $H_2{}^+$.

1.3.6 Zero Photon Processes

As well as BH another form of wavepacket trapping exists, which leads to Zero Photon Dissociation (ZPD). Whereas the BH process centres on the three photon avoided crossing, ZPD is dominated by the dynamics around the one photon avoided crossing. Like in the case of BH, part of the wavepacket crosses the gap (in this instance the one photon crossing) on the leading edge of the laser pulse. As the pulse intensity increases this part of the wavepacket gets trapped and cannot follow the bond softening fragmentation channel. Dissociation finally takes place as the pulse intensity decreases and the induced potential well flattens out (figure 1.14).

ZPD only occurs for the sub-set of molecules occupying vibrational states above the one photon crossing rather than the total population, the location of which is strongly dependent on wavelength. And as the population is typically described by a Franck-Condon distribution centred at v=3 for the wavelengths used in the experiments that comprise this thesis ZPD is very unlikely. For lower wavelengths, such as those used in the work of Posthumus [Posthumus et al., 2000] ZPD becomes more likely, as the one crossing occurs lower down the $1s\sigma_g$ potential well.

As ZPD is characterised by having no net absorption of photons from the field the Corresponding experimental signature of ZPD, is the observation of proton signal centred about zero energy.

1.3.7 Coulomb Explosion

As well as dissociation resulting in the production of a neutral hydrogen atom, H(1s), and a proton, H^+, hydrogen molecules can be Coulomb exploded through interaction with intense laser pulses (see equations 1.37 and 1.38). Coulomb Explosion (CE) occurs when the molecule or molecular ion is rapidly ionised, leading to an energetic break up of the molecule due to the mutual Coulomb repulsion between the positively charged constituent ions. Consequently, the experimental signature of CE is the detection of high energy protons. Also for CE to be possible the laser pulses used must be considerably more intense than those that can bring about the photodissociation process outlined in sections 1.3.4-1.3.6.

$$H_2 + n\hbar\omega \quad \rightarrow \quad 2H^+ + 2e^- \tag{1.37}$$

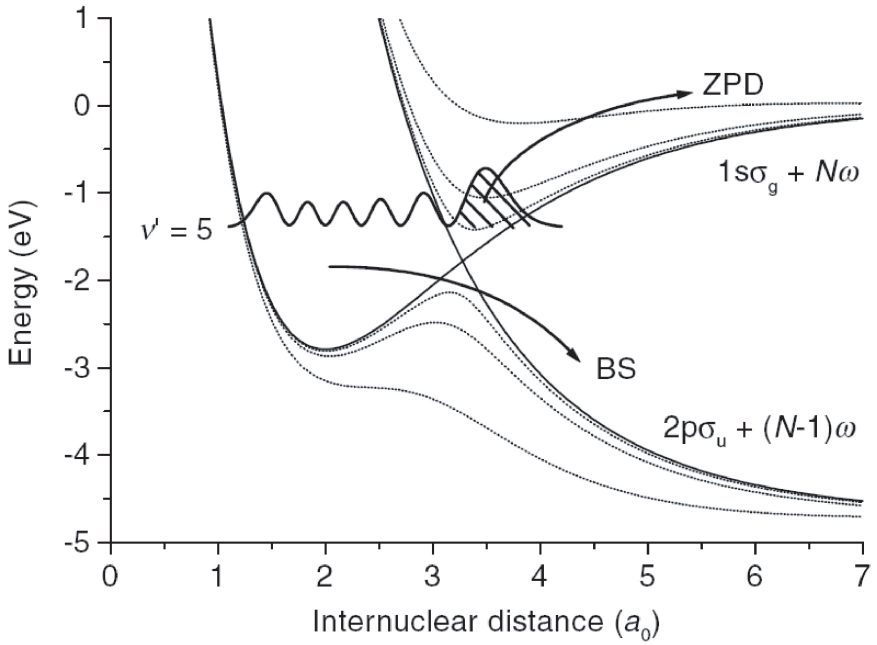

Figure 1.14: The mechanism of Zero Photon Dissociation (ZPD). Wavepackets in vibrational levels below the one photon resonance disociate via Bond Softening (BS) whilst those in levels above the crossing can follow an alternative path to ZPD. Reproduced from [Posthumus et al., 2000]. Note the LIP curves shown are for a field centred at a wavelength of 266nm.

$$H_2^+ + n\hbar\omega \quad \rightarrow \quad 2H^+ + e^- \tag{1.38}$$

At first glance one may assume that the process defined in equation 1.37 may seem the most likely. However, many experiments (for instance [Codling et al., 1988, Walsh et al., 1997]) have shown that Coulomb explosion occurs from the molecular ion (see equation 1.38), rather than the neutral. It is proposed that initially the molecule is singly ionised on the leading edge of the laser pulse [Frasinski et al., 1987]. These ions then begin to dissociate via BS or another mechanism before being promoted onto the Coulomb curve at the peak of the laser pulse [Thompson et al., 1997], (see figure 1.15). This is backed up by the observation of protons with $E_{kin}\approx$4 eV, suggesting that the CE event takes place at R≈6 a.u. Direct CE would produce protons with $E_{kin}\approx$20 eV. Such energetic protons have never been seen in experiments of the type (laser frequency, intensity and pulse duration) reported here.

The study of CE dynamics has also lead to a new experimental method in order to track the dynamics of molecular dissociation. Coulomb Explosion Imaging (CEI) allows the extraction of the internuclear separation by conducting a traditional pump-probe spectroscopy (section 3.3.2) experiment, but with the laser intensity of the probe pulse sufficient to

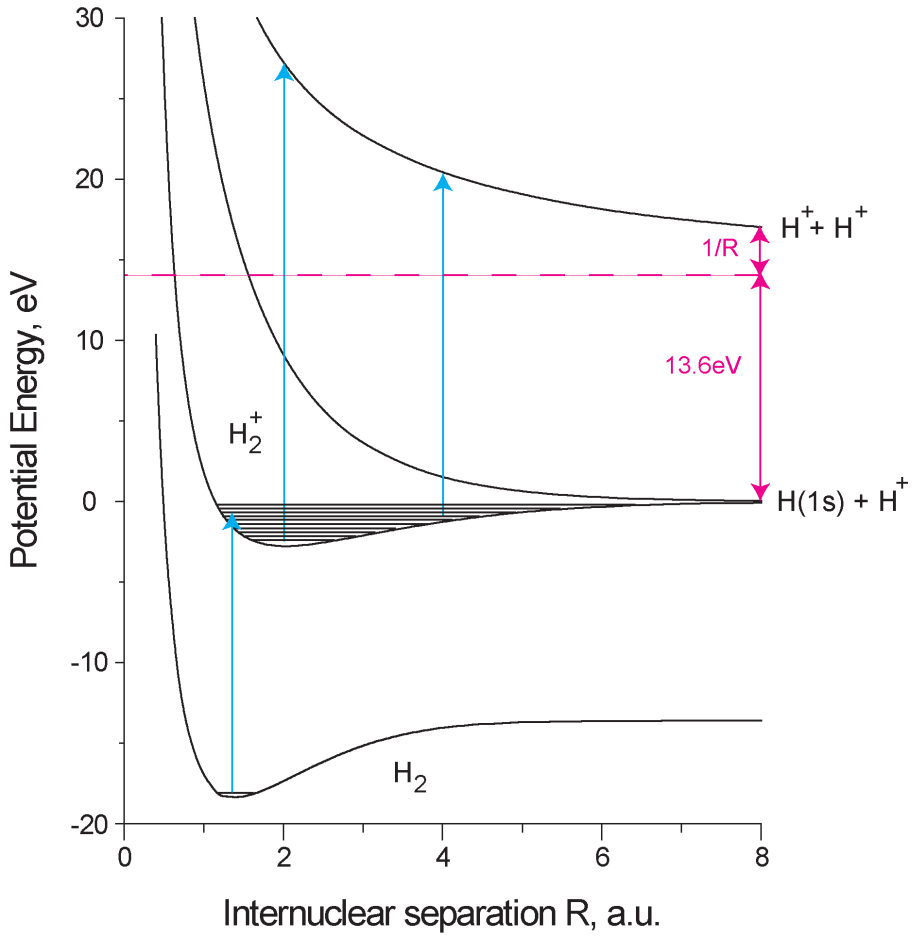

Figure 1.15: The potential energy of the H_2 system. The ground state of H_2 is shown, as are the $1s\sigma_g$ and $2p\sigma_u$ levels of $H_2{}^+$. The Coulomb potential curve is also shown. The cyan arrows indicate the Coulomb explosion process favoured by the system, and the magenta arrows explain the energetics behind these dynamics.

induce CE. The time between the laser pulses can then be controlled, thus the evolution of the nuclear wavepacket can be tracked. This idea was pioneered on hydrogenic systems [Trump et al., 1999, Posthumus et al., 1999] in the late nineties and has since been developed by several groups world wide, including our own.

Using CEI the internuclear separation at fragmentation, R_e, can be established by measuring the kinetic energy of release, $E_{kinetic}$, and using equation 1.39 where Q_1 and Q_2 are the atomic charges of the molecules constituent atomic cores and C_m is an empirical factor specific to a given molecule.

$$E_{kinetic} = \frac{13.6 C_m Q_1 Q_2}{R_e} \tag{1.39}$$

1.3.8 A Classical Model of Field Ionisation

$$I_p \approx I_p(H_{atom}) + \frac{1}{R} \tag{1.40}$$

The ionisation potential, I_p, of the hydrogen molecular ion is dependent on the internuclear separation of the molecular ion's constituent protons, [Yu et al., 1998, Zuo et al., 1993] as expressed in atomic units by equation 1.40. This fact, the fact that protons emanating from CE have energies of ≈4 eV suggested that the CE occurs when the internuclear separation is considerably larger than the equilibrium distance given by the $1s\sigma_g$ potential of two atomic units. A possible reason for this can be illustrated using a simple model of field ionisation for diatomic molecules and ions [Seideman et al., 1995].

In this one dimensional treatment, the potential of the molecule and the laser field, V(z, R, E_0), is given by equation 1.41. The molecule is considered to be aligned parallel to the z-axis and the laser's electric field, which is considered to be static. As before, R represents the internuclear separation and E_0 the amplitude of the lasers electric field and the individual nuclear charges are q_1 and q_2 respectively.

$$V(z,R,E_0) = -\frac{1}{\sqrt{\left(z-\frac{R}{2}\right)^2}} - \frac{1}{\sqrt{\left(z+\frac{R}{2}\right)^2}} - zE_0 \tag{1.41}$$

$$E_L = \frac{(-E_1 - \frac{q_2}{R}) + (-E_2 - \frac{q_1}{R})}{2} \tag{1.42}$$

$$E_{maxshift} = \pm E_0 \frac{R}{2} \tag{1.43}$$

The subsequent energy levels of the valence electron, E_L, are then given by equation 1.42. First used by Posthumus et al [Hatherly et al., 1994, Posthumus et al., 1995, Posthumus et al., 1996] to predict appearance intensities for molecular ionisation, the model can easily be adapted for the hydrogen molecular ion by substituting the relevant charges. The electric field also Stark shifts the energy level of the valence electron, creating two evenly populated states within which the valence electron resides. This energy splitting, from the original level, can be defined at large values of R by equation 1.43.

Figure 1.16 shows the results of equations 1.40-1.42 for an electric field of 0.06 atomic units (equivalent to a laser intensity of 1.2×10^{14} Wcm^{-2}) and four different internuclear separations, 3 a.u., 6 a.u., 9 a.u. and 12 a.u. respectfully. In panel (a), where the internuclear separation is 3 a.u. and at lower values of R the two least bound energy levels still occupy the same potential well. This allows the electron to oscillate freely between both nuclei. As the internuclear separation increases (see panels (b) and (c)), the lower of

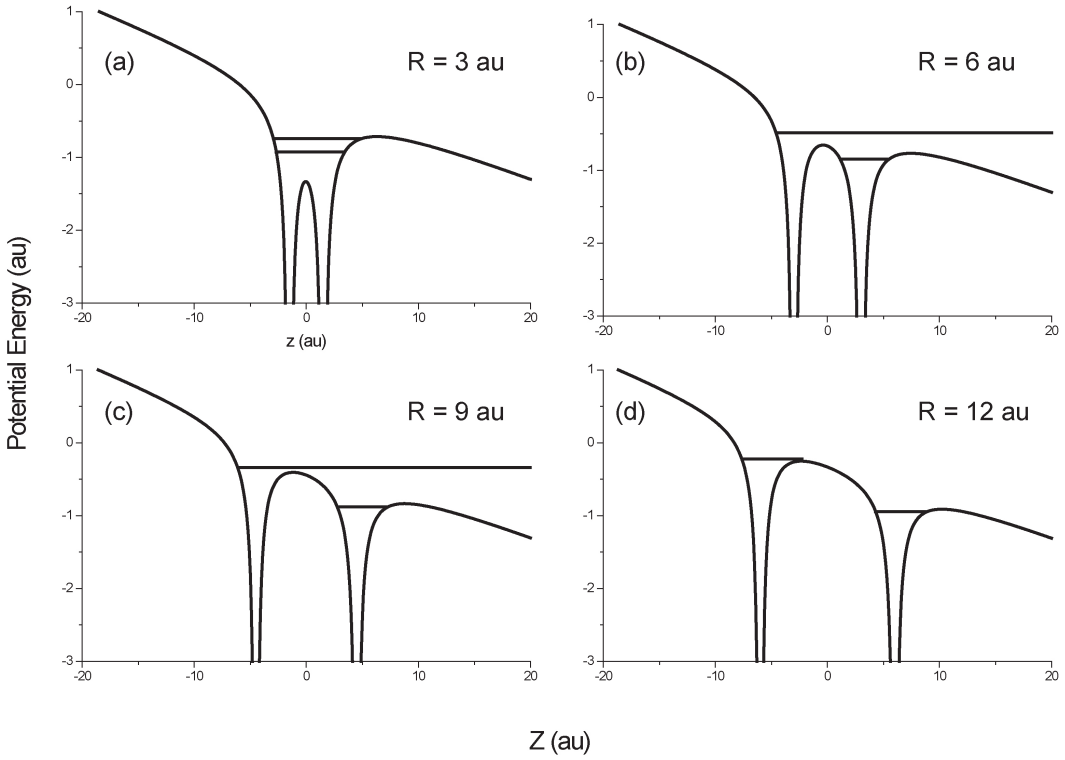

Figure 1.16: The potential energy of an electron in the combined electric field of two protons located at $\pm\frac{R}{2}$ and a static field of 0.06 a.u. (I$\approx$1.2$\times10^{14}$ Wcm^{-2}) The horizontal lines represent the lowest energy levels in this simple model of a $H_2{}^+$ ion in a laser field. The potential is obtained using equation 1.41 and the electronic states from equations 1.40 and 1.42.

the two levels becomes restricted to one of the nuclei. This electron localisation leads to an increased ionisation rate, for when the sign of the E-field switches the lower localised state is raised up and is free to escape.

If the separation of the nuclei is increased further still (see panel (d)), the potential barrier becomes significantly large to restrict the electron oscillating between the nuclei at all and the system behaves like an atom. This causes a drop in the ionisation rate.

1.3.9 Charge Resonance Enhanced Ionisation (CREI)

A more precise treatment of the ionisation rate's dependence on the internuclear separation was presented by Zon and Bandarauk [Zuo and Bandrauk, 1995]. This treatment involved obtaining numerical solutions to the three dimensional TDSE within the Born-Oppenheimmer approximation for molecules aligned with the field. As illustrated by figure 1.17, their calculations suggested two regions of enhanced ionisation; one centred at 7 a.u. and the second at 10 a.u.. The second of these peaks is well predicted by the classical model

of field ionisation described in section 1.3.8 and can be thought of as a consequence of the strong coupling between the relevant electronic states. Also as R increases, the dipole matrix element $\langle 1s\sigma_g|ez|2p\sigma_u\rangle$ diverges as R/2 (see equation 1.27 and [Bates, 1951]) and ionisation from these charge resonant states [Mulliken, 1939] is enhanced. Above 10 a.u. the rate drops due to the increased width of the inner barrier which inhibits tunnelling between the two wells.

The first region around 7 a.u. however, is thought to have its origin in a different process called Charge Resonance Enhanced Ionisation (CREI). This is thought to be caused by an asymmetric charge distribution in the two wells and the subsequent competition between tunnelling between the wells and ionisation from the upper state. This ratio is dependent on the laser intensity and frequency, a fact which can be seen by comparison of the different calculations shown on figure 1.17.

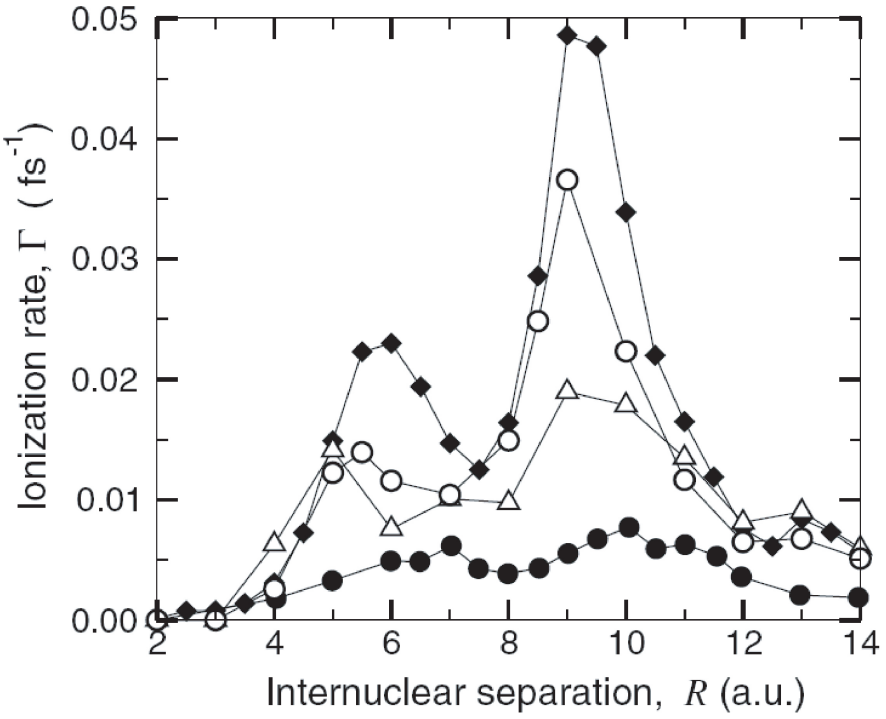

Figure 1.17: The ionisation rate of $H_2{}^+$ against internuclear separation of the molecules constituent protons at a maximum intensity of 1×10^{14} Wcm^{-2}. The dependence of the ionisation rate on the laser frequency is also illustrated as data points from two wavelengths are shown. Filled diamonds correspond to time independent cycle averaged static field rates [Plummer and McCann, 1997], while hollow [Peng et al., 2003] and filled circles [Zuo and Bandrauk, 1995] signify time dependent rates all at λ=1064 nm. Hollow triangles correspond to time dependent rates at λ=800 nm [Peng et al., 2003]. Reproduced from [Peng et al., 2003].

In figure 1.17 three sets of calculations [Zuo and Bandrauk, 1995]

[Plummer and McCann, 1997] and [Peng et al., 2003], are shown. The calculations are a mixture of time-dependent and time-independent approaches at wavelengths of 790 nm and 1064 nm. But all these treatments predict the CREI feature and the peak associated with the increased coupling between the two charge resonant states.

Although CREI was first predicted in 1995 it took nearly ten years for it to be observed in femtosecond pump-probe experiments [Pavičić et al., 2005, Ergler et al., 2006c].

1.4 Molecular Alignment

In ionisation studies of molecules alignment plays a critical role
[Stapelfeldt and Seideman, 2003] with those molecules that are aligned to the electric field of the laser, being more easily ionised than those that are not [Frasinski et al., 1987, Schmidt et al., 1994, Thompson et al., 1997]. Typically, alignment is quantified using the $cos^2(\theta)$ parameter, where θ is the angle between the electric field vector and the molecular bond. This type of alignment, along a specific axis, is only is possible with linearly polarised laser fields, as the polarisation vector of circularly polarised light varies too quickly [Ellert and Corkum, 1999]. However, with circularly polarised light, molecules can be aligned to a plane.

In a thermal sample of a diatomic gas the molecules will be randomly aligned, as there is no preferred axis. However, once the molecules are exposed to an electric field, any anisotropy in the polarisability of the different natural axes of the molecule will result in alignment effects, with the more polarisable axis, aligning with the field. This is even the case in homonuclear diatomics such as hydrogen, where the asymmetry is relatively small. If laser pulses are used with durations equal to or longer than the natural rotational period of the molecule in question pendular states are created and the system exhibits a high degree of alignment throughout the pulse [Friedrich and Herschbach, 1995].

If the laser field, however, is shorter in duration than the natural rotational period of the molecule, the alignment is more transient in nature, and can be thought of as the molecule experiencing an impulse or kick towards alignment [Seideman, 1999]. This dynamic alignment results in the initiation of a rotational wavepacket that then evolves in time experiencing full and fractional revivals, see section 1.5.1 and chapter 8. This dynamic alignment has the advantage of outlasting the pulse and is therefore often referred to as field-free alignment.

In the case of perfect alignment the $\cos^2(\theta)$ parameter is equal to unity. Anti-alignment, or disk alignment (alignment into the plane perpendicular to the electric field) corresponds to $\cos^2(\theta)$=0, While $\cos^2(\theta)$=1/3 for a randomly aligned sample. (The $\cos^2(\theta)$ parameter is discussed in more detail in chapter 8.)

As the ionisation process can be controlled through alignment, lots of experimental and theoretical work has been done to study both the adiabatic and dynamic alignment of molecules with strong laser pulses. Good overall reviews of such work can be found in the literature, for example; see the experimental review [Rosca-Pruna et al., 2001] and numerical modelling review [Springate et al., 2001] .

1.5 Quantum Wavepacket Revival

Wavepackets are used to describe the behaviour of quantum systems which exhibit particle like behaviour, such as locality [Merzbacher, 1998]. Unlike particles, wavepackets tend to disperse as they propagate in time. In some systems however, this dispersion or loss of coherence may naturally reverse itself and the system may return to a state almost identical to its original composition. This behaviour is known as quantum revival, whereas the loss of coherence that occurs is referred to as a collapse of the wavepacket. This use of language can be confusing as traditionally the use of the term collapse would be employed to describe a situation where a system that resides in a superposition of states, is transferred into a single eigenstate of the system by a measurement. To avoid such confusion, I shall avoid this term unless using it to in its more traditional meaning.

Chapters 7 and 8 of this thesis deal with the idea of quantum wavepacket revivals in the nuclear dynamics of hydrogenic systems. In the first instance these revivals occur in the vibrational dynamics of the hydrogen molecular ions, whilst the second section deals with revivals that occur in the rotational degree of freedom of neutral hydrogen molecules. In each instance the nuclear dynamics are initiated and then imaged using a few cycle laser pulse pump-probe set up described in section 3.3.2.

1.5.1 Dynamic Alignment and Rotational Wavepackets

As mentioned in section 1.4 molecules can be dynamically aligned by laser pulses shorter in duration than the molecules' natural timescale. As this topic is the subject of the body of chapter 8, only a brief treatment is presented here. In the experiments the first (pump) laser pulse excites a superposition of rotational states, Ψ(t), in the ground state of the neutral molecule, given by equation 1.44. Here J and M are the rotational and magnetic quantum numbers, and, E_J is the energy of a given J-state (obtained using the rigid rotor model, equation 1.45) and a_j quantifies the weighting of the specific J-states.

$$\Psi(t) = \sum_J a_j \exp\left[-i\frac{E_J}{\hbar}t\right] \mid J, M\rangle \tag{1.44}$$

$$E_J \approx hcB_0J(J+1) \tag{1.45}$$

The second (probe) laser pulse can then be used to image the time-evolution of the rotational wavepacket by Coulomb Explosion Imaging (CEI).

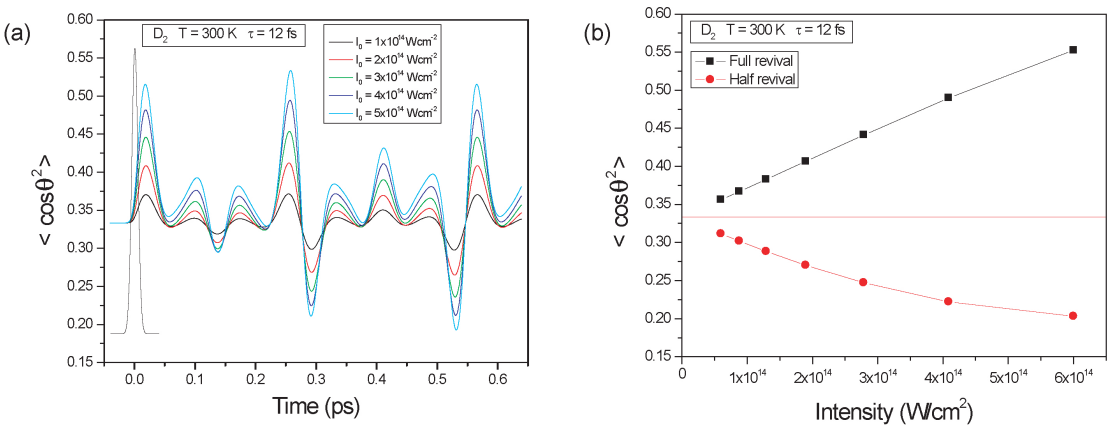

Figure 1.18: The alignment of D_2 molecules after the interaction of a 12 fs laser pulse. The degree of dynamic alignment is quantified using the $\cos^2(\theta)$ parameter. Panel (a) shows how the rotational wavepacket evolves through time for different laser intensities. Both the full revival (at 560 fs) and the fractional revivals (1/4 at 140 fs, 1/2 at 280 fs and 3/4 at 420 fs) are apparent. Panel (b) shows how the degree of alignment changes with intensity for the disk alignment and for the parallel alignment. Figure reproduced from a private communication with Dr. R. Torres of Imperial College London.

Using the $\cos^2(\theta)$ parameter to quantify the degree of alignment, see figure 1.18, the wavepacket dynamics can be evaluated [Dooley et al., 2003, Torres et al., 2005]. The nuclear spin statistics [Banwell, 1983, Hollas, 2002] of the molecule must also be considered in the evaluation of the wavepaket's evolution, as they govern which J-states in the superposition can beat with one another.

For deuterium, a bosonic molecule of nuclear spin 1, the consideration of the nuclear spin statistics confines the beating of the J-states to $\Delta J = \pm 2$ and subsequently the frequency of the beating is given by equation 1.46 where ω_1 equals the frequency of the $J=1$ rotational state.

$$\Delta\omega_{J,J+2} = (4J+6)\frac{\omega_1}{2} \tag{1.46}$$

The results reported in chapter 8 and in Bryan et al, [Bryan et al., 2007a] on the impulsive alignment of deuterium represent the second published experiment on deuterium, after the work of Lee et al [Lee et al., 2006]. More recently Bocharova et al [Bocharova et al., 2008] and Chen et al [Chen et al., 2007] have published complementary studies and it is within the frame work of these studies that our experiments are analysed.

1.5.2 Vibrational Wavepackets

As in the case of the rotational wavepackets, pump-probe techniques have been used to initiate and then image vibrational wavepackets [Vrakking et al., 1996]. Results with hydrogenic molecular systems form the main body of chapter 7 in this thesis. The vibrational wavepackets however, exist in the ions created by the first pulse rather than in the neutral population and the superposition of states is across an array of v-states rather than J-states.

The mathematics used to describe the vibrational wavepackets are very similar to those used in the rotational case. This can be seen by comparing equations 1.44 and 1.47. However, this should not be surprising as the dynamics both occur in anharmonic potentials and, as such, the analysis of their behaviour should be similar.

$$\Psi(R,t) \quad = \quad \sum_{v} a_v \exp\left[-i\frac{E_v t}{\hbar}\right] \psi_v(R) \tag{1.47}$$

Equation 1.47 shows the superposition of vibrational states, Ψ(R,t), as a function of internuclear separation, R, and the evolution time, t, where ψ_v(R) represents the individual wavefunctions of the vibrational eigenstates, v of energy E_v and a_v represents the v-states' overlap integrals with the v=0 ground state in the neutral molecule.

The wavepacket is thought to be formed on the inside of the 1sσg level of the molecular ion following ionisation from the neutral ground state. The wavepacket then evolves, with each v-state proceeding back and forth across the potential well with their respective time periods. This leads to the wavepacket experiencing periods of dephasing and then revival. In the experiments CEI is used to image this motion as a function of evolution time (the delay between pump and probe pulses).

Figure 1.19 shows a theoretical prediction of the behaviour of a vibrational wavepacket in $D_2{}^+$ as a function of the internuclear separation and the wavepacket evolution time. Dephasing and revival of the wavepacket can be observed in the plot and correspond to the wavepacket having a high degree of locality or coherence (at formation and subsequent revival) or a lack of coherence (locality) when the wavepacket has fully dephased.

More details can be found in chapter 7, which contains a more complete comparison of experiment and theory for vibrational wavepacket dynamics in $H_2{}^+$, HD^+ and $D_2{}^+$.

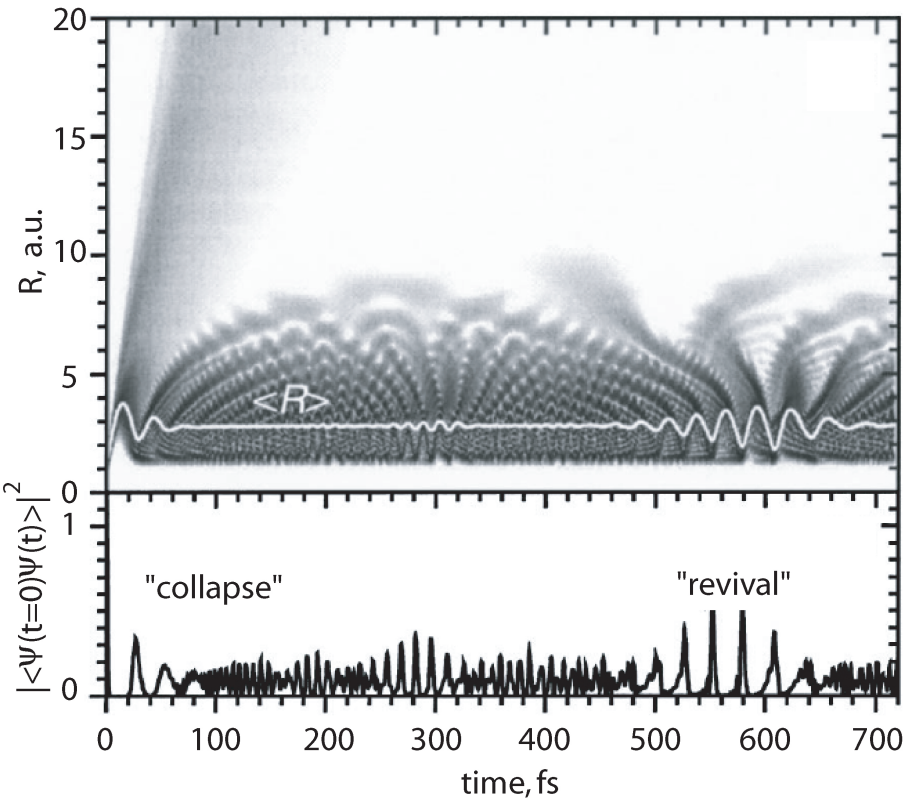

Figure 1.19: Coherent motion of the D_2^+ nuclear wavepacket following ionisation of $D_2(v{=}0)$ in a 5 fs, $1{\times}10^{15}$ Wcm^{-2} laser pulse. The upper panel shows how the probability density evolves in time whilst the lower panel shows the autocorrelation function. Also shown on the upper panel is the mean value of the internuclear separation R. On the upper panel, dark areas represent regions of high intensity on a logarithmic grey-scale. Reproduced from [Feuerstein and Thumm, 2003].

1.5.3 Rydberg Wavepackets

As well as nuclear wavepackets in molecules, Rydberg wavepackets have been a fruitful arena within which scientists have conducted experiments to understand and control quantum phenomena. For a detailed list of previous and current approaches see the recent review by Fielding [Fielding, 2005]. Rydberg atoms and molecules are systems with high principal quantum numbers. Typically, their classical periods are of the order of ≈10 ps rather than ≈100 as, which would be a typical period of a ground state orbital. Correspondingly, the electron orbitals are also spatialy large, as governed by Kepler's third law ($T^2 \propto r^3$).

Work in this area of research was initiated to test the correspondance principle and as a possible pathway to coherent control. The earliest studies started with investigations into atomic systems [ten Wolde et al., 1988, Yeazell et al., 1990, Meacher et al., 1991] and

then progressed onto molecules [Stavros et al., 1999, Minns et al., 2003] including hydrogenic systems [Texier and Jungen, 1998]. Molecular systems were a natural progression in the field, as Rydberg molecules offer some of the complications of expanded systems of biological and chemical interest whilst remaining experimentally tractable. As the natural period of motion is of the order of thousands of picoseconds, laser pulses one picosecond in duration are adequate to image the wavepacket motion.

Typically, treatments are based on semiclassical theories, such as that of Altunata et al, [Altunata et al., 2002], have been used to understand the excitation process and resulting dynamics. However, insight can be obtained into the problem by considering the problem in simplified manner.

$$|\Psi(r,t)|^2 = r^2 \left| \sum_n a_n R_{nl}(r) \exp\left[-i\omega_n t\right] \right|^2 \tag{1.48}$$

Initially, the system is in the ground state. After excitation (usually by the first (pump) pulse in a pump probe scheme) a superposition of high Rydberg states is created, as defined by equation 1.48 where r represents the radial coordinate, a_n, and ω_n are the amplitudes and the angular frequencies of each Rydberg state in the superposition. The excitation is such that the wavepacket is formed on the inner turning point of the orbitals. As in the previous instances of wavepacket revivals, an anharmonicity in the potential surface of the wavepacket leads to a spatial dispersion of the wavepacket followed by repeated localisations in space or revivals.

Figure 1.20 shows the evolution of a Rydberg wavepacket in hydrogen. The wavepacket is formed at small r and localises at the outer turning point of the potential well. Over time the degree of this localisation diminishes until the wavepacket is spread right across the r coordinate. Given time the wavepacket revives, not shown here, and the localisation returns. Partial and fractional revivals are also observed in Rydberg systems. For a complete review of systems within which revival phenomena are apparent, see the recent review by Robinett [Robinett, 2004].

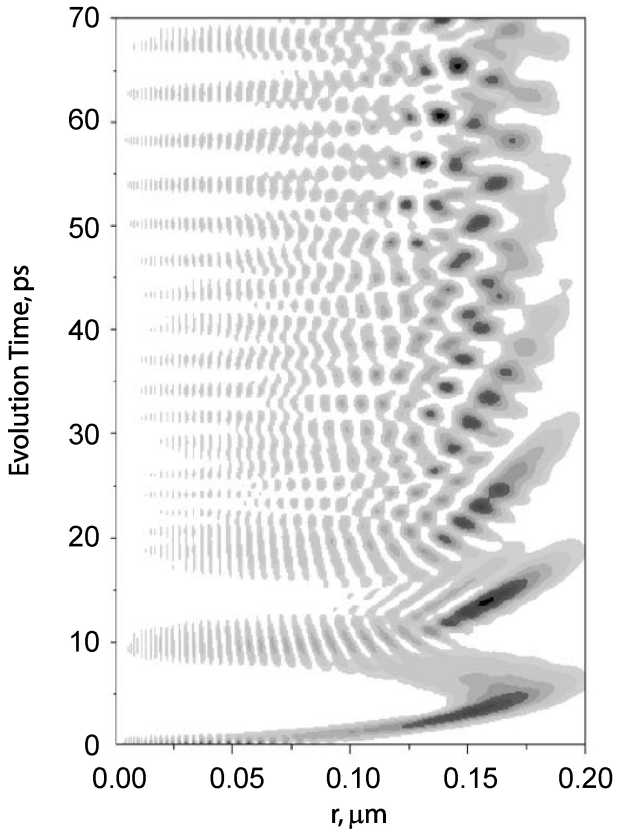

Figure 1.20: Time dependent radial distribution function of a radial wavepacket excited with a 1 ps pulse centred around n=40 in the hydrogen atom. Dark areas represent regions of high intensity. Adapted from [Fielding, 2005].

1.6 Summary

This chapter has given an introduction to the physics discussed in this thesis and provides the necessary foundations for the work I have undertaken. A brief history of strong field ionisation in atoms and hydrogenic molecules has been given, with the major works highlighted. As well the pioneering work in the field, several contemporary ideas have been presented and it is these that will prove to hold most sway over the rest of this document.

As well as high field effects, ultrafast physical phenomena have been discussed, particuarly the time resolved imaging of wavepacket dynamics. Three systems have been mentioned; radial electron wavepackets in Rydberg atoms and both rotational and vibrational wavepackets in hydrogenic molecules. The latter two will be discussed in depth in chapters 7 and 8. It is worth noting that as laser pulse durations are reduced further still, attosecond pulses have begun to be used to probe electronic dynamics, for example [DiMauro, 2002]. As such short pulses were unavailiable to our researh group, the discussion of these dynamics has been omitted.

Chapter 2

Experimental Configuration

2.1 Introduction

The experimental results reported in this thesis were obtained using target area one (TA1) of the Astra laser whilst working in collaboration with Professor Ian Williams' group from Queen's University Belfast. This laser is located at the STFC Rutherford Appleton Laboratory and comprises part of the Central Laser Facility in the UK. The system is capable of generating 500 μJ, 10 fs laser pulses at a repetion rate of 1 kHz and 25 mJ, 35 fs pulses but at a reduced repetition rate of 10Hz.

As well as a comprehensive description of the laser system, this chapter includes details of the two experimental chambers employed: an ultra high vacuum time of flight mass spectrometer (TOFMS) and a fast positive ion beam apparatus (Ion Rig). The TOFMS mass spectrometer was constructed at UCL [Thomas, 1999], whilst the Ion Rig was built in Belfast [McKenna, 2000], however, both systems are maintained and operated by the collaboration collectively when at Astra. The laser is setup in a Master Oscillator Power Amplification (MOPA) configuration (see Figure 2.1) and utilises Chirped Pulse Amplification (CPA) [Strickland and Mourou, 1985, Maine et al., 1988] techniques to ensure that the high energy ultrashort pulses it produces are of a high quality and that damage to the system during amplification is avoided.

Finally, there is a discussion of the optical metrology used in target area one. This primarily contains information on methods used to measure the pulse duration, but also includes a brief synopsis of the optical spectrometers used to check the pulse bandwidth. Note all pulse durations quoted in this thesis are Full Width Half Maximum (FWHM) values, unless stated otherwise.

2.2 The Astra Laser

The Astra laser provides pulses to two target areas simultaneously; a Tera-Watt (TW) target area (TA1) and a Peta Watt (PW) target area (TA2). Details of the laser system and target area one can be found below, however, the extra amplification stages and beam transport for target area two are not discussed.

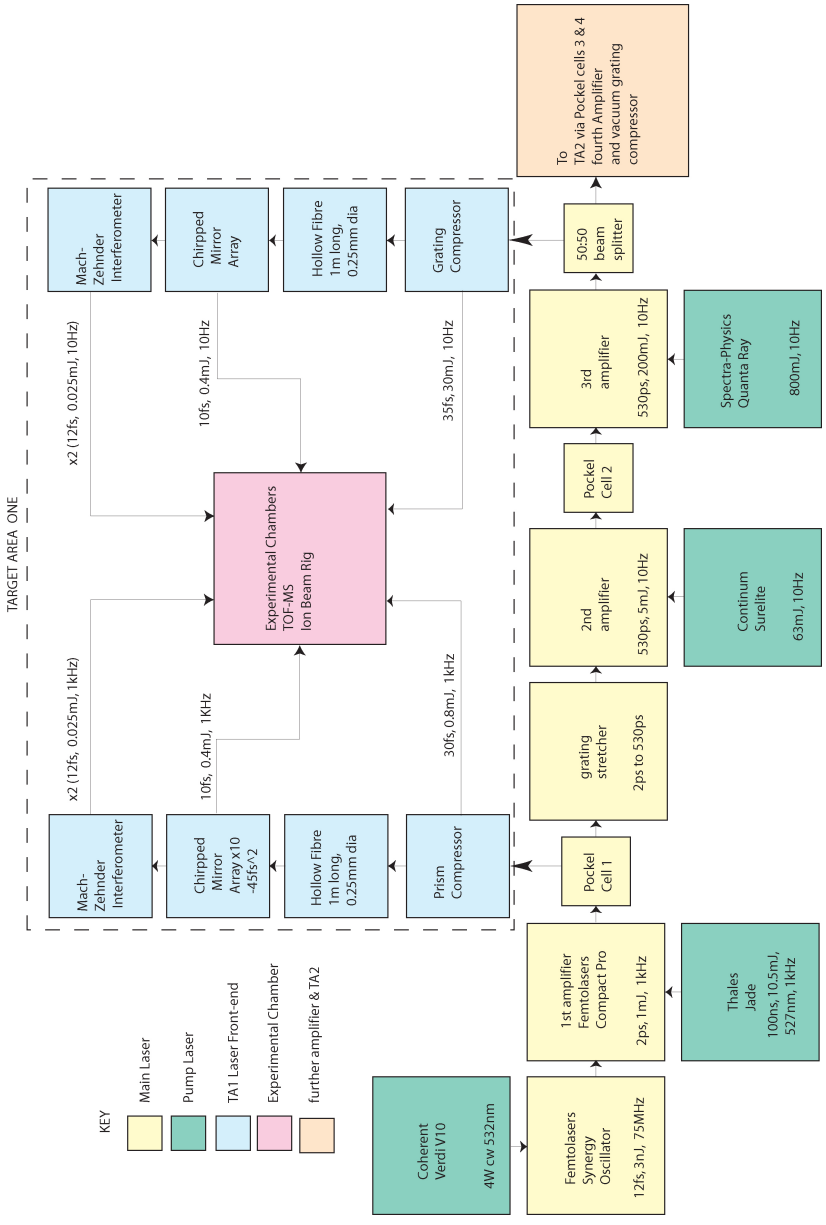

Figure 2.1: Flow diagram of the Astra laser and target area one.

2.2.1 Oscillator and 1 kHz, 1 mJ, 30 fs, System

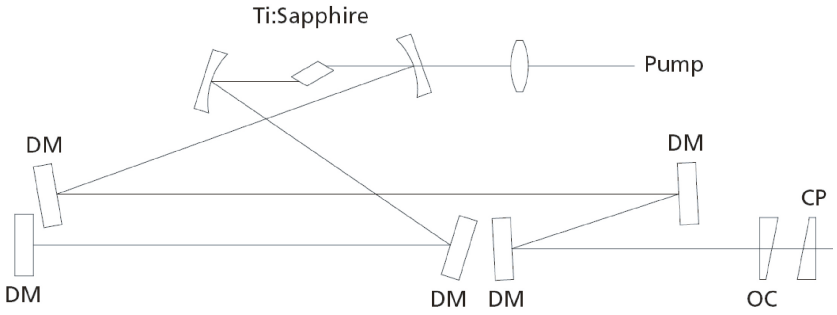

Figure 2.2: Schematic of the synergy oscillator reproduced from http://www.femtolasers.com DM = dispersive mirror, OC = output coupler and CP = wedged glass plate.

The oscillator of the Astra laser (Figure 2.2) is commercially available from Femtolasers GmbH. It produces pulses of 12 fs duration about a central wavelength of 800 nm with a 100 nm bandwidth at a repetition rate of 75 MHz. The titainium doped sapphire (Ti:S) crystal [Moulton, 1986] in the oscillator is pumped by a frequency-doubled Verdi V10 (Coherent Inc.) laser operating at 532 nm. Inside the system dispersive mirrors are employed as a means of compensating for broadband inter-cavity group delay dispersion [Stingl et al., 1995].

Following the oscillator, the 75 MHz pulse train is amplified (Femtopower Compact Pro) [Hentsche et al., 2000], also made by Femtolasers GmbH, (figure 2.3). On leaving the oscillator, the pulses are stretched to a duration of 20 ps by material dispersion within a 100 mm long block of SF57 glass. The pulse duration is increased to avoid damaging sensitive components in the amplifier, such as the Ti:S crystal. A Faraday isolator is also employed to reduce the risk from amplified back reflections. The pulse duration is expanded in this way for simplicity and to avoid the added complication of alignment issues a grating or prism system would introduce. The temporal stretch also involves an acousto-optic programmable dispersive filter (AOPDF) or Dazzler. This is used to shape the pulses ensuring maximum contrast on target (see section 2.2.4). These shaped pulses are then amplified in a second crystal, which is held in a vacuum chamber and Peltier cooled to 258 K. The Ti:S gain medium, which is Brewster cut and 3.5 mm long, is pumped by a Jade (Thales Inc.) laser, which supplies the amplifier crystal with 100 ns pulses at a wavelength of 527 nm, an energy of 10.5 mJ and repetition rate of 1 kHz. The amplifier is operated in a multi-pass configuration. After the first four passes a Pockel cell selects a fraction of the pulses and subsequently the repetition rate drops to 1 kHz. This is done to reduce the Amplified Spontaneous Emission (ASE) background. Once the selected pulses have passed through the amplifier cyrstal four more times, they are ejected from the amplifier and the beam's diameter is reduced. This is done in order to

optimise the mode overlap of pump and seed beams to ensure the highest possible energy extraction from the pump on the following two final passes through the crystal. Finally, the pulse train leaves the Compact Pro system at an energy of 1 mJ per pulse and a repetition rate of 1 kHz. Throughout this amplification, great care is taken to ensure the broadband pulses are amplified in a manner that ensures a high contrast ratio (10^9), a low B-integral (1), good pointing and energy stability and pulse profile. This is primarily done by controlling the third and fourth order dispersion via chirped mirrors. I.e. actively compensating the unwanted effects of the amplifier components and the extreme stability of the pump lasers.

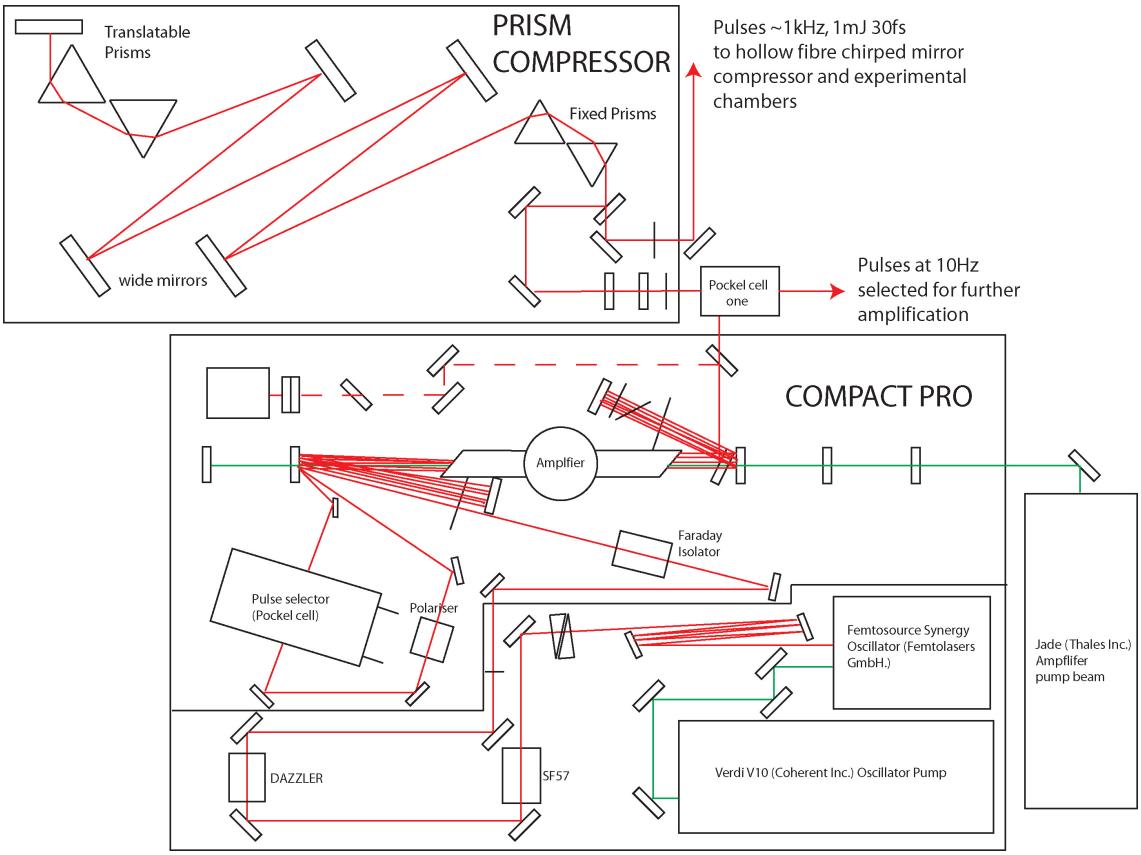

Figure 2.3: A schematic of the Compact Pro, Pockel cell and Prism Compressor employed at Astra.

2.2.2 Grating Stretcher

After leaving the Compact Pro, one in every hundred pulses is selected by Pockel cell one for further amplification. The remaining pulses are fed directly into the target area and comprise the 1 kHz (990 Hz) beam-line in TA1. The selected pulses, at 10 Hz, have to be stretched to allow further amplification. This is essential to conserve the beam's

profile, which would otherwise be severely degraded by non-linear optical affects. A pair of gratings (1500 lines per mm) is employed to increase the duration of the pulses by making the shorter wavelengths in the pulse travel further than the longer wavelengths. This positive chirping of the pulses takes them further from their Fourier transform limited duration, allowing further amplification without beam distortion and/or damaging the optics in the beamline.

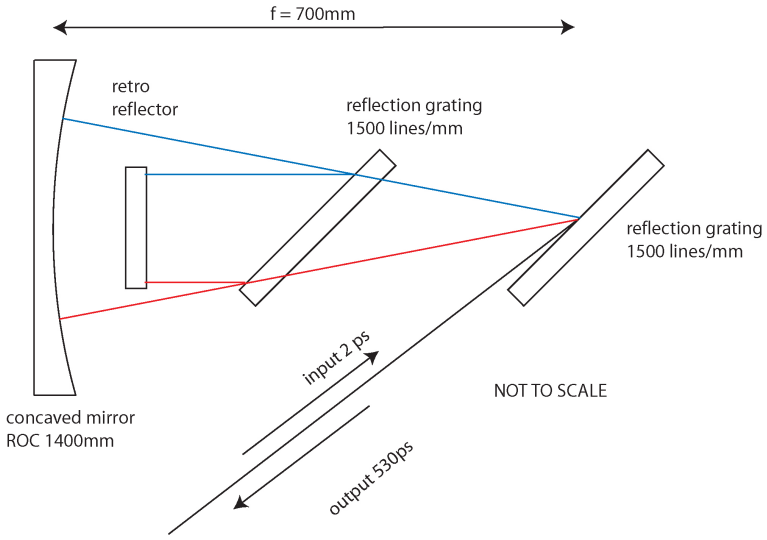

Figure 2.4: Schematic of the grating stretcher used for the high energy 10 Hz beam. (Figure adapted from http://www.clf.rl.ac.uk/Facilities/AstraWeb/AstraTour1.htm).

2.2.3 Energy Amplification

Once the pulses leave the stretcher, they are over half a nanosecond in duration. The additional amplification is done by two amplifiers (figure 2.5). The first raises the beam energy to 5m J and the second to 200 mJ. Both amplifiers in the chain are arranged in a multipass configuration; the first having three passes, and the second four.

The first amplifier is built around a 10 mm diameter, 7 mm thick (Ti:S) crystal that is pumped by counter propagating beams from a 532 nm 63 mJ neodynium-yag (Nd:YAG) pump laser (Continuum Surelite). The beam passes through the crystal three times in a *bow tie* configuration. On leaving this power amplifier the beam diameter is increased to a diameter of 5 mm. It then enters a Pockel cell, which cleans up the pulse profile by removing any ASE and through selecting just one of the amplified pulses. (More than one pulse can be amplified.)

The second Ti:S cystal is also pumped by counter propagating beams from a 532 nm Nd:YAG laser (Spectra-Physics Quanta Ray). Again, the pulse train passes through the crystal in a *bow tie* like configuration, but this times it makes four passes. The Ti:S crystal

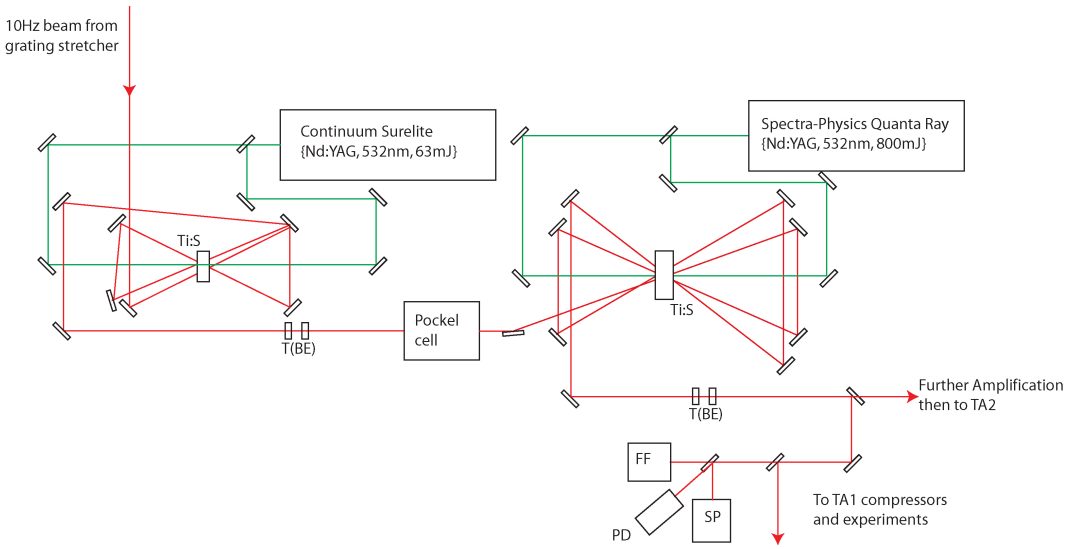

Figure 2.5: The amplification system for the 10 Hz, 25 mJ, 50 fs beam. The angles of the beams through the crystals are greatly exaggerated for clarity. (Figure adapted from [Watson, 2005] and http://www.clf.rl.ac.uk/Facilities/AstraWeb/AstraMainPage.htm)

is 10 mm in diameter and 12 mm thick. These dimensions and the pump beam focussing ensure that a gain region with a uniform intensity profile is established with a 6 mm diameter, allowing very efficient energy amplification. On leaving the amplifier, the beam diameter is increased to 18 mm. A beamsplitter then sends half the beam into Target Area one and half the beam on to the next stage of amplification ready for Target Area two.

2.2.4 Acousto-Optic Programmable Dispersive Filter (AOPDF) or Dazzler

After the first stages of amplification and before the pulses are recompressed, there is a Dazzler [Tournois, 1997, Verluise et al., 2000] in the beam path. (NB. Dazzler is the trade name of the Acousto-Optic Programmable Dispersive Filter (AOPDF) invented and manufactured by Fastlite, however this trade name is used almost exclusively, hence its inclusion here.) This is used to modify the pulse profile in order to ensure the highest possible contrast ratio in the beam. (The contrast ratio (r) is the ratio between the peak intensity and that of the pedestal.) A high contrast ratio is an essential requirement for the majority of experiments conducted in the PW target area, TA2.

The Dazzler allows one to modify the phase and amplitude profile of a laser pulse arbitrarily. This is realised by co-propagating an acoustic wave with the laser pulse along the fast axis of a birefringent crystal. By varying a Radio Frequency (RF) field (both spatially and temporally) using a transducer, the acoustic wave can be fully manipulated. This

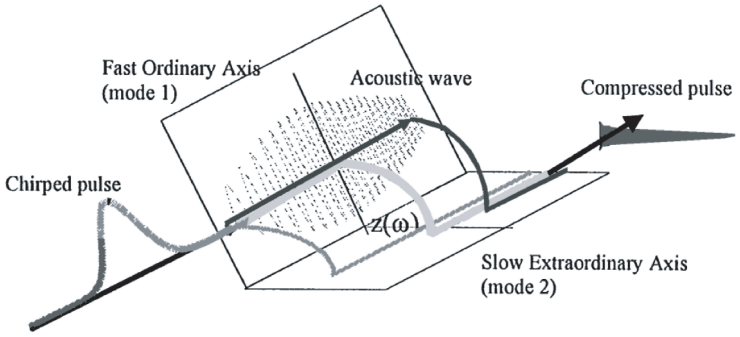

Figure 2.6: The acousto-optic programmable dispersive filter (Dazzler). Reproduced from [Verluise et al., 2000]. In this schematic, the dazzler is used to compress a chirped pulse to its Fourier transform limited profile.

means the refractive index experienced by the optical pulse can be altered. The resulting phase matching leads to the optical pulse experiencing different degrees of diffraction at different depths in the crystal. The result of which is to switch varying amounts of the pulse from the fast (mode 1) to the slow axis (mode 2) of the crystal at different crystal depths, see figure 2.6. As the different axes have different refractive indices, each frequency component of the optical pulse experiences a unique time delay and the phase profile of the optical pulse can be controlled.

Essentially, the Dazzler comprises of an acousto-optic crystal unit that is placed in the optical beam path. This is connected to a RF transducer and a Personal Computer (PC), from which the device is controlled using Fastlite software developed in LabVIEW.

At Astra, the primary use of the Dazzler is to pre-compensate for the unavoidable gain narrowing that occurs during the amplification process. Secondly, it can reduce unwanted dispersion effects introduced by optical components in the beam line to optimise the pulse profile. The first of these is achieved by amplitude shaping, and the second by using the phase shaping capability of the device.

2.2.5 Grating Compressor

The grating compressor works in a similar manner to the grating stretcher discussed earlier (Section 2.2.2). It consists of two diffraction gratings and a flat mirror, see figure 2.7. Initially, the pulses enter the compressor vertically polarised, however, the polarisation vector must lie perpendicular to the rulings on the gratings so the polarisation is rotated 90^o (made horizontal). This is done by rotating the top mirror in the entrance periscope by 90^o to make the normals to the reflective surfaces of the periscope mirrors perpendicular with respect to one another. However, most of our experiments require vertically polarised pulses so the bottom mirror in the exit periscope is also rotated to restore the

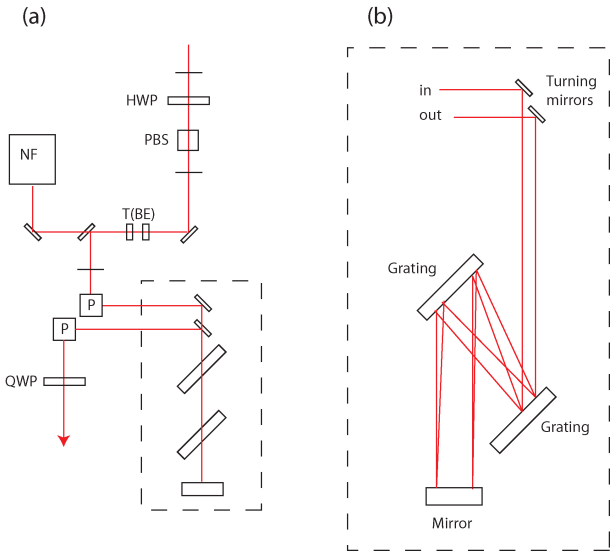

Figure 2.7: The grating compressor in TA1 (a) plan view (b) side elevation. The compressor negatively chirps the positvely chirped 530 ps imput pulses by making the low frequency components of the beam travel further than the higher ones. This results in near Fourier transform limited pulses of 35 fs leaving the compressor with an energy of 25 mJ. HWP and QWP refer to Half and Quarter Wave Plate respectively. PBS refers to a Polarising Beam Splitter, T(BE), a Telescope or Beam Expander and NF, a Near Field monitor. The entrance and exit periscopes are indicated by P.

beam's initial vertical polarisation. Extreme care must be taken when aligning the compressor to produce the shortest possible pulse. The separation of the gratings controls the second order dispersion, or Group Delay Dispersion (GDD), whilst the angle of the gratings is responsible for the degree of Third Order Dispersion (TOD) imparted on the beam. Ideally, both are set to account for the effects of the stretcher, and other dispersive optical components in the beam line, meaning Fourier transform limited pulses leave the compressor.

2.2.6 Prism Compressor

The majority of pulses leaving the *Compact Pro* are sent to a prism compressor system (figure 2.3). Here the pulses are compressed to around 30 fs from an initial duration of 2 ps. The required negative dispersion is generated geometrically. As in the case of gratings (see sections 2.2.2 and 2.2.5), this is done by altering the optical path length each frequency component of the beam has to travel. In the case of the prism compressor [Fork and Martinez, 1984] this is done by making the travel time for the higher (blue) frequencies shorter than that of the lower (red) frequencies.

The compressor comprises of four prisms in a configuration designed by

[Proctor and Wise, 1992], but operated in a double pass mode. Each prism is made of fused silica and cut so that the angle of minimum dispersion coincides with the Brewster angle. The second prism pair (top left of figure 2.3) is mounted on a linear translator aligned parallel to the first face the beam encounters. By altering this translator, the beam's path length in this second prism pair can be changed and the subsequent dispersion imparted to the beam by the compressor controlled. Typically, the path length between the two prism pairs is set at 3 m (6 m due to double pass).

Initially, the beam enters the compressor horizontally polarised with a diameter of 4 mm. The beam diameter is increased to 10 mm before reaching the first prism. On incidence at the first prism, the shorter wavelengths are refracted further than the longer ones. This causes spatial divergence, which continues in the second prism. On leaving the second prism, the beam travels around 3 m to the second prism pair, bouncing off four flat mirrors in the process. The second prism pair is orientated opposite to the first (see figure 2.3). This results in a collimated beam leaving the fourth prism. The light then hits a flat mirror and retraces its path through the prisms and leaves the compressor. The return path is fractionally higher than the incoming route. This allows the compressor output to travel over one of the input optics and reach the relevant output mirror. Finally, the polarisation of the beam is made vertical by rotating the bottom mirror of the exit periscope as before.

Inside the fused silica prisms the pulses experience positive material dispersion. However, as the red edges of the spectrum have further to travel in the prism than the blue, the net effect of the two prism pairs is to slow down the red end of the spectrum with respect to the blue and in so doing impart negative dispersion on the beam. The path length between the prism pairs is set precisely, as this, coupled with the linear translator of the second prism pair, controls the beam path length in the prisms and the dispersion imparted by the compressor on the laser pulses.

Prisms have several advantages over gratings. They tend to be significantly easier to align and generally prove to be more efficient. More importantly, especially when dealing with ultra-short pulses, prisms have negative third order dispersion (TOD). Gratings, as well as the transmission optics earlier in the beam path have positive TOD. Subsequently, a prism compressor can compensate TOD effects more easily. A comprehensive analysis of the second and third order dispersion characteristics of prism sequences can be found in [Sherriff, 1998]. One disadvantge however, is that they are less dispersive than gratings and this explains the neeed for such a long beam path between the prism pairs. More recently, grism compressors and stretchers for CPA based laser systems have been developed [Kane and Squier, 1997], which attempt to maximise the benefits of both grating and prism based systems.

2.2.7 Hollow Fibre

When the laser pulses leave the prism compressor they are 30 fs in duration and have a FWHM band width of 30 nm. In order to reduce the pulse duration, extra bandwidth has to be generated, i.e. the energy of the pulse must be spread out over more frequencies. The physical process utilised to provide this function in the laboratory is Self-Phase-Modulation (SPM) [Agrawal, 2007] in a hollow core optical fibre [Stolen and Lin, 1978, Zheltikov, 2002]. Pulses with the bandwidth required for few-cycle pulses, 100 nm, cannot be amplified to the 1 mJ level directly, due to progressive gain narrowing on each pass of the amplifier cystal.

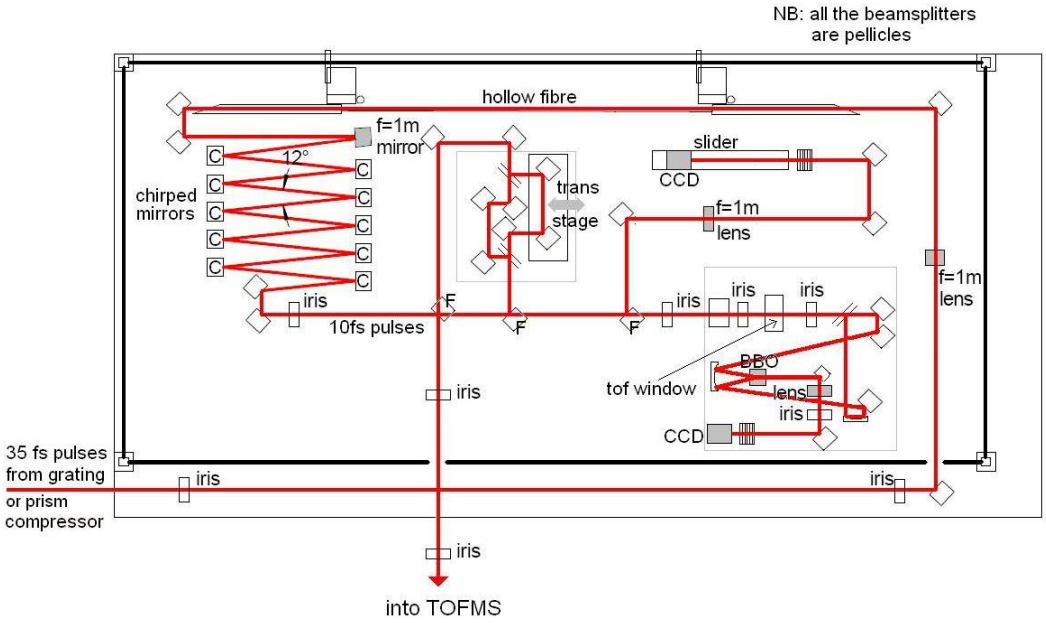

Figure 2.8: Layout of 10 fs optical table showing the hollow fibre and the chirped mirror array. The second harmonic intensity autocorrelator, Mach Zehnder interferometer and spatial overlap camera are also shown.

The hollow fibre chirped mirror configuration used in TA1 (figures 2.8 and 2.9) was constructed by *Attosecond Technololgy* based at Imperial College London [Robinson et al., 2006, Tisch et al., 2005]. The hollow fibres used are a metre in length with an internal diameter of 0.25 mm and are made of fused silica at the Optoelectronics Research Centre based at the University of Southampton. When inserted into the spectral broadening system, the fibre is held in place by a sophisticated mounting system which includes; 0.3 mm thick Brewster cut entrance and exit windows, a large diameter (4 mm) support cladding in which the fibre is held, a gas flow system incorporating a dry membrane diaphragm pump (Leybold DIVAC 0.8LT) and a metering valve (Swagelock SS-4L-MH). There is also a CCD alignment system that monitors the entrance to the fibre, in order for the laser coupling to be optimised. This is of particular importance if the ultra-short pulses generated

are to be energetic enough for use within the experiments.

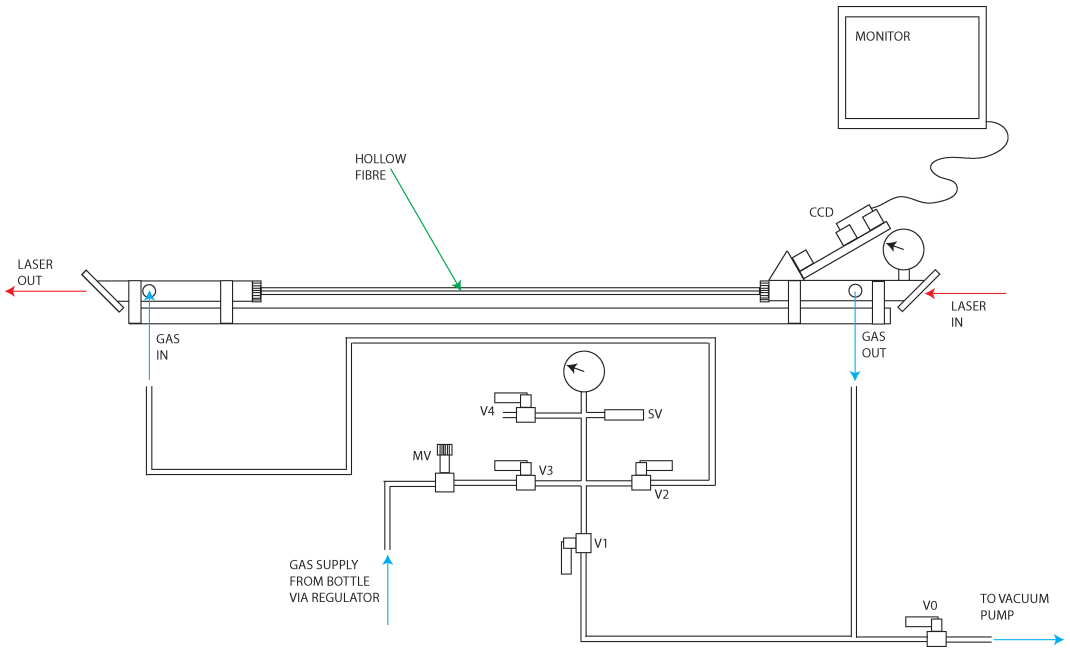

Figure 2.9: The hollow fibre spectral broadening system. The fibre assembly is shown alongside the gas handling system. MV refers to Metering Valve used to control the gas flow after the regulator. Plug Valves, labeled V0-4 are used to define the gases pathway through the system. A Safety Valve, SN, is also included to protect the fibre from pressures exceeding 2.5 bar.

SPM of the laser beam inside the hollow fibre leads to an increase of the bandwidth of the laser pulses and hence the possibility of generating few cycle pulses [Nisoli et al., 1996]. SPM of a light pulse depends on the non-linear refractive index of the medium, in this case a noble gas such as argon or neon, within which the pulse is travelling. As the refractive index is related to the pulse intensity by the optical Kerr effect, different parts of the pulse *see* different refractive indices (equation 2.1), with the more intense parts of the pulse, experiencing a greater refractive index within the active medium. Alternatively, one can consider a time varying refractive index as the laser pulse travels through a point in the medium. This leads to a shift in the instantaneous phase of the pulse and hence the instantaneous frequency, [Nisoli et al., 1997] as the instantaneous frequency is the time derivative of the phase, see equation 2.2.

$$n(I) = n_0 + n_2 \cdot I \tag{2.1}$$

$$\omega(t) = \frac{\delta}{\delta t}\phi(t) \tag{2.2}$$

The frequency chirp ($\delta\omega$) is linear across the region of highest intensity for a Gaussian pulse, figure 2.10(c). This results in the leading edge of the pulse being shifted to lower frequencies whilst the trailing edge of the pulse is shifted to higher frequencies. The new frequencies generated this way are also responsible for the multiple peaks in the frequency spectrum of the broadened light [Siegman, 1986], figure 2.10(d). They arise due to interference between equal spectral components occurring at different times in the pulse. This is brought about by the shape of the frequency shift, illustrated by the dashed lines on figure 2.10(c).

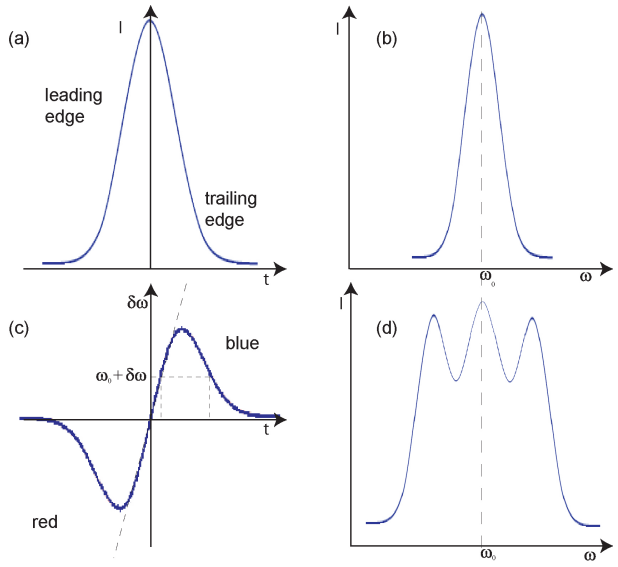

Figure 2.10: Principle of SPM. Adapted from [Rulliere, 1998]. Panel (a) shows the intensity profile of the pulse as a function of time before entering the hollow fibre. (b) shows the same intensity profile but as a function of frequency. (c) illustrates the linear frequency chirp imparted across the most intense part of the pulse due to SPM in the hollow fibre. (d) shows the intensity profile of the pulse after experiencing spectral broadening by SPM in the hollow fibre.

A good approximation to quantify the degree of broadening achievable by SPM is given by the relation 2.3 taken from [Tisch et al., 2005], where E and τ are the energy and duration of the input laser pulse, respectively, η_2 is the non-linear refractive index per bar of gas pressure and p is the gas pressure. This relation also indicates the parameters that can be *tweaked* in the laboratory to optimise the output pulses.

$$\delta\omega \propto \frac{Ep\eta_2}{\tau^2} \tag{2.3}$$

Coupling the light correctly into the fibre is also very important also for optimal broadening. It is possible for several optical modes to be transmitted down the fibre, however,

the most efficient one for this specific case is the EH_{11} hybrid mode.
[Marcatili and Schmeltzer, 1964]. This gives a profile governed by the zero order Bessel function. In order to obtain the best possible coupling, the beam diameter should be 0.65 times the inner diameter of the fibre, which in this case is 0.16 mm. A deviation from this results in increased coupling of higher order modes and subsequently an overall decrease in the hollow fibre's efficiency. To obtain this diameter, the laser beam is focused using a planar convex lens of 1 m in focal length, mounted on a micrometer-driven linear translator. As well as SPM, the laser beam experiences positive dispersion as it travels through the fibre, leading to added dilation of the pulse duration.

$$p(x) = \sqrt{p_0^2 + \frac{x}{L}(p_L^2 + p_0^2)} \tag{2.4}$$

Initially the hollow fibres used in pulse compression systems were statically filled. However, the system in TA1 is run in a differentially pumped mode. This means that the gas pressure in the fibre increases along its length. The dry membrane pump is attached directly to the fibre assembly by the entrance window of the fibre, whilst the gas supply, either neon or argon, is released into the fibre by the exit window via a needle valve (see figure 2.9). This leads to a pressure gradient along the fibre, p(x), described by equation 2.4, where L is the length of the fibre and p_L and p_0 are the gas pressures at the end and the start of the fibre, respectively. Typically, the system is used with the fibre evacuated at the entrance window and with pressures of 0.3 bar for argon and 2.0 bar for neon at the exit window. Running the system in this way has many advantages [Suda et al., 2005, Robinson et al., 2006], the primary one being plasma formation is more easily avoided at the entrance window, which drastically effects efficency and prevents fibre damage.

Figure 2.11 shows the effect of changing the pressure at the exit window on the pulse bandwidth. The optimal situation, with argon, was found to be a pressure of 0.35 bar giving a pulse duration of around 10 fs and an energy around 500 nJ. (From an input pulse of 30 fs duration containing 800 μJ of energy.)

SPM does not alter the temporal profile of the pulse however, dispersion inside the fibre (from both the gas inside the fibre and the grazing incidences the beam makes with the inside of the fibre walls) will alter the temporal profile. This means the pulses leaving the fibre are stretched considerably and subsequently must be recompressed. In the laboratory, this is acheived using chirped mirrors, although other compression schemes can be used. Chirped mirrors are selected as they have the ability to provide a constant GVD right across the laser pulses spectral width [Suda et al., 2005].

The hollow fibre SPM method does have some severe limitations. Pulse energies in excess of 1 mJ cannot be focussed into the fibre and the whole system is susceptible to drifts in

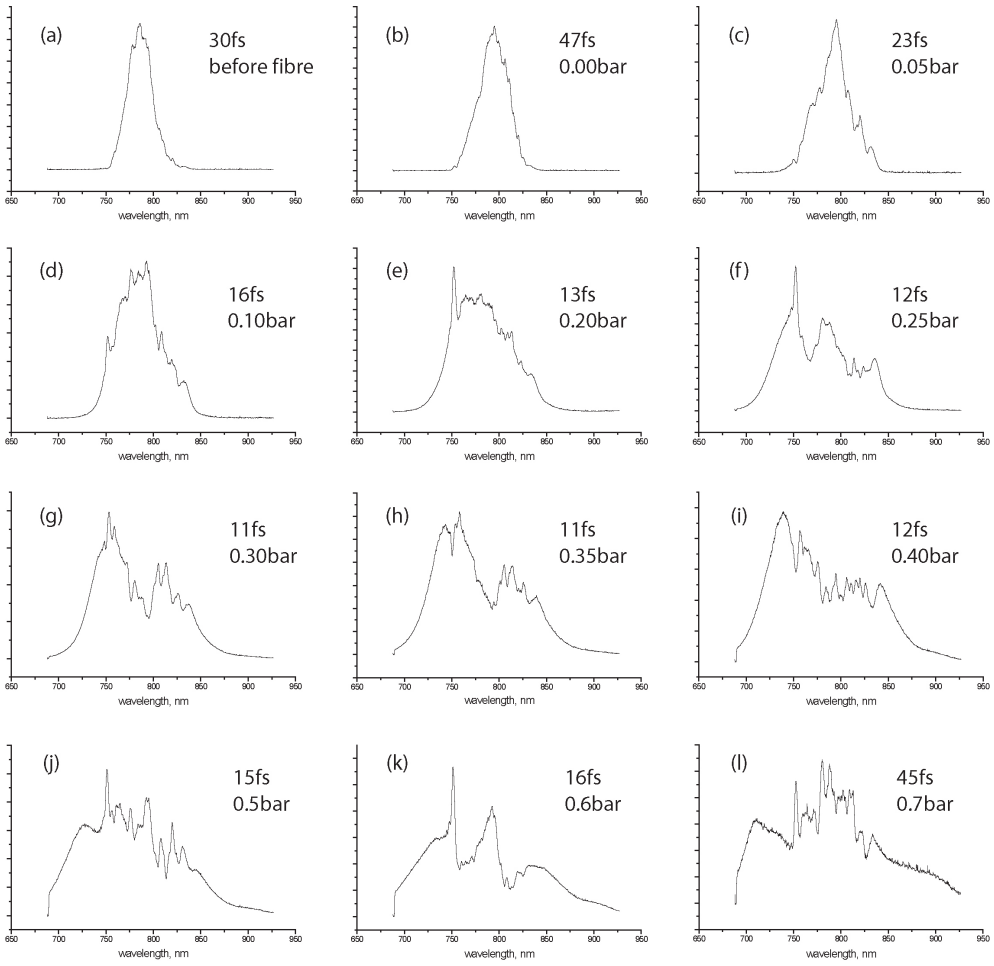

Figure 2.11: Wavelength spectra for different argon pressures, p_L, in the hollow fibre (b-l). The pulse durations given were measured after the chirped mirror array and following transmission through the a window similar to those on the experimental chambers. (a) shows the spectrum for the input pulses to the fibre.

the beam's pointing stability or energy. The first of these affects the mode propagating in the fibre and so reduces efficiency, whilst the second affects the broadening which impacts on the duration of the output pulses. Other methods of generating the bandwidth required for ultrashort pulse include SPM in bulk materials [Rolland and Corkum, 1988] and white light filamentation [Hauri et al., 2004]. The latter of which, overcomes the energy limitations suffered by the hollow fibre method employed in this study.

2.2.8 Chirped Mirrors

After leaving the fibre all the mirrors used must be reflective over the whole bandwidth if the shortest possible pulse length is to be realised. To this end, we only use mirrors with an ultra broadband, 600-1000 nm, protected silver coating specifically designed for femtosecond applications after the fibre. On leaving the fibre, the beam is recollimated by a 1 m focussing mirror (Layertec GmbH 101825). The beam then makes ten bounces off negatively chirped mirrors (Layertec GmbH 100470), each bounce imparting -45 fs^2 of Group Delay Dispersion (GDD). This reduces the temporal duration of the pulses to 10 fs after the transmission through a 3.3 mm thick fused silica window on the UHV system (Allectra 110-VPQZ-CF40-UV). The pulses are then sent to the experimental chamber or to one of the available pulse diagnostics, see section 2.3.

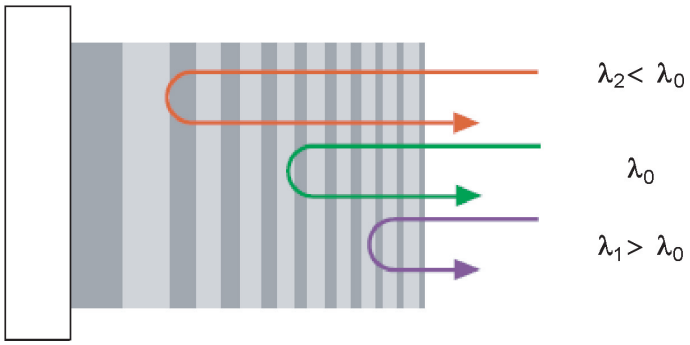

Figure 2.12: Principle of negatively chirpped mirrors; adapted from [Brabec and Krausz, 2000].

Negatively chirped mirrors [Szipocs et al., 1994, Kärtner et al., 1997] are made from dielectric layers laid on top of one another. The depth of these layers increases with depth from the mirror surface, see figure 2.12. An incoming photon is reflected most effectively from whichever layer is closest in depth to its wavelength. The net effect of this behaviour is that longer wavelengths in the incoming pulse travel further and hence are delayed with respect to the shorter ones, negatively chirping the pulse. However, in the the laboratory the incoming pulses are positively chirped so the chirped mirrors effectively flatten the spectral phase of the pulses, bringing them closer to the Fourier transform limited duration. In actual fact, the chirped mirrors over-compensate the pulses positive chirp to allow for the dispersive effects of optics later in the beam path, particularly the fused silica windows of the experimental chambers.

Custom chirped mirrors can now be purchased, which match the dispersive characteristics of individual beam paths [Matuschek, 1998, Matuschek et al., 1999]. Although, this facility is not currently availiable at Astra, the *off-the-shelf* chirped mirrors used behave well, see figure 2.11.

2.3 Laser Pulse Diagnostics

Before the laser pulses can be used to investigate the atomic and molecular physics of interest, they must first be characterised. Since the first autocorrelation measurement on short pulsed lasers [Weber, 1967] many techniques have been developed [Steinmeyer, 2003, Trebino and Walmsley, 1996, Mauritsson, 2003], several of which are used at Astra.

2.3.1 Intenstity Autocorrelation

The first method of pulse characterisation employed is single shot non-colinear second harmonic generation (NC SHG) autocorrelation. This method allows the duration of the laser pulses to be measured, but gives no information on the pulse shape. It is a robust instrument and is also used to ensure temporal overlap when using the Mach Zehnder interferometer for pump probe experiments. The instrument works by splitting the pulse train into two and then recombining the two components inside a second harmonic generating crystal (BBO - beta barium borate, Beta-Ba_2BO_4) at a small angle. This non-colinear method was first suggested by Janszky [Janszky et al., 1977] and then realised by Gyuzalian [Gyuzalian et al., 1979] and Kolmeder [Kolmeder et al., 1979]. In order for this method of autocorrelation to work, the pulses must be spatialy short compared to the beam waist of the overlap region [Krausz et al., 1986].

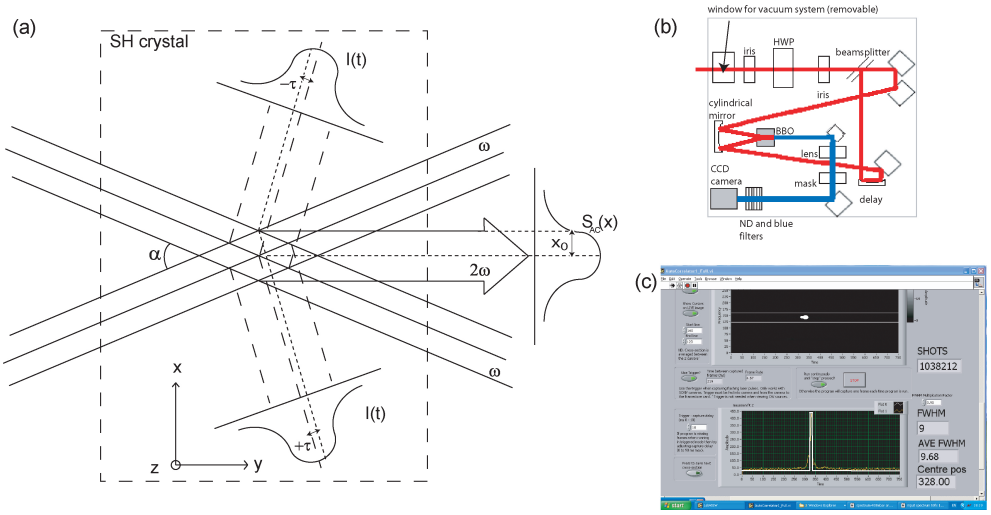

Figure 2.13: Non-colinear second harmonic method of intensity autocorrelation (a) geometery of the overlap region, (b) schematic of the single shot autocorrelator used in TA1, (c) an autocorrelation of a few-cycle pulse. Note, the angles through the crystal are greatly exaggerated for clarity. (Panel (a) adapted from [Rulliere, 1998].)

The scheme works by converting the intensity distribution of the frequency doubled light into a spatial intensity distribution along the x-axis (figure 2.13 and equation 2.5). As *blue*

light is created only when the pulses overlap in both space and time, the resulting spatial intensity distribution imaged by the calibrated CCD camera (equation 2.6) yields a quasi form of the second order autocorrelation function, from which the pulse duration can be extracted. As indicated by equations 2.5 and 2.6, the variables in which are defined in figure 2.13,

$$\tau = \frac{\kappa x_0 sin(\alpha/2)}{c} \tag{2.5}$$

$$S_{AC}(x) = \int_{-\infty}^{+\infty} I_1(t+\tau) I_2(t-\tau) dt \tag{2.6}$$

After filtration of the infra-red signal, the output of the crystal is imaged on a calibrated (one pixel equals 0.9 femtoseconds) Charge-Coupled Device (CCD). From the measurement of the signal detected and the pulse shape, the duration can be obtained. However, as the autocorrelation yields no phase information, the pulse shape needs to be inputted into the deconvolution manually. This gives a factor by which the autocorrelation signal is longer than the pulse intensity profile [Kolmeder et al., 1979], $\kappa = 1$ for a square pulse, 1.41 for a Gaussian pulse and 1.54 for a sech^2 pulse, see equation 2.5.

2.3.2 Frequency Resolved Optical Gating (FROG)

Frequency-Resolved Optical Gating (FROG) is a technique that can be used to retrieve both the amplitude and the phase of the laser pulses. Unlike autocorrelation (Section 2.3.1) this allows one to reconstruct the entire pulse shape. This is made possible by collecting information as a function of frequency and not just time within the pulse.

The notion of measuring the intensity against time in a pulse for different spectral slices was commonplace in the field of acoustics when it was first applied to ultra-short laser pulses [Treacy, 1971]. However, Treacy's dynamic spectrogram took twenty years to be realised; with the first Frequency Domain Phase Measurement (FDPM) [Chilla and Martinez, 1991] fully reconstructing a complete laser pulse profile for the first time in 1991.

$$S_{FROG}(\omega, \tau) = \left| \int_{-\infty}^{+\infty} E(t) E(t-\tau) exp(-i\omega t) dt \right|^2 \tag{2.7}$$

From these ideas emerged the FROG technique [Kane and Trebino, 1993a]
[Kane and Trebino, 1993b, Trebino and Kane, 1993, DeLong et al., 1994], which soon became dominant due to its relative simplicity and the ease of replication in the laboratory. The mechanics of the system are very similar to those of an intensity correlation, but

rather than measuring energy against delay, spectral intensity is measured instead. In Second-Harmonic Generation (SHG)-FROG this is done by placing a spectrometer behind the frequency doubling crystal (Figure 2.14(a)). As in the autocorrelator method, the pulses are split into two and then crossed in a frequency doubling crystal. The resulting *blue* light is then sent to a simple grating lens spectrometer and the spectral intensity measured, see equation 2.7 and figure 2.14(a). An iterative algorithm is then used to try to recreate the experimental FROG trace. Once the best match to experiment is obtained, the calculated pulse responsible for the match can be extracted as a full representation of the experimental one.

It is worth noting that other types of FROG devices do exist. As with intensity autocorrelation most non-linear processes will suffice. Also different processes can be used to gate the interaction. For example Third-harmonic Generation (THG)-FROG, Self-Diffraction (SD)-FROG and Polarisation Gating (PG)-FROG are just a few of the ideas currently being used elsewhere.

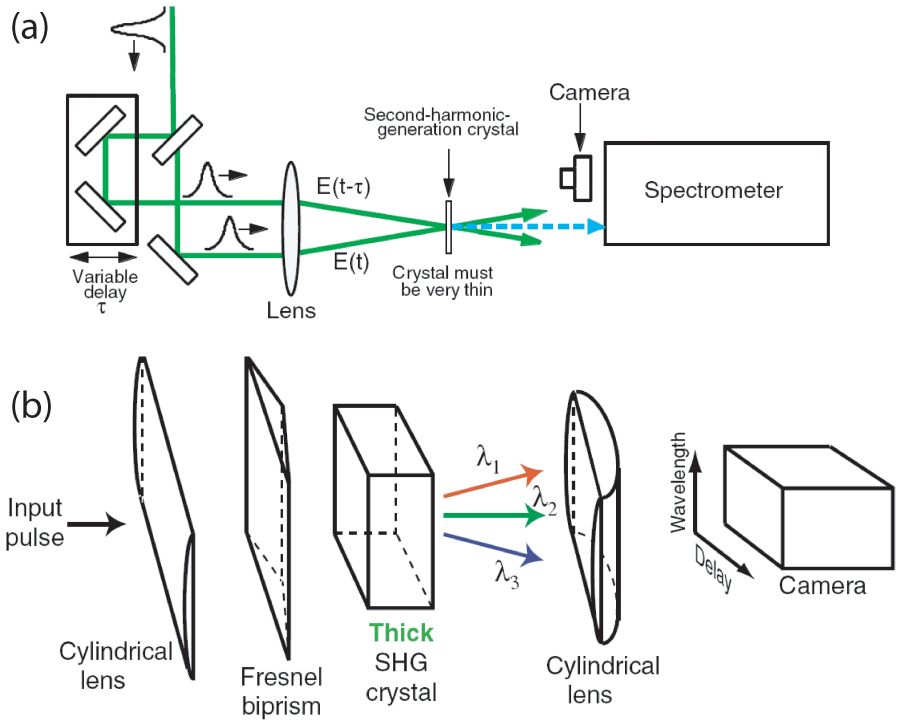

Figure 2.14: The FROG technique (a) and its simplified version, the GRENOULLIE (b). In the GRENOUILLE the beamsplitter, delay line and recombining optics of the conventional FROG device are replaced by a Fresnel biprism, and the thick SHG crystal acts as both the non-linear time gate and the spectrometer. This allows single-shot SHG-FROG traces to be obtained with ease and at relatively low cost. (Adapted from [Trebino et al., 2001].)

The devices used at RAL are called GRENOUILLE [O'Shea et al., 2001] (GRating-Eliminated

No-nonsense Observation of Ultra-fast Incident Laser Light E-fields); grenouille is french for frog. These are essentially simplified FROG devices that require fewer alignment considerations (Figure 2.14(b)). Two of these systems are available in the laboratory; one that measures pulses in the range 20-200 fs (Swamp Optics 8-20USB) and another that measures pulses down to a duration of 10 fs from 100 fs (Swamp Optics 8-9USB). The first of these is used on the beam leaving the prism compressor and the second on the output of the hollow fibre chirped mirror system. To handle the extra bandwidth of the shortest pulses, the second device implements crystal angle-dithering [O'Shea et al., 2000]. This maximises the phase-matching bandwidth within the SHG crystal, enabling the extraction of pulse information across the entire frequency range of the laser pulses.

The advantages of the GRENOUILLE system are obtained from the use of the Fresnel biprism and the thick SHG crystal. The biprism [Hecht, 1998] produces two beams that are intrinsically aligned w.r.t. one another in space and time. Subsequently alignment issues are greatly reduced. The thick crystal, which replaces the thin crystal, and the spectrometer brings several advantages. Firstly, the use of a thicker crystal results in higher signal strengths. Secondly, the reduced phase-matching bandwidth of the thick crystal (often seen as a disadvantage in pulse measuring systems) is used advantageously, as it results in the phase-matched wavelengths produced to vary with angle thus effectively acting like a simple spectrometer. The cylindrical lenses also present in the GRENOUILLE design are used to couple the light in the crystal and CCD camera respectfully. The first ensures that the beams are focused tightly enough in the SHG-crystal to ensure there is a large enough range of entrance and exit angles for all the frequency components in the pulse. This is done by creating a line focus horizontally across the crystal. The second lens maps the exit angle of each frequency into position on the camera. This is done by creating a line focus vertically half the distance from the lens to the CCD array, within which the wavelength of the light follows a near-linear function of vertical position. This also allows a slit to be placed at this focus to filter out other beams from reaching the CCD camera.

In the laboratory, the GRENOUILLE is placed on the optical table and a small fraction of the beam energy is sent towards it. This is done by either a suitable beam splitter or a combination of a mirror in a flip mount with a wave plate and Polaroid to reduce the beam energy. The GRENOUILLE cameras are then connected to a PC running the relevant software (Mesa Photonics VideoFROG) and the characteristic of the pulses are recorded and/or displayed in real-time. This is particularly useful when tuning the prism separation in the prism compressor, as the effects of moving the prisms on the spectral phase of the pulses can be witnessed immediately. Subsequently, pulse optimisation can be done swiftly.

2.3.3 Spectral Phase Interferometery for Direct Electric-field Reconstruction (SPIDER)

A SPIDER is also at our disposal in the laboratory, however, it is primarily used to supply the Dazzler with phase information about the pulses, see section 2.2.4. SPIDER was developed [Iaconis and Walmsley, 1998, Iaconis and Walmsley, 1999] in the late 1990s as a technique for measuring the relative phases of the different spectral components in ultra-short laser pulses. The device at Astra was built in collaboration with UCL following a published design [Shuman et al., 1999] used to measure laser pulses of similar duration elsewhere. A schematic of the optical components that make up the SPIDER can be seen in figure 2.15(a).

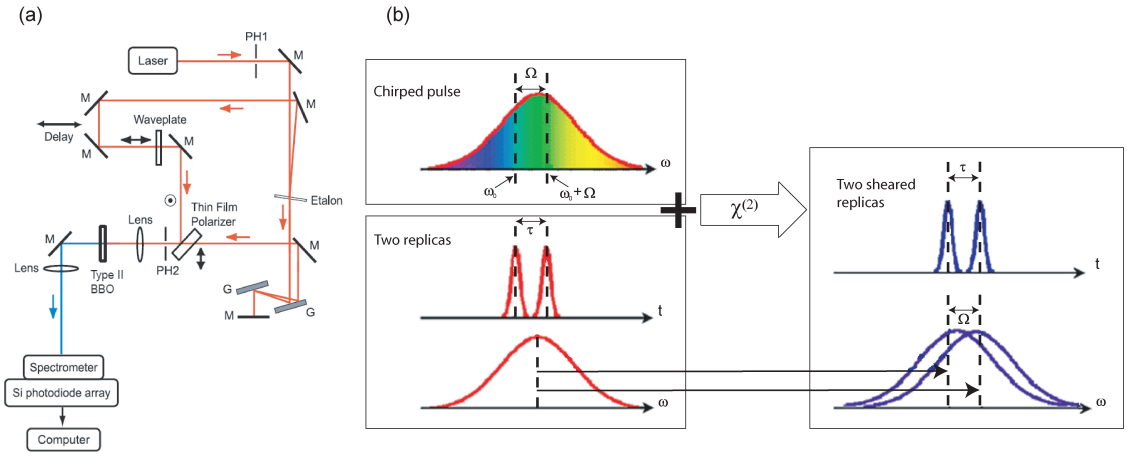

Figure 2.15: (a) Schematic of a SIPDER similar to the one used in TA1 at Astra. M corresponds to a mirror, PH to a pin hole and G to a grating (1200 lines/mm). (b) The priniciple of spectral shearing. ((a) Reproduced from [Shuman et al., 1999] and (b) adapted from http://ultrafast.physics.ox.ac.uk/spider/tech.html.)

Unlike FROG, which is a spectrographic technique, SPIDER is as its name suggests is interferometric in nature, utilising interference between different frequencies in the spectrum of the pulse to measure it spectral phase, and subsequently the temporal profile of laser pulses. The pulses to be measured are first split into three; two weak components and one containing most of the beam energy. The energetic beam is stretched to a duration several hundred times its original. The chirp across this stretched pulse does not have to be perfectly linear, however, it should be as constant as possible across a time window equal to the duration of the original pulse. The other two weaker pulses are separated in time so that they do not overlap temporally with one another. This is done using an etalon rather than a Michelson Interferometer. An etalon was chosen as the added stability and reduced alignment complications were seen to outweigh the advantage of manipulating the separation between the pulses (an ability that would be gained with the inclusion of an interferometer).

After travelling the same path length and through a half wave plate, the two replicas are recombined with the stretched pulse in a type II SHG-crystal. As the replicas are separated in time, they interact with different sections of the stretched pulse, and given that this pulse is strongly chirped, different spectral slices. Thus the up-converted light leaving the crystal from one of the replicas is spectrally sheared from that of the other (see figure 2.15(b)). Finally, the resulting interferogram is resolved by a spectrometer. This inferogram is illustrated by equation 2.8 with the variables defined in figure 2.15.

$$S_{SPIDER}(2\omega,\tau) \quad = \quad |\int_{-\infty}^{+\infty} E_{2\omega+\Omega}(t)E_{2\omega}(t-\tau)exp(-i2\omega t)dt|^2 \tag{2.8}$$

The interferogram contains sinusoidal fringes brought about by constructive and destructive interference of the spectrally sheared up-converted light. If the spectral phase of the original pulse is flat, then these fringes are equally spaced. If, however, their separation is seen to vary, then some the spectral phase of the original pulse must be structured (possibly due to dispersion earlier in the beam line).

A full analysis of the interferogram is conducted on a PC using software written in LabVIEW. This analysis is adapted from Fourier Transform Spectral Interferometery (FTSI) and utilises Fast Fourier Transforms (FFT) [Takeda et al., 1982]. Subsequently, the spectral phase of the original pulse is retrieved algebraically. This is simpler and more direct than the computational steps of the FROG or GRENOUILLE techniques, as the pulse is retrieved rather than implied through a series of iterative steps.

2.3.4 High Dynamic Range Third Order Cross-Correlator

When working with ultrashort laser pulses, one of the frequently avoided problems is that of pre- and post-pulses forming a pedestal upon which the main few cycle pulse sits. These artefacts are often dismissed as they only contain a tiny fraction of the total pulse energy. However, this argument is not valid when using high energy pulses to look at atomic and molecular physics. For instance, if you consider a 10 fs pulse of intensity 10^{15} Wcm^{-2}, a pedestal of 0.1% i.e. 10^{12} Wcm^{-2} is still sufficient to affect the dynamics of certain atoms and molecules. Subsequently, one must be very careful when discussing the results of experiments with reference to pulse duration and discussion of pulses in simple terms of a single FWHM duration should be questioned. This issue is discussed further in section 6 where a novel method for establishing the pulse duration/shape on target is outlined. One tool at our disposal in the laboratory, which can be used to measure the beam profile, is a third order cross correlator. This is a commercial product built by Amplitude Technologies (http://perso.orange.fr/amplitude-technologies/company.htm). Figure 2.16 shows a typical measurement of an ultrashort laser pulse.

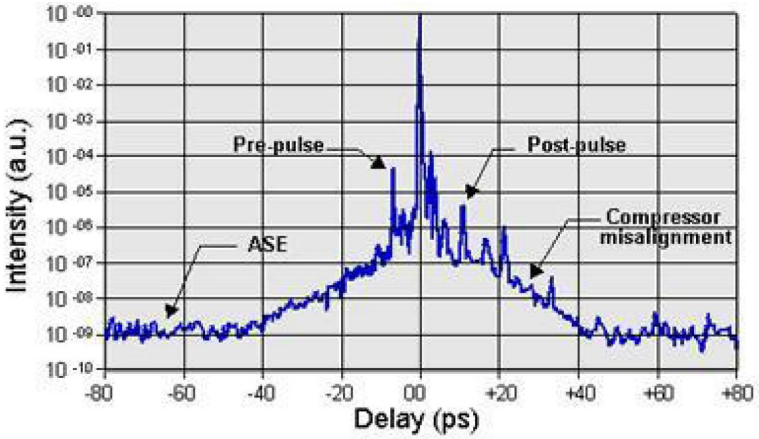

Figure 2.16: A typical Sequoia measurement on the 30 fs,1 kHz beam after the prism compressor. Figure reproduced from the webpages of amplitude technology

Recently the importance of considering the whole pulse shape (including pre and post pulses) when describing the physics of few-cycle laser pulse interactions with molecular systems has been acknowledged by our German competitors [Rudenko et al., 2005, Feuerstein et al., 2007] who have taken to publishing typical autocorrelations and SPIDER traces alongside their experimental findings.

2.3.5 Spectrometers; Bandwidth Measurements

In the laboratory, often the first test (and the quickest) when trying to diagnose a problem or when wishing to characterise the laser pulses used in the experiments, is to take the wavelength spectrum of the light. Two spectrometers are routinely used; Stellar Net Inc. EPP2000S and Ocean Optics Inc. USB4000-VIS-NIR. The second of the two spectrometers covers a wider range of wavelengths (350-1100 nm compared to 600-1000 nm) and is consequently favoured when measuring the pulses that have been spectrally broadened in the hollow fibre. Both systems, which are very user friendly and portable, have optical fibre collectors and rely on diffraction gratings to separate the different frequency components of the pulse. Common instances when these tools are used are to check the bandwidth of the pulses entering the target area and to check the bandwidth after the hollow fibre. Spectra are also always taken before and after experimental runs. Figure 2.17 shows typical wavelength spectra taken with the Stellar Net spectrometer. The bandwidth of the pulses are 50 nm and 80 nm, respectfully. The structure in the wavelength spectrum of the 10 fs pulses is discussed in section 2.2.7.

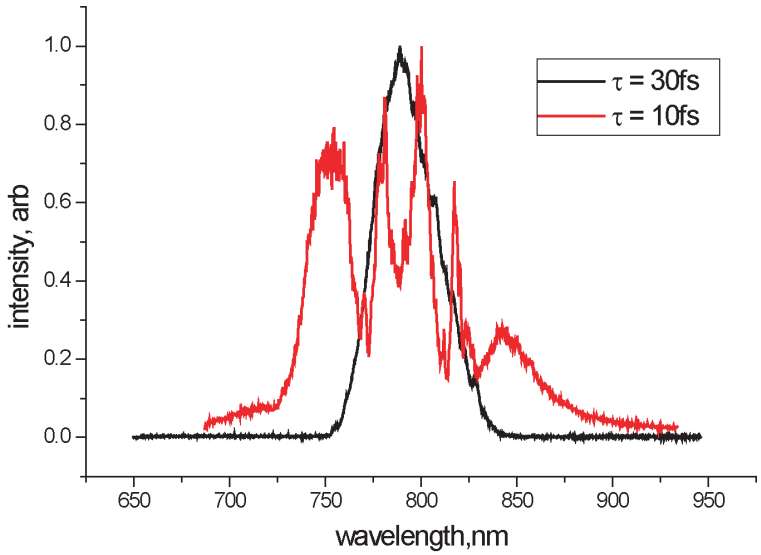

Figure 2.17: Typical wavelength spectra of the kHz pulses before (30 fs) and after (10 fs) spectral broadening in the hollow fibre system.

2.4 Time-of-Flight Mass Spectrometer

Time-of-flight mass spectrometry is a well known and used technique for the energy analysis of charged particles. It has several advantages over other detection systems and its inherent simplicity also makes it ideal for a system that must be portable.

2.4.1 Time-of-Flight Technique

Time-of-flight is a method used to analyse the energy of dynamic particles originating from a pulsed source. The method was first suggested by Stephens in 1946. [Stephens, 1946] Seven years later the first spectra were published [Wolff and Stephens, 1953], however, the idea only became commercially viable with the seminal paper by Wiley and McLaren in 1955 [Wiley and McLaren, 1955], which enabled higher energy resolutions to be realised due to the employment of *time lag focussing*. (see Appendix A.)

The system used here can be run either in the Wiley-McLaren mode or in the spatial mode; the difference being in the potential difference applied to the acceleration grid (see figure 2.19). In the spatial mode this voltage is equal to that of the top extraction plate, whereas when the spectrometer is set to operate in the Wiley-McLaren mode the acceleration grid voltage is three times that of the top extraction plate. This 3:1 ratio causes focussing of the ions within the drift tube resulting in better timing resolution (but at the cost of reduced spatial information, since ions from the entire imaged interaction region arrive at the detector at the same instant, regardless of their initial location).

Spatial focussing geometry is used for atoms; Wiley-McLaren geometry for molecules. For simulations using SIMION (Scientific Instrument Services Inc) and experimental justification of this decision see, Watson 2005 [Watson, 2005].

2.4.2 Ultra High Vacuum System

The time-of-flight detector is housed within an Ultra-High Vacuum (UHV) chamber (see figure 2.18), collectively referred to as the time-of- flght mass spectrometer (TOFMS). The system is built round a single four way cross with 203 mm conflat flanges at each end (Vacuum Generators ZBX415RI). To allow laser light into the system, a 70 mm conflat tubulated flange (Vacuum Generators ZBFT41) was vacuum-welded onto each side of the system, where the four arms intersect, giving the chamber the appearance of a reducing six-way cross. High quality fused silica windows (Allectra 110-VPQZ-CF40-UV) were fitted onto the 70 mm flanges to provide entrance and exit windows. A triple axis manipulator (Caburn-MDC E PSM 1502) and mirror mount (made at UCL to my design) replaces the exit window for the experiments with the few-cycle pulses. The chamber is pumped by a water-cooled turbo molecular pump (Pfieffer TPU 450 H) attached directly to the bottom flange of the four way cross, backed by a diaphragm pump (Pfeiffer MD4), thus providing a dry vacuum system. Both pumps are controlled through an electronic drive unit (Pfeiffer TCP 380), which also operates a magnetic venting valve (Pfieffer TSF 012) and a heating band for bake-out. This makes day-to-day operation of the system relatively simple. All UHV seals are made with standard Oxygen-Free Copper (OFC) gaskets, except for the seals around view-ports where annealed OFC gaskets are used. The internal pressure of the system is monitored with a hot cathode ion gauge (Vacuum Generators VIG 22; controller Vacuum Generators IGC 27). Target gas can be leaked into the system via a needle valve (Vacuum Generators MD6) mounted on the top flange within the cradle of the detector, see figure 2.19. There is also a residual gas analyser on the system, which is described in section 2.4.5.

2.4.3 Micro Channel Plate Detector

The main body of the detector is supported by a cradle hung from the top flange of the four way cross as shown in figure 2.19. The electrical connections into the vacuum chamber are made by an 11-pin electronic feed-through (Vacuum Generators ZEFT16NW). The detector head comprises of a matched pair of Micro-Channel Plates (MCP) (Philips Photonics G25-25DT/13) held together, so the channels in the two plates form a chevron-like pattern. The typical gain of the plates is around 10^6 with an applied voltage of 1.2 kV across each plate. All the potentials to the detector head and the extraction plates are supplied from individual extra high tension (EHT) supplies (Southern Instruments (Contracts) Ltd Harwell 95/2124-1/6) mounted together in a single rack.

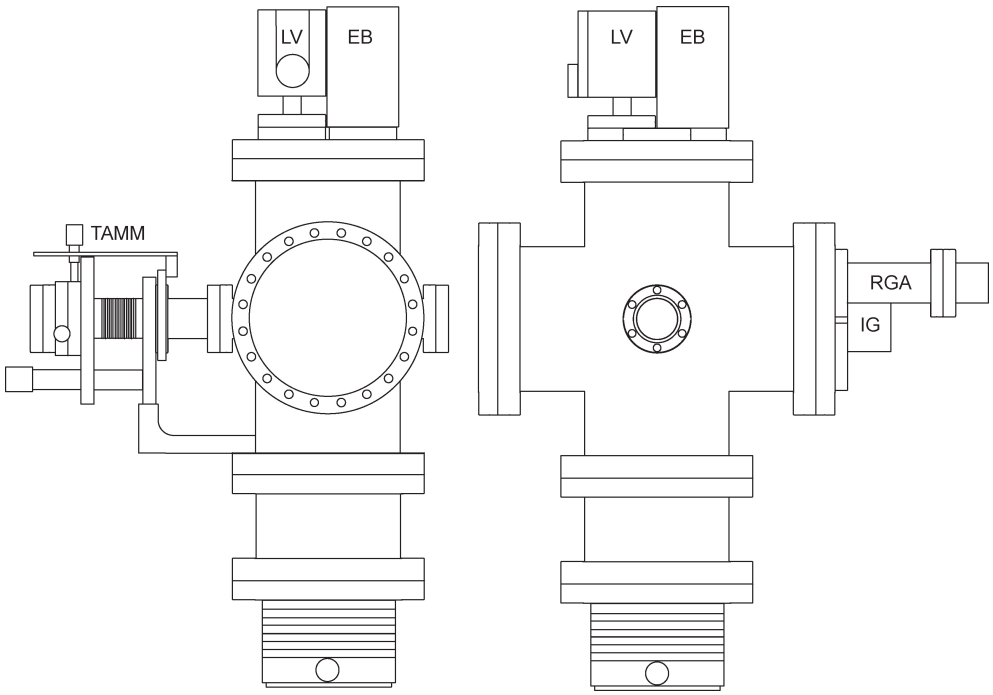

Figure 2.18: Side elevation (left) and front view (right) of the UHV TOFMS Chamber. On the left the Triple Axis Mirror Manipulator (TAMM) can be seen in the place of the exit window. The Electronics Box (EB) for the detector head can be seen alongside the Leak Valve (LV)on the top flange of the chamber. The Residual Gas Analyser (RGA) and Ion Gauge (IG) are also shown to the right of the figure.

Gas is leaked into the chamber's interaction region between the extraction plates, which are 20 mm apart, through a stainless steel hypodermic needle. The gas flow is regulated by the needle valve and monitored on the ion gauge, typically taking the background chamber pressure from 10^{-10} mbar to 10^{-7} mbar. Higher pressures are not used to avoid space-charge [Cornaggia et al., 1990, Busch, 2004] effecting the energy resolution of the spectrometer. The laser is then focussed into the chamber. The charged particles that result from the laser gas interaction feel the extraction field generated by the potentials on the plates. This homogenous electric field attracts positively charged particles through a 0.25 mm aperture in the top extraction plate. This aperture is used to limit the angular acceptance/field of view of the spectrometer (4^o for a 1 eV deuteron). Details of which can be seen in appendix C. After passing through the aperture, the ions pass through the acceleration grid and into the 110 mm long drift tube. Exiting the drift tube though a second grid, the ions reach the collection grid. Here their energy is raised to 2.7 keV, to enhance the detection sensitivity and efficiency of the MCPs.

Positive ions that strike the front face of the first MCP cause electrons to be knocked off the surface of the channels. The number of electrons increases as they collide with the inner walls of the channels. This process leads to a cascade of electrons travelling through

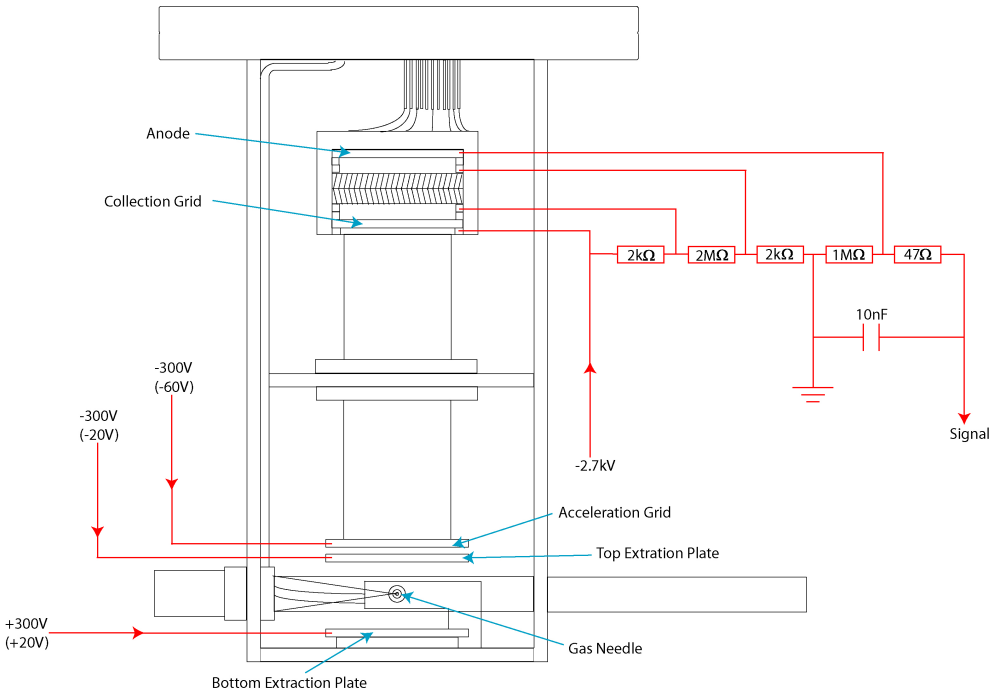

Figure 2.19: The TOFMS detector cradle. In the figure laser pulses enter from the bottom right and are reflection focussed from an internal concave mirror. Target gas is leaked into the system between the extraction plates. The detection electronics are shown including the RC circuit used for signal processing. The potentials shown for the extraction plates are those used for atomic targets (Ne, Ar, Kr and Xe) and in brackets hydrogenic molecular targets (H_2, HD and D_2).

the first plate and into the second. On leaving the second MCP, the electrons strike a copper anode. As this flux of electrons is directly proportional to the number of ions hitting the first MCP, an effective ion yield can be obtained. The output of the anode is sent through a 1 MΩ resistor to ground and the resulting potential difference recorded. Note a Resistor Capacitor (RC) circuit is used to dilate the electron pulses (from 10 to 50 ns) from the anode to allow the digital storage oscilloscope (DSO) (Tektronix TDS 6804B), used to process the data to operate at slower sampling rates. Between the electronics box and the DSO, the signal is amplified by a fast pre-amplifier (Ortec VT120C). This also protects the DSO from any harmful voltage spikes. Co-axial cable (50 Ω) is used to carry the signal from the electronics box to the pre-amplifier and then the DSO.

Figure 2.20 shows a typical time-of-flight spectrum obtained from the TOFMS system used in this study and described here.

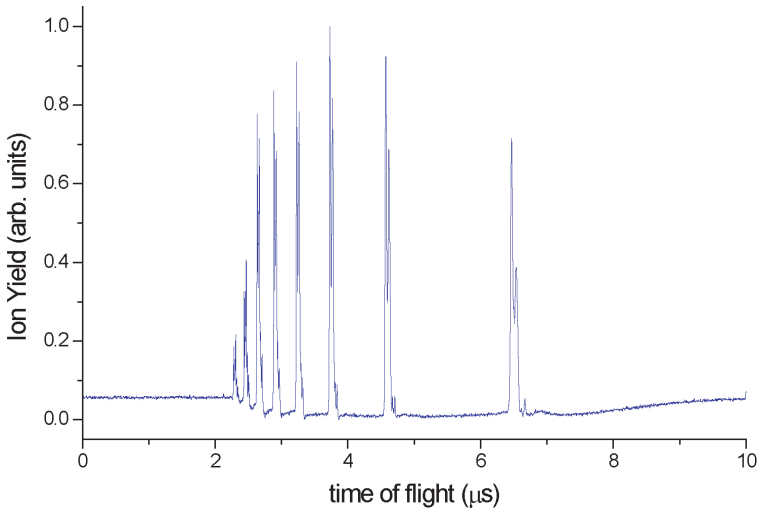

Figure 2.20: A typical time-of-flight spectrum obtained from the interaction of 30 fs, 800 μJ laser pulses with 4.0×10^{-7} mbar of xenon gas. The first eight charge states can be seen clearly, with the higher charged products receaching the detector first. One can also see the evidence of the isotopes of xenon in the multiple peaked structure of each charge state.

2.4.4 Interaction Region and Laser Beam Focussing

The laser particle interaction takes place between the extraction plates of the TOFMS. When the 10 fs 1 kHz pulses are used, the laser pulses are reflection focussed from a concave mirror (f=50 mm Layertec GmbH 101718 or f=75 mm Layertec GmbH 101883) located inside the chamber. When the multi millijoule 35 fs 10 Hz pulses are used, the pulses are transmission focussed by a plano-convex lens (f=250 mm Melles Griot BV 01 LUP 038/077). The Layertec mirrors have a broadband protected silver coating to ensure that as much of the pulse energy as possible is focussed without increasing the pulse length. The lens used for the focussing of the high energy pulses is simply AR coated. In both instances the focussing optic can be translated parallel to the detection axis, and therefore enables intensity selective scanning [Hansch et al., 1996, Bryan et al., 2006b] experiments to be realised. In the case of the 10 fs pulses, this is done by manually adjusting the z-axis of the triple axis manipulator from which the mirror is mounted. However, when the lens is used, the situation is completely computer controlled. This is done using a translation stage (Newport Corp. M-MFN25CC) powered by a control box (Newport Corp. MM4005) governed by a PC running software written in the LabVIEW package from National Instruments. The Newport controller is also used for polarisation management. In this instance wave plates can be mounted in a rotation stage (Newport Corp. M-URM100ACCHL). The wave plates used in the 10 fs experiments were ultra-broadband ($\lambda/4$ Femtolasers GmbH OA-229; $\lambda/2$ Femtolasers GmbH OA-232) and designed to have a very low dispersion. In the 35 fs experiments standard wave plates are used ($\lambda/4$

Melles Griot BV 02-WRC-033/800; $\lambda/2$ Melles Griot BV 02-WRC-035/800). General beam transport was done using protected silver mirrors. In the case of the 10 fs pulses one inch mirrors were employed that had the capacity to support a bandwidth of 600-1000 nm (Layertec GmbH 100767). For the longer pulses, two inch mirrors were used (CVI laser LLC TLMB-800-45-1940). Their coating means they can only support wavelengths in the range 740-860 nm, however this is more than sufficient. Two inch optics are used for the high energy low rep-rate pulses, as the beam diameter is 22 mm. The ultra-short pulses have a diameter of 7 mm, therefore smaller optics are appropriate.

2.4.5 Residual Gas Analyser

The residual gas analyser (Spectra Physics: Leda-Mass Model: 160 121 001) is used primarly to detect contaminants and/or leaks in the system. It comprises a quadrupole mass spectrometer with a twin filament analyser and dual detector (Faraday cup and electron multiplier). It has a mass range of 1-100 amu and is controlled through a computer interface and/or control unit (model:100D). It also has a leak detector system, which can be used in conjunction with a source of helium gas. The control unit emits a tone, which increases in pitch as the amount of helium detected increases. This allows the source of the leaks to be narrowed down to a individual weld or conflat seal.

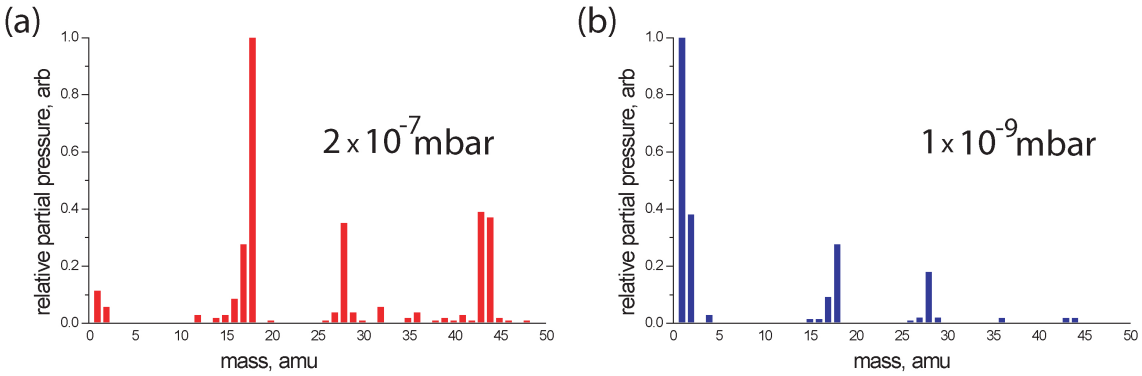

Figure 2.21: Panel (a) a spectra from the RGA taken to diagonose a possible leak. The largest peak, at 18 amu, corresponds to H_2O^+. Other contaminents can be deduced from their mass eg. $CO_2{}^+$ at 44 amu and $N_2{}^+$ at 28 amu. Panel (b) shows the situation after the leak has been fixed. In both panels the pressure reading from the TOFMS's ion gauge is shown.

Figure 2.21(a) shows the output from the RGA when a leak in the system was suspected (before the system was baked-out). As the peaks correspond to molecular species from the air, we were able to eliminate contamination from pump oil or any other organic residue. The flanges were all checked and the leak isolated and fixed. Panel (b), of the same figure, shows the stituation after subsequent bake-out and cooling of the apparatus.

2.4.6 External Gas Line

The gases used in the TOF-MS system are of spectral quality (99.999% pure for the atomic gases used) and are delivered to the UHV system via an external gas line (see figure 2.22). The gas is introduced into the system from a regulated lecture bottle. A rotary vane pump (Edwards E2M18) is used to evacuate the external gas line to ensure target purity. The pump used has an ultimate pressure of 10^{-3} mbar, which is monitored via a Pirani gauge (Vacuum Generators M6A; controller IGC 27). The main body of the gas line is constructed from a mixture of a quarter inch stainless steel piping, connected by swagelok fittings and Edwards aluminium vacuum piping sealed with viton O-rings. A sorption trap is also included in the gas line to minimise the risk of pump oil getting in to the otherwise clean UHV system. During a typical experiment the pressure in the gas line is of the order of 1 bar.

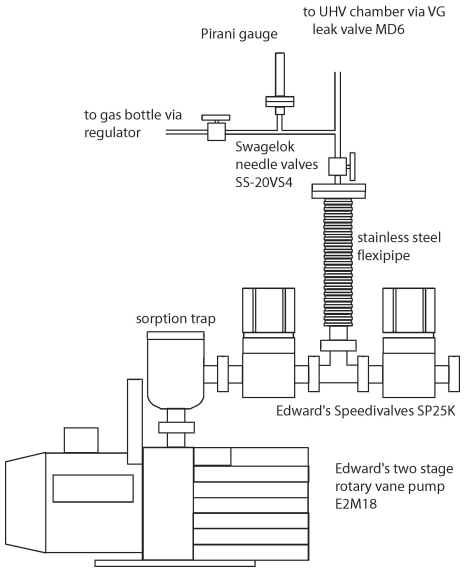

Figure 2.22: The gas supply system for the TOF-MS.

2.5 Ion Beam Apparatus

The ion beam aparatus was built [McKenna, 2000] and is mainly run
[Calvert and McKenna, 2006] by the QUB half of the collaboration. However, having worked closely with the team from QUB I have a working knowledge of the day-to-day operations of the system.

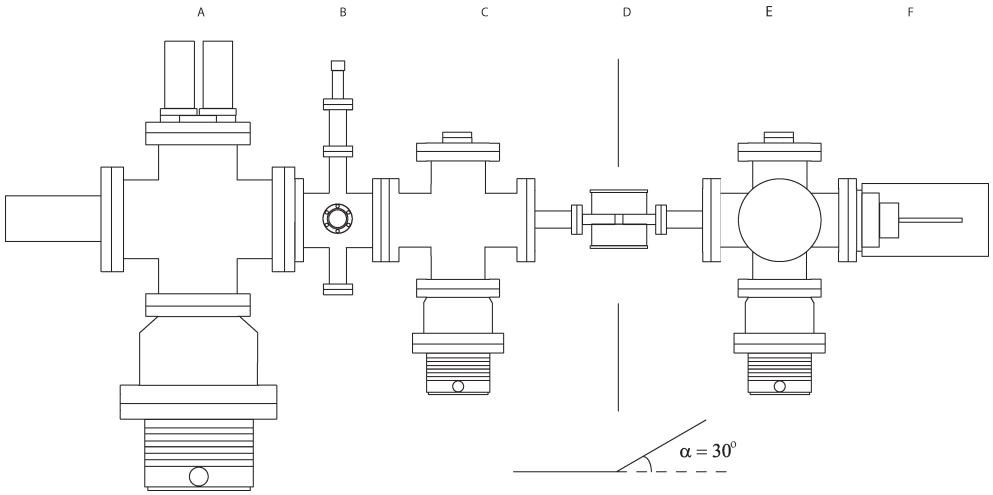

Figure 2.23: Schematic of the Ion Beam apparatus. The main regions are marked as follows; A analyser, B interaction, C focussing and deflection, D momentum selection, E extraction and focussing and F ion source. The apparatus is constructed with an angle of 30^o between the extraction and focussing and deflection regions in order to assist in the momentum selection of the beam. This is indicated at the bottom of the figure below region D.

2.5.1 Vacuum System and External Gas Line

The ion beam rig (figure 2.23) is considerably larger than the TOFMS, although its vacuum system contains many similar parts. It is built around a series of standard four way crosses, joined together by conflat flanges. The system is differentialy pumped by three turbomolecular pumps (Analyser region - Leybold Turbovac 1000C; controller Leybold NT 20, Interaction region - BOC Edwards EXT250M; controller BOC Edwards EXC300M and Source region Leybold Turbovac 600C; controller Leybold NT 20). The pressure of the system is measured on a hot cathode ion gauge (Vacuum Generators VIG 22; controller Vacuum Generators IGC 27) in the analyser region and by a wide range gauge, a dual Pirani and Penning gauge (Edwards WRG-S-NW25; controller Edwards AGC-D38651000) in the source region. The turbomolecular pumps are backed by two scroll pumps (BOC Edwards GVSP30 and BOC Edwards ESDP12) making the system completely oil free. (Backing a turbo molecular pump refers to the use of a more robust vacuum pump to lower the pressure the turbo pump has to work against. This prolongs the lifetime of the more expensive turbo pump and allows lower pressures inside the UHV chamber to be achieved.)

The first of these scrolls is also responsible for evacuating the external gas line (figure 2.24) used to supply the ion source with gas. The pressure in this part of the system is monitored by a Pirani gauge (Edwards WRG-S-NW25; controller Edwards AGC-D38651000). During operation, the smaller of the two scroll pumps is set to back only the source turbomolecular

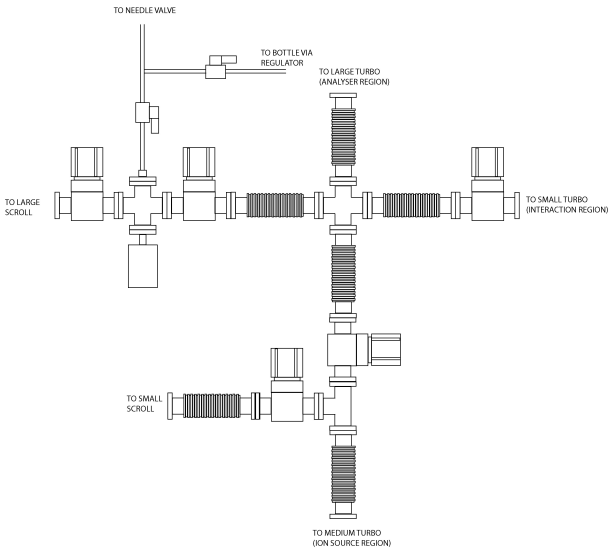

Figure 2.24: The external gas line for the ion beam apparatus.

pump, whilst the larger scroll pump backs the turbomolecular pumps on the analyser and interaction regions. This is done because pressures in the source region are much higher than anywhere else in the system (a few 10^{-6} mbar as supposed to around 10^{-9} mbar in the analyser region) and consequently this pump must handle a larger gas through-put.

2.5.2 Ion Source

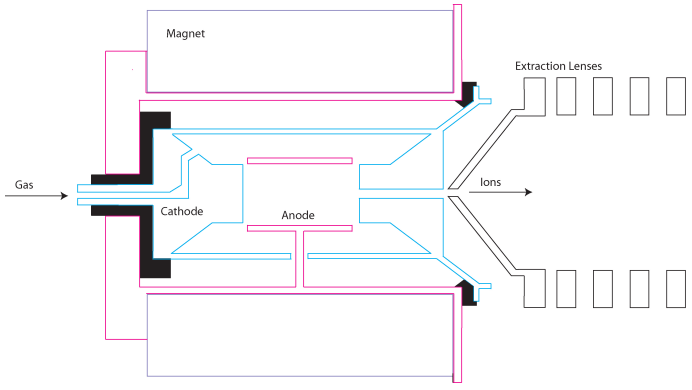

Figure 2.25: A cross section of the ion source. The anode is outlined in magenta and the cathode is shown in cyan. The magnet that provides the confining axial B-field, and the extraction ion optics are also shown. Adapted from [Suresh, 2005].

The ions that form the beam are generated in the source region of the apparatus, figure 2.25. The source, a Penning discharge type, is based on a well established design [Baumann and Bethge, 1974]. Gas is introduced into the source through a needle valve

(Vacuum Generators MD6) between a cathode and anode. These electrodes are cylindrical in shape and are encased by a cylindrical magnet that supplies the region with a axial field of 0.1 T. Typically, gas pressures in the region are between 10^{-6} and 10^{-5} mbar. The anode and magnet are supplied with a common positive voltage of between 1-2 kV, as the cathode potental is floated at a voltage -1.5 kV (with respect to the magnet and anode). This set up ensures the discharge is confined to the region between the electrodes. The ions arise due to electron stripping (ionisation), caused by the potential difference between the electrodes. The electrons precess around the axial field lines, leading to more collisions with the target gas and more ionisation events. Simultaneously, the ions are accelerated towards the cathode and are extracted through a 2 mm aperture. The molybdenum aperture is replaced regularly, as it suffers persistent sputtering due to ion impact during operation of the rig.

2.5.3 Extraction, Energy Selection and Beam Focussing

After the ions leave the source region they are confined to travel down the axis of the apparatus. Energy and species selection are also critical in producing a useful target with which to conduct experiments. The confining or focussing of the beam is done by a series of electrostatic extraction lenses placed immediately after the source region. These lenses are usually operated at negative high voltages and provide localised cylindrically symmetric electric fields, which force the positive ions to travel in a given direction.

Species selection is realised using the magnetic field (B-field) of an electromagnet to define a desired mass to charge ratio (m/q). The field lines from the magnet are set perpendicular to the ions flight path, so that the resulting Lorentz force bends the ion beam horizontally. By varying the strength of the B-field (current in the magnets coils) the ions with the desired m/q can be sent down the centre of the beam line exiting the magnet region. Note this part of the beam line is set at an angle of 30^o to the earlier sections of the beam line. Further details of this selection process are given in appendix E. After the bending magnet, there is a 2 mm aperture followed by an Einzel lens and a series of deflectors to re-focus and position the beam.

2.5.4 Interaction Region, Laser Beam Focussing and Ion Beam Profiling

The interaction region is where the laser beam meets the ions. The laser is focussed into this region from outside the vacuum system by a f=250 mm plano:convex lens (Melles Griot BV 01 LUP 038/077) and travels through a 3 mm thick fused silica viewport (Caburn-MDC (UK) 9722205) on its way to the target. The focussing optic can be translated parallel to the laser beam (perpendicular to the ion beam), thus controlling the part of the laser focus that interacts with the ion beam. The polarisation and energy of the laser

light is also controlled outside the vacuum system, with many of the components being similar to those used in the TOFMS experiments described earlier (Section 2.4.4).

Usually the polarisation axis of the laser light is chosen to lie parallel to the ion beam. Consequently the resulting fragments from the ion laser interaction continue to travel down the ion beam path and into the analyser region at the end of the apparatus, within which their dynamics can be evaluated.

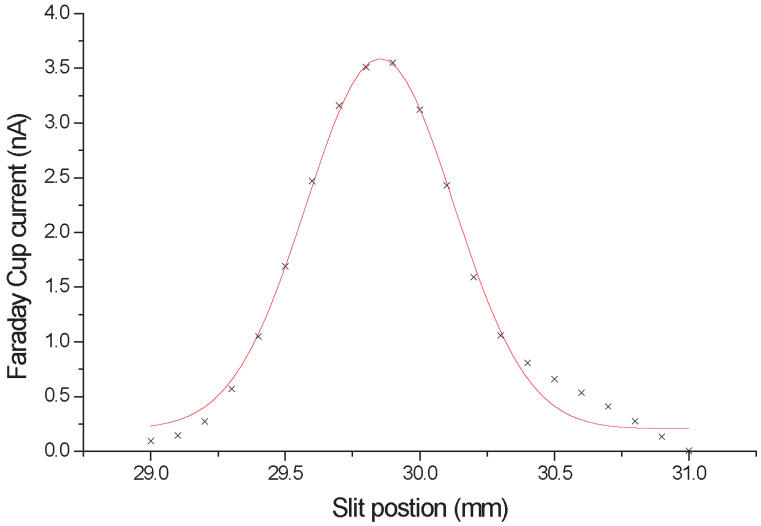

Figure 2.26: The ion beam profile of the Kr^+ beam used to study recombination, see [Williams et al., 2007] and chapter 4. The red curve shows a Gaussian fit with FWHM 0.55 mm. The total ion beam current was 60 nA.

The interaction region is also where the profile of the ion beam can be measured, see figure 2.26. This is done by driving a narrow, 0.12 mm, slit systematically through the beam and recording the ion current at each stage. This is always done when the laser is not present and gives a good indication of the ion beam spatial profile. This information is particularly useful when trying to understand the laser beam focussing geometry and the interaction of the two crossed beams.

2.5.5 Parallel Plate Analyser and Double Channeltron Detector

The products of the laser ion interaction are measured by a parallel plate analyser (figure 2.27). The analyser is comprised of three stainless steel plates mounted at 45^o to the incoming particles; an on-axis Channel-Electron Multiplier (CEM) and a second CEM orientated perpendicular to the axis of the ion beam adjacent to a Faraday Cup (FC). The first of these plates is held at earth, the second at a high negative voltage (V_A) and the third at 2 V_A. These voltages, along with the geometry of the plates and detectors, mean that when ions of a given m/q are steered into the FC, ions with half that m/q are

sent to the off axis CEM. Neutral particles are unaffected by the potentials of the parallel plates and proceed along their original path and on to the on axis CEM. The CEMs used in the detector are channeltrons (Burle Electro-Optics Inc. 4830G). Channeltrons where selected due to their sensitivity and relative low cost when compared to MCPs. They work in a similar manner to the MCPs described earlier in that they create a cascade of electrons that can be measured, and an ion yield subsequently implied. In essence, a channeltron is a large single channel MCP, curled up into the shape of a horn. The curled shape maximises electron collisions with the walls of the channeltron and minimises ion feedback; hence the amplitude of the resulting electron cascade is high. However, unlike MCPs they cannot be used to give positional information (not that the current TOFMS utilises this facility). Both CEMs are run at 2.0 kV on the back face and 0V on front. A positive voltage is used for the neutral CEM and a negative one for the off axis CEM. These potential differences are provided by an EHT power supply (Wallis HiVolt Ltd)

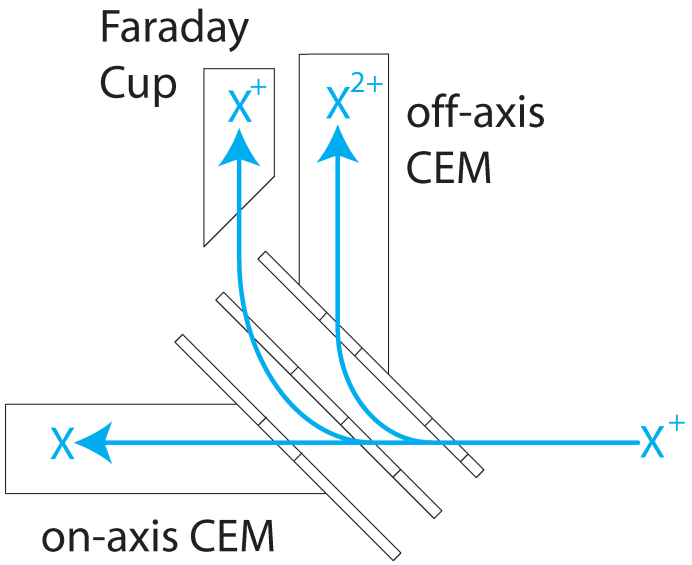

Figure 2.27: A Schematic of the parallel plate anlyser. The paths taken by a beam of atomic ions are illustrated.

Usual practise would be to set the parent ions on a trajectory onto the FC. The FC can cope with high fluxes of ions and is connected directly to an electrometer (Keithley Instruments 602). Once this is done, the laser is allowed into the interaction region and the interactions can be recorded either in the neutral (on axis CEM) or positive channel (off axis CEM). For example, with hydrogen gas in the source region a beam of H_2^+ can be extracted. This can then be sent to the Faraday cup, whilst products of the laser: H_2^+ interaction can be monitored by either measuring the H^+ (Coulomb Explosion) yield on the off-axis CEM or the H (photo-dissociation) yield on the on-axis CEM. Alternatively if an atomic gas is leaked into the source, a beam of atomic ions can be extracted, $X^{(n)+}$. Then the off-axis CEM can be used to detect further ionisation events, $X^{(n+1)+}$, and neutralising events, X, on the on-axis CEM after the laser ion interaction. There is also a pair of deflectors

(powered by Fluke (UK) Ltd. 415B EHT supply) between the interaction region and the parallel plates. These can be used to optimise detection of molecular fragments resulting from laser molecule interaction that have non-zero velocity components perpendicular to the axis of the ion beam.

As in the case of the TOFMS, the detection system is triggered to run only when a pulse from the laser is present. This cuts down background counts and avoids swamping the digital storage oscilloscope (DSO) (Tektronix TDS 744A) used for data collection. Additionally, a fast pre-amplifier (Ortec VT120C) is used to amplify the CEM signal and protect the DSO from harmful voltage spikes. During experiments, however, the ion beam runs continuously. This means that even if the data collection system is switched off between laser shots, the on-axis channeltron would still be bombarded by ions. Therefore, to prolong the life of the channeltron an electrostatic deflector, before the interaction region, is pulsed between laser shots. This prevents ions reaching the CEM when the laser is off. A square potential of 100 V with a width of 100 ms and separation of 200 μs is used and is obtained by combining a fast amplifier (custom built) and a digital delay generator (Stanford Research Systems DG535).

2.6 Summary

This chapter has provided the reader with background information on the laser system used for the experiments described in this thesis. The main physical process involved in the generation and transport of the laser pulses have been discussed and, where relevant, full descriptions of the processes involved have been given. The equipment employed in the experiments has also been evaluated, as have the mechanical details listed and the physical principles behind their operation.

Chapter 3

Data Acquisition and Experimental Methods

3.1 Introduction

The previous chapter of this thesis dealt with the laser system and the hardware used in the laboratory. Here, a discussion of the data collection procedure is given. The main techniques employed are explained in depth and their merits evaluated. Some techniques employed by other groups active in this area of research are also outlined and evaluated.

3.2 Instrumentation and Data Acquisition

The main experimental chambers are operated manually. However, the data collection system, once initiated, is an automatic process, see figure 3.1. It was devised within the research group, [Bryan, 2001], and relies on a Personal Computer (PC) running software that simultaneously controls an oscilloscope which records the experimental data and a motion controller, controlling the laser beams polarisation and focussing.

3.2.1 LabVIEW Virtual Instruments

LabVIEW is a graphical development environment produced and marketed by National Instruments, http://www.ni.com/labview/. It is used by a wide range of scientists to tackle problems in many fields of research and engineering. Its popularity within the research community is due to its scalability and the ease with which it can be made to interface with real-world signals.

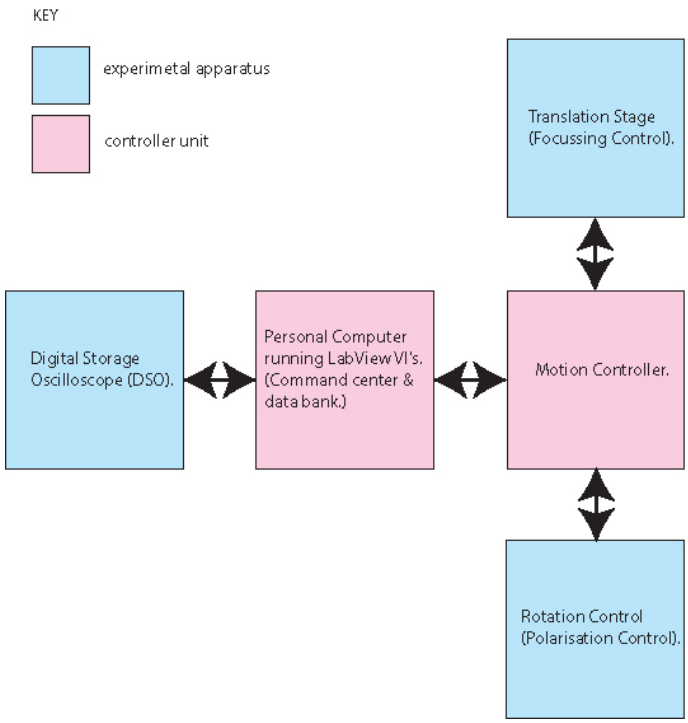

Figure 3.1: The data collection scheme. The pale blue squares in the flow chart represent parts of the system that interact directly with the experimental apparatus, whilst the pale pink squares represent the control modules.

In the work reported here, this software was used to run the data acquisition system, turning the electronic signals from the detectors into text files (****.txt). These text files can then be stored easily or analysed directly on a second PC. The majority of the data presented and analysed in this thesis was done using programs written in LabVIEW, although other software was used including Wolfram Technologies Mathematica (http://www.wolfram.com/) and Mathworks MatLab (http://www.mathworks.com/).

3.3 Experimental Methods

There are two main experimental techniques used in this thesis. The first is Intensity Selective Scanning with Effective Intensity Matching (ISS-EIM). This technique is used to investigate ionisation processes occurring within the focus of a single laser pulse and has been used with both the TOFMS and the Ion Beam apparatus. The second experimental technique used is a pump-probe procedure with a precisely controlled time delay between the first laser pulse (pump) and the second laser pulse (probe). These have been used, primarily to investigate nuclear dynamics in hydrogenic systems, although atomic systems have also been studied as a laser pulse diagnostic used to evaluate the at focus pulse

duration, see chapter 6. As of yet these pump-probe experiments have been confined to the TOFMS apparatus.

3.3.1 Intensity Selective Scanning with Effective Intensity Matching (ISS-EIM)

Intensity Selective Scanning (ISS) [Hansch and Woerkom, 1996, Hansch et al., 1996] was developed by Van Woerkom's group at Ohio State University in the mid-nineties as a way of investigating multiphoton ionisation over a broad intensity range, without the need for different focussing geometries.

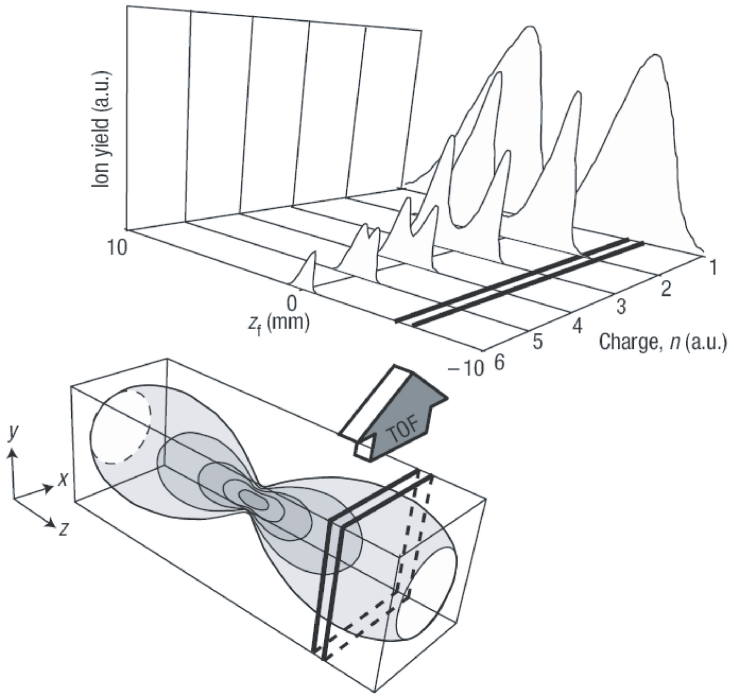

Figure 3.2: The ISS-EIM technique. Translating the focussing optic w.r.t. the z-axis combined with the limited acceptance of the MCP detector in the TOFMS effectively leads to the sampling of sections or *cuts* through the laser focus. Raw ISS-EIM results for Ar^+ to Ar^{6+} are also shown to illustate the method more clearly. Figure reproduced from Bryan et al[Bryan et al., 2006c].

In ISS-EIM experiments, laser pulses (τ = 55 fs, λ = 790 nm, E = 20 mJ, dia. = 22 mm) of known polarisation are softly focused into an ultra high vacuum chamber by a lens mounted on a translation stage. The chamber is then filled with a target gas, for instance argon, to a pressure of 1×10^{-8} mbar. A Time Of Flight Mass Spectrometer with a 250 μm entrance aperture is then used in conjunction with the precise movement of this focussing lens to produce a complete ISS-scan of the interaction region. See figure 3.2 and El-Zein et al. [El-Zein et al., 2001]) for an ilustration of the ISS process.

Typically, linear and circularly polarised pulses are used in the experiments in order to investigate recollision ionisation. In such instances the circularly polarised pulses are used as a control, as any freed electrons will not recollide with their parent ions when exposed to such a field. Thus, the ion yields obtained with circularly polarised light are, to a good approximation, only through sequential ionisation processes.

To allow such a comparison we employ ISS-EIM. This involves finding a constant ratio, R_{EIM}, between the linear and circular polarisation laser intensities, such that the relative ion yield is kept constant regardless of polarisation, as the detector is translated across the focus. For experiments with both atomic and molecular targets, this is obtained by setting the linear intensity to be 0.65 that of the circular [Suresh et al., 2005].

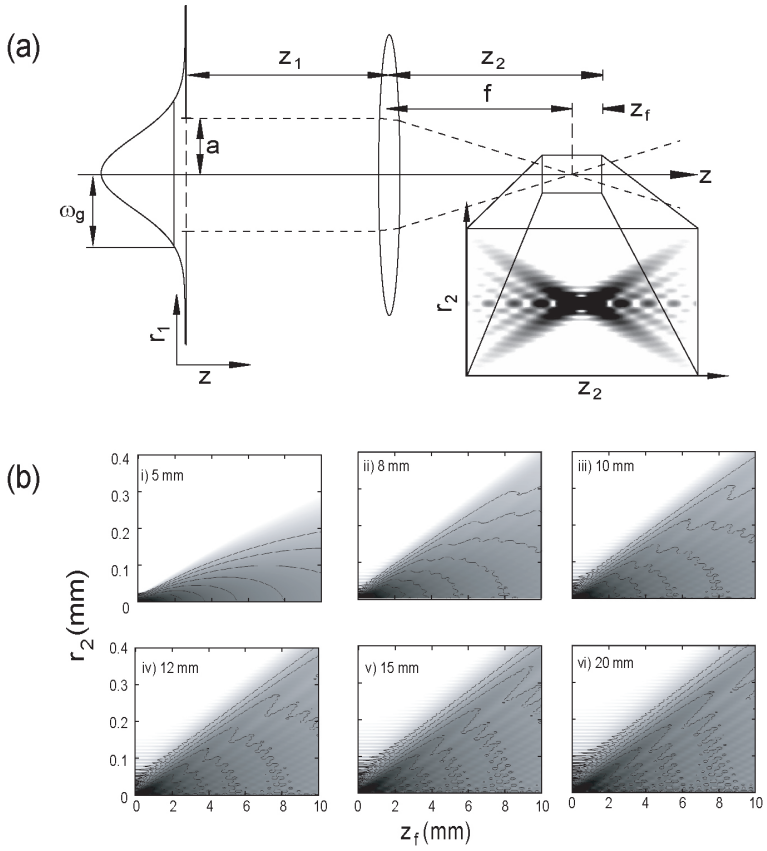

Figure 3.3: (a) The optical system employed in the 10 Hz, 25 mJ pulse experiments. The aperture, radius a, lies in the input plane at z = 0 with radial co-ordinate r_1. The resulting focus lies in the output plane at $z = z_1 + z_2$, with radial co-ordinate r_2. The focal length of the lens is f and $z = z_2 + f$ is a position in the vicinity of the focus. (b) Simulated intensity distributions in logarithmic grey scale with isointensity contours, separated by an order of magnitude. The aperture radius has been kept constant at 11 mm whilst the beam radius has been increased from 5 mm to 20 mm, panels (i)-(vi). Panel (a) taken from Bryan et al [Bryan et al., 2006b] and (b) from Wood et al [Wood et al., 2005].

This value was deduced from extensive tests with neon in a TOF-MS apparatus. Neon was selected for the calibration as it exhibits low levels of non-sequential ionisation [Augst et al., 1989], allowing comparison across the widest possible range of z, δz=10 mm, which is equivalent to an intensity range of 10^{13}-10^{16} Wcm^{-2}.

Ultrafast high power laser systems typically generate pulses with a Gaussian profile in the far-field, yet, geometric constraints imposed by the optical transport system prevent this perfect profile from reaching the experimental chambers. For many practical applications this poses no problem, as the con-focal volume normally lies within the acceptance angle of the detector employed. However, this is not the case with intensity selective scanning where the acceptance angle of the detector is physically limited. Therefore, it is essential to quantify the spatial distribution of intensity within the laser focus in order to fully understand the laser atom system under investigation. Starting from the Collins form of the Huygens-Fresnel integral, an analytical solution has been deduced for the propagation of a truncated Gaussian laser beam through an arbitrary ABCD optical system, see figure 3.3. The solutions from which, are then employed to remove the influence of diffraction in the laser focus from the atomic ionisation measurements. The removal of the volume is done in a manner much akin to that described by Walker [Walker et al., 1998], but with the on axis intensity distribution given by our non-Gaussian treatment. Such analysis yields geometry and diffraction independent ionisation probabilities as a function of intensity, which in turn allows the determination of the dominant ionisation mechanism.

To remove the volume and diffraction effects and achieve the de-convoluted ionisation rates, a complete z-scan must be taken with linear and then circular polarisation (see figure 3.4(a)). Usually this involves compiling time-of-flight spectra from 500 or more laser shots at each z position chosen, typically 0.25 mm apart. These scans are then integrated to give relative ion yields (see figure 3.4(b)).

In order to establish how the dominant sequential ionisation mechanism changes with the intensity, intensity is expressed in terms of the Keldysh parameter, γ, see equations 3.1 and 3.2.

$$\gamma = \frac{\omega_{laser}}{\omega_{tunneling}} \tag{3.1}$$

$$\gamma = \sqrt{\frac{E_i}{2U_p}} \tag{3.2}$$

The Keldysh parameter, γ, relates the laser frequency, ω_{laser}, to that of the tunnelling electron frequency, $\omega_{,tunnelling}$. E_i is the ionisation potential of the atom and U_p is the pondermotive potential of the laser field ($U_p = 9.33\times10^{-14}$ I Wcm^{-2}), both expressed in terms of electronvolts. When $\gamma \gg 1$, MultiPhoton Ionisation (MPI) dominates, as the

laser frequency is much greater than the tunnelling frequency. When the two frequencies are almost equal, $\gamma \approx 1$, Tunnelling Ionisation (TI) dominates. If the laser frequency is much lower than the tunnelling frequency, $\gamma \ll 1$, then the most prominent mechanism is field ionisation (FI).

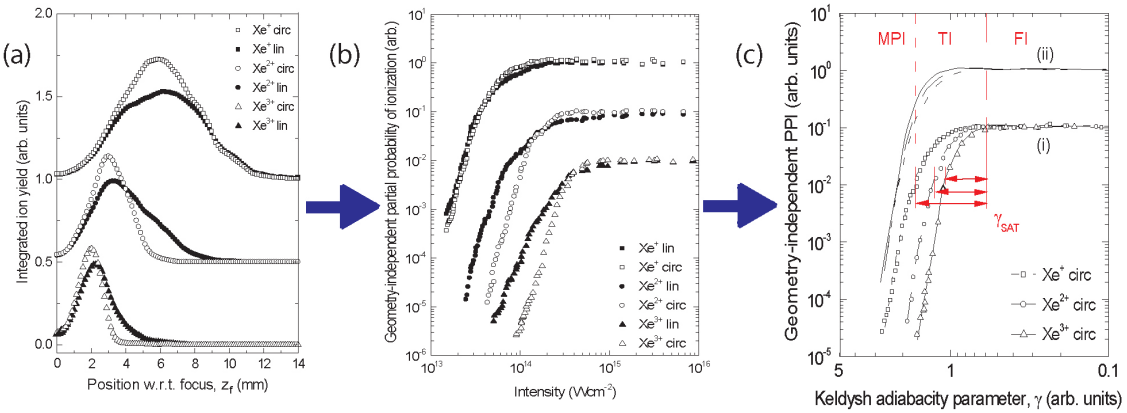

Figure 3.4: The non-Gaussian deconvolution process allows transition from ISS-EIM data to ionisation probabilities, allowing the contributions from different ionisation mechanisms to be isolated. (a) Raw EIM-ISS for the ionisation of xenon. Ripples in the ion yield indicate the presence of diffraction. (b) Geometry and diffraction independent ionisation probabilities as a function of laser intensity for the first three charge states of xenon. The saturated probability is unity in each case, but for clarity each charge state is separated by an order of magnitude. (c) Partial Probabilities of Ionisation as a function of the Keldysh Parameter, (i) as a direct conversion. (ii) with constant scaling factors; 1 for Xe^{+}, 0.76 for Xe^{2+} and 0.62 for Xe^{3+} done to improve the clarity of γ_{SAT}.

In Figure 3.4(c) the FI region gives a zero gradient. Where MPI dominates, a constant positive gradient is observed, from which the number of photons involved can be deduced. The remaining section of the graph is the region where TI dominates. This region is seen to vary with charge state, although the point of saturation, γ_{SAT}, of the Partial Probability of Ionisation (PPI) curves is similar for all the states shown.

Recently this work on ISS-EIM was published by the group [Bryan et al., 2006b] and has proven to be readily received. Other techniques for overcoming this problem exist, such as Intensity Difference Spectrum (IDS) [Wang et al., 2005, Wang et al., 2006] developed by Ben-Itzhak's group in Kansas State University. A second world leading ion beam research group, Figger's group at the Max Planck Institute for Quantum Optics in Garching, evade volume effects by having a very thin ion beam, 50 μm, compared to a Raleigh length in excess of 300 μm. Thus only a small part of the focus is imaged by their spectrometer [Sändig et al., 2000].

3.3.2 Pump Probe Experiments - The Mach-Zehnder Interferometer

In chapters 7 and 8 the nuclear dynamics of hydrogenic systems are investigated using few-cycle pulses in a pump-probe configuration. This technique was first used with ultrashort pulses [Saito and Kobayashi, 2002] to investigate conformational change in photoisomerisation processes and in experiments with hydrogenic systems [Trump et al., 1999, Posthumus et al., 1999]. (Other notable poineering papers include [Stapelfeldt et al., 1998], [Niikura et al., 2006] and [Vogt et al., 2006].) In this instance, the pump and probe pulses are made by splitting the output beam from the hollow fibre or prism compressor into two replicas and then recombining them with a controllable time delay between the pulses. This is done with a Mach-Zehnder interferometer, a schematic of which is shown in figure 3.5.

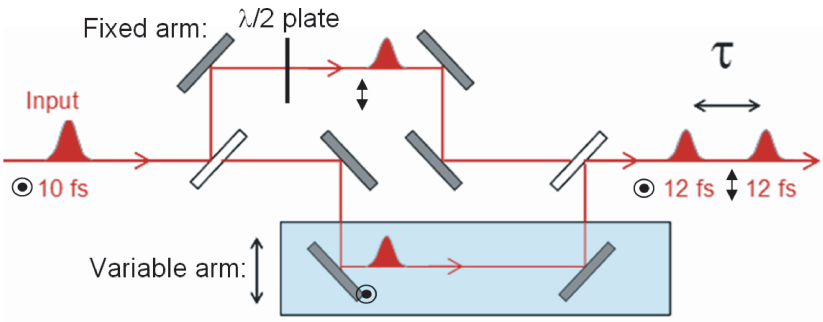

Figure 3.5: A schematic of the Mach-Zehnder Interferometer. The linear translator is shown as a pale blue box. A half wave plate is shown in the fixed arm, which rotates the polarisation from out of the plane of the paper (vertical) to in the plane of the paper (horizontal). This configuration is used in the work on nuclear wavepackets (chapters 7 and 8). Plane mirrors are indicated by dark blue rectangles and the pellicle beamsplitters by white rectangles.

The interferometer comprises of two pellicle beamsplitters, a linear translator and six plane mirrors. The linear translator (Newport Corp. M-MFN25CC) is computer controlled using a PC and a control unit (Newport Corp. MM4005) and offers 0.05 μm (1/3 fs) resolution over an range of 25 mm (>165 ps). The pellicle beamsplitters (Melles Griot 03 BPL 001/04) are made of optical grade nitrocellulose and are $\leq$2 μm thick. Pellicle beamsplitters are used to avoid ghosting and preserve the pulse duration as much as possible. The plane mirrors (Layertec GmbH 100767) are placed such that each optical path contains four reflections and one transmission, thus ensuring the interferometer does not impart a phase difference between the optical paths.

In order for the pump-probe experiments to work, the interferometer must be set up so that the beams are both temporally and spatially overlapped. The spatial alignment is done using a CCD camera and a soft-focussing lens acting as a far field monitor. The interferometer output is set so that the beams overlap on the far field monitor for the

entire drive range of the linear translator, i.e. they are made essentially collinear. Once the spatial overlap has been established, the translator setting that corresponds to the temporal overlap is located. This is done by sending the output of the interferometer into the intensity autocorrelator described in see section 2.3.1. This process is illustrated in figure 3.6.

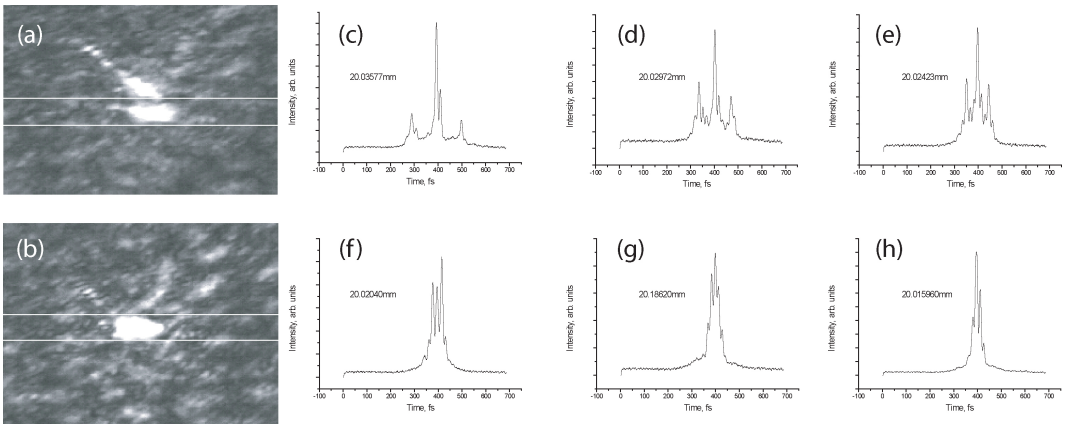

Figure 3.6: Panels (a) to (b) show screen dumps from the far field monitor. (a) with the beams misaligned and (b) with the beams overlapped. Panels (c)-(h) show the integrated output of the intensity autocorrelator for a given translator position. The large peak centred on t=400 fs is the second harmonic signal from the fixed arm. As the variable arm brings the second pulse toward temporal overlap with the first, its second harmonic signal is imaged on the autocorrelators CCD. This signal is seen as two peaks, which approach the central peak from opposite sides. The optimum temporal overlap is obtained when the spots are at their smallest and brightest. This optimal case can be seen in panel (h) where the translator is set to 20.015980 mm.

Once the temporal overlap has been found it is refined (see chapter 2) using xenon atoms in the TOFMS. From this experiment the pulse duration and shape of the laser pulses can also be established (see chapter 6). This is achievable due to the intensity dependence of the ionisation process and the optical interference the two pulses create as they overlap.

This interference can be seen in figure 3.7. In the figure, the time between the peaks of the pulses is indicated on the y-axis. The laser pulses that follow the fixed path can be seen as a horizontal stripe across the figure, whilst the laser pulses that follow the variable arm can be seen as the diagonal stripe running from the bottom left to the top right hand corner of the figure. In the simulation, the pulses were composed with just one single frequency, 3.75×10^{14} Hz, which corresponds to a wavelength of 800 nm. This is obviously not the case in the experimental situation, although strong interference effects are witnessed in the lab both visually (fringes can be observed during the alignment procedure) and in the ion signal from the TOFMS.

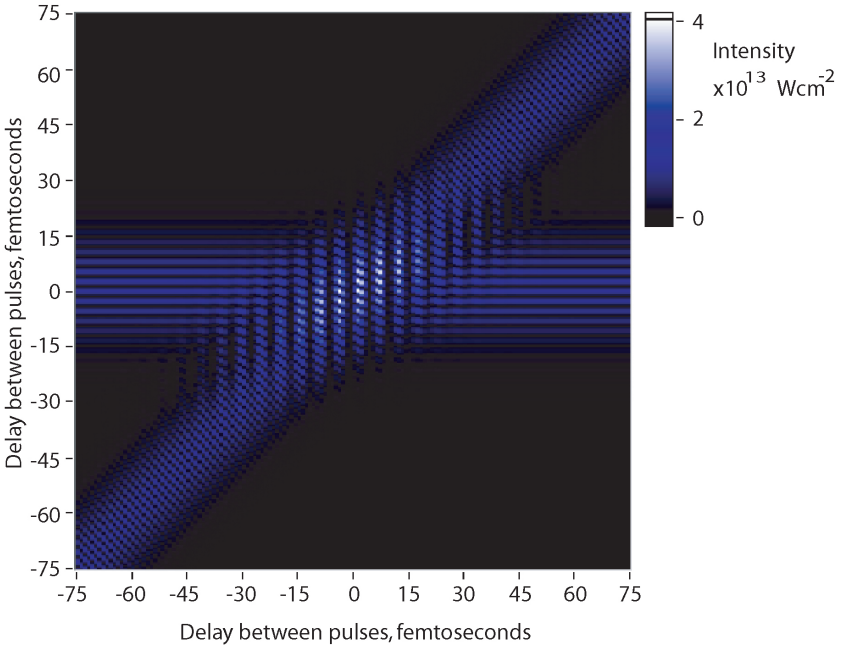

Figure 3.7: The Interference pattern created by 800 nm, 20 fs pulses in each arm of the Mach Zehnder Interferometer. Each pulse has a peak intensity of 1×10^{13} Wcm^{-2}. Hence at t=0 fs constructive interference leads to a peak intensity of 4×10^{13} Wcm^{-2}. Because of the double-pass nature of the variable arm in the interferometer, a movement of 0.15 μm results in a time delay between the pulses of 1 fs.

3.3.3 Chirping Few Cycle Pulses

As part of our investigation into the nuclear dynamics of hydrogenic systems (chapters 8 and 7) the pulse duration was varied. In separate trials the pump and the probe pulse duration was increased, with the other pulse being kept at the minimum duration of 12 fs. This temporal stretching was done by including cover slips of different thicknesses into each arm of the interferometer to induce a small degree of chirp into the pulses by material dispersion.

The results of this are shown in figure 3.8. The black squares indicate the experimental values used in the study and the red curve the theoretical prediction for the pulse width obtained using the *Refraction* computer program. *Refraction* is a computer program that calculates the Group Velocity Dispersion (GVD) and Third Order Dispersion (TOD) of optical components in typical laser systems. It was developed by Peter Dietrich of the Freie Universität Berlin for use in setting up ultrafast lasers and can handle bulk materials, prisms and gratings.

The initial pulse characteristics, such as the pulse duration and any GVD or TOD present, are inputted into the program initially and then any effects of the optical components

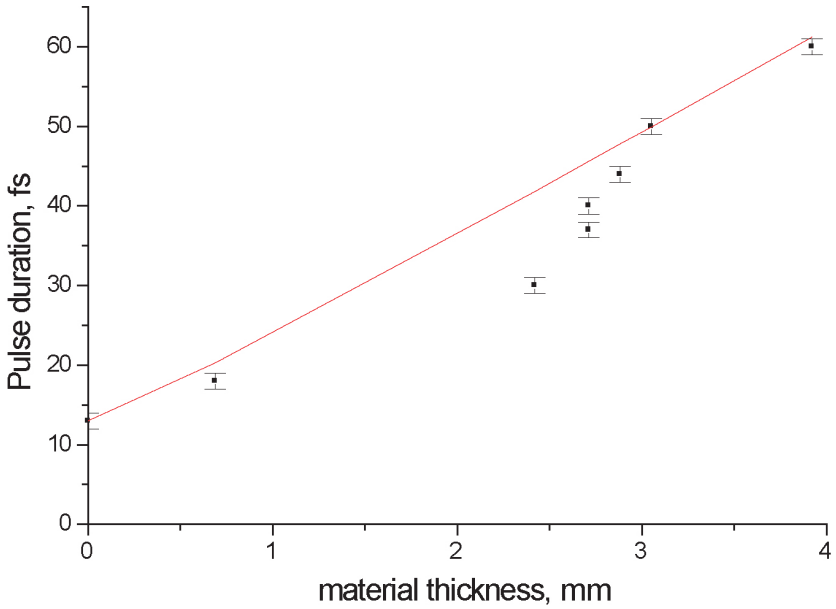

Figure 3.8: A plot of pulse duration against material thickness. The experimental points were measured on the intensity autocorrelator, whilst the simulated pulse widths were calculated using the *Refraction* program written by Dietrich. The data points are taken from our recently published [Bryan et al., 2007b] article discussing vibrational wavepackets, which is explored further in chapter 7.

are calculated. In this instance the pulses were assumed to leave the hollow fibre at a bandwidth limited duration of 13 fs with a Gaussian pulse profile. This goes some way to explain the slight mismatch between experiment and theory, as the pulses are known to have a sech^2 profile [Nisoli et al., 1996]. And although they are near bandwidth limited, some mismatch in the spectral phase of the pulse will no doubt lead to non-zero GVD and TOD values.

3.4 Contemporary Experimental Schemes and Methods

The experiments that form the backbone of this thesis are unique, however, there are several groups spread across the world working in this area of physics. In general, our apparatus may seem rather more basic than that of our competitors, i.e. our lack of Position Sensitive Detection (PSD), however, our experimental chambers are ideally suited to our needs, being highly transportable, robust and relatively easy to operate and repair.

3.4.1 Covariance Mapping

Covariance Mapping (CM) is a technique used in conjunction with time-of-flight mass spectroscopy that enables the complete identification of the origin of all the detected fragments resulting from intense laser pulse experiments with molecular targets. This is of particular interest, as under normal circumstances it is impossible to differentiate between the fragmentation channels a given species may have taken to reach the detector. For example, in an standard TOFMS experiment with CO, it would be impossible to know whether an observed C^+ ion came from a one specific process rather than another. i.e. $[CO^{2+}] \rightarrow C^+ + O^+$ rather than $[CO^+] \rightarrow C^+ + O$ or $[CO^+] \rightarrow C + O^+$ or any other possible pathway allowed by energy conservation.

Initially the method was applied to the ionisation of diatomic molecules
(CO [Frasinski et al., 1989], N_2[Fransinski et al., 1989] and H_2 [Frasinski et al., 1992]) by picosecond laser pulses. The Reading group that revived the technique (like many optical methods the technique was originally devised for treating radio waves and acoustics) were also the first to expand the method to look at the experiments involving triatomic molecules (N_2O [Codling and Frasinski, 1993] and CO_2 [Frasinski et al., 1994]) where the technique has found its niche.

The CM technique works by collecting individual Time-Of-Flight (TOF) spectra after each laser shot. The covariance between pairs of TOF spectra points then provides a measure of the strength of correlation between two randomised events. Where fragment ions are related to one another, a correlation between the events shows up, given that the process is repeated over a high number ($\approx 10^5$) of laser shots. This covariance is usually displayed graphically (see figure 3.9) as a colour map. However, it can be best understood by considering the covariance co-efficient, $C(t_1,t_2)$, which is defined in equation 3.3 as the difference between the average vector product minus the vector product of the averages of $S(t_1)$ and $S(t_2)$, where $S(t_1)$ and $S(t_2)$ are the TOF spectra array points at times t_1 and t_2, respectively. Expanding this idea to account for a large set of spectra, one gets equation 3.4 from which the covariance maps presented in the literature are created.

$$C(t_1, t_2) = < S(t_1)S(t_2) > - < S(t_1) >< S(t_2) > \quad (3.3)$$

$$C(t_1, t_2) = \frac{1}{N} \sum_{i,j=1}^{N} [S_i(t_1)S_j(t_2)] - \frac{1}{N^2} \sum_{i=1}^{N} S_i(t_1) \sum_{j=1}^{N} S_j(t_2) \quad (3.4)$$

In such CM all events that form the peaks lying along the diagonal, running from bottom left to top right, show correlations with themselves and are subsequently ignored. The other peaks or islands that appear off this diagonal line are correlations between forward-backward ions and backward-forward ions, (forward ions are those which initally move

towards the detector and backward ions are those which are initially moving away from the detector inside the interaction region of the spectrometer.) and by measuring their magnitude the ratios between the fragmentation channels can be established. This can be clearly seen in figure 3.9, where the fragmentation channels observed are boxed on the figure and listed to the right. One limitation of the technique, however, is that false coincidences can occur if more than one fragmentation event takes place in the laser shot. An example of this is shown in the figure 3.9 circled in red, where a C^{2+} ion is correlated to a C^{+}, which could not have come from the same OCS parent molecule. False coincidences can be kept to a minimum by reducing the gas pressure in the TOFMS, to try to ensure only one molecule is in the laser focus per shot. For our experimental parameters this equates to a typical gas pressure of around $3{\times}10^{-9}$ mbar from a base level of $2{\times}10^{-10}$ mbar.

Within our group [Bryan, 2001, Goodworth, 2002] this technique has recently been developed fully into three dimensions, to analyse ionisation pathways in triatomic molecules [Bryan et al., 2006a]. It has also been the motivation for an orginal Computer Aided Topography (CAT) technique that allows the reconstruction of atomic ionisation probabilities [Goodworth et al., 2005]. Within this brief synopsis of CM, only ion-ion coincidences have been mentioned. However, this technique almost right from conception has been used in the analysis of ion-electron and electron-electron coincidences.

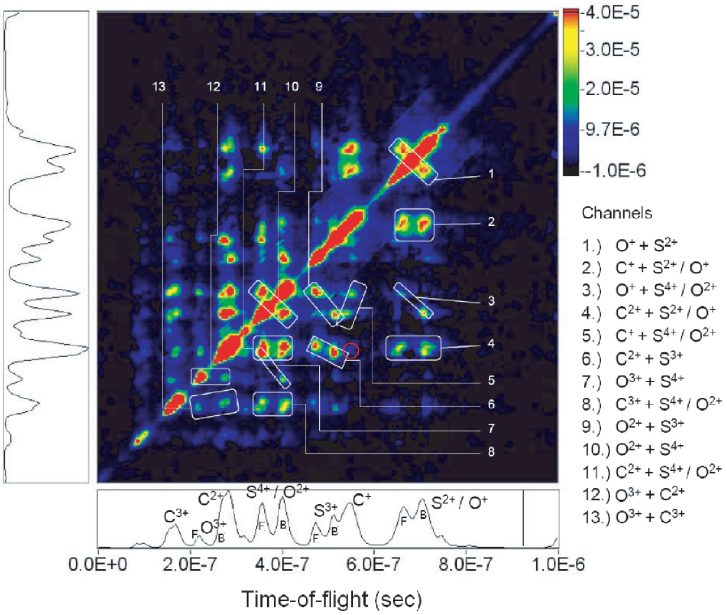

Figure 3.9: Covariance map of carbonyl sulphide. The map is built up from TOFMS measurements of 10^4 laser pulses, 55 fs in duration, at a central wavelength of 790 nm and a peak intensity of $2\text{x}10^{15}$ Wcm^{-2}. (Figure reproduced from [Sanderson et al., 2001])

3.4.2 Mass Resolved Momentum Imaging

Mass Resolved Momentum Imaging (MRMI) is a technique which was developed in Japan in the late nineties [Hishikawa et al., 1998b, Hishikawa et al., 1998a] to investigate the Coulomb explosion of small molecules in intense laser pulses. Like covariance mapping (see section 3.4.1), MRMI is based upon the traditional Time Of Flight (TOF) technique used this thesis. This technique has become less popular as experiments continue to increase in complexity, however, its reliance on relatively simple equipment means it is still considered to be a useful technique [Hishikawa et al., 1999, Hishikawa et al., 2001]. Today MRMI tends to be used in conjunction with coincidence measurements (see section 3.4.3), and continues to be a good source of high profile publications [Hasegawa et al., 2001, Hishikawa et al., 2006].

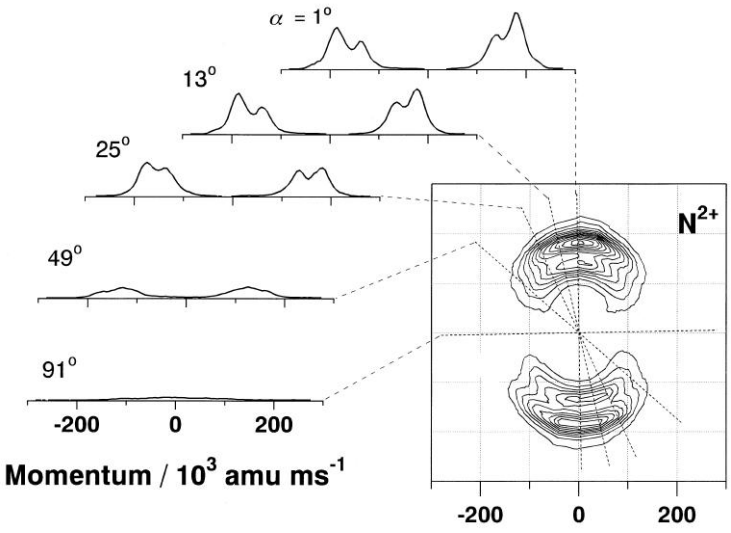

Figure 3.10: MRMI maps are constructed from momentum-scaled TOF spectra taken with different laser polarisations (measured w.r.t. the detector's TOF axis with α=0 corresponding to the case when the laser polarisation is parallel to the TOF axis). The contours in the two lobes connect smoothly regions of the same intensity level in the momentum-scaled TOF spectra. This figure is reproduced from [Hishikawa et al., 1998a] and shows the N^{2+} Coulomb explosion results from an experiment with an N_2 target and 52 fs laser pulses of peak intensity 3.5×10^{15} Wcm^{-2}.

The momentum maps (see figure 3.10) are comprised of high resolution (m/Δm = 620) TOF spectra taken with laser light of different polarisations. The polarisation of the laser beam is controlled using a half wave plate and is measured with respect to the TOF detector's main axis. These spectra are then momentum-scaled and combined to produce the final experimental images.

It is this momentum-scaling that is the key to the technique. Fundamentally, it involves the transformation of the TOF spectra into momenta. A second transformation to polar

co-ordinates is then undertaken. This is more complex and has to account for the finite angular acceptance of the instrumentation and hence the image's angular resolution. This process is explained in full in [Hishikawa et al., 1998a].

The MRMI maps that result from this process allow one to distinguish between different fragmentation channels (more energetic processes, such as Coulomb explosion, appear at greater radii in the images and tend to be more concentrated around 0^o) and any geometrical deformation (changing of bond angles) or alignment behaviour can be isolated [Bryan et al., 2000]. In general, high energy fragments do not appear around 90^o, due to the detector's limited angular resolution.

3.4.3 Coincidence Experiments

Another way that fragmentation channels can be measured is in coincidence experiments [Continetti, 2001]. Coincidence experiments measure both the resulting ions and electrons from laser target interactions simultaneously. Usually this is realised by detecting the electron and then setting an observation window, within which any correlated ions can be detected. Like the CM technique, section 3.4.1, false coincidences must be reduced by ensuring only one molecule is in the laser focus per shot.

The initial type of coincidence technique was PhotoElectron-PhotoIon COincidence imaging (PEPICO) devised in the 1970s [Danby and Eland, 1972]. Since its inception it has continuously evolved [Eland, 1979, Vallerga et al., 1989, Eland and Pearson, 1990] [Powis, 1993], often being merged with other modern methods (see sections 3.4.2, 3.4.4 and 3.4.5).

Figure 3.11 illustrates how a modern PEPICO experiment operates. Electrons are measured on one TOF detector while the ions are measured on a second. These detectors share an interaction region where the laser beam crosses either an atomic or molecular beam target. Typically, PSDs are used for each detector, resulting in high angular resolution.

As these techniques utilise all the emitted fragments they have become very popular and have been used by many groups in the field to obtain numerous important results, for example [Witzel et al., 2000, Lafon et al., 2001, Peterson and Bucksbaum, 2001, Chaloupka et al., 2003]. It is also particularly useful in separating sequential fragmentation from explosion events, hence its suitability for studying double/multiple ionisation events.

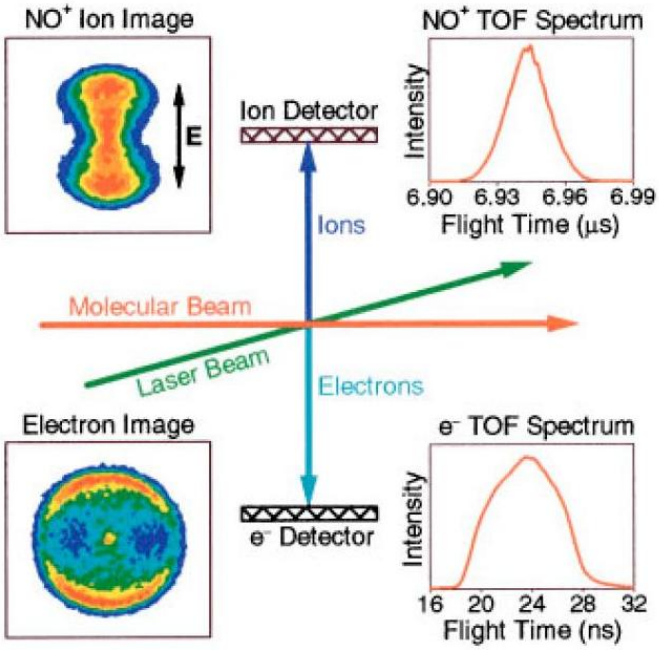

Figure 3.11: A schematic of PEPICO imaging. This figure is reproduced from [Davies et al., 1999], and shows dissociative multiphoton ionization of NO_2 in 100 fs laser pulses of peak intensity 10^{12} Wcm^{-2} at a central wavelength of 375 nm. NO^+ ions are measured in coincidence with the relevant photoelectrons. The polarisation of the laser is indicated by a black arrow on the detected images

3.4.4 Velocity Map Imaging Spectrometry

Velocity Map Imaging Spectrometry (VMIS) [Vallance, 2004] enables the user to measure both the energy and angular distributions of fragment ions from laser interactions with atomic and molecular targets. The technique is based upon TOF spectroscopy and PSD technology, see figure 3.12a. The fragments are produced between a pair of extraction plates and then are allowed a free field flight on to a MCP/phosphor screen.

Only ions with a specific mass to charge ratio m/q are detected. This is achieved by pulsing the voltages to the MCPs, so that they only operate within a restricted time window. Of the ions detected, their displacement from the centre of the detector is proportional to their fragmentation velocity, see figure 3.12c. This is achieved in part by additional electrostatic lenses [Eppink and Parker, 1997], that ensure all ions of the same velocity are mapped onto the same point in the detector. The images displayed on the phosphor screen are recoded by a CCD camera. Typical such detectors yield spatial resolutions of the order 100 μm. Which corresponds to and energy resolution of 1.4% at one electronvolt [Ni, 2006].

The key to the VMIS technique is the way the detected images are converted into the true velocities of the fragments. Initially, this was done by means of an inverse Abel

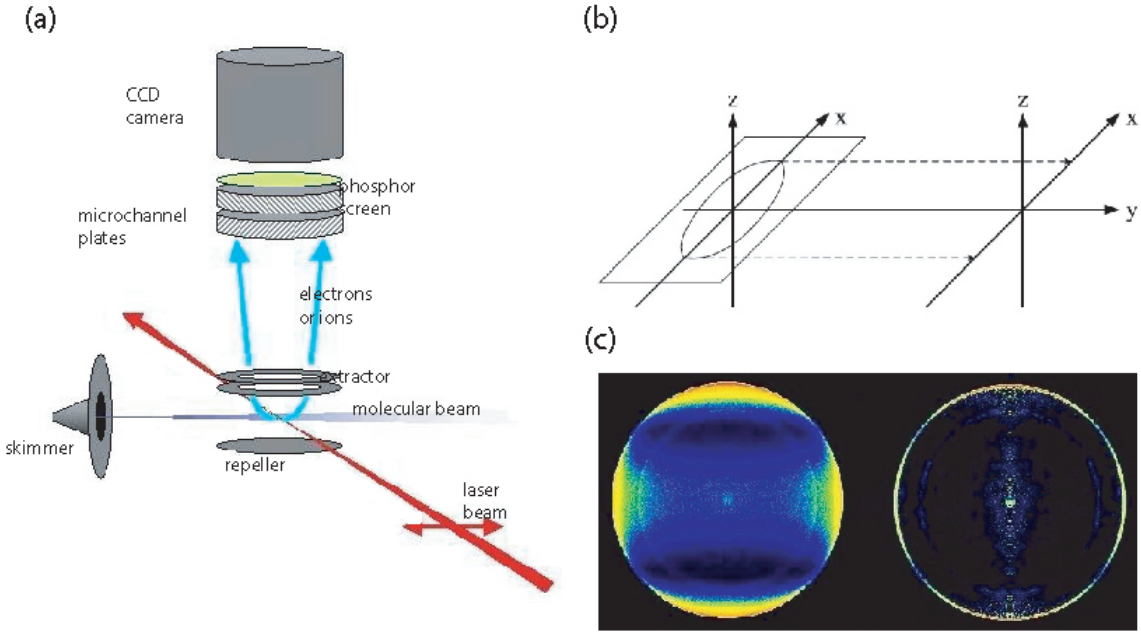

Figure 3.12: The principle of Velocity Map Imaging (VMI). Panel (a) is a schematic of a VMIS. Panel (b) shows how an Abel Inversion maps a 2D slice of a 3D image into a line in a 2D plane. Panel (c) shows a typical result; the image on the left is the raw data, whilst the image on the right is a slice through a 3D velocity distribution, obtained by the Abel-inversion of the raw image. Particles of the same energy and mass to charge ratio form rings in the resulting images. The results are from an experiment investigating two-photon ionisation of argon by 532 nm laser light. Panels (a) and (b) are reproduced from the web-pages of Professor Vrakking (http://www.amolf.nl/research/xuvphysics/imaging.html) and panel (c) is reproduced from the PhD thesis of Yongfeng Ni [Ni, 2006].

transformation, see figure 3.12b. This involves taking Fourier transforms of each line across the detected images. However, a new iterative method [Vrakking, 2001], which is less sensitive to image noise, is now favoured. This has improved clarity of the reconstructed velocities and reduced the data processing time required. VMI has also been developed to study electrons.

Along with COLTRIMS (see section 3.4.5) this technique has become one of the most dominant experimental devices in the field of ultrafast dynamics. Particular success has been obtained with attosecond pulse trains (Vrakking (AMOLF-The Netherlands) and L'Huillier (Lund-Sweden)). There also exists a VMIS development network within Europe which has substantial UK interest, (European Product Imaging and Correlation: Non-adiabatic Interactions in Chemistry (PICNIC) Network (http://www.chem.leeds.ac.uk/PICNIC/research%20areas/velocity.htm)) that works towards extending the technique.

Recently VMIS has also been adapted for use alongside synchrotrons [Rolles et al., 2005,

Garcia et al., 2005] and Free Electron Lasers (FELs) [Johnsson et al., 2007]. These developments are in their infancy, however they look to have great potential and will possibly offer a second doorway into the femtosecond/attosecond domain.

3.4.5 Cold Target Recoil Ion Momentum Spectroscopy

COLd Target Recoil Ion Momentum Spectroscopy (COLTRIMS) [Ullrich, 2004] has been the subject of many review articles [Ullrich et al., 1994, Ullrich et al., 1997] [Dörner et al., 2000, Dörner et al., 2002, Ullrich et al., 2003] in atomic and molecular physics journals, which underlines its importance in this field of physics. It is widely considered to be the state of the art experimental device for practical work in this area of research. Not only is it capable of measuring the momentum of both positively and negatively charged particles emitted from a fragmentation event, it can be operated in either coincidence or standard mode as it has an angular acceptance of 4π steradians (up to an energy of 10^2eV) enabling detection of all the emitted fragments emanating from laser: target interactions leading to kinematically complete experiments [Dörner et al., 1997].

Crudely, one can think of a COLTRIMS device as a hybrid of a time-of-flight mass spectrometer and a time of flight-electron-spectrometer sited end to end with a common interaction/extraction region (see figure 3.13), both incorporating multi-hit position sensitive detectors. The target gas is injected into the spectrometer through the nozzle of a supersonic gas jet. The resulting supersonic expansion cools the target particles resulting in enhanced image resolution (initial momenta parallel to the laser polarisation direction are of the order of 0.1 au).

Both detectors are held inside a uniform magnetic field generated by a pair of Helmholtz coils, see figure 3.13. This causes the electrons to spiral around the B-field lines increasing their time-of-flight and subsequently the detector's resolution. (This also negates the effects of stray or uncontrolled magnetic fields such as the Earth's magnetic field might have on the flight path of the electrons). The ions are also deflected by the magnetic field, however, their significantly larger mass means this is a much smaller effect. Weak electric fields supplied by copper ring electrodes are also used to guide the fragmenting particles onto the MCP detector heads.

Since the technique's inception in the mid 1990's [Moshammer et al., 1994] [Dörner et al., 1994, Mergel et al., 1995, Wu et al., 1995, Moshammer et al., 1996] COLTRIMS has been steadily improved. A particularly exciting prospect is Magneto Optical Trap Recoil Ion Momentum Spectroscopy (MOTRIMS) [van der Poel et al., 2001, Turkstra et al., 2001, Flechard et al., 2001]. These devices are very similar to conventional COLTRIMS apparatus, however, the target particles are loaded directly from a Magneto Optical Trap (MOT) [Raab et al., 1987] rather than a supersonic gas jet. This results in a much cooler target, and hence the possibility of improved image resolution and the ability

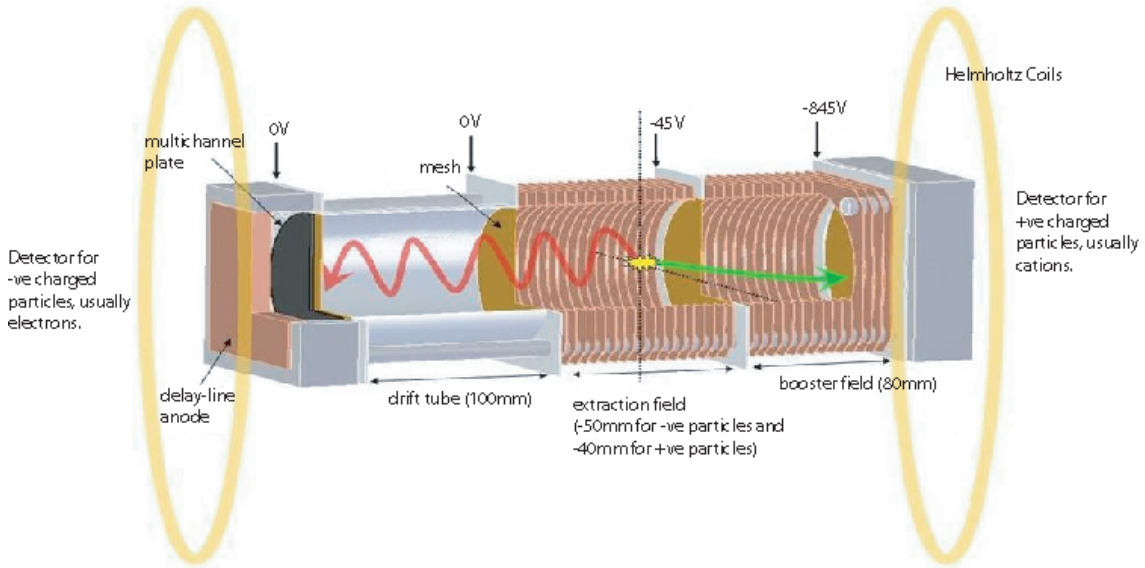

Figure 3.13: COLTRIMS devices consist of two position sensitive detectors; one for positive particles (usually ions) and a second for negative ones (usually electrons). Both detectors are held inside a uniform magnetic field, and electrostatic lenses allow particles to be detected over 4π steradians, which in turn allow for the complete reconstruction of the 3D momentum vectors of each charged fragment. Target species enter the detector as a supersonic jet, consequently high energy resolutions can be achieved. This figure is reproduced from the web-pages of Professor Boosh at the Technical University of Berlin (http://www.physik.tu-berlin.de/cluster/researchColhtml.html).

top study ever more subtle phenomena.

3.4.6 Pulse Shaping

Femtosecond pulse shaping [Weiner et al., 1988] has developed over the last twenty years to become one of the most likely techniques to offer scientists the ability to manipulate molecules on their natural timescales [Weiner, 2000, Sharan and Goswami, 2002]. Recent successes of pulse shaping include, enhanced high harmonic generation [Bartels et al., 2000], improved pulse compression [Zeek et al., 2000] and bespoke pump-probe experiments [Vogt et al., 2006].

Several shaping techniques are being employed at present, however, they all rely on the relationship between the bandwidth of the laser pulse and its temporal duration. The next key issue is to separate the frequency components of the initial laser pulse in space so that their amplitudes, A_ν and or relative phases, ϕ_ν, can be modulated *independently* of one another.

Typically this is done using a $4f$ setup, see figure 3.14. Such devices usually contain

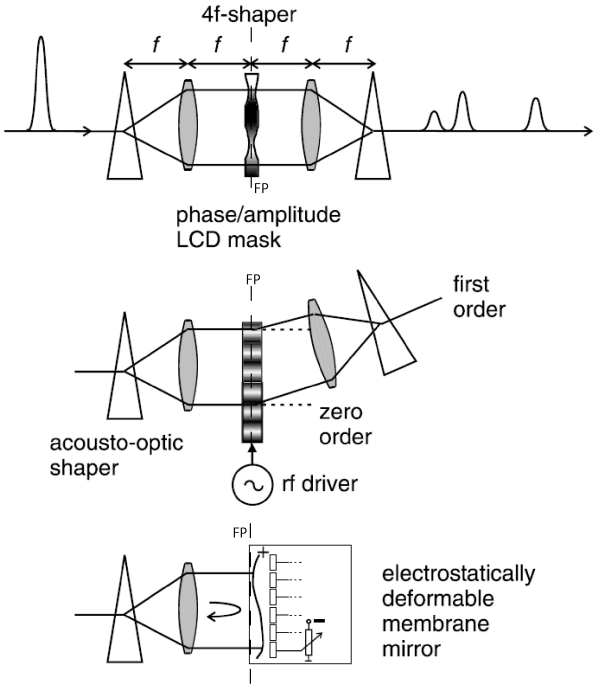

Figure 3.14: $4f$ Pulse Shaping Techniques. Panel (a) shows a pulse shaper with a liquid crystal array as the control element. Such devices can modulate both the amplitude and the relative phases of an incoming pulse. Panel (b) shows an acousto-optical modulator pulse shaper. By transmitting a shaped rf wave through the crystal the profile of the first order diffraction from the crystal can be controlled. Panel (c) shows a pulse shaper with a flexible membrane mirror as the controlling element. This shaper works by modulating the relative phases of the pulses constituent frequencies. In each shaper, the Fourier Plane (FP) is shown by a dashed line. Figure reproduced from [Steinmeyer, 2003].

two dispersive elements, usually a matched pair of gratings and a pair of convex lenses of focal length f. A collimated beam of flat spectral phase enters the device. After initial dispersion, the beam is recollimated but with an expanded diameter. Here the pulse reaches the central region or Fourier Plane (FP) of the device, where its constituent frequencies are separated spatially but propagating in parallel with one another.

It is in this FP that the individual frequencies can be modulated by either changing each frequency's amplitude and or relative phase. This is done by placing a controlling element at the FP of the $4f$ shaper. These controlling elements come in many forms, a few of which are shown in figure 3.14 and are described in brief below. (Note the similarities between the $4f$ pulse shaper and the pulse compressor (section 2.2.5) and pulse stretcher (section 2.2.2) described in the previous chapter.)

The first control elements used were fixed spatial masks. As their name suggests, these can only effect the incoming laser pulse in one way. Typically, specific frequencies are cut from

the incoming spectrum. Although the technique offers no capability to be programmable, its simplicity means it is still widely suitable as an early diagnostic in pulse shaping investigations.

A more popular device used as the control element in a $4f$ pulse shaper is the Liquid Crystal Array (LQA), see figure 3.14a. These devices are commercially available and comprise a Liquid Crystal Display (LCD), the pixels of which can be manipulated by applying controlled voltages [Weiner et al., 1992, Stobrawa et al., 2001]. This can be used to affect the relative phases and amplitudes of the frequency, which have been spatially sheared from one another by the time they reach the FP of the pulse shaper. Some commercial devices also contain polarisation control elements, allowing an even larger parameter space within which the incoming laser pulses can be controlled.

Also increasingly popular, Acousto-Optical Modulators (AOM) [Hillegas et al., 1994] can be used in the FP of a $4f$ pulse shaper, see figure 3.14b, to manipulate a laser pulse's profile. Often this method is favoured if high contrast ratios are required, as it works via a diffraction process rather than a transmission one. Usually, the AOM crystal is placed at its Bragg angle in the FP of the pulse shaper. An RF generator can then be used to transmit a shaped RF pulse across the crystal. This acts like a diffraction grating, with the incoming frequencies being diffracted independently of their neighbours. The first order output from the crystal is then recollimated and leaves the pulse shaper. (Note the similarity of this arrangement with that of the Dazzler described early in section 2.2.4.)

A fourth technique uses Flexible Membrane Mirrors (FMM) [Vdovin, 1995], see figure 3.14c. FMM are comprised of silvered silicon nitride membranes that can be deformed by a number of precise electrostatic actuators. This means that the individual frequencies of the spectrally dispersed pulse entering the FP travel different distances from one another, the effect of which, is a relative phase shift of the frequencies and hence a change in the laser pulse profile leaving the shaper.

Many pulse shaping experiments have been developed to include a high level of computer control. This control tends to be exerted through learning loops or evolutionary algorithms [Judson and Rabitz, 1992, Bardeen et al., 1997, Brixner et al., 2003]. Typically, a number of desired parameters (with tolerances) are input into the control computer with a set of initial constraints for the control element of the pulse shaper. Laser pulses are then sent to the shaper and the results compared to the objective. This process is then repeated until the obtained pulse shape has the characteristics required. For example, see figure 3.15, which shows a feedback loop used to obtain a rectangular pulse from a Gaussian like input.

Although pulse shaping devices and experiments are becoming more extravagant and ambitious, they do possess some inherent problems. These stem from the sensitivity of few cycle pulses to dispersion. This was discussed in the previous section as unwanted

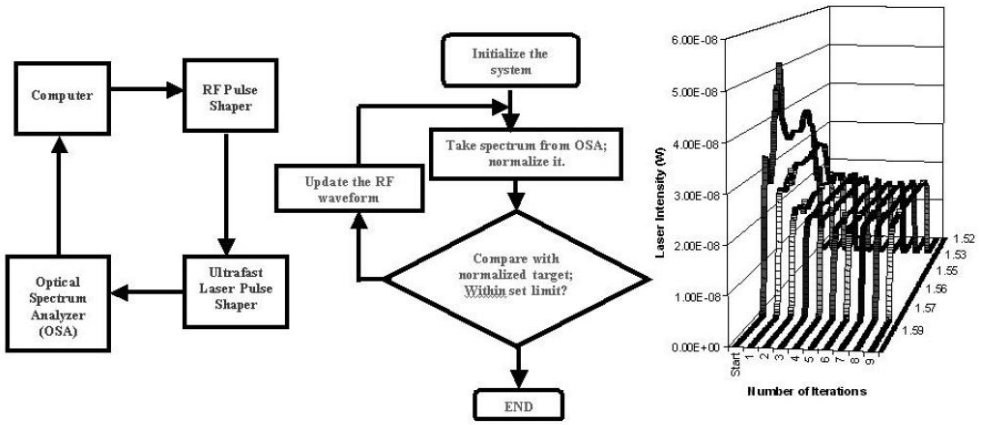

Figure 3.15: A schematic of a computer controlled pulse shaper. On the left, the feed back loop is outlined. The centre panel illustrates the logic behind each step in the scheme. Whilst on the right, the results of each iteration are shown. After the 9^{th} iteration, the desired pulse profile is obtained (in this instance a rectangular pulse). Figure reproduced from [Sharan and Goswami, 2002].

dispersion and is one of the major hurdles that must be overcome to obtain high energy ultrashort laser pulses. Generally, such effects are not completely negated, but are reduced with the residual effect compensated by additional pulse shaping.

3.4.7 Ion Beam Techniques

Other than the UCL/QUB collaboration there are relatively few groups that utilise ion beam technology to produce targets for ultrashort laser pulses. Our main competitors in the field are the groups of Prof. Ben-Itzhak at Kanasas State University (USA) and Dr. Figger's group at the MPQ in Garching (Germany). There are other active groups, such as Prof. Zajfman's at The Weizmann Institute of Science (Israel), Dr. Greenwood's group at Queens University Belfast (UK) and Prof H. Helm's group at Freiburg (Germany) that also use similar ion beam technology.

A second group of ion target experiments exist, however, these tend to be with much heavier ions (i.e. high Z ions), and take place at large scale facilities such as the TSI Heidelberg and GSI Darmstadt, both in Germany. Some of the groups listed above also work at these facilities, as both techniques are considered complementary to one another.

Although individual apparatus have their own nuances the majority of the technology employed is commonplace. This section briefly outlines the most common components in these systems that differ from our own. Often these differences seem to be advances

offering better ion beams (in terms of contrast, ion current and stability). However, our system is one of the oldest, pre-dating its rivals by several years and its relative simplicity means it is ideally suited to our experimental requirements (it is highly portable and easily set-up and taken down).

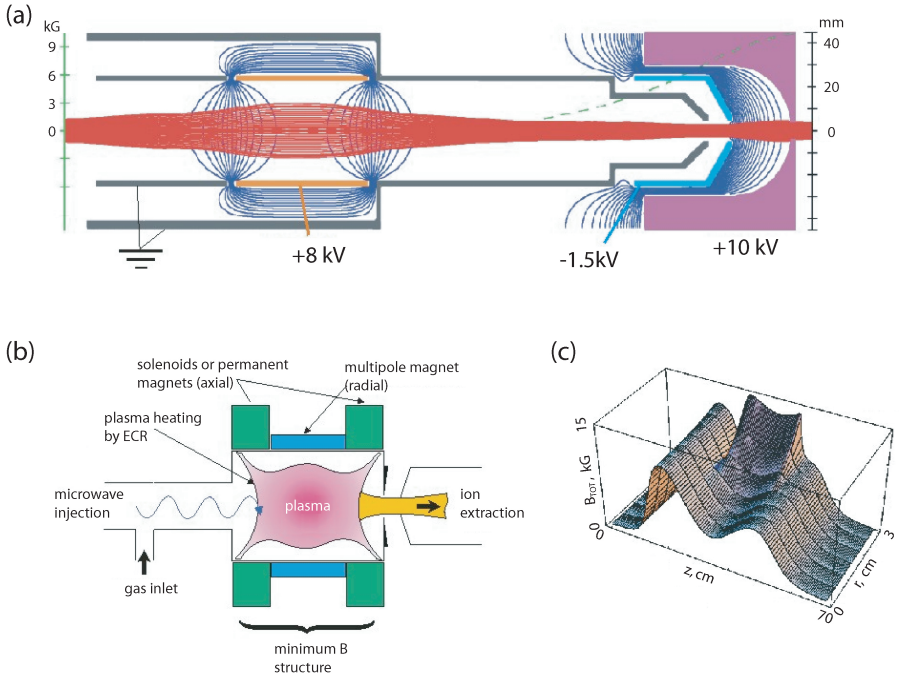

Figure 3.16: Panel (a) shows a simulation of an argon ion beam (red lines) extracted from an ECR ion source. Panel (b) illustrates the principles behind the operation of an ECR source and Panel (c) maps the minimum B-field surface responsible for the electron confinement, which contributes significantly to the efficiency of the ECR to generate highly charged ion beams. This figure is reproduced from the web-pages of Roland Trassl, http://www.strz.uni-giessen.de/ ezr/english/prinzip.html.

The Electron Cyclotron Resonance (ECR) ion source [Broetz et al., 2001] has become the favoured source technology to produce ions for interactions with ultrashort laser pulses, see figure 3.16. At its heart, it relies upon the resonant heating of cyclotron electrons by the electric field of a microwave generator.

Gas is injected into the source typically via a needle valve. Here an elaborate magnetic field is maintained called the minimum B-field structure, see figure 3.16c. It is usually generated by a mixture of permanent magnets in Halbach formation [Halbach, 1980] and solenoids and is engineered such that the magnetic field strength (B-field) increases in magnitude in every direction from the centre of the source region. This maintains a degree of electron confinement within the source region, whilst enforcing the electrons into cyclotron motion in the centre of the apparatus.

This cyclotron motion occurs due to the Lorentz force (see equation 3.5) felt by the

electrons; the effect of which is an acceleration of the electrons around the B-field lines in the centre of the source region. This circular motion has a characteristic frequency, ω_{cyc}, called the cyclotron frequency.

$$\mathbf{F} = q(\mathbf{E} + v \times \mathbf{B}) \tag{3.5}$$

$$\omega_{hf} = \omega_{cyc} = \frac{e}{m} \cdot B \tag{3.6}$$

A microwave source with precise frequency, ω_{hf}, control can then be used to match this frequency so that equation 3.6 is satisfied. This leads to resonant acceleration of the electrons depending on the phase of the E-field of the microwaves and their transverse velocity. The net effect of this heating is an increase in the electron kinetic energy and subsequently an increase in the number and magnitude of collisions they undergo with the plasma's ions. This leads to further ionisation by electron impact, resulting in the production of a population of highly charged positive ions.

Throughout this process the related ions are effectively stationary due to their larger m/q ratio and are only confined by the positive attraction from the space charge of the plasma's electrons. Finally, the ions are extracted through the superposition of a strong electric field (see figure 3.16a) across the entire source region. As in the case of other source technologies generic ion optics are used for further focussing and ion selection.

As well as different source technologies, some ion beam apparatus contain storage devices or *traps*. One such device is the linear ion trap developed by Prof. Zajfman's group at the Weizmann Institute of Science in Israel [Zajfman et al., 1997, Dahan et al., 1998] (see figure 3.17) and now in use in laboratories across Europe (Stockholm, Louvain-la-Neuve, Belfast and Freiberg) as well as in the Oak Ridge National Laboratory in the USA. It works in a manner analogous to a simple laser cavity, but with apertures held at high potential differences acting as electrostatic lenses, rather than the traditional optics one would find inside a laser cavity, see figure 3.17(b).

Such electrostatic traps are particularly useful when dealing with polar molecules, as they enable experimentalists to produce molecules in specific vibrational states, rather than the Franck-Condon distribution of vibrational states (for example, see appendix I and J and [von Busch and Dunn, 1972]) produced typically in ion sources. For example in the instance of deuterium hydride ions, (HD^+), the transition between the v=1 level to v=0 level has a lifetime of 60 ms. Thus assuming a initial Franck-Condon population of ions leaving the source region, a confinement time of 500 ms would yield an ion beam almost entirely in the v=0 (99.9%) level [Orr et al., 2007].

These devices are loaded by a high quality and ideally mono-energetic ion beam. The ions, usually around a few kilo-electronvolts in energy, enter through a series of narrow

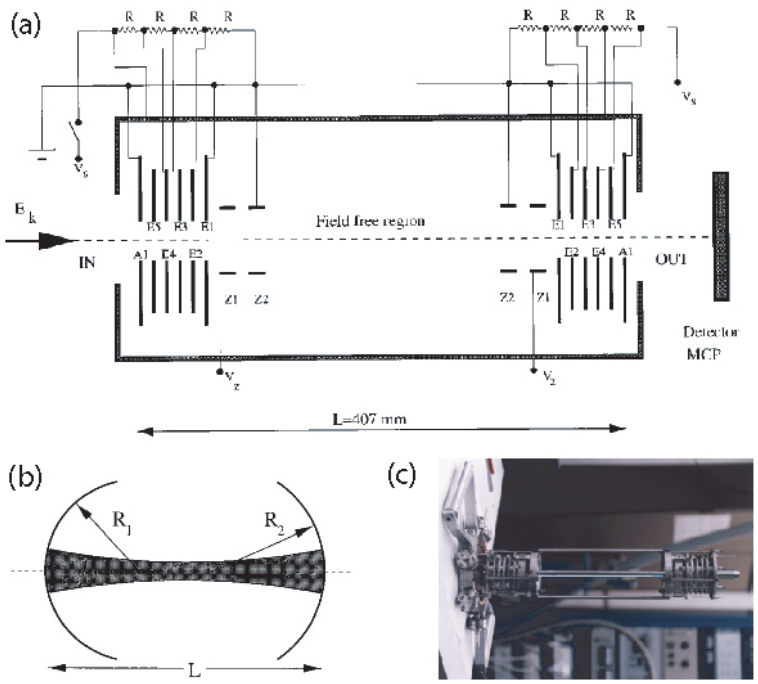

Figure 3.17: A schematic of a linear ion trap as used for ion beam storage. Panel (a) shows the layout of the electrodes in the ion trap. The operation of the device can be best understood by analogy with a laser cavity or optical resonator, as illustrated in panel (b). Panels (a) and (b) are reproduced from [Dahan et al., 1998]. Panel (c) shows a photo of the first such device. Image taken from http://www.weizmann.ac.il/particle/molecule/.

apertures, see figure 3.17(a). At the opposite end of the trap, there is a similar array of apertures. Potential differences of steadily increasing magnitude are applied to these apertures, which initially slow and then turn the ions through 180 degrees before accelerating them back towards the entrance end of the trap. Matching potentials are then applied to the entrance series of apertures. This results in the ions performing repeat trajectories across the trap, i.e. the ions become trapped within the device. At the centre of the device, the electrons experience a field free region, within which they can interact with laser pulses. Only the ions travelling along the devices axis are trapped; this leads to a lack of population with increased storage time, typically 5% remain after 500 ms. The trapped population is also strongly dependent on the energy distribution and spatial profile of the initial ion beam loaded into the trap.

One interesting element of the trap is that its operation is independent of mass. i.e. any charged ions can be trapped, as the device works entirely by electrostatics. This makes the linear ion trap an ideal candidate with which to investigate the interactions between bio-molecules and short laser pulses. On the negative side, the trap must be operated at a very low pressure, 1×10^{-9} mbar, to avoid collisions with background particles, which results in ions leaving the trapped beam.

Different detection schemes also exist. The most sophisticated of which is Ben-Itzhak's position sensitive detection system, see figure 3.18 and reference [Gaire et al., 2007]. It works using commercially available technology (http://www.roentdek.com/) based upon a delay line anode Position Sensitive Detector (PSD).

Similar detection technology is also employed by Dr. Figger's research group, based at the Max-Planck-Institute of Quantum Optics in Garching, Germany; our other major international competitors. In this instance [Pavičić, 2004] the main beam as above is focussed upon a Faraday cup with the fragment ions being recorded on a MCP/fluorescent screen PSD, which is also commercially available from Roentdek.

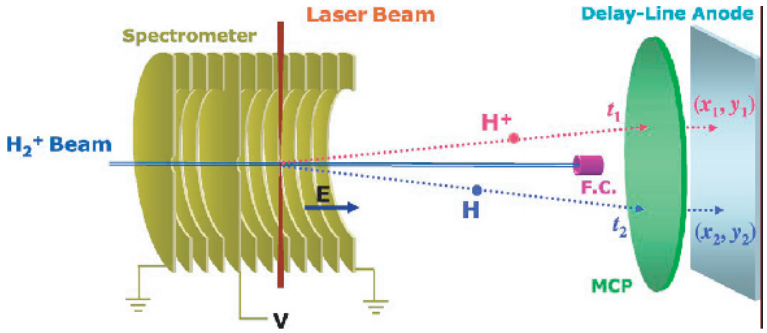

Figure 3.18: A Schematic of the interaction and detection regions of the ion beam apparatus of Prof. Ben-Itzhak based at Kansas State University in the USA. The figure is reproduced from [Gaire et al., 2007] and shows the interaction region within the spectrometer and the position and time sensitive detector. The PSD is set up so that the fragments of the laser ion interaction reach the MCP/delay-line anode, whilst the ion beam itself is collected on a small Faraday Cup, (FC).

3.5 Summary

In this chapter, the main experimental methods have been discussed. Techniques used by other groups in the same field of physics have been introduced briefly and their merits outlined. Section 9.3 discusses how assessment of these other techniques has helped shape our action plan for future study in this field. Particular reference is made to how we currently do not detect all the fragments from the laser-matter interaction and how we could access this additional information.

Chapter 4

Recombination in Metastable Atomic Ions

4.1 Introduction

In this chapter recombination in metastable ions is investigated using the ion beam apparatus. Using the technique of Intensity Selective Scanning with Effective Intensity Matching (ISS-EIM) [Suresh et al., 2005, Bryan et al., 2006b] developed within the group, ion yields for the interaction of singly charged noble gas ions, with both linear and circularly polarised laser pulses, have been measured over five orders of magnitude in intensity. Results are shown from experiments with krypton and argon ions which clearly show the presence of metastable ions in the beam [Greenwood et al., 2002, Newell et al., 2003]. It is these ions in which the signatures of electron-ion recombination have been isolated. The level of recombination is determined using the well known Kramers formula, originally developed by [Bethe and Salpeter, 1957] and later modified by Kim and Pratt [Kim and Pratt, 1983].

The krypton results from this chapter were recently published in Physical Review Letters [Williams et al., 2007] and comprised the first study of recombination to be measured by ion detection.

Electron-ion recombination has been studied widely over the last few decades (for examples, see the topical review by Hahn [Hahn, 1997]) as it is important in many branches of physics. These include the generation of attosecond laser pulses ([Bucksbaum, 2007, Rivière et al., 2008]), the chemistry of the interstellar medium ([Dyson and Williams, 1997]), as well as the attempts to engineer nuclear-fusion based energy generators ([Dendy, 1996] and the Joint European Torus - http://www.jet.efda.org/index.html.).

Other methods exist in which recombination is studied, for example electron coolers

[Heerlein et al., 2003] and ion storage rings [Larsson, 1995].

4.1.1 Recombination Mechanisms

Recombination refers to the process by which an atomic core captures a free electron to form a chemically distinct product. In this instance the atomic core is that of a doubly charged noble gas atom, A^{2+}, and the product is the corresponding singly charged ion, A^{+}. The electron which is recaptured is thought to come from the tunnel ionisation of the same A^{+} system, as described by Corkum's three step model of recollision or Non-Sequential Ionisation (NSI).

Electron-ion recombination exists in many guises, many of which are inter-related to one another [McDaniel et al., 1993]. The most simple recombination process, and the one investigated here is radiative recombination (see expression 4.1), where z stands for a positive integer and * corresponds to an electronic excitation. Simplistically this process can be thought of as the inverse of photo-ionisation [Dendy, 1996].

$$e^- + A^{z+} \rightarrow A^{(z-1)+*} + h\nu \tag{4.1}$$
$$e^- + A^{z+} \rightarrow A^{(z-1)+*} \rightarrow A^{(z-1)+} + h\nu \tag{4.2}$$
$$e^- + e^- + A^{z+} \rightarrow A^{(z-1)+} + e^- + h\nu \tag{4.3}$$
$$e^- + A^{z+} + B \rightarrow A^{(z-1)+} + B \tag{4.4}$$
$$h\nu + e^- + A^{z+} \rightarrow A^{(z-1)+} + 2h\nu \tag{4.5}$$
$$e^- + AB^+ \rightarrow A + B \rightarrow A^+ + B^- \tag{4.6}$$

The other recombination process illustrated in expressions 4.2-4.6 are not dealt with here, but are outlined for completeness. Expression 4.2 illustrates the process of dielectronic recombination, wherein existing electrons in the atomic core rearrange themselves to reduce the nuclear screening felt by the incoming electron. As this is a resonant process, the corresponding cross section is characterised by a series of individually resolvable peaks, for examples see [Griffin, 1989] and [DeWitt et al., 1994].

In systems with high electron densities, recombination may occur alongside superelastic and inelastic conditions. This dissipates energy and acts to stabilise the process. This is called collisional-radiative recombination, see expression 4.3. Another viable process in high density environment is termolecular electron-ion recombination (expression 4.4), within which a second atomic system stabilises the system rather than additional electrons. However, process 4.4 is more likely than process 4.3 in these systems.

If the recombination process takes place in a laser field, stimulated radiative recombination

can occur, see expression 4.5. This causes the recombination process to be increased by a gain factor. However, such effects are dismissed in explaining our results as the laser field is negligible at the time of recombination, see section 1.2.7 and figure 1.6 of this thesis for details.

Recombination can also lead to the dissociation of the system to which the electron becomes bound. This type of recombination is commonly referred to as dissociative recombination followed by ion-pair formation and is illustrated in expression 4.6.

Finally it is worth noting that most published recombination experiments involve merged-beam techniques, wherein an electron beam is co-propagated with an ion beam. This offers high energy resolutions but is notoriously difficult to setup and operate successfully. Contrary to this, our crossed beam experiments are considerably easier to conduct and the use of a laser rather than an electron gun offers the chance of improved energy resolution as the spread in photon energy is typically smaller than the energy spread of electrons originating from an electron gun.

4.2 Theoretical Background

Radiative Recombination (RR) occurs when an electron approaches a nucleus and becomes bound to the system. This process is less likely than the electron scattering from the nuclei (the incoming electron being repulsed by the Coulomb field of the atomic core and outer electrons), but under the right conditions is far from being a negligible process. In the instance of our experiments, the recombining electrons are sourced from tunnelling ionisation and are correlated to the atomic cores with which they recollide, thus further increasing the chances of witnessing recombination events. Although electron absorption is a fast process, the delay due to photon emission means the overall process is relatively slow and subsequent RR rates and cross sections are small.

4.2.1 The Kramers Formula

The model used to understand the RR process observed in our experiments is based upon the original work of Kramers [Kramers, 1923], who was one of the pioneers of early X-ray theories. From his work, Bethe and Salpeter [Bethe and Salpeter, 1957] developed the Kramers Formula (equation 4.7) to quantify the cross-section for RR, σ_n, into a state of principal quantum number, n, where ϵ corresponds to the electron energy, c the speed of light and Z_{eff} the effective nuclear charge of the atomic core. This hydrogenic treatment has been used widely by experimentalists to understand the RR to many different ionic systems, for example see [Andersen et al., 1990] and [McLaughlin and Hahn, 1991].

$$\sigma_n = \left(\frac{32\pi}{3\sqrt{3}c^3}\right)\frac{(0.5Z_{eff}^2)^2}{n\epsilon(0.5Z_{eff}^2+n^2\epsilon)} \tag{4.7}$$

Initially Z appeared in Bethe and Salpeter's equation rather than Z_{eff}. This correction was introduced by Kim and Pratt [Kim and Pratt, 1983] as a means of accounting for electron screening effects in non-bare nuclei and is defined by equation 4.8, where Z_i is the charge state of the ion and Z is the ionic charge of the bare nucleus. Since its introduction, the use of Z_{eff}, rather than Z, has become widespread in recombination studies involving non-bare ions, see for example [Andersen and Bolko, 1990].

$$Z_{eff} = \frac{(Z_i+Z)}{2} \tag{4.8}$$

The validity of this amendment has also been tested against more rigorous quantum mechanical treatments [Hahn, 1997, Zerrad and Hahn, 1998] and has found to be surprisingly accurate (±10% for low energy recombination) given its apparent simplicity. Z_{eff}, however, is a compromise in that it tends to lead to an over estimation of the cross section at low energy and an under estimation at high energy. As higher energy electrons typically *see* more of the nuclear charge, Z_{eff} should really scale with energy.

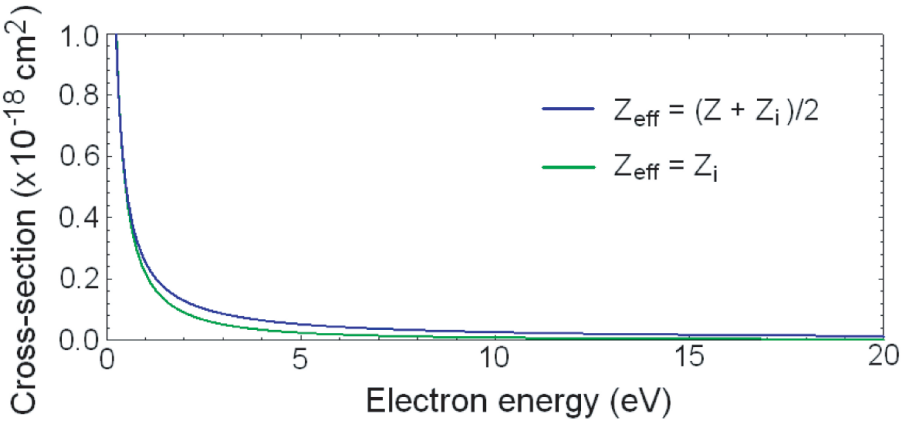

Figure 4.1: The effect of Z_{eff} in the Kramers Formula for the recombination of a Kr^{2+} nucleus and a free electron. The curve for Z_{eff}=Z_i has been multiplied by a factor of 100 and their respective values are shown in table 4.1. Reproduced from [McKenna, 2006].

Figure 4.1 shows how the inclusion of Z_{eff} into the Kramers formula effects the calculation of the cross section. At small energies both Z and Z_{eff} give similar values but diverge for higher energies.

Atomic Ion	n	Z	Z_i	Z_{eff}
Ar^{2+}	3	18	2	10
Kr^{2+}	4	36	2	19

Table 4.1: Values of n and Z_{eff} used in equation 4.7 for recombination of the ionised electron with the doubly charged np^4 core.

4.2.2 The Recombining Electron Energy and Corkum's Three Step Model

In the analysis of the recombination process, the energy of the electron, ϵ, has been deduced using ideas from Corkum's three step model of recollision [Corkum, 1993] discussed earlier in section 1.2.7 of chapter 1 and an earlier paper discussing the Above Threshold Ionisation (ATI) recollision model [Corkum et al., 1989]. In this seminal paper, Corkum states ...*The most likely and the maximum velocity of an electron passing the nucleus corresponds to an instantaneous kinetic energy of 3.17 times the pondermotive potential...*

Subsequently, the values of ϵ used are those that correspond to $3.17U_P$. Now as the intensity of the laser varies through the focal volume (along the z-axis), different values of z in an ISS-EIM experiment correspond to different values of the pondermotive potential, U_P, as given by equation 4.9. Assuming the laser pulses have a Gaussian focus [El-Zein et al., 2001], the intensity variation in the pulse w.r.t. z naturally translates into a variation of U_P w.r.t. z, allowing a picture of the recombination process to be built up for numerous electron energies.

$$U_p = \frac{e^2 E_0^2}{4 m_e \omega^2} = 9.33 I(W cm^{-2}) \lambda^2(\mu m) \tag{4.9}$$

Figure 4.2 shows some results obtained from Corkum's model that influenced the choice of $3.17U_P$ for the electron energy. Panel (a) shows how this value corresponds to the maximum value of the electrons energy, whereas panel (b) indicates that it is the also the most probable energy value obtained by an electron allowed to evolve in the driving laser field.

It is worth noting that if multiple passes of the atomic core are allowed [Moreno et al., 1995], the maximum energy of $3.17U_P$ still holds, although it ceases to be the most likely electron energy. In this treatment, however, only single approaches of the atomic core are considered and hence the energy of the electrons at a given z in the focus is that which corresponds to the appropriate $3.17U_P$.

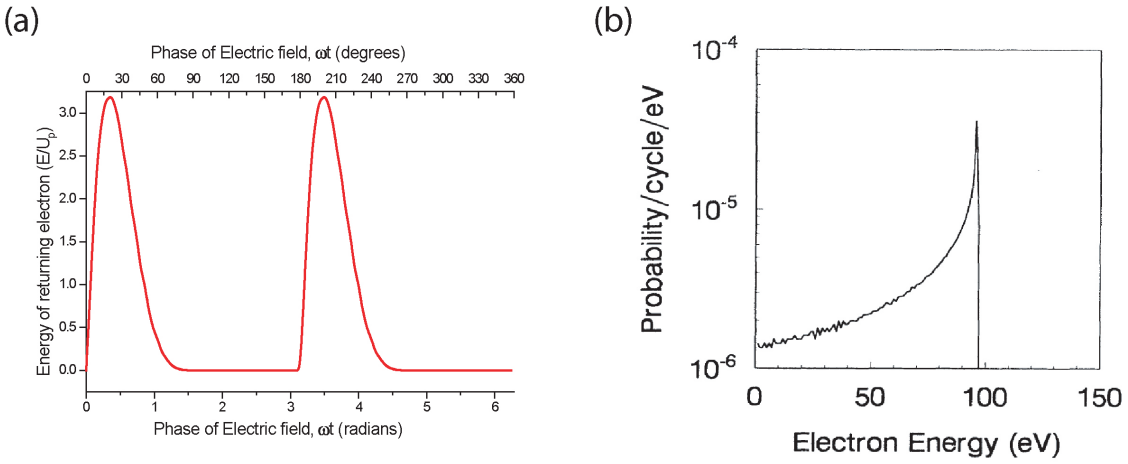

Figure 4.2: Panel (a) shows the energy of the returning electron as a function of the phase of the electric field at the instant of ionisation. The maximum energy of $3.17U_p$ occurs around a phase of 17^o. Panel (b) shows the velocity distribution for electrons at the time of their first encounter with the ion, as calculated by Corkum. The parameters used for this calculation were those of helium with light intensity of 5×10^{14} Wcm^{-2} and wavelength 800 nm. The sharp cut-off in the electron energy occurs at $3.17U_P$. Panel (b) is reproduced from [Corkum, 1993], whereas (a) has been calculated using the equation from the same publication.

4.3 Experimental Approach

The experiments conducted to isolate the RR in noble gas ions were done using the ion beam apparatus described previously. In each instance, beams of singly charged ions were extracted from the ion source, focussed and then transported to the instrument's interaction region. The beam itself is made primarily of ions in their electronic ground states, as most excited states decay whilst travelling from the source to the interaction region. However, various metastable electronic states survive, and it is in these ions that the recombination process has been isolated.

In the interaction region of the ion beam apparatus, the ion beam is crossed with the focussed laser beam and a ISS-EIM experiment is conducted. Details of the experiments, a discussion of the metastables in the beam and a justification of the EIM ratio used is briefly outlined below.

4.3.1 The Experimental Method

In the experiments used to study recombination, the ion beam apparatus is used. As the ion beam has been described previously in section 2.5 and elsewhere
[Calvert and McKenna, 2006], it is only mentioned in passing here. Spectrally pure gas is

leaked into the ion source and singly charged ions are extracted through a 2 mm aperture. Further confinement and focussing of the beam to improve its stability and profile takes place before the beam reaches the interaction region.

Figure 4.3 shows the profile of the ion beam used in the krypton study. It has a Gaussian profile, with a FWHM of 0.55 mm and a beam current of 60 nA. In the Argon experiment the beam profile was similar in shape to that displayed in figure 4.3 but with a FWHM=0.60 mm and a beam current of 65 nA.

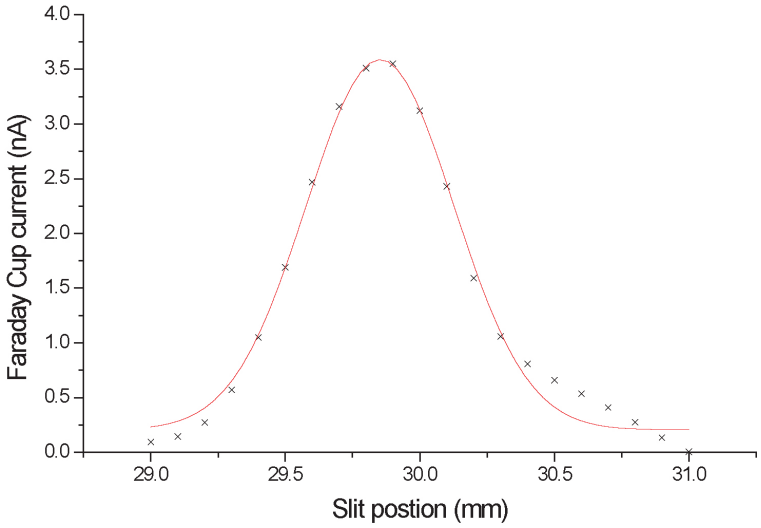

Figure 4.3: The Kr^+ ion beam profile used for the study of recombination. The beam comprises a total ion current of 60 nA. Black crosses are experimental readings and the red curve a Gaussian fit of FWHM=0.55 mm.

The laser pulses used in the experiment come from the 10 Hz source. In both experiments the pulses where generated by the 10 Hz laser system at Astra. The beam energy, E_{pulse} and pulse duration, τ_{pulse}, varied slightly between the experiments and were as follows; for krypton τ_{pulse}=40 fs and E_{pulse}=22 mJ, for argon τ_{pulse}=35 fs and E_{pulse}=16 mJ.

In both instances the peak intensity of the pulses is verified by measuring the spot size and beam energy. Comparisons are also made between ionisation experiments with the pulses in the Time of Flight Mass Spectrometer (TOFMS) detector to the results of [Yamakawa et al., 2004]. In the case of the krypton experiments, the maximum intensity was found to be 6×10^{16} Wcm^{-2} and in the argon case 2×10^{16} Wcm^{-2}. (Note each beam has its own diffraction limit, δ, see [El-Zein, 2001] for more details of the affects of diffraction limits on Gaussian foci.)

In the ISS-EIM experiments (see chapter 3 section 3.3.1 and [Bryan et al., 2006b]) the laser beam was focussed using a 250 mm plano-convex lens mounted upon a linear translator stage. The focus of the laser is then translated through the ion beam in 0.25 mm steps of z, with the yield of the doubly charged ions, (Kr^{2+} or Ar^{2+}) being averaged over 500

laser shots and recorded for pulses of both circular polarisation at full intensity and linear polarisation at 0.65 of the full intensity. In this manner a complete z-scan can be complied showing how the A^{2+} ion yield varies with z. In each instance, the ion yield of the three plus, A^{3+}, and four plus, A^{4+}, ions were also recorded from the interaction of the laser pulses with the singly charged ion beam, A^{+}. These plots are shown below alongside the main experimental results.(Note; A represent a generic atom, in this instance either Ar or Kr.)

In the experiments, polarisation and intensity control is achieved using a quarter waveplate (polarisation) and a combination of a halfwaveplate and a linear polariser (intensity).

4.3.2 Obtaining and Verifying the Choice of EIM Factor

At the heart of this work is the ISS-EIM experimental procedure developed within the research group to isolate the effects of recombination. In this work the results from tests with circular polarisation are compared to those with linear laser polarisation as a means of isolating these effects; as recollision is classically forbidden in the case of circular polarisation [Corkum, 1993]. A comparison to results with linear polarisation (where recombination is expected) allows the separation of ion signal from other competing ionisation mechanisms present in the data.

For a direct comparison to be made, the overall ion yield in each instance should be the same for all points in the z-scan. Classically, the same ion yield could be expected to be obtained from linearly polarised pulses of half the intensity of a corresponding circularly polarised pulse. However, in practice (and after numerous trials) this has been shown not to be the case. Therefore, a different ratio has to be used that gives the best possible fit.

In order to establish a suitable effective intensity matching ratio, tests were conducted on neon atoms in the TOFMS, see figure 4.4 and Suresh et al [Suresh et al., 2005]. Neon was selected due to its low level of Non-Sequential Ionisation (NSI), as shown in several studies by our group [Suresh et al., 2005] and others, for example [Augst et al., 1989] and [Becker and Faisal, 1999].

Here (figure 4.4), different EIM ratios were tested simultaneously. This was done to ensure the same laser focussing and target gas conditions. Only the best three results are presented, with the ratio 0.65 proving to be the optimum EIM value. The use of an EIM of 0.7 leads to excessive ionisation and an EIM of 0.6 too little, making linear/circular comparisons more difficult.

With this optimum value of the EIM ratio, the ionisation of krypton atoms was investigated. Here laser pulses of τ_{pulse}=50 fs and E_{pulse}=20 mJ were focused (using a f=250 mm lens) on to a target of gas pressure of 2×10^{-8} mbar and a ISS-EIM experiment conducted.

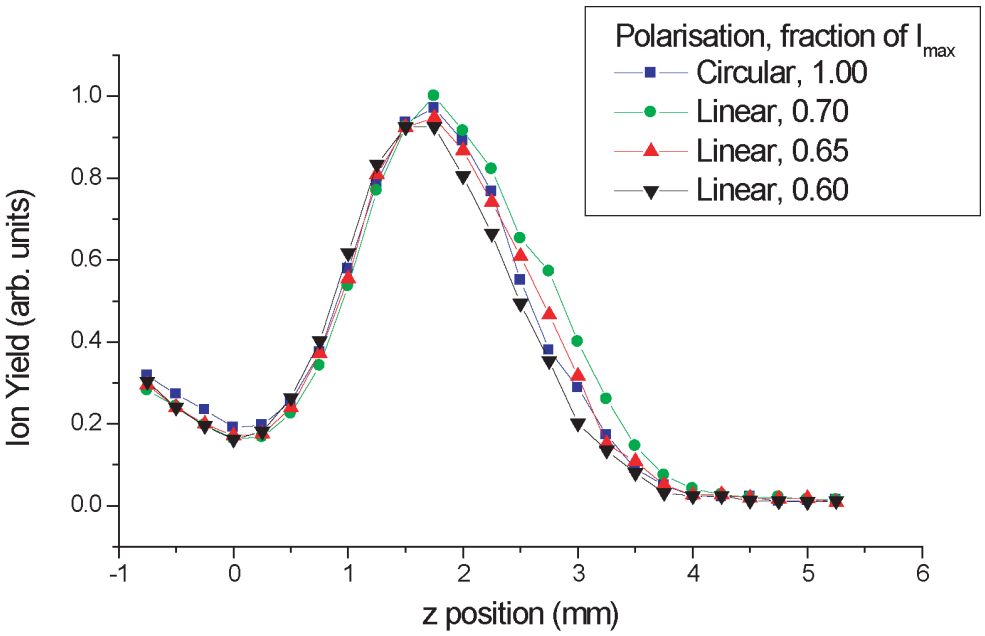

Figure 4.4: Raw ISS-EIM results from tests conducted with neon (2×10^{-8} mbar) in the TOFMS apparatus. The peak shown is a z-scan of Ne^+ ions from Ne neutrals. Blue squares represent circular polarisation at full power. Whereas green dots, red triangles and black triangles represent linear polarisation at 0.70, 0.65 and 0.60 of full power respectively.

Figure 4.5 shows these results in the form of a time-integrated z-scan.

Each charge state is shown on a different plot and then again as a component of the total ionisation yield (panel (i)). These results agree well with those previously published by our group on work with a xenon target [Suresh et al., 2005]. The difference in the heights of the ionisation peaks is a consequence of recollision leading to further NSI which in-turn results in a higher charge state being achieved. Therefore the reduction in height of the linear polaristion Kr^+ peak seen in panel (a) appears as a increase in linear polarisation Kr^{2+} yield panel (b). This continues for all higher charge states until the signal from each polarisation become indiscernible from one another. (A consequence of the limiting intensity employed in the study and the limits this places on the charge states produced.) If the ionisation was purely sequential then both curves would indicate the same ionisation yield at all values of z and subsequently lie on top of one another. Effectively circular polarisation acts as a NSI control.

Particularly important to the following recombination work is the final panel of the figure, panel (i), which shows all the ionisation products obtained from the target. In the panel the data indicates that the total number of ions observed is the same at any z for either polarisation. This verifies the choice of 0.65 for the EIM ratio and plays an important role in the isolation of the recombination signal in the ion beam experiments.

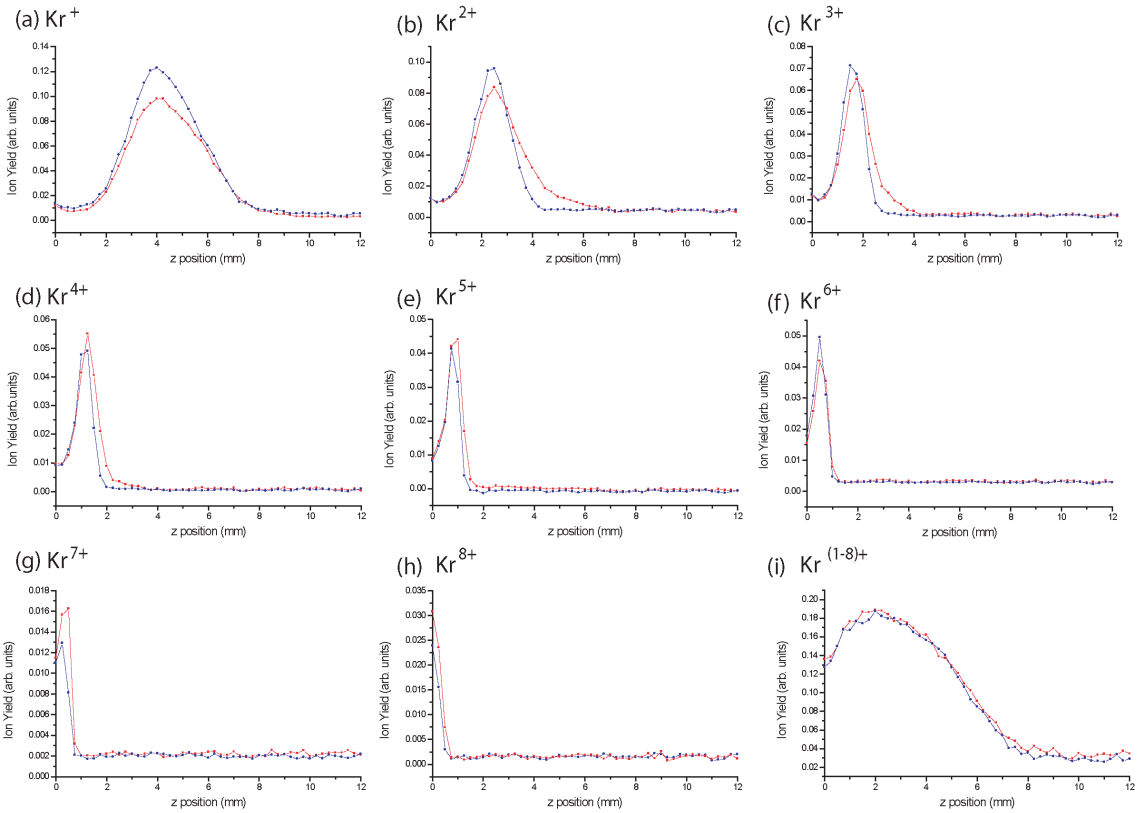

Figure 4.5: The raw ISS-EIM results for Kr^{+} to Kr^{8+}, panels (a)-(h) respectfully. Panel (i) shows a summation of the ion yields of all the charge states. This data was taken with krypton gas of pressure 2×10^{-8} mbar in the TOFMS detector and laser pulses λ=800 nm, E=20 mJ and τ=50 fs. The results from tests conducted with circular polarisation are displayed in blue and those done with linear polarsation and an EIM ratio of 0.65 in red.

All the work shown so far concerning the EIM ratio has been done with neutral targets in the TOFMS. Now as the recombination study uses the ion beam apparatus, the EIM ratio tests were also conducted using this apparatus. For the ground state peak a ratio of 0.65 was found to be the optimum matching factor. However, for the metastable peak no factor that matched the curves across their whole widths could be found, see figure 4.8 in the results section of this chapter for more details and further discussion. In actual fact it is this lack of an appropriate matching factor and discounting NSI and recollsion effects where discounted that first suggested another process (i.e. recombination) was being observed.

4.3.3 The Metastable Ions

In both of the ion systems studied here the recombination process has been isolated in the metastable population. These metastable ions reach the interaction region of the ion

beam apparatus as their decay times are longer than the time it takes the ions to go from the ion source, where they are produced, to the interaction region, where they are met by the laser pulses. The contributing states are believed to be $^4D_{7/2}$, $^4F_{9/2}$, $^4F_{7/2}$ and $^2F_{7/2}$ [Hagstrum, 1956], as shown in table 4.2. All other excited states thought to be populated in the ion source decay along the flight path of the apparatus, which for a 2 keV beam is of the order of microseconds.

Electronic State	Atomic Ion	
	Ar^+	Kr^+
$^4D_{7/2}$	16.41	14.90
$^4F_{9/2}$	17.63	15.62
$^4F_{7/2}$	17.69	15.86
$^2F_{7/2}$	18.50	16.32

Table 4.2: The metastable state energies. Values given are in eV and are taken above the corresponding $^2P_{3/2}$ ground state of the ion. Data obtained through the NIST atomic data base from the following publications; [Whaling et al., 1995] for argon and [Saloman, 2007] for krypton.

The metastable states have such long lifetimes due to transitions from them being electric dipole forbidden. This can be understood by consideration of Laporte's rule, which states that electronic transitions conserving either symmetry or asymmetry with respect to an inversion centre are forbidden.[Laporte and Meggers, 1925] i.e. if a molecule has a centre of symmetry, transitions within a given set of p or d orbitals (those which only involve a redistribution of electrons within a given subshell) are forbidden. On the other hand, excited states with electric dipole allowed transitions, relax much quicker and hence do not reach the interaction region of the apparatus. Typically, metastable states decay via electric quadrupole interactions or collisional processes.

Although these metastables are thought to comprise only a fraction of the beam 0.6% [McKenna, 2006] to 2.4% [Varga and Winter, 1978], due to the ISS technique, the large focal volume leads to enhanced signal. The statistical weightings of the individual metastable states is unknown, subsequently they are grouped together and treated as a single entity.

4.4 Results and Analysis

The results of the investigation are presented below. First of all the tests with the Kr^+ ion beam are discussed. This is followed by a concise treatment of the Ar^+ ion beam results as the two systems and the analysis are very similar. For instance in the case of the recombination in the krypton ion the electron recombines with the $4p^4$ core of the Kr^{2+} ion, as supposed to the $3p^4$ core of the Ar^{2+} ion in the argon case.

4.4.1 Krypton

Figure 4.6 shows the observed yield of Kr^{2+} ions from the ISS-EIM experiment on the Kr^{+} ion beam profiled in figure 4.3. The data are presented as a time-integrated z-scan with ion yield plotted against the z position of the focus. The narrow peak close to z=0 is the result of single ionisation from the ground state of the Kr^{+} ion to form Kr^{2+} ions. In this region the EIM ratio holds well and the results from tests conducted with circular and linear polarisation mirror one another well. This suggests that there is little if any NSI taking place in the ground state population. (A result reported previously by our group using tests on an Ar^{+} ion beams [Greenwood et al., 2002, Newell et al., 2003] with comparison to data from the corresponding isonuclear neutral target.)

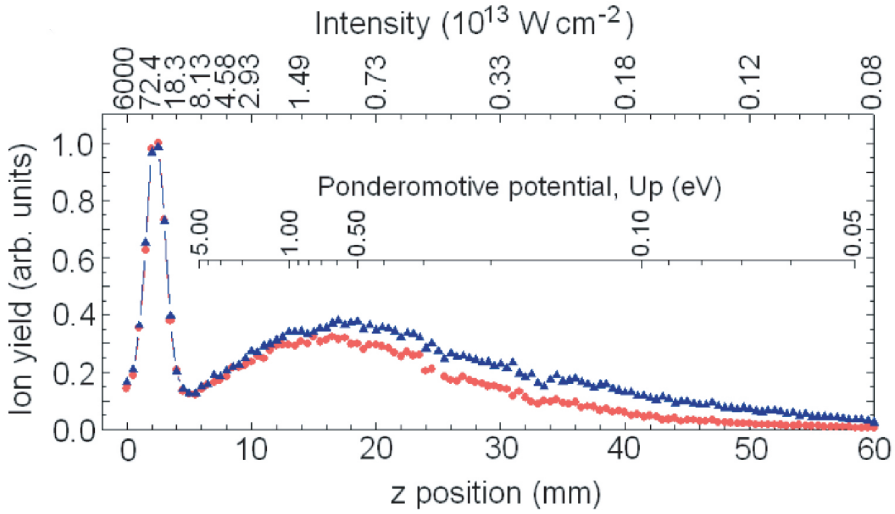

Figure 4.6: Raw ISS-EIM results for Kr^{2+} production from a 60nA beam of Kr^{+} ions. The high, but narrow, peak at low z corresponds to signal from the ground state population, whereas the low broad peak is the signal from the metastable population. the blue data points are the results of the tests with circular polarisation and the red those with linear polarisation.

Looking at the metastable peak however, the results from the different polarisations are quite noticeable with a much lower ionisation yield being obtained for the case of linear polarisation as compared to circular polarisation. This is the evidence of recombination being sought; if the ionised electron and the resulting Kr^{2+} ion core recombine, this would result in a loss of Kr^{2+} ion yield in the signal from the linear tests, as shown in the figure, when compared to their circular polarisation counterparts.

However, before this can be classed entirely as the signature of recombination in the metastable ion population, other possible causes for this discrepancy must be dismissed. One possible mechanism that might be responsible is recollision leading to NSI of the Kr^{2+} ion core. In this instance, however, this loss of flux from the Kr^{2+} z-scan (figure 4.6)

would show up in the corresponding Kr^{3+} z-scan (figure 4.7) as is the case for the neutrals (figure 4.5). As no such enhancement in either the Kr^{3+} or Kr^{4+} yield is seen, NSI via recollision can be safely dismissed as being the cause of this difference.

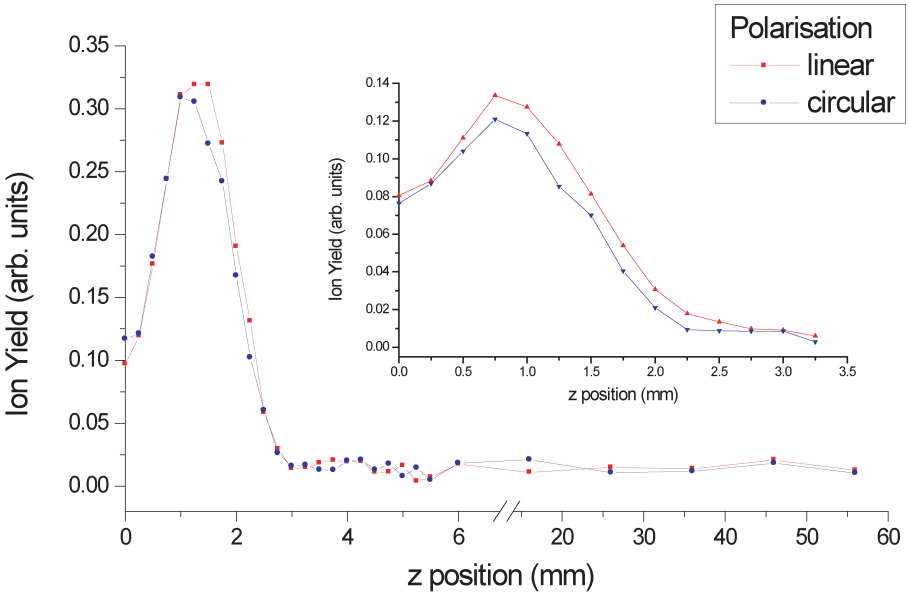

Figure 4.7: ISS-EIM results for Kr^{3+} and Kr^{4+} (inset) production from a 60 nA beam of Kr^{+} ions. The y-axes in each plot are relative to the one in figure 4.6. Note the x-axis break in the Kr^{3+} plot. With increasing charge state the peaks become narrower and smaller in height due to the reduced laser volume capable of generating the ion signal.

Also, the laser intensity and corresponding pondermotive energy, available to any electron allowed to evolve in the laser field at the z values corresponding to the metastable peak, would be low and hence the chance of recollision imparting sufficient energy to ionise the Kr^{2+} ion core small. (See for example the experimental cross sections for electron impact of singly [Man et al., 1987] and doubly charged [Man et al., 1993] noble gas ions, as well as a more recent measurement for the electron impact of multiply charged krypton ions [Loch et al., 2002] for confirmation.)

A second consideration is that the EIM ratio breaks down for the metastable peak. The nearest matches for this EIM_{meta} value, are shown in figure 4.8, although none prove to match both the leading edge of the curve at low z and the tail of the peak at high z. One slight change however, is that the peak now spreads a much broader range of intensity, as compared to the TOFMS results and the ground state peak of figure 4.6, where an EIM=0.65 was so successful. Could this be due to the EIM being dependent on the ionisation regime, i.e. when the dominant regime switches from Tunnelling Ionisation (TI) to Multi-Photon Ionisation (MPI), as it does within the metastable peak where the treatment breaks down?

This question, however, is not completely answerable, but the idea that circular pathways

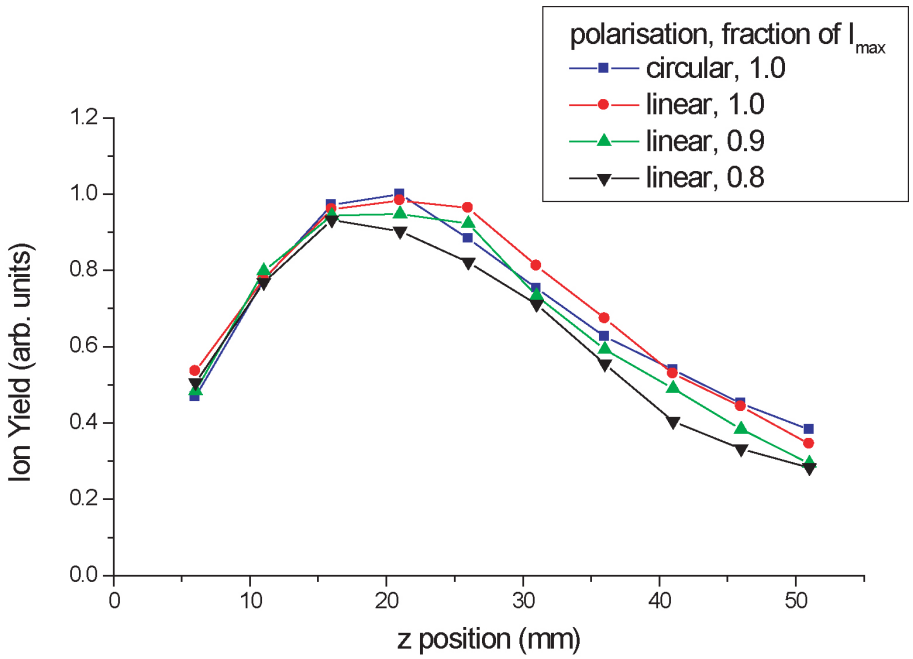

Figure 4.8: ISS data from a Kr^+ ion beam for different EIM values. The peak shown is the metastable peak within which the recombination process has been isolated. Blue squares represent circular polarisation at full power, red dots represent linear polarisation also at full power. Whereas green and black triangles represent linear polarisation at 0.9 and 0.8 of full power respectively.

towards ionisation in the MPI regime outnumber those available to linear light seems unlikely, due to the large amount of angular momentum that would have to be imparted to the system. Also resonant processes can be dismissed due to the broad intensity range for which the discrepancy in the ion yield is apparent. Also the EIM ratio of 0.65 has proven to be sound for a whole series of atomic and molecular targets prior to this study, for examples see Suresh et al [Suresh, 2005].

Another point to promote recombination as the responsible mechanism is that the difference in the signal disappears as the ground state ionisation threshold is reached. This is consistent with a recombination argument, as here a recombination to the ground state of the Kr^+ ion would result in re-ionisation to Kr^+, and hence the linear polarisation ion yield and the circular polarisation ion yield should be expected to match. This would also suggest a reason as to why recombination has not been isolated in an ion signal before!

The final piece of evidence comes from fitting the experimental data to Kramer's formula for RR. In order to do this the electron energy was taken to be $3.17U_P$, as discussed previously in the chapter, and the discrepancy in the ion yield for the two polarisations normalised for the number of electrons thought to be present. This normalisation was done in a rather simple manner by dividing the difference of the two signals (S_C-S_L) by

the value of the circular signal, S_C, considered as a control.

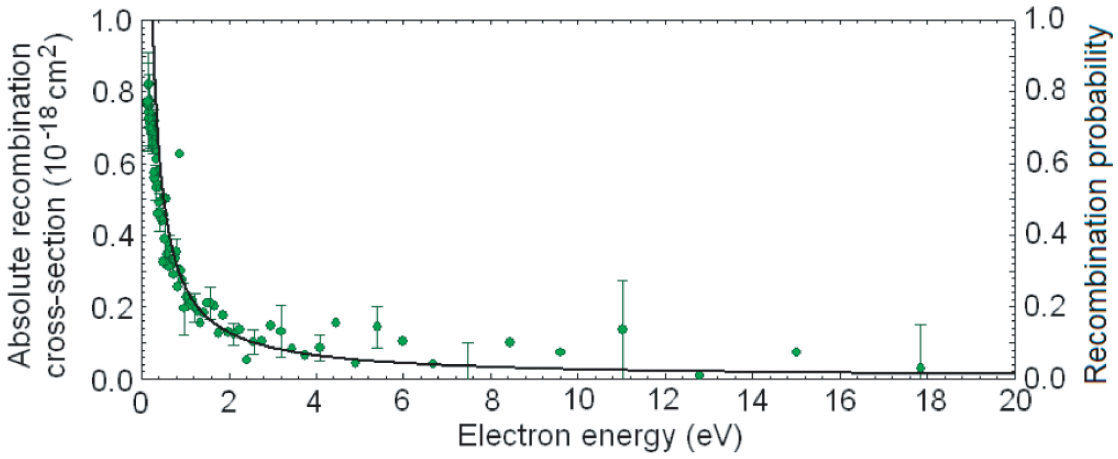

Figure 4.9: Experimental recombination probability (right scale and green dots) [(S_C-S_L)/S_C] as a function of the recollision energy of the electron ($3.17U_P$) for the radiative recombination of electrons and Kr^{2+} ions to form Kr^+ ions. The absolute recombination cross section is also shown (left scale black curve) as calculated from equation 4.7. The error bars shown are representative of the error on each data point presented in the plot. Reproduced from [Williams et al., 2007].

The results of this treatment can be seen in figure 4.9. Here, the predictions of the Kramer's formula are plotted on the left scale, and the scaled experimental recombination probability on the right. A good match to the theoretical curve is obtained, although some deviation is apparent. However, given the simplicity of the model, the match between experiment and theory is considered good and supports the conclusion that evidence of radiative recombination has been witnessed.

4.4.2 Argon

In this section the results from the argon ion beam are presented. As in the krypton case above, the recombination occurs between the electron initially ionised from the singly charged ion beam and its corresponding doubly charged ion core, as described by expressions 4.10 and 4.11.

$$Ar^+(ionbeam) + laser \rightarrow e^- + Ar^{2+} \quad (4.10)$$

$$e^- + Ar^{2+} \rightarrow Ar^+ + h\nu \quad (4.11)$$

Baring a slight reduction in overall laser power and an increase in the diffraction limit of the laser beam, the two experiments were more or less the same. Consequently, only the

major results are shown here.

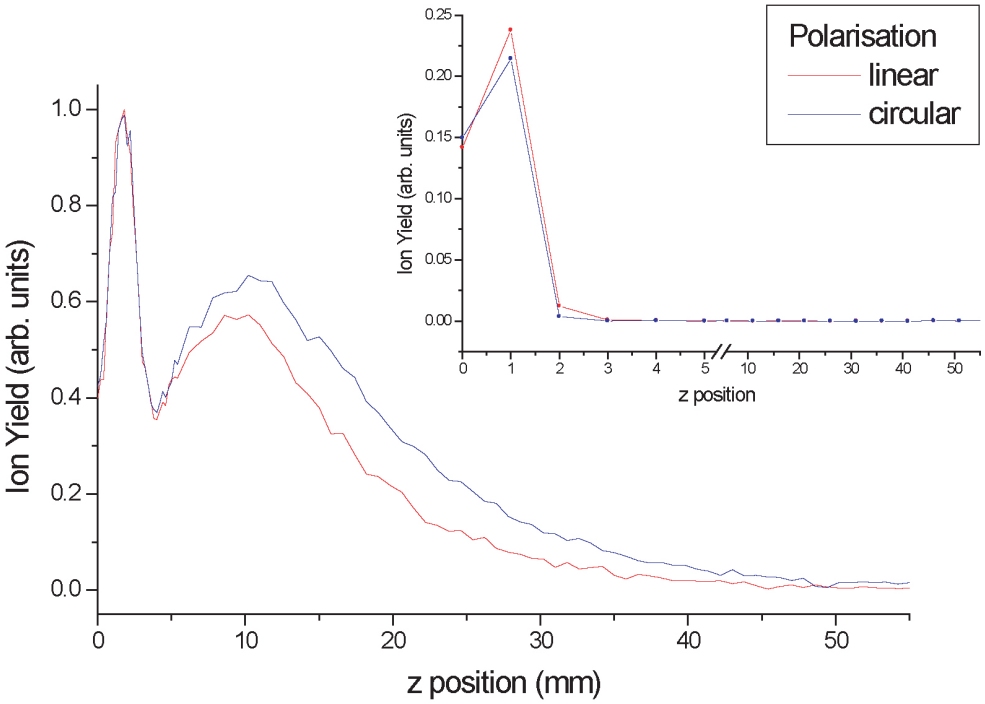

Figure 4.10: ISS-EIM results for Ar^{2+} (and Ar^{3+} inset) production from a 65 nA beam of Ar^{+} ions (FWHM diameter of 0.6 mm). Note the axis break in the Ar^{3+} plot.

Figure 4.10 shows the ISS-EIM results for the production of Ar^{2+} ions from the Ar^{+} ion beam. As was the case with krypton, two distinct peaks are observed; one from the metastable population (the low broad peak at high z) and one from the ground state population (high narrow peak at low z). The ion yields of the linear and circular polarisation data match one another well for the ground state scenario, but not for the metastable peak, where the linear polarised light produces significantly less ionisation than the corresponding circularly polarised light. Inset in the figure are the results of ionisation to Ar^{3+} ions from the same Ar^{+} ion beam, which illustrates that the mis-match is not a consequence of rescattering.

Finally, figure 4.11 is presented as a fit of the difference in the metastable signal, in comparison to the recombination cross-section obtained using the Kramer's formula (equation 4.7) and the relevant values of Z_{eff} and n. As in the case of the krypton ions, the agreement between the experimental recombination probability and the theoretical cross section is good and shows the majority of the features predicted. As before, some deviation exists at high and low values of the electron energy, possibly due to the use of a fixed Z_{eff}, rather than one explicitly dependent upon energy (as discussed previously). Overall the fit is good and gives further weight to the discrepancy in the two signals being the signature of radiative recombination.

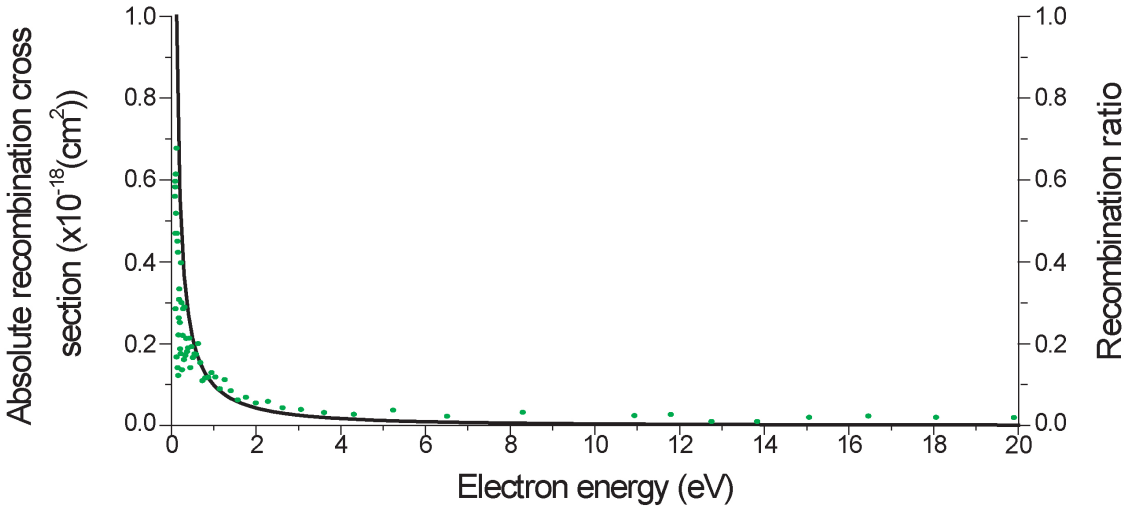

Figure 4.11: Recombination probability (right scale and green dots) $[(S_C\text{-}S_L)/S_C]$ as a function of the recollision energy of the electron ($3.17U_P$) for the radiative recombination of electrons and Ar^{2+} ions to form Ar^+ ions. The absolute recombination cross section is also shown (left scale black curve) as calculated from equation 4.7.

4.5 Summary

The signature of radiative recombination has been detected in the ionisation of singly charged ion beams with ultrashort laser pulses for the first time. In both instances reported here, the ionisation of the singly charged species to its corresponding doubly charged ion counterpart was followed by the recombination of the ionised electron with the ion to re-form the singly charged ion. By comparing the results to cross sections obtained from the Kramer's formula and by dismissing other possible causes of these effects, the recombination process has been unveiled.

Chapter 5

Recollision-Free Atomic Excitation in Argon and Krypton Ions

5.1 Introduction

Over the past few decades experimentalists have looked towards semi-classical theories based upon the pioneering work of Keldysh [Keldysh, 1965] to understand their observations. Recently, extensions to traditional ADK theories [Ammosov et al., 1986] and [Perelomov et al., 1966] have become more popular, as improvements in accuracy and efforts to extend the range of the Keldysh parameter [Keldysh, 1965] for which theories are valid, are sought. (See the review by Popov [Popov, 2004] for examples and the deficiencies in Single Active Electron (SAE) approaches to explain the experimental findings in both atoms [Moshammer et al., 2000] and molecules [Hankin et al., 2000].) One of these extensions is Multi-Electron Tunnel Ionization (METI), which is described here and then used to analyse the results of our experiments with two noble gas atom targets, argon and krypton.

In this chapter the ideas behind METI are discussed and presented alongside our experimental results. In general the calculations are independent of focussing geometry and therefore comparisons are made to our experimental results post deconvolution (See section 3.3.1 and [Bryan et al., 2006b] for more details on this process.) Experiment-theory comparisons from other groups are also discussed as a means of illustrating the theory's validity.

By employing our deconvolution technique [Bryan et al., 2006b] a complete comparison between experiment and theory has been obtained with corresponding papers published for Argon[Bryan et al., 2006c] and Krypton[Bryan et al., 2006d] ions.

5.2 Theoretical Approach

The METI theory was initially developed by Zon [Zon, 1999, Zon, 2000b] as a means of incorporating the effects of *shake up* into the traditional ADK formulation. As an extension of single active electron methods (for recent examples see [Scrinzi et al., 1999, Eichmann et al., 2000]) METI allows the bound system to evolve during the ionisation process. The method, however, is not an *ab initio* method and consequently does not require extraordinary computer power. Ab initio methods, such as S-matrix theory (see the recent review by Becker and Faisal [Becker and Faisal, 2005]) as well as approaches within the Strong Field Approximation, for example [Fabian et al., 2003], have yielded exciting results. However, the reduced computer power required by METI and its relative simplicity make it more approachable for laboratory researchers.

At the heart of METI is the *shake up mechanism*. It was first proposed by Carlson [Carlson, 1967, Carlson et al., 1968] as a means of explaining the excitation of a second electron following the single UV photon ionisation of a first. Shake up itself relies upon the *sudden approximation* (see for example [Schiff, 1955, Zettili, 2006]) which states that a quantum mechanical system subjected to a rapid change in environment has insufficient time for the functional form of the system to adapt, and so its probability density remains unchanged through the change. The approximation is valid in the case of tunnel ionisation when the ionisation potential is much greater than the excitation energy of the ion. This results in a fast or *sudden* excitation of low lying bound states during the tunnelling process.

In *shake up*, the ionisation of a first valence electron leads to the excitation of the remaining electron population via a *sudden* process that acts to lower the required laser intensity (electric field strength) to induce further ionisation, which distinguishes the model from traditional sequential multiple ionisation treatments.

This process is illustrated in figure 5.1 where the Coulomb potential of the first two charge states of argon is shown alongside some of the low lying states opened up to further ionisation via shake up. (Further comment on those states that satisfy the sudden approximation, and are subsequently affected by shake up, is given later in this chapter.)

A similar mechanism to *shake up*, *shake off* [Fittinghoff et al., 1992] was proposed prior to METI. Here, the initial ionisation stage results in the ionisation rather than excitation of some of the remaining electrons. However, after investigation [Becker and Faisal, 2002] this theory was found to be several orders of magnitude smaller than recollision ionisation and subsequently dismissed, which is probably why the mechanism of shake up has only been tested recently. This is also why circular polarisation was employed in the present study, as this suppresses the recollision mechanism almost entirely [Corkum, 1993] and avoids the signatures of shake up being masked in the experimental data. The generalised N-electron METI theory published in Kornev et al [Kornev et al., 2003] is used here and

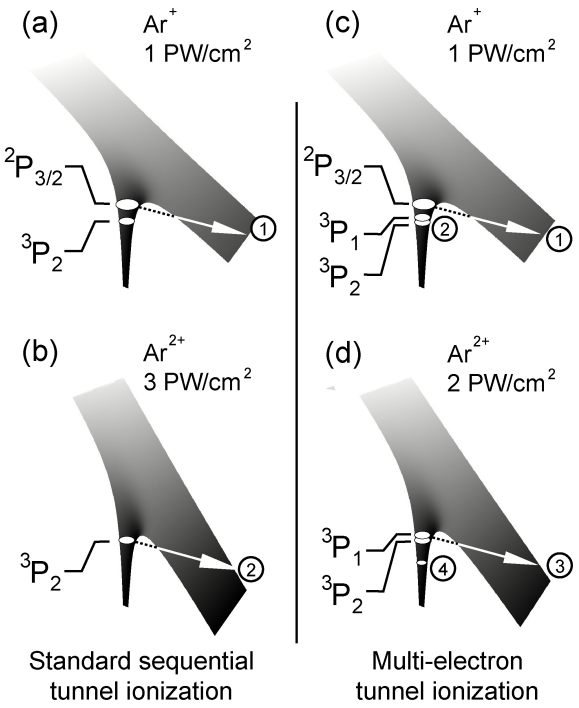

Figure 5.1: Tunnelling ionisation in argon ions at two intensities for standard sequential ionisation, panels (a) and (b), and multi electron tunnelling ionisation, panels (c) and (d), within which shake-up excitation plays a major role. In panel (a) I=1×10^{15} Wcm^{-2} the Ar^+ ground state $^2P_{\frac{3}{2}}$ has a significant probability of tunnel ionisation (1). Increasing the laser intensity to I=3×10^{15} Wcm^{-2}, panel (b), the Ar^{2+} ground state $^3P_2$ can also ionise (2). Panel (c) shows the multi-electron process where the ionisation of the ground state $^2P_{\frac{3}{2}}$ of the Ar^+ ion (1) excites population from the $^3P_2$ state to the $^3P_1$ state in the Ar^{2+} ion (2). This leads to the situation in panel (d) where a lower intensity, I=2×10^{15} Wcm^{-2}, can then produce a high degree of ionisation (3) and (4) as in panel (b) in which the excitation process was neglected. Reproduced from [Bryan et al., 2006c].

outlined briefly below.

5.2.1 The METI Formulation

In this study the METI formulation [Kornev et al., 2003] is employed to understand ultrafast processes in atoms. however, METI ideas have also been used to invesigate the ultafast ionisation of molecules [Litvinyuk et al., 2005].

METI is built upon SAE approaches through the introduction of several new parameters outlined below. The first of these is C_{vl} and is given by equation 5.1. This constant quantifies the asymptopic electron wave function if N equivalent electrons are removed from an atom via tunnelling ionisation within the quasiclassical approximation.

$$C_{vl} = \frac{1}{\sqrt{2\pi\nu}} \left(\frac{2}{\nu}\right)^{\nu} \left(\frac{1-\epsilon}{1+\epsilon}\right)^{\left[\frac{\frac{1}{2}(l+1)}{2}\right]} \left(1-\epsilon^2\right)^{\frac{-\nu}{2}} \tag{5.1}$$

Here ϵ, equation 5.2, gives a measure of the eccentricity of the electrons classical orbit with l representing the orbital angular momentum quantum number and ν is the effective principal quantum number as calculated by equation 5.3. Here Z is the atomic number of the residual ion core, E_b is the binding energy of the electrons, a is the Bohr radius as given by 5.4 with m_e and e being the mass and charge of the electron respectively.

$$\epsilon = \frac{\frac{1}{2}(l+1)}{\nu} \tag{5.2}$$

$$\nu = \sqrt{\frac{NZ^2e^2}{2aE_b^N}} \tag{5.3}$$

$$a = \frac{\hbar^2}{m_e e^2} \tag{5.4}$$

The second important parameter is the N electron Keldysh parameter, γ_N, as given by equation 5.5, where ω is the laser frequency and F the electric field strength. In this tunnelling treatment it is assumed γ_N<1.

$$\gamma_N = \frac{\omega}{eF} \frac{\sqrt{2m_e E_b^{(N)}}}{N} \tag{5.5}$$

The next parameter is the residual core's electric field F_a as defined by equation 5.6.

$$F_a = \frac{e}{a^2} \left(\frac{Z}{\nu}\right)^3 \tag{5.6}$$

Finally an index {m} is defined to represent the magnetic quantum numbers of successive tunnelling electrons, m_1, m_1, ..., m_N such that equation 5.7 is satisfied.

$$M = \sum_{j=1}^{N} m_j \tag{5.7}$$

Brought together, this allows the rate of tunnelling ionisation for equivalent electrons in one half cycle of the laser field, $W_{N_{lin}}$, to be expressed by equation 5.8 in which Q is the overlap integral between the wave functions of the electrons in their initial states of the atom or ion with the wave functions in the excited state. (This is discussed further in the appendix of [Kornev et al., 2003] alongside the method used by the authors to calculate the atomic and ionic wavefunctions.)

$$\begin{aligned} W_{N_{lin}}^{(nl\{m\})} &= \frac{\sqrt{3\pi}\hbar}{a^2 m_e}\left(\frac{M!(2l+1)^N C_{vl}^{2N}}{2^{(M-\frac{3}{2})}N^{(M+\frac{3}{2})}}\right)Q^2\left(\frac{Z}{\nu}\right)^{[3N-1]} \\ &\quad \times \prod_{j=1}^{N}\frac{(l+|m_j|)!}{(|m_j|!)^2(l-|m_j|)!}\left(\frac{2F_a}{F}\right)^{\left[2N(\nu-1)-M+\frac{1}{2}\right]} \\ &\quad \times \exp\left[-\frac{2NF_a}{3F}\right] \end{aligned} \tag{5.8}$$

For circular polarisation the rate of tunnelling ionisation depends on the magnetic quantum number of the tunnelling electrons. As the magnitude of the electric field is fixed these magnetic quantum numbers are only conserved in the direction of the laser pulse. (The electric field vector precesses about the direction of propagation and as such the magnetic quantum number cannot be conserved along this axis.) Then within the dipole approximation the electric field of a laser propagating along the z-axis can be defined by equation 5.9 in terms of the unit vector along the corresponding x- and y-axes and the ellipticity of the polarisation, η. (Where η=0, linear polarisation; η=+1, right handed circular polarisation; η=-1, left handed circular polarisation respectively.)

$$\mathbf{F}(t) = F(\cos(\omega t)\mathbf{e}_x + \eta\sin(\omega t)\mathbf{e}_y) \tag{5.9}$$

The electron-field interaction energy, V, can then be defined by equation 5.10. Where θ and ϕ are the polar and azimuthal angles of the vector $\mathbf{r}$ in the cartesian co-ordinate system.

$$V = \mathbf{F}e\mathbf{r} = erF\sin\theta\cos(\phi - \mu\omega t) \tag{5.10}$$

Finally the corresponding ionisation rate for circular polarisation, $W_{N_{circ}}$, where D represents the electron wavefunctions, is given by equation 5.11

$$W_{N_{circ}}^{(nl\{m\})} = \sqrt{\frac{\pi F_a}{3F}} \sum_{m'_1,\ldots,m'_N} \left| D^l_{m'_1 m'_N}(0, \frac{\pi}{2}, 0) \ldots \times D^l_{m'_N m_N}(0, \frac{\pi}{2}, 0) \right|^4 W_{N_{lin}}^{(nl\{m'\})}. \quad (5.11)$$

In their analysis Kornev at el [Kornev et al., 2003] also considered the kinetics of the multicharged ion formation. This was done along the lines of previous studies by Kulander's group at JILA in the USA [Fittinghoff et al., 1992, Kulander et al., 1995], with both single and multielectron cascade transitions being asessed. The number of such cascades increases with increasing charge state, X.

Table 5.1 shows the lowest and therefore most accessible states for shake up excitation in argon and krypton that comply with the sudden approximation.

Charge State, X	Shell	Term	Argon State Energy (cm^{-1})	Krypton State Energy (cm^{-1})
0	p^6	$^1S_0$	0.0	0.0
1	p^5	$^2P_{\frac{3}{2}}$	127109.8	112914.4
		$^2P_{\frac{1}{2}}$	1431.6	5370.1
2	p^4	$^3P_2$	222848.2	196475.4
		$^3P_1$	1112.2	4548.4
		$^3P_0$	1570.2	5312.9
		$^1D_2$	14010.0	14644.3
		$^1S_0$	33265.7	33079.6
3	p^3	$^4S_{\frac{3}{2}}$	328550.0	298020.0
		$^2D_{\frac{3}{2}}$	21090.4	17036.8
		$^2D_{\frac{5}{2}}$	21219.3	18699.9
		$^2P_{\frac{1}{2}}$	34855.5	31055.2
		$^2P_{\frac{3}{2}}$	35032.6	33404.9
4	p^2	$^3P_0$	481400.0	423400.0
		$^3P_1$	765.2	3742.9
		$^3P_2$	2028.8	7595.3
		$^1D_2$	16298.9	19722.9
		$^1S_0$	37912.0	39203.9
5	p^1	$^2P_{\frac{1}{2}}$	606000.0	521800.0
		$^2P_{\frac{3}{2}}$	2207.1	8108.0
6	p^0	$^1S_0$	734000.0	633100.0

Table 5.1: Ionisation and exciation levels for Ar and Kr ions in units of cm^{-1}. Only the lowest excited states are displayed. Reproduced from [Kornev et al., 2003], originaly sourced from the NIST atomic database, http://physics.nist.gov/cgi-bin/AtData. Note 8065.6 cm^{-1} is equivalent to 1 eV.

5.2.2 Theoretical Results for Ar and Kr Ions

In order to compare the results of Kornev et al's METI model with our experimental data the results of the calculations are displayed in terms of C_f. Where C_f is the ratio of n_f (ions, A, in a given charge state, X+), divided by the total number of ions, n_{tot}, in the initial neutral sample as defined by equations 5.12-5.14,

$$C_f = \frac{n_f}{n_{tot}}, \tag{5.12}$$

$$n_f = n(A^{X+}), \tag{5.13}$$

$$n_{tot} = \sum_{f=0}^{f_{tot}} n_f. \tag{5.14}$$

Before the comparison to experiment is presented the results of the METI model are compared to a non-METI ADK theory. The results are shown in figures 5.2 for argon and 5.3 for krypton ions.

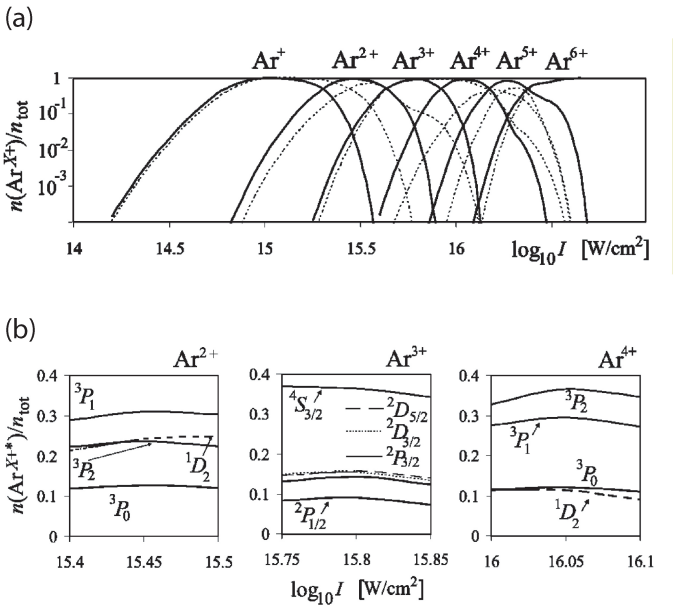

Figure 5.2: METI calculations for argon ions. Panel (a) shows the concentration of multiply charged Ar ions, Ar^+ up to Ar^{6+}, as a function of intensity. The solid lines represent the METI calculations, while the dotted lines represent ADK like calculations. Panel (b) shows the populations of the ground states of ions Ar^{2+} up to Ar^{4+} as a function of intensity. In both instances the results are obtained for 50 fs laser pulses of circular polarisation. n_{tot} is the initial concentration of neutral atoms. Reproduced from [Kornev et al., 2003].

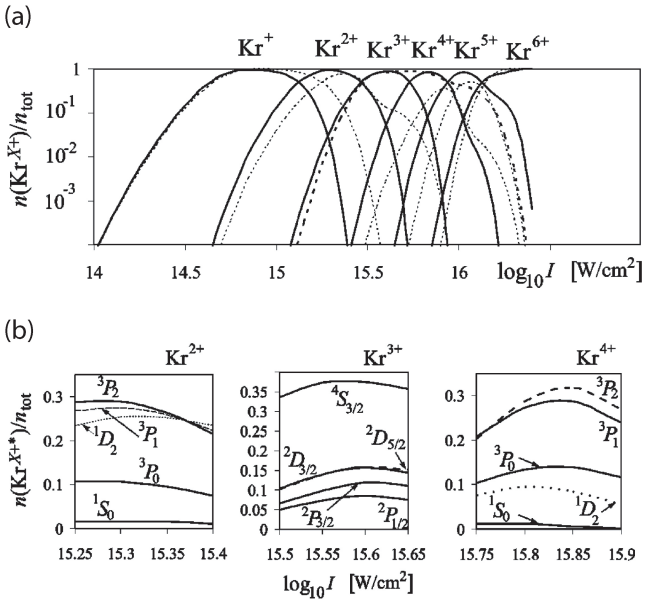

Figure 5.3: METI calculations for krypton ions. Panel (a) shows the concentration of multiply charged Kr ions, Kr^+ up to Kr^{6+}, as a function of intensity. The solid lines represent the METI calculations, while the dotted lines represent ADK like calculations. Panel (b) shows the populations of the ground states of ions Kr^{2+} up to Kr^{4+} as a function of intensity. In both instances the results are obtained for 50 fs laser pulses of circular polarisation. n_{tot} is the initial concentration of neutral atoms. Reproduced from [Kornev et al., 2003].

In panel (a) of both figures the C_f parameter is plotted against intensity for charge states up to six plus. For the singularly charged species, both models predict similar values of C_f, but as the charge state is increased the two models diverge. This coincides with the number of excitable states available to shake up within the sudden approximation and results in the effective reduction of the laser intensity required to ionise subsequent states.

Panel (b) of the two figures shows the population of the respective ground and excited states against $\log_{10}$ intensity. Argon and krypton both have excited states, accessible within the sudden approximation, for excitation via shake up (see table 5.1). As these levels have significant population, ionisation from these states is thought to be important to overall ion yields and the reason for the discrepancy between the ground state (ADK like) and excited and ground state (METI) predictions.

5.3 Experimental Configuration

The results used in this investigation of the METI model were obtained using the high power (30 mJ) low repetition rate (10 Hz) laser beam in TA1 of the ASTRA laser as described in chapter 2 section 2.2.3. The laser pulse polarisation was made circular by

the inclusion of a quarter waveplate in the beam path prior to the focussing optic. The pulses were focussed into the Time-Of-Flight Mass Spectrometer (TOFMS) (see chapter 2 section 2.4.) by a plano-convex lens of focal length 250 mm. This f/11 focusing allows peak intensities of $\approx 10^{17}$ Wcm^{-2} to be realised. Inside the spectrometer spectrally pure (99.999%) gas (Ar or Kr) is leaked into the system to an ultimate pressure of $\approx 2\times10^{-8}$ mbar. This pressure range was selected to avoid space charge effects whilst maximising the signal to noise ratio.

By employing the ISS-EIM technique (see chapter 3 section 3.3.1) developed in the group [Bryan et al., 2006b], the laser focus is translated across the highly apertured TOFMS building up a z-scan of the ionisation process, as illustrated in the left hand side of figure.5.4

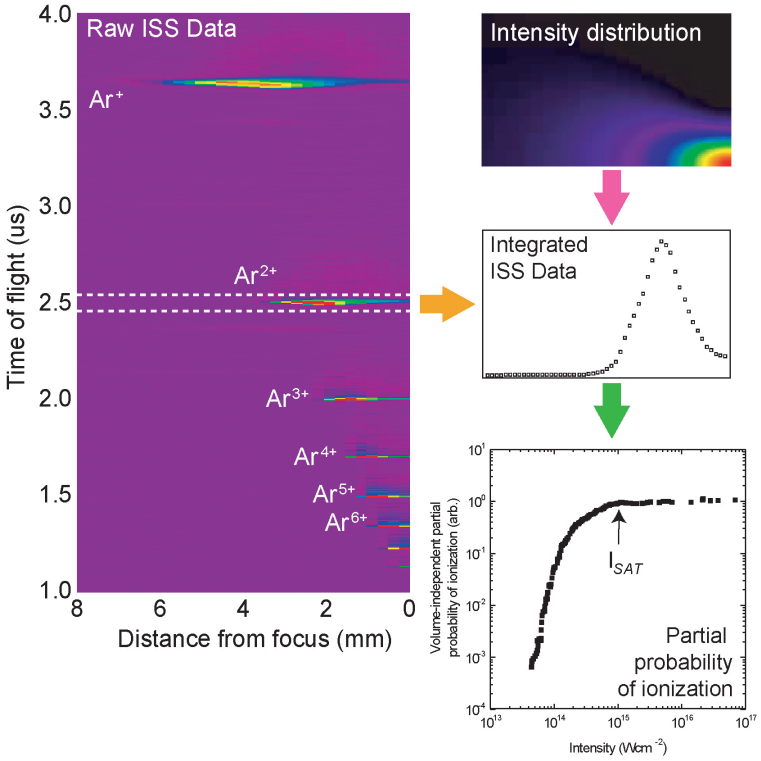

Figure 5.4: The left hand panel shows the initial z-scan results of argon ionisation. Each ion signal in the z-scan is then integrated over time to produce a measure of the ion yield w.r.t. the position of the laser focus,z (middle right panel). Combined with knowledge of the laser focusing geometry (top right panel) this ion yield is transferred into a probability of ionization (bottom right panel)that can then be subsequently compared to the C_f factor generated from the METI model.

Integrating each ion signal and removing the focusing geometry allows the Partial Probability of Ionisation (PPI) for each charge state to be obtained. However, in order to compare our experimental results with theoretical predictions the PPI measurements obtained via

ISS-EIM must be converted into conserved probability of ionisation (CPI) values. This is done by enforcing the condition expressed by equation 5.15, which states that for every intensity the total CPI of the system should equal unity.

$$1 = \sum_{X=1}^{X=6} CPI(A^{X+}) \tag{5.15}$$

In practise this is done by normalising all the PPI to unity and then subtracting these normalised PPIs from one another, i.e. $A^{(X+1)+}$ from A^{X+}. Repeating this process for all charge states results in CPI curves for each charge state, as shown in figure 5.5

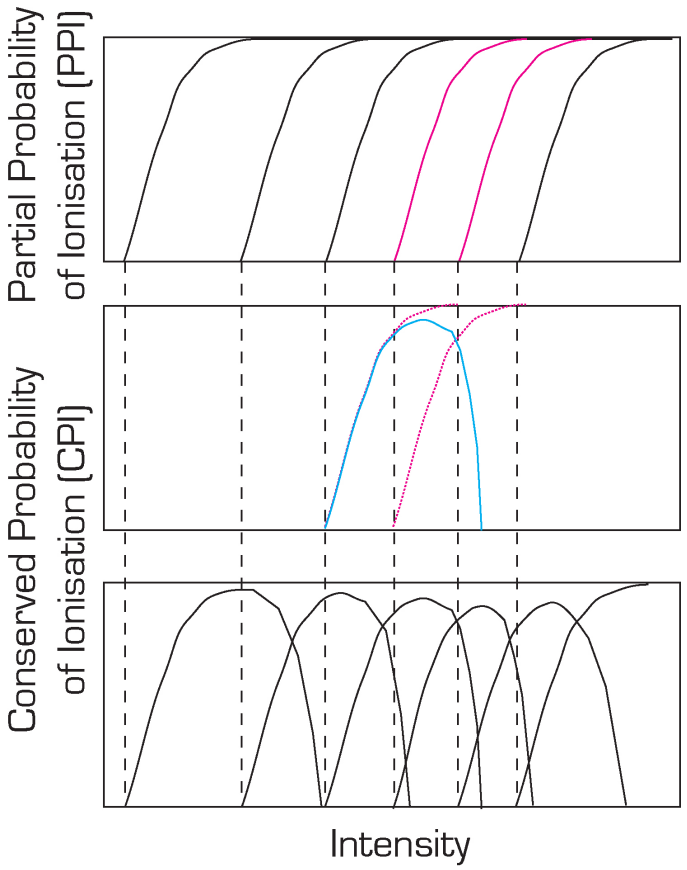

Figure 5.5: To obtain CPI values the PPI measurements are normalised to unity. Then at each intensity a given normalised PPI measurement is subtracted from the normalised PPI measurement of its adjacent lower charge state. This process is illustrated for A^{4+} charge state of a generic ionic system, where PPI(A^{4+})-PPI(A^{5+}), both shown in magenta, results in the CPI(A^{4+}), cyan curve, being obtained. Doing this for all charge states PPI (top panel) measurements can be transferred into CPI values (bottom panel).

5.4 Comparison of Experimental Data and Theory

Experiments were conducted with both argon and krypton and the results of these studies are presented separately below.

5.4.1 Argon

Figure 5.6 illustrates the results of the argon tests. At low intensity, less than 2×10^{14} Wcm^{-2}, neither theory matches the experimental results on the rising edge of the CPI peak of the first charge state. This is the result of the ionisation being dominated by Multi Photon Ionisation (MPI), the effects of which are neglected in both tunnelling theories. In this region both tunnelling theories predict the same degree of ionisation. This is expected as the *shake up* excitation only occurs post the departure of the first electron, see figure 5.1. The discrepancy of the data and METI curve (which match one another well) from the ADK curve on the falling edge of the Ar^+ is due to excitation effecting the ionisation into Ar^{2+}, and causing a loss of population of Ar^+ ions.

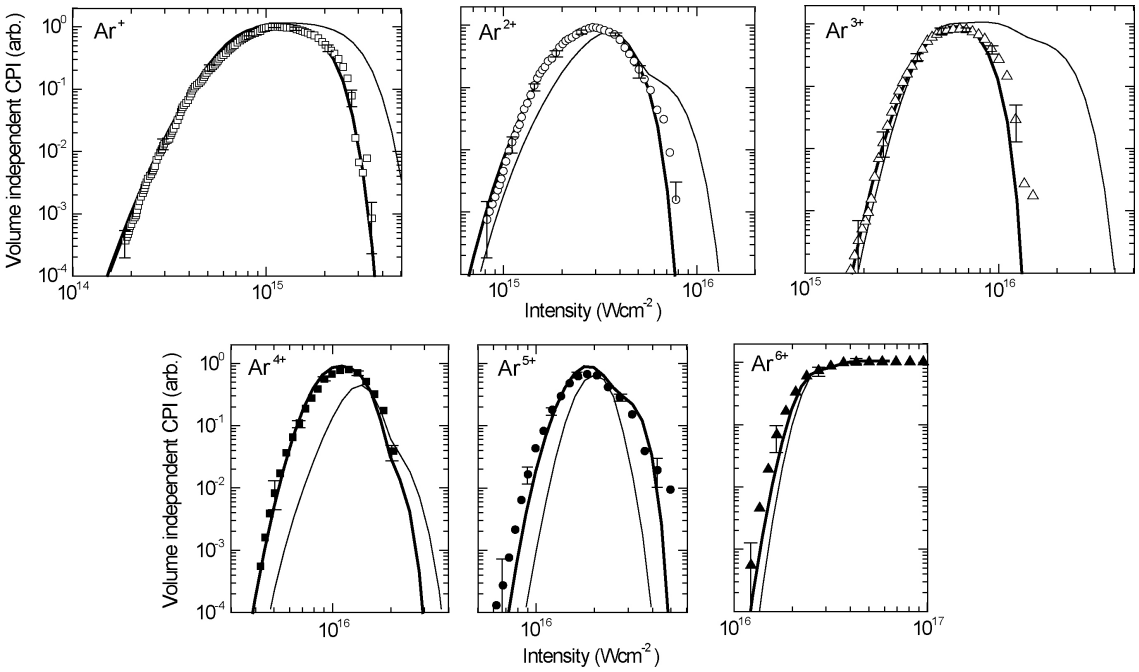

Figure 5.6: Conserved probability of ionisation for argon ions. In each panel the data are presented alongside predictions of ADK theory [Ammosov et al., 1986] (thin curve) and METI theory [Kornev et al., 2003] (thick curve). The experimental data fits the METI prediction much better than the ADK curve suggesting that shake up excitation is an important factor in atomic ionisation in the tunnelling regime (a fact particularly noticeable in the CPI curves of Ar^{2+} and Ar^{3+}). Reproduced from [Bryan et al., 2006d].

For the intermediate charge states reported, Ar^{2+} to Ar^{5+}, the METI curves consistently match the experimental results to a high degree of accuracy, with the same degree of ionisation in each charge state occurring at a lower laser intensity than predicted by the ADK theory. For the final charge state reported, Ar^{6+} the METI results again make a good match to the experimental data.

5.4.2 Krypton

The results of the krypton tests are shown in figure 5.7. In general the experimental data and theoretical predictions are similar to those for argon above. As before, MPI processes mean that both tunnelling theories fail to predict the experimental data at low intensity. For the intermediate charge states, Kr^{2+} to Kr^{5+}, the METI curves out perform the ADK prediction and fit the experimental results to a high degree.

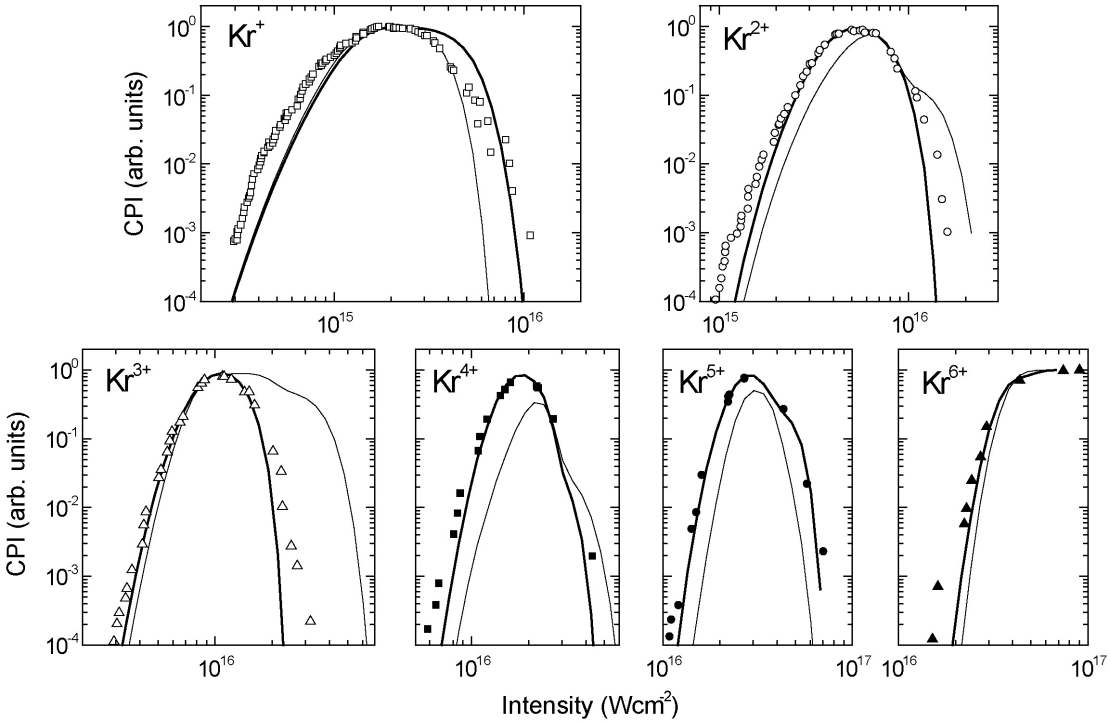

Figure 5.7: Conserved probability of ionisation for krypton ions (a) Kr^{+} through to (f) Kr^{6+}. In each panel the data are presented alongside predictions of ADK theory [Ammosov et al., 1986] (thin curve) and METI theory [Kornev et al., 2003] (thick curve). The experimental data fits the METI prediction much better than the ADK curves, suggesting that shake up excitation is an important factor in atomic ionisation in the tunnelling regime. Reproduced from [Bryan et al., 2006d].

5.4.3 Other Experimental Studies

Many studies of tunnelling ionisation in noble gases have been conducted over the last few decades. Therefore it is natural to question why shake-up effects have not been witnessed previously. To illustrate why this might be a comparison of the krypton experimental data has been made, without the volume effects of the laser focussing being removed, see figure 5.8. As seen in the volume free measurements, see figure 5.7, METI predictions appear to match the experimental data better than the ADK ones. However above saturation, the turning point in each charge states' ionisation probability, the picture becomes far from clear and any distinction between the two models is debatable. Comparing the two figures use of the non-Gaussian deconvolution method [Bryan et al., 2006b], which removes the effects of the laser focussing, makes the differences between the ADK and METI predictions more apparent.

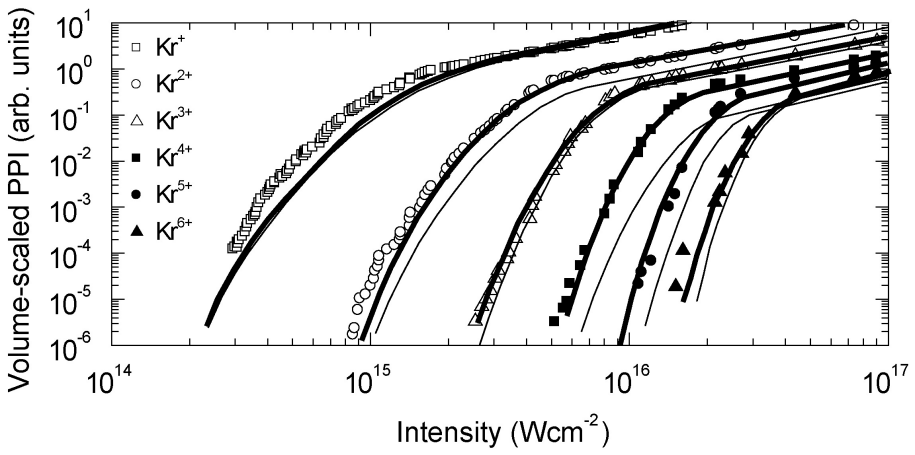

Figure 5.8: Volume scaled PPI for Krypton ions. The differences between ADK (thin curve) and METI (thick curve) predictions are much harder to differentiate over the full intensity range without removing the effects of the laser focussing. Reproduced from [Bryan et al., 2006d].

Another comparison to the METI model was made by Kornev et al themselves [Kornev et al., 2004]. In this comparison they used their theory and the experimental results of Flittinghoff et al [Fittinghoff et al., 1994] to look at tunnelling ionisation in neon.

As illustrated in figure 5.9 the METI predictions out-perform those from the ADK model for Ne^{2+}, with the characteristic vertical shift in the scaled yield of ions. As in our volume inclusive plot, figure 5.8, METI's improvements are obvious above saturation for the two plus charge state. Whether or not this trend would continue for higher charge states is unknown, as Flittinghoff et al [Fittinghoff et al., 1994] concentrated their study on double ionisation.

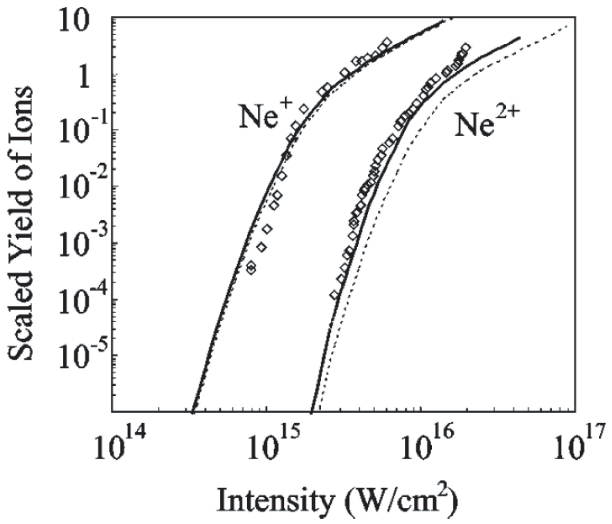

Figure 5.9: METI (bold curve) and ADK (dashed curve) predictions compared to the experimental results of Flittinghoff et al [Fittinghoff et al., 1994] for circularly polarised pulse 120 fs in duration and a central wavelength of 614 nm. Reproduced from [Kornev et al., 2004].

In Kornev et al's [Kornev et al., 2004] comparison to experiment, the authors state that no difference between the METI and ADK predictions for He^{2+} were obtained. (Flittinghoff et al [Fittinghoff et al., 1994] had investigated this ion in their experimental report.) A fact they put down to the high excitation energy required to excite states of He^{+}.

In other recent experiments on argon ([Guo et al., 1998] Ar^{+}-Ar^{2+}, τ=30 fs, λ=815 nm) and krypton ([Gubbini et al., 2006] Kr^{7+}-Kr^{13+}, τ=30 fs, λ=815 nm) METI effects have not been explicitly isolated. In the first case this is due to the method in which the intensity was varied, complicating any volume removal procedure. In the second instance a deviation of the experimental results from ADK predictions is observed, but putting this down to METI can only be speculative as the model has not been run for such high charge states

5.5 Summary

In this chapter results from experiments into Multi Electron Tunnelling Ionisation METI have been presented in argon and krypton. In both instances the METI predictions from Kornev et al [Kornev et al., 2003] fit the experimental data more accurately than the ADK [Ammosov et al., 1986] predictions, suggesting that the shake up excitation of the residual electrons following the initial ionisation stage is important to the ionisation of higher charge states, effectively reducing the laser intensity required for the subsequent ionisation of higher charge states.

This observation has been made possible by the use of circular polarisation and our non-Gaussian deconvolution method [Bryan et al., 2006b]. The circular polarisation helps by suppressing the recollision mechanism [Corkum, 1993] behind non-sequential ionisation, thought to have masked the METI process in previous experimental studies; recollison effects are orders of magnitude greater than those due to excitation [Eichmann et al., 2000]. Another masking effect in previous work may have been the focussing geometry of the laser pulses employed, clouding comparisons to theory. By removing these effects and any laser dispersion from the experimental data, comparison to theory has become more clear and subsequently the experimental signatures of METI clearer.

This work has been published in peer reviewed journals; argon [Bryan et al., 2006c], krypton [Bryan et al., 2006d].

Chapter 6

Ionisation of Xenon: At-Focus Laser Pulse Diagnostic

6.1 Introduction

As discussed in chapter 2 many diagnostics are available in the laboratory in order for experimentalists to characterise the laser pulses they use in experiments. All these methods (for example Intensity Autocorrelation (IA), Frequency Resolved Optical Gating (FROG) and Spectral Phase Interferometery for Direct Electric-field Reconstruction (SPIDER)) however, measure the laser pulses in their unfocused state, while they are in the beam line. For most applications this is sufficient, but the unfocussed beam is not fully representative of the light that interacts with the atoms and molecules used in the experiments reported here. Consequently a technique has been developed using a pump-probe style experimental configuration to study the ionisation of xenon atoms, which gives a measure of the laser pulse duration at the focus.

6.2 Theory

The idea behind many of the commercially available pulse diagnostics is the interaction of the unfocussed laser beam with a non-linear medium, such as a crystal. In this instance the non-linear medium used to quantify the laser pulse is the ionisation of xenon. Xenon was chosen for its handle-ability in the laboratory environment and its low ionisation potentials (see appendix F and table 6.1).

In order to quantify this interaction the ADK formula was employed in its shortened m=0 format, see equation 6.1 and chapter 1 for a justification of this. Multi Electron Tunnelling

Xe^{n+}	Z (a.u.)	I_p(eV)	n^*
0	1	12.13	1.06
1	2	21.21	1.60
2	3	32.04	1.95
3	4	40.91	2.31
4	5	55.11	2.48
5	6	66.70	2.71
6	7	91.60	2.70
7	8	105.98	2.87

Table 6.1: Parameters for xenon atomic ions in the ADK formula. The I_p values are taken from the online NIST database while the values of n^* were calculated from equation 6.2.

Ionisation (METI) effects are thought to be present in the multiple ionisation of xenon; however, to date no METI calculations on xenon have been performed. However, the simplicity of equation 6.1 suits this treatment as the experiments discussed within this chapter are only meant as diagnostic tests and are designed to be conducted swiftly.

$$w_0 = \left(\frac{3e}{\pi}\right)^{\frac{3}{2}} \left(\frac{Z^2}{n^{*\frac{9}{2}}}\right) \left(\frac{4eZ}{n^{*4}E}\right)^{\left(2n^*-\frac{3}{2}\right)} exp\left[-\frac{2Z^3}{3n^{*3}E}\right] \tag{6.1}$$

$$n^* = n - \delta_q = \frac{Z}{\sqrt{2I_p}} \tag{6.2}$$

Equation 6.1 represents the probability of tunnelling ionisation, w_0, in which n^* is the effective principle quantum number of the atomic residue as calculated from equation 6.2, Z is the charge of that residue, I_p the ionisation potential and E is the electric field strength. The values of some of these parameters for xenon are displayed in table 6.1 above.

The experiment is simulated in order to deduce the pulse duration causing the ionisation. In the simulation two 800 nm laser pulses of known duration are passed through one another in 1/4 fs steps (1/3 fs steps are used in the experiment) and the expected ion yield for each ion calculated.

6.3 Experimental Results

Like all the experiments reported in this thesis the experiment was conducted using the Astra laser at the Central Laser Facility (CLF); Rutherford Appleton Laboratory. Two similar pulse trains are produced and run through one another, in 1/3 fs steps, by splitting a single 12 fs pulse, from a hollow fibre plus chirped mirror compressor setup (for more

details see chapter 2) in a Mach-Zehnder type interferometer, one arm of which is of variable length controlled by a computer operated translation stage (for more details see chapter 3). The pulses are then focused into the interaction region of the TOFMS (also described in chapter 2), containing low pressure xenon gas, by a f=75 mm spherical mirror.

The experiment was repeated with 30 fs pulses, generated straight from the prism compressor system. Both data sets are presented later in this chapter in figure 6.2.

The positive ions resulting from the laser matter interaction are detected by the spectrometer, see figure 6.1, for each delay-time between the two pulses. In the spectrum shown, six charge states of xenon can be seen. The singly charged state has the slowest flight-time due to its high mass/charge (m/q) ratio. Conversely, the six plus charge state has the fastest flight-time.

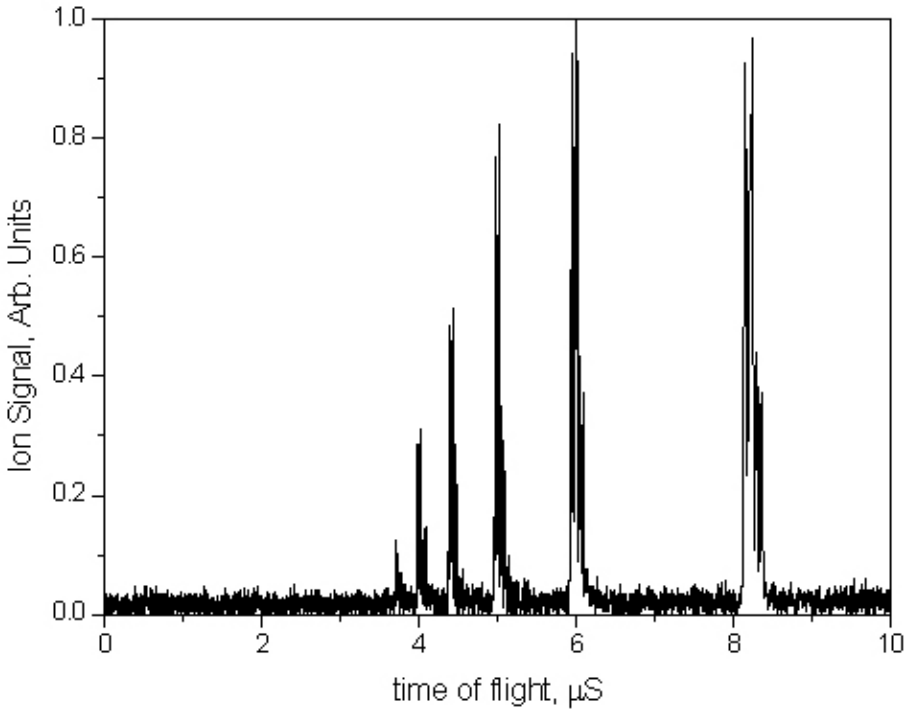

Figure 6.1: A typical xenon ion spectrum compiled from 500, 30 fs, 65 μJ, laser shots. Six charge states of xenon can be identified in the spectra with each higher charge state requiring a higher laser intensity for formation and arriving at the detector in a shorter flight time.

In order to see the effects of running the laser pulses through one another, the experimental data are shown as time-of-flight colour maps, see figure 6.2. These colour maps comprise time-of-flight spectra for each delay setting, plotted alongside one another along the x-axis. Each charge state has a considerable width in flight time (along y-axis) due to the fact xenon has several relatively abundant isotopes, which the TOFMS separates out via their differing m/q ratios, see appendix H.

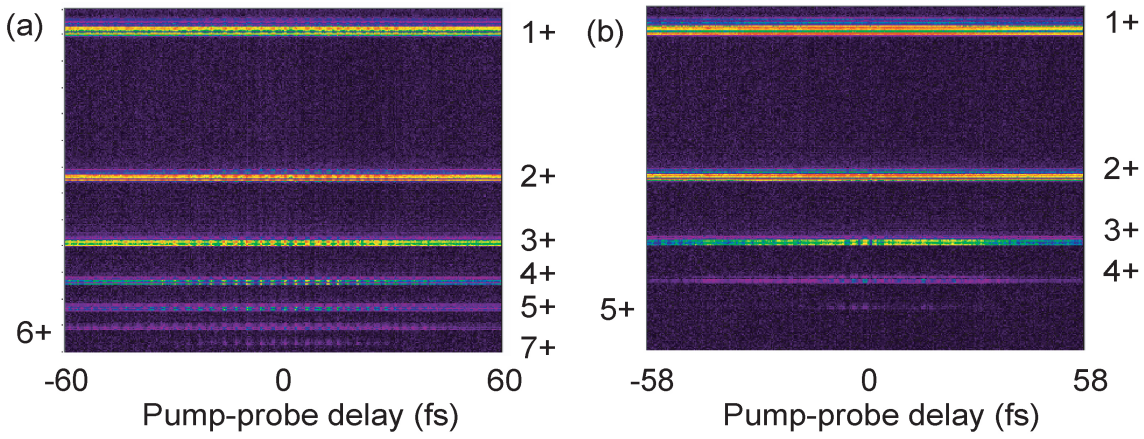

Figure 6.2: Time-of-flight colour maps showing how the ionisation of xenon varies with the time-delay between the two pulses. Panel (a) was produced with 30 fs: 65 μJ pulses and (b) with 10 fs: 17 μJ pulses. The striping in the ion yield around zero delay is a consequence of optical interference between the two laser pulses.

In the region of pump probe delay where the pulses overlap, constructive and destructive interference occurs. This can be seen in each of the ion signals as peaks and troughs. The separation of these peaks is equal to the optical cycle, T_{OC}, of the central wavelength of the pulses which is 8/3 fs; as the pulses used are centred on a wavelength of , λ_c=800 nm.

6.4 Analysis

In order to deduce the pulse width of the laser pulses the observed ion yields, are compared with those generated by the simulation. The ion yield is calculated from the ADK rate, obtained from equation 6.1, for each charge state in 1/4 fs steps across the combined pulse's laser profile. From these values overall ion yields are then found via a simple summation process, similar to the one used in the METI analysis in chapter 5. This is done in order to conserve the number density of the ions in the sample, thus maintaining a realistic number of ions and to better replicate the experiment. This process is then numerically integrated over the laser focus, giving all the ion yields for one delay-time. Finally the procedure is repeated for all other delays and the pseudo-experimental ion yield as a function of delay obtained.

The width of the laser pulses in the model can then be altered to find the best match with the experimentally obtained results. This is done using a simple least squares fitting procedure and results in the pulse duration at the focus being established.

The results from of the simulation are compared to the experimentally obtained time-integrated ion yields in figure 6.3. In this instance the laser pulse width used in the

simulation matches that measured in the unfocussed beam at 15 fs. This suggests that the focusing of the pulses does not lead to significant dilation of the pulse duration. This is expected due to the broadband nature of the coating on the focusing optic and the fact that the spherical aberration imposed on the beam by the spherical reflective surface is small, ΔT_{SA}=0.46 fs, due to the beam's narrow width (r=5 mm).

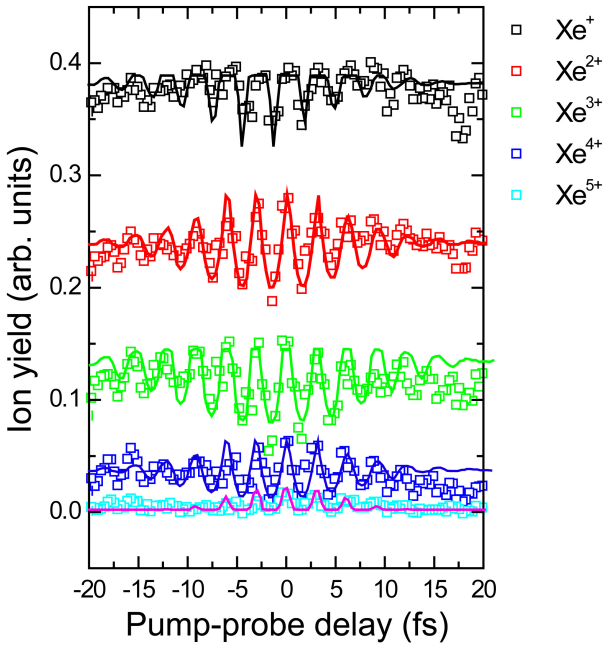

Figure 6.3: Integrated ion yields as a function of pump-probe delay for the first five charge states of xenon. The data markers indicate the experimentally obtained values and the curves those simulated using two Gaussian shaped laser pulses with FWHM durations of 15 fs.

The model can also be used to output probabilities of ionisation as a function of the delay-time between the two pulses. This is illustrated in figure 6.4, alongside the respective intensity profiles. The situation for delay-times of 0fs, $1/2T_{OC}$ (1.3 fs), $2T_{OC}$ (5.3 fs), 11.4 and 25 fs are illustrated. When the two pulses constructively interfere, the laser intensity of the composite pulse is high and a high degree of ionisation is observed. Likewise, if the interference is destructive the electric field of each pulse works to cancel out the electric field of the other; resulting in a low overall intensity and a low ion yield comprising fewer charge states.

6.4.1 Possible Improvements - Obtaining the Pulse Shape

Figure 6.5 shows xenon ion yields from a separate data set, but conducted with similar few-cycle micro-Joule pulses. In the figure the ionisation yield is displayed on a linear,

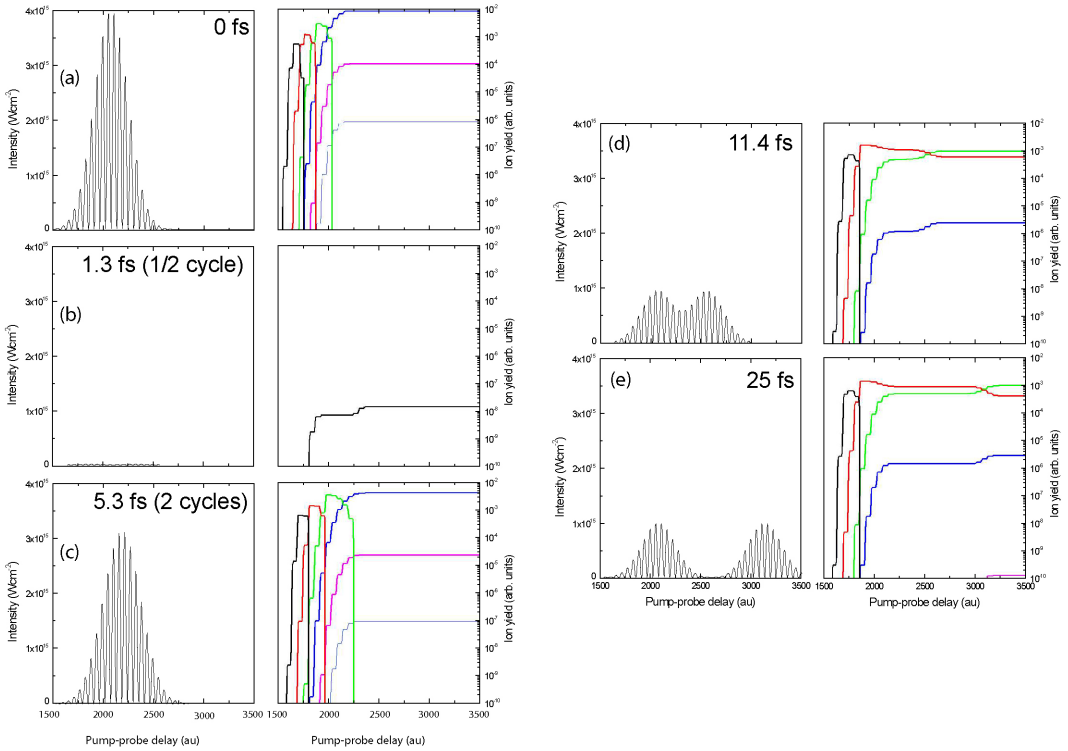

Figure 6.4: Laser intensity and ion yield as a function of pump probe delay for five instances through a simulation using two 15 fs pulses. The delay times, the intensities and ion yield extracted from the model are shown on each panel of the figure (a)-(e). The colour scheme for the different charge state ion yields are as follows: 1+ black, 2+ red, 3+ green, 4+ blue and 5+ magenta. When the two laser pulses interfere constructively the high intensity leads to the formation of several charge states. However, when destructive interference occurs the opposite is true and only low levels of ionisation are recorded.

panel (a), and a logarithmic scale, panel (b). As before, when the pump and probe delay time is zero the two pulses are both temporarily and spatially overlapped. This results in optical interference, producing the characteristic peaks and troughs in the detected ion yield.

As before the model above can be used to deduce a most probable pulse duration of the order of 15 fs. However, a variation in the ion yield with charge state can also be observed. This is seen in the interference pattern, which extends past the boundaries one would expect for two 15 fs pulses and is most prominent in the singly charged ion yield where the interference striping extends out towards a time delay of 100 fs.

Now this interference striping of the ion yields becomes less apparent as the charge state increases, which suggests the light responsible must be of lower intensity than the main 15 fs pulse. Subsequently one may conclude that the interference in the wings is due to either a low intensity pulse pedestal or low intensity pre- or post-pulses associated with

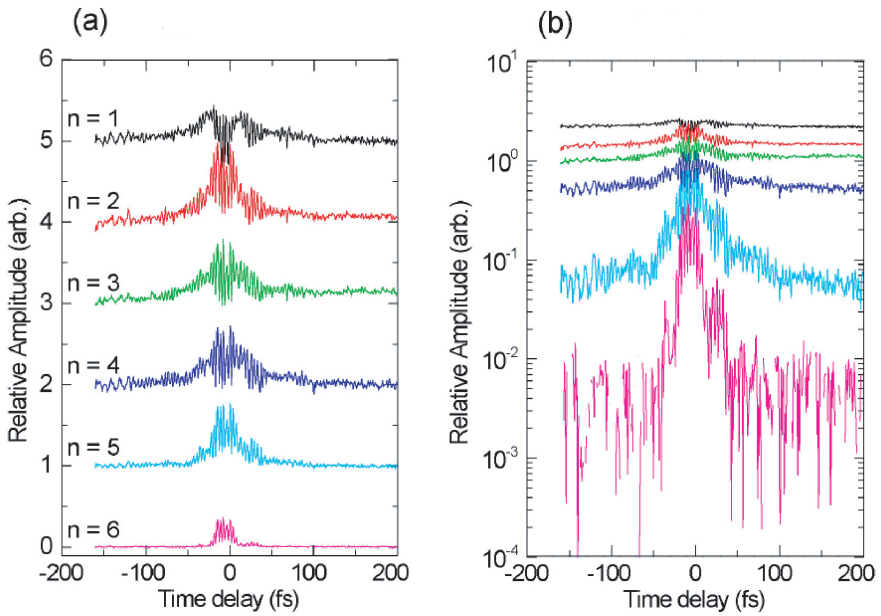

Figure 6.5: Xe^{n+} (n = 1 to 6) ionisation yields as a function of pump-probe delay time for two 15 fs laser pulses. In panel (a) the experimental data are ploted on a linear scale whereas in panel (b) a logarithmic scale is used along the y-axis. In each figure the charge states have been separated along the y-axis for clarity.

the main 15 fs laser pulse.

Development work is undergoing to take this process a step further and try to characterise the full pulse profile and hence deduce the extent of any low intensity pedestal pulse in our experiments.

6.5 Summary

This preliminary method appears to be successful at enabling the pulse length at the focus of an intense few cycle pulse to be determined and should enable a better knowledge of the laser focus. As the diagnostic uses the same experimental apparatus (TOFMS and Mach-Zehnder interferometer) employed in some of the major experiments, it should be particularly helpful in the analyis of experimental findings in the future.

A better comparison of experiment and theory could be obtained if METI results were used. This may enable the extraction of the pulse profile as well as duration of the laser pulse in the future. But needless to say, this should only be seen as a complementary method to other more well established diagnostics.

Chapter 7

Vibrational Wavepacket Dynamics in D_2^+, HD^+ and H_2^+: Few Cycle Pump-Probe Experiments I

7.1 Introduction

Sub-vibrational-period imaging of the nuclear motion of the hydrogen molecular ions is achieved using a few-cycle laser pulse pump-probe configuration and time-of-flight mass spectroscopy. The recent surge in few cycle laser pulse technology has lead to a renewed interest in using pump-probe techniques [Légaré et al., 2005, Alnaser et al., 2005, Ergler et al., 2005] as a means of tracking nuclear motion. Now since pulse durations are on a comparable and in some cases even shorter time scale than the nuclear motion of even the smallest molecules, the imaging of their dynamics has become feasible. Recent experiments on three small molecules, including D_2^+, are reported here. At the end of the chapter and in the companion publications [Wood et al., 2006, Bryan et al., 2007b], the suitability of vibrational wavepackets, and their potential to be a framework in which full quantum control of molecular systems in an ultra-short intense laser field can be realised, is evaluated.

7.2 Theoretical Treatment

When the pump pulse ionises the neutral molecule, the neutral molecule's ground state is projected onto the $1s\sigma_g$ potential of the molecular ion, as illustrated in figure 7.1. As the projected wavepacket is not an eigenstate of its new bounding potential, it must be described as coherent superposition of the ion's eigenstates. Using the ion's eigenstates as

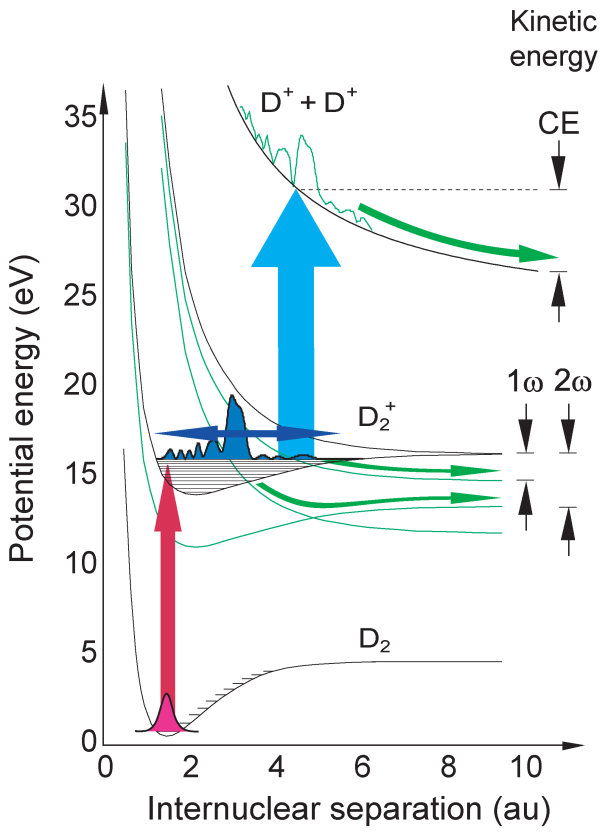

Figure 7.1: In the pump-probe method the vibrational wavepacket is initiated by ionisation from the neutral target gas by the first (pump) pulse (red arrow). The superposition of states is then allowed to evolve (dark blue arrow) for the time between the two laser pulses, before being imaged by the second (probe) laser pulse into the fragmentation pathways (green arrows). The wavepacket is imaged by causing bond fracture, either via Coulomb explosion (cyan arrow) or photodissiciation through the one (1ω) and/or two photon (2ω) channels.

a basis set, this superposition can be written as the Fourier expansion, equation 7.1,

$$\Psi(R,t) \quad = \quad \sum_k a_k \exp\left[-i\omega_k t\right] \psi_k(R). \tag{7.1}$$

Here the ion's individual vibrational eigenstates are represented by ψ_k, each having its own characteristic energy E_k and frequency, ω_k (see equation 7.2).

$$\omega_k \quad = \quad \frac{E_k}{\hbar} \tag{7.2}$$

The values of a_k are obtained within the Franck-Condon approximation, (in this notation the Franck-Condon Factors (FCF) are represented as ${a_k}^2$) as the overlap integrals between the eigenstates, ψ_k, and the v=0 level of the neutral ground state. For each molecule studied in this work the electronic potential surface [Sharp, 1971] is the same, however, due to their different masses they have different vibrational (and rotational) levels, with the lighter systems' vibrational levels separated further from one another in energy.

At a given time, t, the probability density, $|\Psi(R,t)|^2$, can be written as shown in equation 7.3. This is obtained by squaring and then re-writing equation 7.1 using the following relation $e^{\pm\omega t} = \cos\omega t \pm i \sin\omega t$.

$$|\Psi(R,t)|^2 = \sum_k |a_k|^2 |\psi_k|^2 + \sum_{k\neq j} a_k a_j^* \psi_k \psi_j^* \cos[(\omega_k - \omega_j)t] \tag{7.3}$$

The first term in equation 7.3 contains no time dependence, as it is just a summation of standing waves and normalised radial wavefunctions. The second term therefore contains all the time dependence of the wavepacket.

At t=0, the cosine function in the second term of equation 7.3 equals unity for all the terms in the summation. As the wavepacket evolves, however, this term varies with its ultimate value being determined by the individual interference terms between separate vibrational levels. Therefore the value of $|\Psi(R,t)|^2$ is governed by the phase differences between separate eigenstate components as the wavepacket evolves.

$$\omega_{kj} = \omega_k - \omega_j \tag{7.4}$$

The beat frequencies, ω_{kj} that govern the time evolution of the wavepacket can be written as in equation 7.4. Beating takes place for all values of $\Delta\omega_{kj}$, with the strength of each beat's contribution to the total being governed by the relevant FCF.

The beat periods present in the wavepacket can be obtained using equation 7.5. Table 7.1 shows these beat periods, T_{kj}, for the $\Delta\omega_{kj}$=1 beats for each molecular ion.

$$T_{kj} = \frac{E_k - E_j}{\hbar} \tag{7.5}$$

For $\Delta\omega_{kj}$ greater than one, the associated beat frequencies are dominated by contributions from beats with time periods of less than ten femtoseconds. As the duration of the laser

Vib Levels, $v_k \leftrightarrow v_j$		Beat Period, $T_{v,v+1}$ (fs)		
v_k	v_j	D_2^+	HD^+	H_2^+
0	1	21.2	17.4	15.2
1	2	22.1	18.3	16.1
2	3	23.0	19.3	17.2
3	4	24.0	20.4	18.3
4	5	25.1	21.6	19.5
5	6	26.3	22.9	21.0
6	7	27.6	24.3	22.6
7	8	29.0	25.9	24.4
8	9	30.5	27.8	26.6
9	10	32.2	29.8	29.2
10	11	34.0	32.2	32.4
11	12	36.1	35.1	36.4
12	13	38.4	38.5	41.8
13	14	41.0	42.8	49.3
14	15	44.0	48.2	60.7
15	16	47.5	55.5	80.0

Table 7.1: Principal vibrational beat periods of D_2^+, HD^+ and H_2. The more massive systems beat more slowly. Consequently, the fidelity with which these wavepackets can be observed is higher.

pulses used in the experiments is greater than this, these beats are not expected to be resolved.

The results of the wavepacket simulation for D_2^+ are shown in figure 7.2, where the value of $|\Psi(R,t)|^2$ is plotted for wavepacket evolution times between 0 and 632 fs. Initially the wavepacket is well defined at small values of the internuclear separation, R. This is a consequence of the equilibrium separation of the D_2 ground state potenial being 1.4 a.u. as supposed to 2.0 a.u. in the ion. This leads to high FCF for the lower vibrational states, which are restricted to a tight range of low R values.

Following oscillation back-and-forth across the $1s\sigma_g$ potential well of the ion the wavepacket is seen to disperse in R (dephase) and then regain its locality (revive). This dephasing and subsequent revival is predicted to continue until an external factor causes the system to breakdown (lose coherence).

At the revival time, 552 fs in figure 7.2, all the v-states in the superposition that make up the wavepacket are in phase with one another and the wavepacket is localised in R. To a lesser extent this localisation occurs at intermediate times, called fractional revivals [Averbukh and Perelman., 1989]. However in these instances, there is a π phase difference between the odd and even eigenfunctions [Vrakking et al., 1996] in the wavepacket, with some of the v-state contributions at the outer turning point of the potential, and the rest at the inner turning point. The shape of $|\Psi(R,t)|^2$ near the first half revival is shown in

figure 7.2, the curve at t=283 fs .

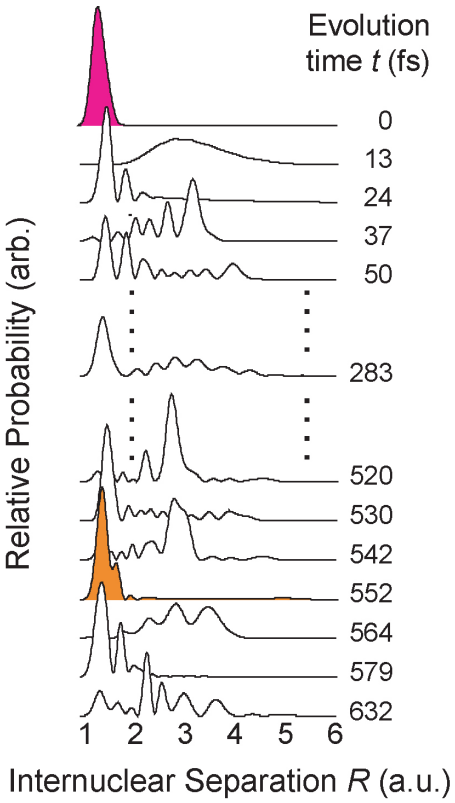

Figure 7.2: Snap-shots of the $D_2{}^+$ vibrational wavepacket motion in the potential well of the $1s\sigma_g$ bound state. Initially (t=0), the wavepacket is well defined in terms of the internuclear separation, R. As the wavepacket evolves, it disperses out in R. This is due to the anharmonicity of the potential surface, causing the various v-state components of the superposition of states to *get out of step* (phase) with one another. This period of dephasing is then followed by a period where the wavepacket revives. This can be seen by following the panels of the figure down, until an evolution time of 552 fs. At revival, the wavepacket matches its original form to a high degree of accuracy, as illustrated by the orange and magenta wavepacket distributions in the figure.

The theory presented here and used throughout this chapter of the thesis has been develloped with the help of Dr McCann's theory group based at Queen's University Belfast. Not presented here are more sophisticated simulations done by Dr McCann et al in which the coupling of the $1s\sigma_g$ and the $2p\sigma_u$ is included in the simulation of the experimental ion yield. This has yielded new information about the dissociation processes in $D_2{}^+$ and offered insight to possible control mechanisms [Murphy et al., 2007a, Murphy et al., 2007b]. However, these findings have also proven to support the more intuitive model used here, in that its predictions replicate those of the more complex model to a high degree of accuracy (see Calvert [Calvert, 2008] for more details).

7.3 Experimental Configuration

The experiments were conducted in TA1 of the Astra laser at the CLF as described in chapter 2. Following spectral broadening in the hollow optical fibre and recompression in the chirped mirror array, the resulting pulses (0.25 mJ, 10 fs, 7 mm dia, 1 kHz, 0.4 W) are split in a Mach-Zender interferometer to give trains of pump and probe pulses (see figure 7.3 and chapter 3 section 3.3.2 for more details) with a delay-time resolution of 1/3fs.

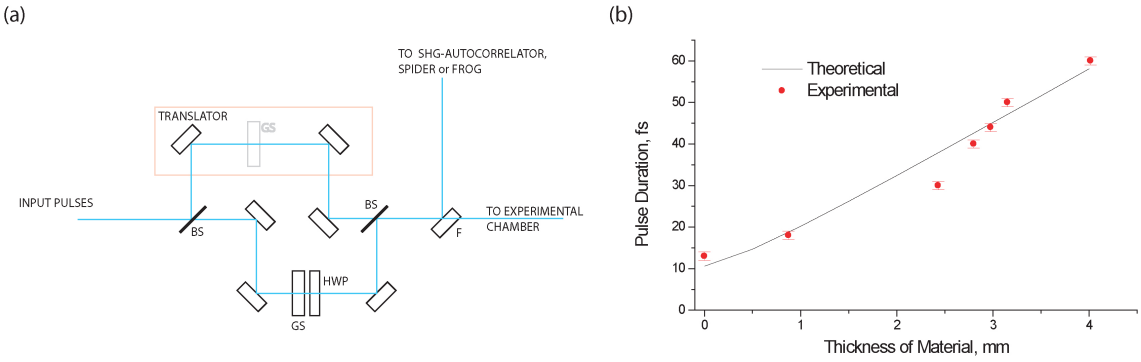

Figure 7.3: Panel (a) is a schematic of the Mach-Zehnder type interferometer employed in the current work. The fixed arm containing a half waveplate (HWP) is at the bottom of the figure and the variable arm at the top. Glass slides (GS) are placed into either arm of the interferometer to stretch the pulses independently of one another. After, the interferometer the pulses can be sent for diagnostic tests or directly to the experimental chamber via use of a *flip mirror* (F). Panel (b) is a plot of pulse duration against the thickness of the glass slides inserted into one of the arms of the interferometer, in order to stretch the pulses. The theoretical curve was generated using the *Refractn* computer program [Dietrich, 2005]. The experimental values shown are obtained from measurements taken with a SHG-autocorrelator. For clarity, only the points shown for the stretching of the probe pulse are shown.

In the majority of the experiments reported here, a $\lambda/2$ plate is placed in the fixed arm of the interferometer to make the polarisation of the pump pulse perpendicular to that of the probe pulse and the axis of the time-of-flight spectrometer, which are parallel to one another. The BeamSplitters (BS) employed are four micron thick pellicles to avoid stretching the pulses unnecessarily; although on leaving the interferometer, the pulses from each arm were measured to be 13 fs in duration. In the tests on wavepacket coherence and distinguishability (see section 7.5) additional control over the pulse length is obtained by the insertion of microscope cover-slips and glass slides, made of BK7 glass, of different thickness into the beam path to induce positive dispersion, which stretches the temporal profile as required (see figure 7.3 and the earlier discussion of this process in chapter 3). The turning mirror immediately after the interferometer is mounted in a *flip-mount* to allow the pulse durations to be monitored immediately before and after each period of data collection.

The D_2^+ (HD^+ or H_2^+) ions are created in a superposition of vibrational states via laser induced ionisation from the respective neutral molecule by the pump pulse. At precisely controlled times the probe pulse then causes these molecular ions to fragment by either Coulomb Explosion (CE) ($D^+ + D^+$) or Photo-Dissociation (PD) ($D^+ + D$). This happens inside the interaction region of the ultra-high vacuum Time-Of-Flight Mass Spectrometer (TOFMS), operated in a Wiley McLaren mode [Wiley and McLaren, 1955], and detailed previously in chapter 2. In all the experiments, the pressure of the target gas is kept low enough to avoid space-charge effects.

In the experiments the laser pulses are f/5 focused on reflection from a spherical mirror mounted inside the UHV tank to give peak intensities of between 0.5 and 0.8 $PWcm^{-2}$ in the individual pulses. The fragment ions are extracted through a 1/4 mm aperture allowing signal from only the most intense region of the laser focus to be imaged.

At each time-delay, time-of-flight spectra are recorded for 500 laser shots and averaged. The delay between the two pulses is then changed in 1 fs steps across the selected range, with the data at each step being recorded.

7.4 Experimental Results and Discussion

Experiments have been conducted with three hydrogenic molecules: hydrogen, deuterium hydride and deuterium. In each case the vibrational wavepacket dynamics are imaged in the molecular ion. The results for each ion are displayed below in turn. In all cases the localisation of the wavepacket is measured by observing the fragmentation products at large R. This is done by either: (i) PD, when the molecule is near the outer turning point of its bounding potential and results in the observation of low energy D^+ fragments; and (ii) CE, which images the wavepacket across a range of R and results in the observation of high energy D^+ fragments, with energies related to their bond length at the instant of fragmentation ($E_{frag} \propto 1/R$).

7.4.1 D_2^+

The D_2^+ vibrational wavepacket is created at the instant of ionisation and is comprised of a superposition of vibrational states (v-states). On creation, the wavepacket exhibits a high degree of coherence (all v states share a common R value). As the wavepacket evolves this coherence de-phases due to the anharmonicity of the D_2^+ $1s\sigma_g$ potential [Sharp, 1971]. At set time intervals, multiples of what is known as the revival time, this initial degree of coherence is regained [Feuerstein and Thumm, 2003]. This behaviour is observed experimentally as an oscillation in the photodissociation signal with a period equal to the weighted average (20-25 fs) of the levels encompassed by the original superposition at a

delay time of around 550 fs.

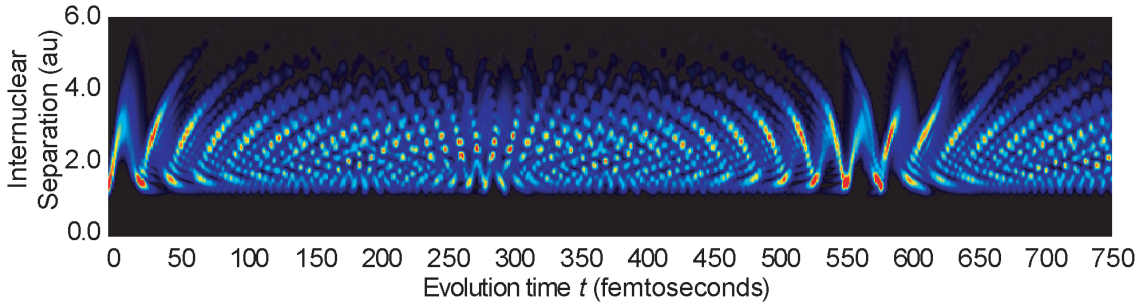

Figure 7.4: Calculated probability distribution of the vibrational wavepacket $|\Psi(R,t)|^2$ as a function of internuclear separation, R, and wavepacket evolution time, t. The vibrational state populations were obtained by calculating the relevant Franck-Condon factors

The simulated $D_2{}^+$ wavepacket probability, $|\Psi(R,t)|^2$, evolution over a time of 0-750 fs and internuclear separation, between 0-6 a.u., is shown in figure 7.4. In the simulation, the results of the initial model were adapted to match the pulse duration used in the experiment (13 fs). At each time the wavepacket probability sums to unity over the entire R range. Dark areas on the plot show regions of low probability and light regions areas of high probability.

In the figure the dephasing region can be seen as the spreading of $|\Psi(R,t)|^2$ across the R range for evolution times 0-100 fs. A fractional revival can also be seen (t= 265 fs) around half the main revival time. The main revival occurs after about 560 fs. Here the wavepacket probability matches its initial profile (t=0) well.

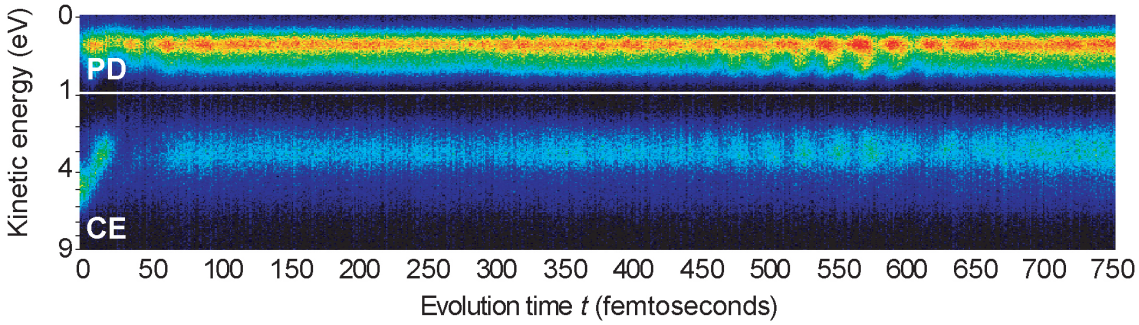

Figure 7.5: A colour map showing the time-of-flight spectra of D^+ ions converted to fragmentation energy as a function of delay-time between the two pulses or evolution time. The top panel is made up of ions resulting from PD while the bottom panel displays the results from CE.

The raw experimental results are displayed in figure 7.5. The figure is comprised of a series of time-of-flight spectra taken in 1 fs delay-time steps. The low energy band (0-1 eV) present in the figure is the result of photo-dissociation fragments, whilst the high energy (2-6 eV) fragments originate from Coulomb explosion.

The periodic modulation in both the PD and CE signals is the signature of the vibrational wavepackets dephasing (t≈0-100 fs) and reviving (t≈500-600 fs). The peaks in the signal modulation correlate to times when the wavepacket is localised about the outer turning point of the bound potential well, where the imaging processes are more likely.

An increase in the ion yield is observed for evolution times less than 25 fs. This is due to pulse overlap, resulting in one shaped laser pulse of high intensity (constructive interference) rather than two individual pump and probe pulses.

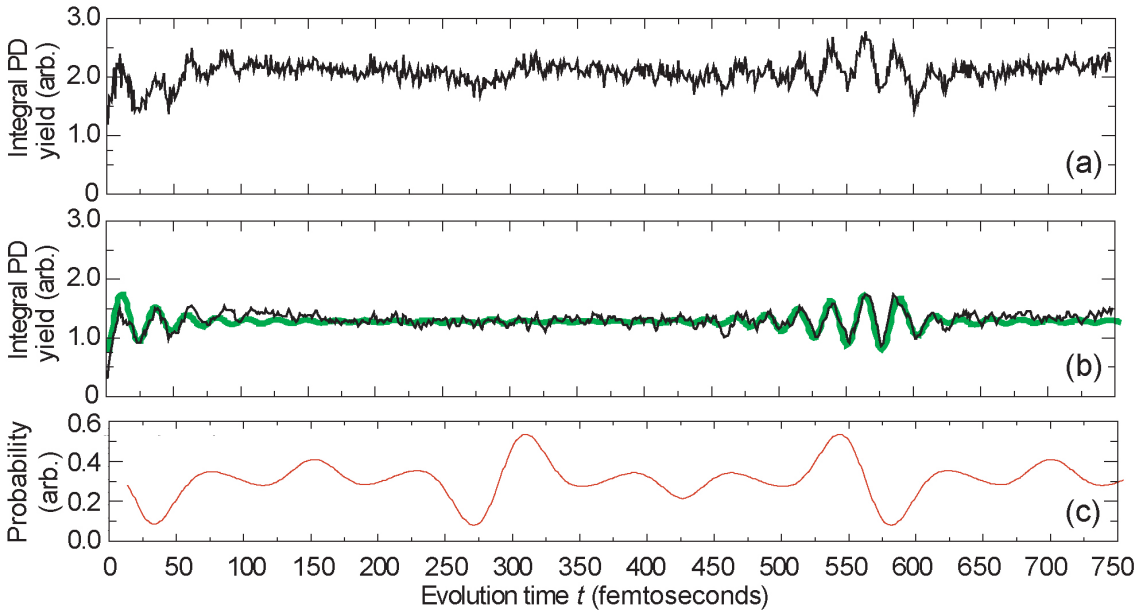

Figure 7.6: Panel (a) shows the integrated ion yield from the upper panel of figure 7.5. This data contains both rotational (D_2) and vibrational (D_2^+) wavepacket data. Panel (b) shows the same integrated ion yield (black) as (a) but with the rotational component removed by subtraction of the rotational wavepacket simulation shown in panel (c) of this figure. An integration of the simulation presented in figure 7.4 for R≥3 a.u. is also shown (green).

The integrated experimental PD ion yield is displayed in figure 7.6(a). In these raw data, signatures of rotational wavepackets in the neutral D_2 molecule are apparent. In order to compare the experimental results to theory, the effects of this rotation upon the data are removed by subtracting the rotational wavepacket simulation shown in figure 7.6(c). These rotational dynamics are discussed in detail in chapter 8.

Once the effects of the rotation have been removed from the data, figure 7.6(b), a comparison to theory can be made more easily. This is done by integrating the wavepacket simulation for all values of R greater than 3 a.u. This range of R was selected, as it encompasses both the one- and three-photon crossing of the $1s\sigma_g$ and $2p\sigma_u$ states when dressed by the laser field, see figure 7.8. The figure shows that experiment and theory

match one another to a high degree.

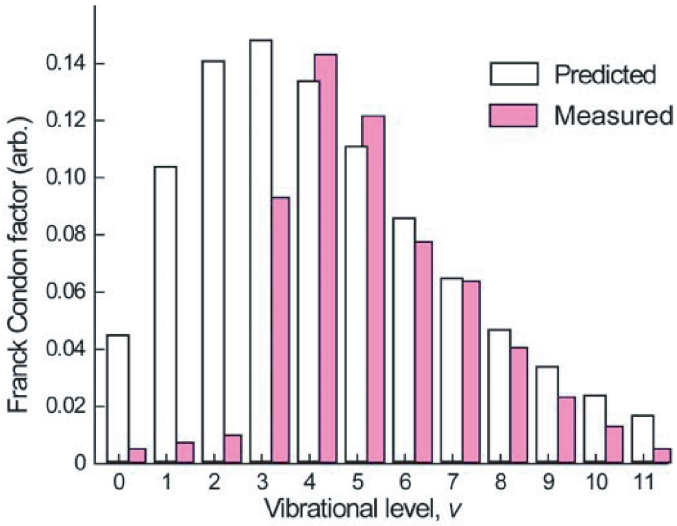

Figure 7.7: Calculated Franck-Condon factors (white bars) for the D_2^+ vibrational wavepacket and measured beat amplitudes (pink bars). The measured distribution is obtained by a Fourier transform of the experimental photo-dissociation results. In the figure, only the beats $\Delta\omega_{kj}$=1 are shown with the beat assigned to the lower of the two v-levels on the x-axis.

The beating of the vibrational states of the wavepacket can also be extracted from the data. This is done by taking the Fourier Transform (FT) of the integrated ion yield. This yields peaks at frequencies matching those given by the $\Delta\omega_{kj}$ array. Assigning each beat peak to its lower v-state, i.e. ω_1-$\omega_0 \rightarrow v$=0, the peak heights can be used to give a measure of the v-state populations. No evidence is found in the FT of the experimental data for $\Delta\omega_{kj}$ greater than one as these beats are too fast to be resolved by our 13 fs pump-probe imaging technique.

The results of the FT are presented alongside the Franck-Condon Factors (FCF) used in the wavepacket simulation in figure 7.7. For v-states greater than v=3 the FCF and the experimental FT results match one another well. However, this is clearly not the case for the lower states. For these, v-states the FCF predict high populations, whereas the FT shows greatly reduced populations. However, this discrepancy is due to the imaging technique employed rather than a difference in the wavepackets.

This is best seen by looking at the D_2^+ potential well, figure 7.8. At the laser intensity (0.6 $PWcm^{-2}$) and frequency (800 nm) used in the experiment the electric field is insufficient to ionise v-states much lower than the three photon crossing, hence only v-states 3 and higher can effectively be ionised by the bond softening mechanism.

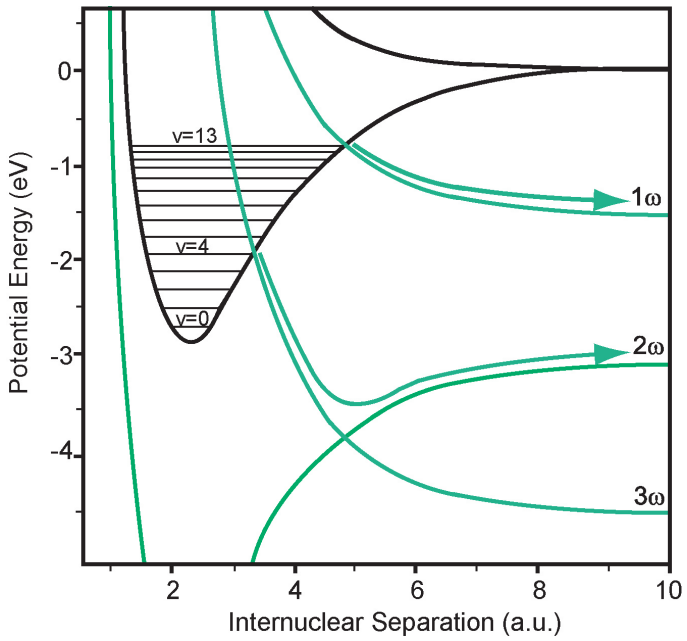

Figure 7.8: Diabatic (black) and adiabatic (green) potential energy curves showing the vibrational levels $0 \leq v \leq 13$ with respect to the avoided crossings for $D_2{}^+$. The green arrows illustrate the dissociation pathways opened by the laser field. 1ω dissociation procedes via the one photon crossing and 2ω dissociation procedes via the three photon crossing. Reproduced from [English, 2007].

7.4.2 HD^+

The experiments on $D_2{}^+$ vibrational wavepackets were repeated for the HD^+ system, the main results of which are published in McKenna et al [Mckenna et al., 2007]. In figure 7.9 the main experimental result is displayed, with the integrated PD yield displayed alongside the wavepacket simulation. The regions of dephasing and revival are reproduced with a high level of clarity. The evolution time over which these processes takes place is reduced from the $D_2{}^+$ case, due to the reduced mass of the HD^+ nuclear system with the revival occurring at an evolution time of around 365 fs.

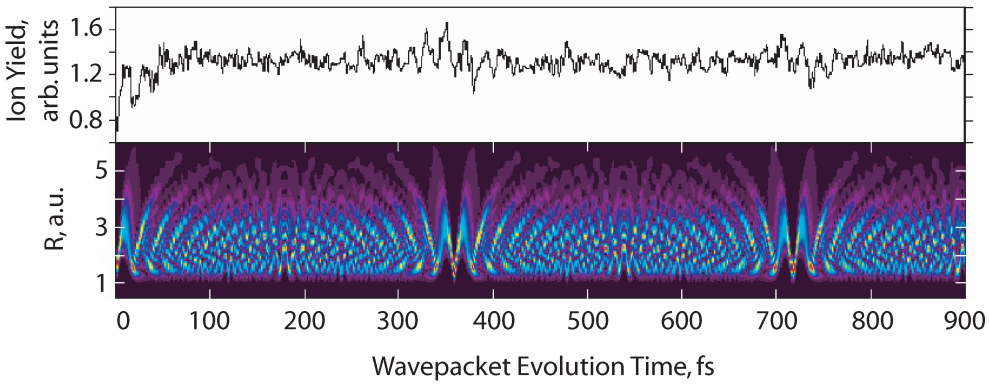

Figure 7.9: The top panel of the figure shows the time-integrated ion yield for experiments on the HD^+ system. Whilst the bottom panel shows the simulation of the bound wavepacket dynamics. A good match between experiment and theory is achieved, with the revival time predicted matching that observed.

7.4.3 H_2^+

Experiments have also been conducted to investigate the bound H_2^+ system, see figure 7.10. In this instance, the phenomena of dephasing and revival are seen. However, the revival is imaged with a reduced fidelity in comparison to revivals of the more massive isotopes reported above.

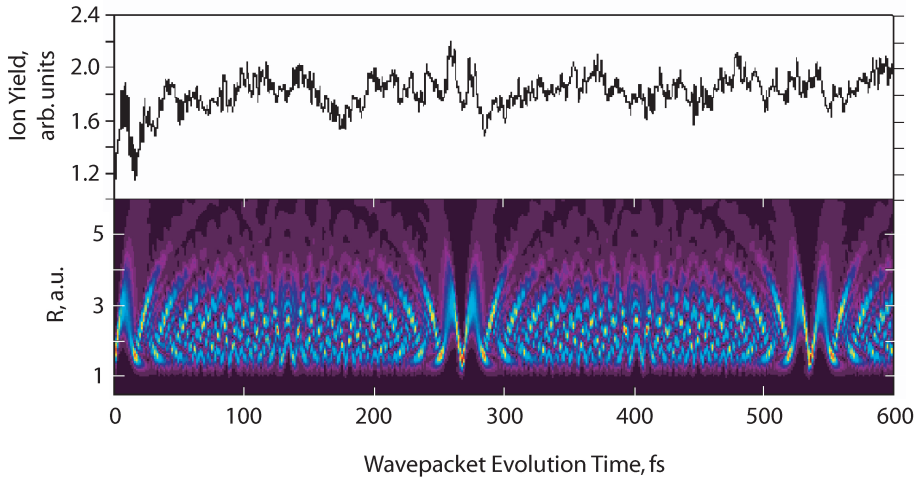

Figure 7.10: The top panel of the figure shows the time-integrated ion yield for experiments on the H_2^+ system. Whilst the bottom panel shows the simulation of the bound wavepacket dynamics. A good match between experiment and theory is achieved, with the revival time predicted matching that observed.

A good match to theory is still achieved with the vibrational wavepacket revival seen at an evolution time of 275 fs as predicted. The dephasing of the initial wavepacket also occurs

as predicted. Again rotational features can be seen in the experimental data (see chapter 8 for more details).

7.5 Quantum Computation Considerations

Through the independent variation of the pump and probe pulse duration, the extent of the temporal and spatial coherence of a nuclear wavepacket is investigated. As the interest in using vibrational wavepacket control for quantum computation [Gollub et al., 2006, Troppmann et al., 2006] and reaction dynamics is flourishing this research has an increasing relevance to a wide scientific community. First the affect of stretching the pump pulse is studied and the effect this has on the resulting wavepackets coherence investigated. Secondly the probe pulse duration is increased in a set of experiments devised to put some imaging constraints on the molecular motion.

In all these tests, deuterium ions were used. This is due to their relatively high mass, making their nuclear motion slower and hence our pump-probe imaging technique more accurate.

7.5.1 Defining Superposition Conditions; Stretching the Pump Pulse

In the first series of experiments the duration of the pump pulse was stretched. Figure 7.11 shows the integrated photodissociation signal as a function of wavepacket evolution time. Also plotted are the theoretical curves obtained from a quantum-mechanical simulation of the vibrational wave packet motion (see figure 7.12), allowing for a variation in the pumps temporal width. A curve showing the characteristic shape of the full rotation revival is also shown on top of the data points. This is thought to arise from a rotational wavepacket comprising a superposition of different rotational states (J-states) in the neutral molecule population that is created through impulsive alignment [Seideman, 2001] by the laser field of the pump pulse. For a more detailed discussion of the rotational dynamics see, chapter 8 of this thesis and the associated publication [Bryan et al., 2007a].

As the pump pulse is stretched, the initial coherence in the vibrational wavepacket is diminished until at a pulse duration equivalent to the vibrational period of the v=0 level of $D_2{}^+$, $T_{v=0} \approx$ 20fs, when it disappears completely. This is observed as a washing out of the fringe pattern in the photodissociation signal with increasing pulse duration. This is clearly seen in figure 7.11, where the experimental signature of the vibrational wavepacket disappears for pump pulse duration greater than the v=0 time period. As the vibrational revival pattern fades out, the rotational revival pattern becomes apparent (see figure 7.11). The theoretical treatment employed only considers the vibrational dynamics of the $D_2{}^+$ ensemble, therefore the rotational behaviour of D_2 population is unaccounted for either

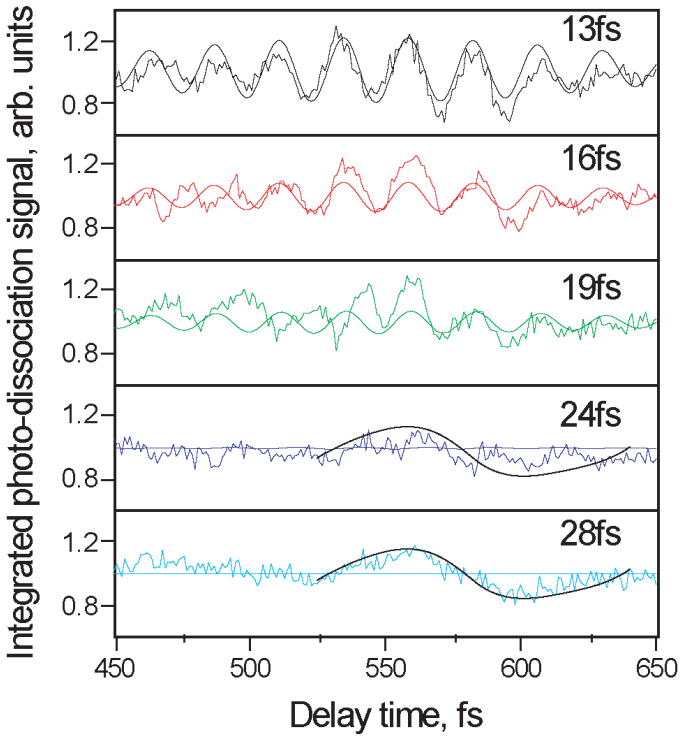

Figure 7.11: A plot of the integrated photo-dissociation signal against pump-probe time delay for experiments in which the duration of the pump pulse was varied (13-28 fs). As the pump pulse is stretched, the signature of the vibrational revival, in the D_2^+ population, recedes to reveal the rotational revival (black curve) feature from the D_2 population. Also shown are the theoretical curves generated for each pump pulse width; these are the smoother of the two coloured oscillations on the top two panels, and the flat lines on the bottom two.

in the theory curves on figure 7.11 or the probability density plots of figure 7.12. A more subtle effect, however, is that the period of the revival pattern also changes, with the period of the oscillation decreasing as the pump width is increased. This occurs because the higher vibrational levels get washed out at the longer pump durations, but the lower lying levels can still revive due to their period being less than the pump duration. Essentially the pump pulse acts as a temporal filter.

7.5.2 Investigating Wavepacket Distinguishability; Stretching the Probe Pulse

In the second series of experiments the duration of the pump pulse was kept constant at 13 fs and the probe duration was varied between 18 fs and 60 fs. In our pump-probe technique the pump pulse can be considered to initiate the dynamics and the probe pulse images them. Therefore, within a photographic analogy, the stretching of the probe pulse

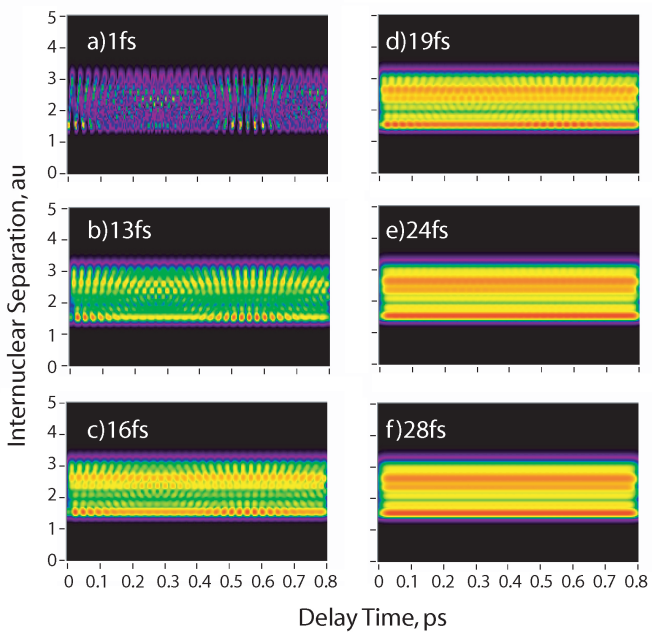

Figure 7.12: Panels (a)-(f) show probability density plots showing the spread of the vibrational wavepacket across the internuclear coordinate R for the D_2^+ system as a function of time delay from production (wavepacket evolution time). Each panel is labelled with the FWHM duration of the pump pulse responsible for its initiation. In each panel the probability density is highest in regions coloured red, and lowest in those coloured black.

can be thought of as increasing our *exposure time* to the nuclear motion. Consequently if the motion being imaged is quicker than the exposure time, a *blurring* or averaging out of the image occurs. From figure 7.13 this seems to occur abruptly at a pulse duration of around twice the period of the v=0 vibrational level (42 fs), which is twice the duration needed to kill off the revival pattern when stretching the pump pulse.

Again, in contrast to when the pump pulse was stretched, the period of the oscillation in the photo-dissociation signal remained constant, as the laser pulse duration was increased. This is because as the pump pulse was the same for all the measurements, so was the vibrational wavepacket excited. Conversely, when the pump pulse was varied, different wavepackets were initiated in each measurement; each one forcing its own characteristic period of oscillation onto the photo-dissociation signal observed.

Figure 7.13 also shows no signs of the rotational revival seen previously. This is the case for two reasons. When the probe pulse durations are short enough to clearly image the vibrational revival, the weaker experimental signatures of the rotational revival are suppressed by the signatures of the vibrational revivals. With probe pulses of greater than 40 fs, these vibrational signatures are suppressed, however, such durations are similar to those of the rotational revival features (see the black curves on figure 7.11 and [Bryan et al., 2007a]). Hence they are not observed.

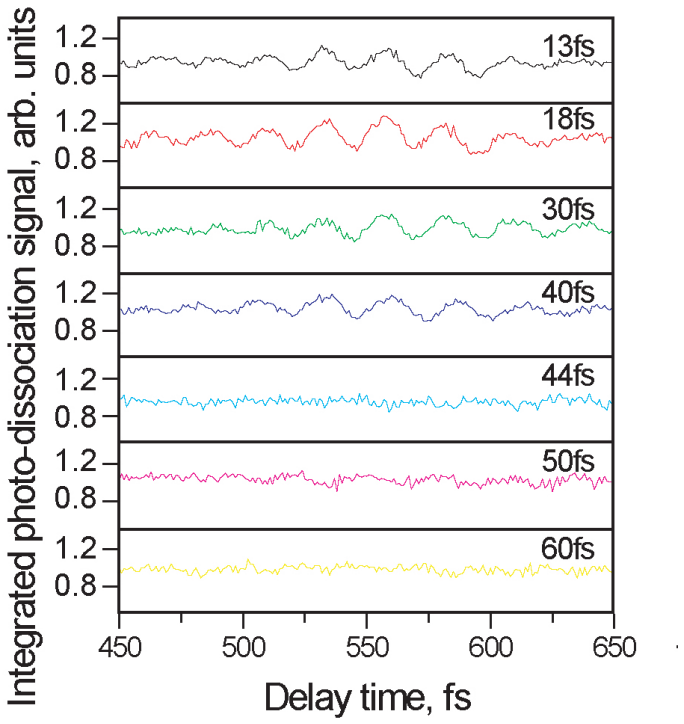

Figure 7.13: A plot of the integrated photodissociation signal against pump-probe delay time for the experiments in which the duration of the probe pulse was varied. The probe pulse duration is displayed in each panel.

7.6 Dynamic Imaging of Dissociative Wavepackets

In the experiments described here, the majority of the discussion has been about the bound wavepacket dephasing and then reviving. In these experiments, the pump and probe pulse polarisations are crossed. However, if the polarisations are both set parallel to one another and the time-of-flight axis, then the dissociating nuclear wavepacket can be imaged [Trump et al., 1999]. The results presented here are also available in Calvert et al [Calvert et al., 2007] and are similar to those obtained independently by other groups [Alnaser et al., 2005, Ergler et al., 2005].

In the experiment, two linearly polarised 15 fs, 0.50 PWcm^{-2} pulses were focused into the TOFMS filled to a pressure of 2×10^{-8} mbar of deuterium gas. Other than polarisation of the pump pulse, all other parameters in the experiment were kept the same as before. The results of the experiment are displayed in figure 7.14, where the dissociating wavepacket has been imaged via the Coulomb Explosion Imaging (CEI) technique [Stapelfeldt et al., 1995, Stapelfeldt et al., 1998]. In the figure, the detected D^+ energy is plotted against evolution time (or delay-time). The red areas of the plot show regions of high ion signal, and blue areas of low ion signal.

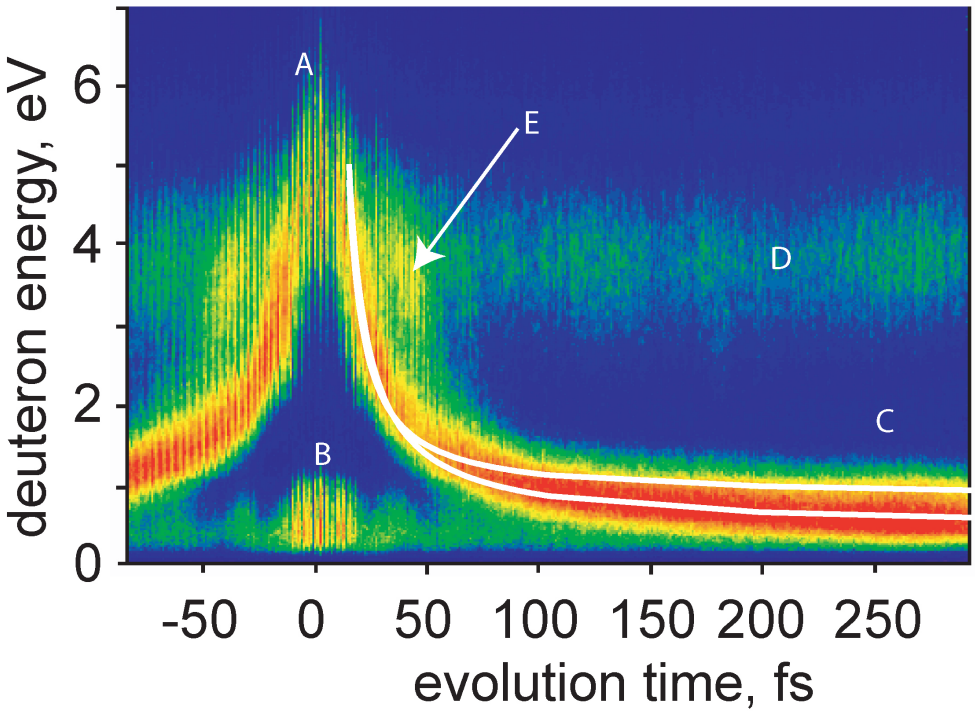

Figure 7.14: The results of a pump-probe experiment on dissociating D_2^+ wavepackets. Both the pump and probe polarisations are parallel to the detector axis. The two laser pulses are 15 fs in duration and have a peak intensity of 0.5 PWcm^{-2}. The white curves on the figure map the predicted CEI results of the two dissociation channels.

When the two laser pulses overlap, T_{evo}=0, there is effectively just one intense (2 PWcm^{-2}) pulse therefore high energy Coulomb Explosion (CE) is observed (point A on figure 7.14). Enhanced Photo-Dissociation (PD) is also seen about this delay time (point B on figure 7.14). In the figure this is seen as a *hot spot* at low energy. Both of these results are consistent with single pulse experiments conducted with equivalent pulses (in terms of energy, frequency and pulse duration) conducted by both our group [McKenna et al., 2005] and others [Rudenko et al., 2005].

About T_{evo}=0 interference effects are also present. The corresponding constructive and destrucive interference fringes result in *striping* of the ion signal detected and are clearly seen in the figure. This is also the mechanism utilised in the preliminary technique presented here (see chapter 6) to extract the at-focus pulse duration.

The band determined by C in the figure indicates the Coulomb explosion imaged, one and two photon dissociation channels (see figure 7.1 for the relevant potential surfaces). The deuterons imaged in this thick red curve running from ≈6 eV at T_{evo}=0 to ≈0.5 eV at T_{evo}=250 fs result from molecules that were ionised in the pump pulse and then proceed to dissociation through one of the two Bond Softening (BS) channels. In the experiment,

these two fragmentation paths are not resolved from one another due to the number of v-states around the avoided crossings, leading to an overlapping of the two resulting energy distributions.

Theoretical curves for the two processes are superimposed on the figure (white curves). These were obtained using simple kinematic arguments, in which the motion of the dissociative channel was modelled classically before being promoted to the Coulomb curve at $T_{evo}=\tau$. Repeating this for all values of τ, 0-250 fs, and using the mean 1ω and 2ω appearance energies, 0.34 eV and 0.74 eV respectively, the curves in the plot were obtained. (The method used is described in more detail by Trump et al [Trump et al., 1999].)

A high energy band, $\approx$4 eV can also be observed in the figure 7.14 (point D). This is in accordance with the fragmentation energy which would be characteristic of the Charge Resonance Enhanced Ionisation (CREI) mechanism [Zuo and Bandrauk, 1995] and was labelled as such by Ergler et al [Ergler et al., 2005].

Also at this energy, signatures of the bound vibrational wavepacket can be seen (point E). At T_{evo}=34-38 fs, which equates to 1.5 mean vibrational periods of the ion wavepacket, there is an enhancement in the ion signal detected. This is thought to be due to the ionisation of a fraction of the wavepacket that remains bound after the first pulse, but is ionised one and a half vibrational periods later [Alnaser et al., 2005] when the majority of the wavepacket's probability distribution is about the $1s\sigma_g$ potentials outer turning point. The bound wavepacket ceases to be imaged past this time due to the dephasing of the wavepacket described earlier in this chapter.

7.7 Summary

Using few cycle laser pulses the sub-vibrational-period imaging of the nuclear motion of D_2^+, HD^+ and H_2^+ions has been achieved. By variation of both the pump and probe pulse durations, the extent of the temporal and spatial coherence of a nuclear wavepacket throughout its evolution has been traced. Additionally, rotational revival structures, arising from an impulsive alignment process towards the pump pulse, have been isolated in the neutral molecules. In all instances these experimental observations were found to be in excellent agreement with our own theoretical models and those of others.

Chapter 8

Rotational Wavepacket Dynamics in H_2, D_2 and HD: Few Cycle Pump-Probe Experiments II

8.1 Introduction

As well as studying the dynamics of vibrational wavepackets in hydrogenic molecular ions an investigation into the rotational dynamics has also been conducted. As before similar experiments have been conducted on heavier diatomic molecules with laser pulses of larger durations. Prior to our study [Bryan et al., 2007a], Lee et al published a paper [Lee et al., 2006] discussing the rotational dynamics of deuterium molecules imaged via Coulomb Explosion Imaging (CEI) with 10 fs laser pulses. Our work will be discussed in relation to this publication and two proceeding ones from separate groups [Bocharova et al., 2008, Chen et al., 2007] in the USA. The first of which utilises CEI and the second a single-shot interferometeric method.

One final constraint to this work particularly affecting the CEI method is the effect of the vibrational dynamics of the molecular ions which are observed simultaneously. This leads to ro-vibrational coupling [Banerji and Ghosh, 2006] and difficulties in separating the ion signal coming from the vibrational superposition of states in the molecular ion, from the ions emanating from the rotational superposition of states in the neutral molecules [Ergler et al., 2006b].

This work has become increasingly popular due to the effect molecular alignment has on the laser molecule interaction, from its effects on the ionisation rate
[Litvinyuk et al., 2003, Pavičić et al., 2007], the high harmonic yield [Kajumba, 2007], [Itatani et al., 2005, Wagner et al., 2007] and electron momentum distributions

[Kumarappan et al., 2008] too the possibilities of viable routes from which coherent control regimes may be realised [Shapiro et al., 2003, Lee et al., 2004].

Finally, I would like to thank Dr Ricardo Torres from Imperial College London who worked with our collaboration on this investigation into the rotational dynamics of hydrogenic molecular systems. His expertise in simulating the rotational dynamics witnessed in our experiments was excellent and improved our understanding of our experimental findings.

8.1.1 Quantifying Alignment: The $\cos^2(\theta)$ Parameter

In general, the degree of alignment exhibited by a population of molecules is quantified using the $\cos^2(\theta)$ parameter, where θ is the angle between the electric field vector and the molecular bond. In the case of perfect alignment the $\cos^2(\theta)$ parameter is equal to unity. Anti alignment, or disk alignment (alignment into the plane perpendicular to the electric field) corresponds to $\cos^2(\theta)$=0, whilst $\cos^2(\theta)$=1/3 for a randomly aligned sample.

The reason the average value of $\cos^2(\theta)$=1/3 for an isotropic distribution can be illustrated by considering the dot product (equation 8.1) of the laser pulses electric field, **E**, and the molecular axis, **A**. Where $\mathbf{A}=A_x\mathbf{i}+A_y\mathbf{j}+A_z\mathbf{k}$ and **i,j,k** are the Cartesian unit vectors. Given that all directions are equally favourable **A**, can be expressed as shown in equation 8.2.

$$\mathbf{E}\cdot\mathbf{A} = EA\cos\theta \tag{8.1}$$

$$\langle\mathbf{A}\rangle = A\left(\sqrt{\frac{1}{3}},\sqrt{\frac{1}{3}},\sqrt{\frac{1}{3}}\right) \tag{8.2}$$

Squaring equation 8.1 and combining the result with equation 8.2, the average value of $\cos^2(\theta)$ can be shown to equal a third, as shown by equation 8.3. This is a result which holds under any coordinate transformation and can therefore be considered general.

$$\left\langle\cos^2\theta\right\rangle = \left(\frac{E\sqrt{\frac{1}{3}}A}{EA}\right)^2 = \frac{1}{3} \tag{8.3}$$

Alignment along a specific axis is only achievable with linearly polarised laser pulses as the polarisation vector of circularly polarised light varies too quickly [Ellert and Corkum, 1999]. However, with circularly polarised light, molecules can be aligned to a plane. Some research groups use a the quantity $\cos^2(\vartheta)$ to quantify alignment [Dooley et al., 2003], where

ϑ is the angle between the molecular axis and the imaging plane. In such instances $\cos^2(\vartheta)$=1, for perfect alignment; $\cos^2(\vartheta)$=0, for perfect antialignment and $\cos^2(\vartheta)$=1/2, for an isotropic sample.

$$\Delta\alpha \quad = \quad \alpha_{\parallel} - \alpha_{\perp} \tag{8.4}$$

For any type of alignment, however, a dipole moment must be present in the molecule. In charged species this dipole will be very strong resulting in the system aligning easily to the laser field. For hetronuclear molecules, such as HCl, this dipole is permanent and is signified by the symbol μ. Homonuclear molecules do not have a permanent dipole moment, as both nuclei have equal electronegativities. However, in the presence of an electric field, a dipole along the molecular bond can be induced as long as the molecule contains an anisotropy in its polarisability, $\Delta\alpha$, which is defined in equation 8.4 and illustrated in figure 8.1. Dipoles perpendicular to molecular bonds can also be formed. However, in diatomic systems like those considered here, it is unlikely as the probability density of the outer electrons is greatest about the molecular bond. Subsequently, $\alpha_{\parallel} > \alpha_{\perp}$ and molecules align with their molecular bonds parallel to the direction of the electric field vector.

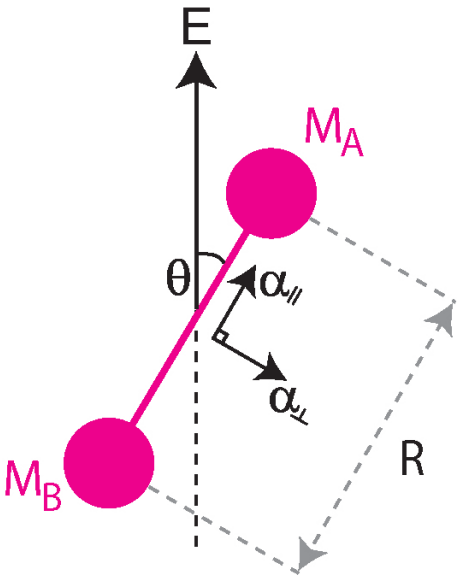

Figure 8.1: The degree of alignment is quantified using the $\cos^2\theta$ parameter, where θ is defined as the angle between the electric field vector of the aligning laser pulse and the molecular bond. The mechanism of impulsive alignment relies on an anisotropy, $\Delta\alpha$, between the parallel ($\alpha_{\parallel}$) and perpendicular ($\alpha_{\perp}$) polarisabilities, also shown here. The internuclear separation, R, is also illustrated.

8.2 Types of Rotational Alignment

As mentioned in section 1.5.1 there are various classes of rotational alignment. For diatomic systems, the situation is simplified, as there is only one natural axis in the molecule, that parallel to the molecular bond. However, there are still two situations of interest, namely diabatic alignment and adiabatic alignment. The boundary between the two is governed by the natural time period for the rotational motion of the system, T_{rot}, i.e. the period of the J=1 level in the system's ground vibrational state and the laser pulse duration, T_{laser}. When the laser pulse is shorter or of the order of the molecules natural time period, governed by equations 8.5 and 8.6 within the rigid rotator model, impulsive alignment occurs. If the laser pulse is long in comparison to the molecule's natural timescale, then any alignment is adiabatic.

$$T_{rot} = \frac{h}{2B_0} \tag{8.5}$$

$$T_{rot}[fs] = \frac{1 \times 10^{15}}{2B_0[cm^{-1}]c[cms^{-1}]} \tag{8.6}$$

Typically the degree of alignment achieved in the adiabatic case is higher. However, in the impulsive regime the alignment persists beyond the pulse, leading to field free alignment, which means that aligned molecules can be investigated without having to consider the presence of the aligning field simultaneously with the probe field. These, and other considerations including possible applications and multiple pulse alignment, are discussed in the recent topical reviews such as those written by Stapelfeldt and Seideman [Stapelfeldt and Seideman, 2003, Stapelfeldt, 2003].

8.2.1 Adiabatic Alignment and Pendular States

When $T_{laser} > T_{rot}$ molecules with a dipole moment, either permanent or induced, align themselves to the laser pulse adiabatically. Adiabatic processes are processes that occur smoothly, and in this instance the degree of alignment in the sample increases steadily with the pulse's intensity profile. High values of $\langle \cos^2 \theta \rangle$ can be routinely achieved ($\approx$0.8), however, these high values of $\langle \cos^2 \theta \rangle$ only last for the duration of the laser pulse and if the intensity is increased too far, the level of alignment decreases due to loss of population from ionisation processes.

The mechanics behind adiabatic alignment were formulated by Friedrich and Herschbach [Friedrich and Herschbach, 1995, Friedrich and Herschbach, 1999] who suggested the interaction potential between the laser field and a polar molecule could be defined by equa-

tion 8.7.

$$V_\alpha(\theta) = \frac{1}{2}E^2\cos^2(\omega t)(\alpha_\parallel\cos^2\theta + \alpha_\perp\sin^2\theta) \tag{8.7}$$

Integrating this equation over the pulse duration and introducing the polarisabitity anisotropy (equation 8.4) and then making the trigonometric substitution $\sin^2\theta$=1-$\cos^2\theta$. The effective potential responsible for the adiabatic alignment process can be written as equation 8.8.

$$V_\alpha = \frac{1}{4}E^2(\alpha_\parallel - \alpha_\perp)\cos^2\theta = \frac{1}{4}E^2(\Delta\alpha)\cos^2\theta, \tag{8.8}$$

the result of which is the formation of pendular states [Ortigoso et al., 1999]. These pendular states are a superposition of the field free states which are angularly confined. If the laser intensity is increased, more of the field free states are drawn into the pendular superposition and the alignment becomes stronger. The rotational temperature of the sample also plays a crucial role in the alignment process, as the lowest lying field free states evolve most readily into the lowest and therefore tightest bound pendular states.

Rotational temperature and how it effects the J-State population also affects impulsive alignment and is discussed more in section 8.3.2 later in this chapter.

In figure 8.2 the adiabatic alignment of I_2 [Stapelfeldt, 2004] is illustrated. These measurements are typical of those from adiabatic alignment experiments. A high degree of alignment is achieved, $\langle\cos^2\theta\rangle$=0.7, with the degree of alignment matching the laser pulse profile. The I_2 molecule has also been aligned impulsively [Rosca-Pruna and Vrakking, 2001]. As I_2 has a natural rotational period of T_{rot} = 450 ps, laser pulses of a duration of T_{laser}=1-10 ps (rather than nanosecond pulses) can be used to produce impulsive alignment.

Such long pulse techniques have been the topic of many investigations, including those of Larsen et al [Larsen et al., 2000] [Larsen et al., 1999] and are particularly suitable to applications requiring high values of $\langle\cos^2\theta\rangle$. Hybrid techniques mixing adiabatic, impulsive alignment and D.C. electric fields (both mentioned below) are also employed, as they try to balance the advantages of each scheme whilst minimising the drawbacks.

Another form of adiabatic alignment is the so called brute force technique. Here a permanent D.C. electric field, ϵ, (rather than a laser pulse) is used to align polar molecules with a dipole moment, μ, along their molecular axis. The resulting interaction potential is given by equation 8.9 [Friedrich and Herschbach, 1995],

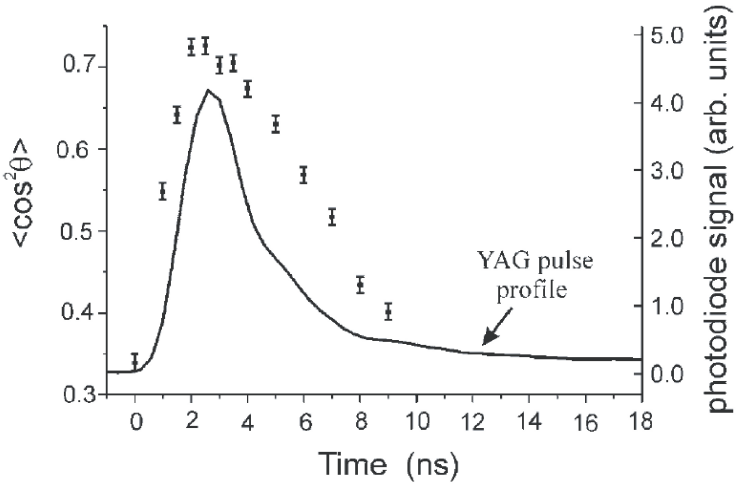

Figure 8.2: The adiabatic alignment of I_2 (data points) and the pulse profile (dark curve) against time. The degree of alignment is quantified using the $\cos^2\theta$ parameter which follows the laser pulse profile well, with the maximum degree of alignment coinciding with the maximum laser intensity. The laser pulses used are 3.5 ns in duration, have a central wavelength of $\lambda = 1064$ nm and an intensity of 1.4×10^{12} Wcm^{-2}. Reproduced from [Stapelfeldt, 2004]. The natural rotational period of I_2 is $T_{rot} = 450$ ps.

$$V_\mu = -\mu\epsilon\cos\theta. \tag{8.9}$$

As this method is not a laser technique, no further discussion of the mechanism responsible will be presented. However, it is worth noting that the brute force technique can be applied to polar molecules to obtain high degrees of molecular alignment. However, as with laser induced adiabatic alignment, the molecular sample is only aligned in the presence of the aligning electric field, which substantially limits further applications of the aligned sample.

8.2.2 Impulsive Alignment and Rotational Revival

Conversely, field free alignment can be achieved using laser pulses for which $T_{laser} \leq T_{rot}$. In this instance, pendular states are not created, but alignment is achieved through the creation of a rotational wavepacket. This wavepacket is comprised of all the possible J-states above the ground vibrational state of the molecule in question.

As before, the anisotropy in the dipole moment of the molecule leads to a preferential orientation for the molecule in the laser field, and as the pulse enters the population the molecules are *kicked* towards this optimal orientation. As individual molecules may lie in different J-states, i.e. $|v{=}0,J{=}i\rangle$ and $|v{=}0,J{=}k\rangle$ where $i{\neq}k$, they rotate with different

periods. As all the constituents of the superposition of J-states share a common initiation, they dephase with respect to one another over time. However, as in the case of the vibrational wavepackets, if the evolution is undisturbed, the system will revive and the superposition of J-states return to being in phase with each other. When the superposition of J-states are in phase with each other, the population is aligned to the laser pulse, and when the phases are mismatched the population is isotropic. Transition between these two extremes is not discrete, with distinct orientations existing at intermediate times. The theory used to describe the impulsive alignment witnessed in the experiments is outlined in brief in section 8.3 later in this chapter.

As before, the degree of alignment achieved is dependent on laser intensity, with higher intensities leading to more aligned samples. This trend holds true unless the laser intensity becomes sufficiently high as to initiate ionisation, which has the effect of reducing the number of molecules in the population and subsequently the maximum value of $\langle \cos^2 \theta \rangle$ obtained.

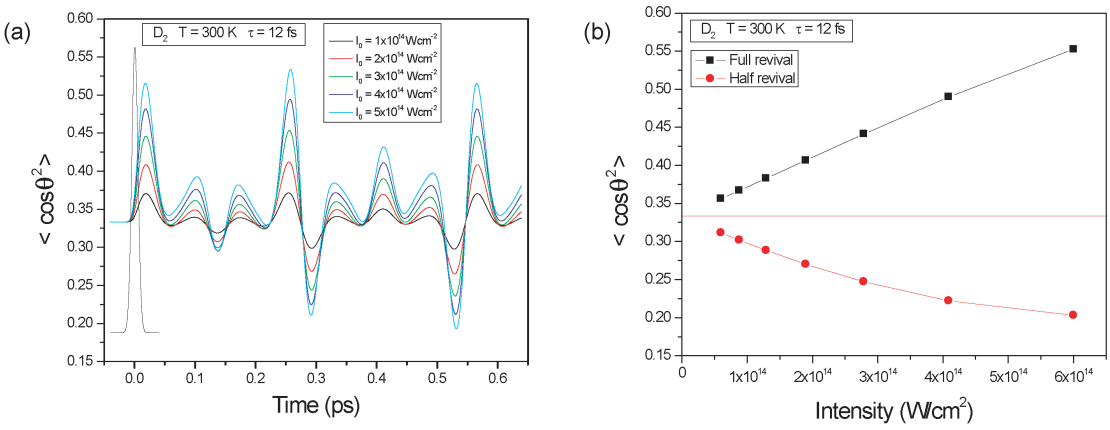

Figure 8.3: The alignment of D_2 molecules after the interaction of a 12 fs laser pulse. The degree of dynamic alignment is quantified using the $\cos^2(\theta)$ parameter. Panel (a) shows how the rotational wavepacket evolves through time for different laser intensities. Both the full revival (at 560 fs) and the fractional revivals (1/4 at 140 fs, 1/2 at 280 fs and 3/4 at 420 fs) are apparent. Panel (b) shows how the degree of alignment changes with intensity for the disk alignment (red curve) and for the parallel alignment (black curve). Figure reproduced from a private communication with Dr. R. Torres of Imperial College London.

Figure 8.3 shows the impulsive alignment of deuterium molecules by 12 fs laser pulses of different intensities. Panel (a) shows the evolution of the $\cos^2(\theta)$ parameter alongside the laser pulse profile for each intensity. In each instance, the samples are aligned by the laser pulse, dephase and then go through periods of fractional and full revival. As the laser intensity is increased, so is the degree of alignment, however, the positions of both the fractional and full revivals remain fixed. Panel (b) is a further illustration how the degree

of alignment varies with laser intensity at the half and full revival times.

The region between the long (adiabatic) and short (impulsive) laser pulse regimes occurs around $T_{laser} \approx T_{rot}$. As usual, the boundary is rather diffuse and the intermediate situation at first glance appears to be a hybrid of both situations. However, one method of distinction is that any adiabatic alignment should end after the laser pulse has passed, so if field free alignment is witnessed then the mechanism responsible for the rotational dynamics of the system must be impulsive.

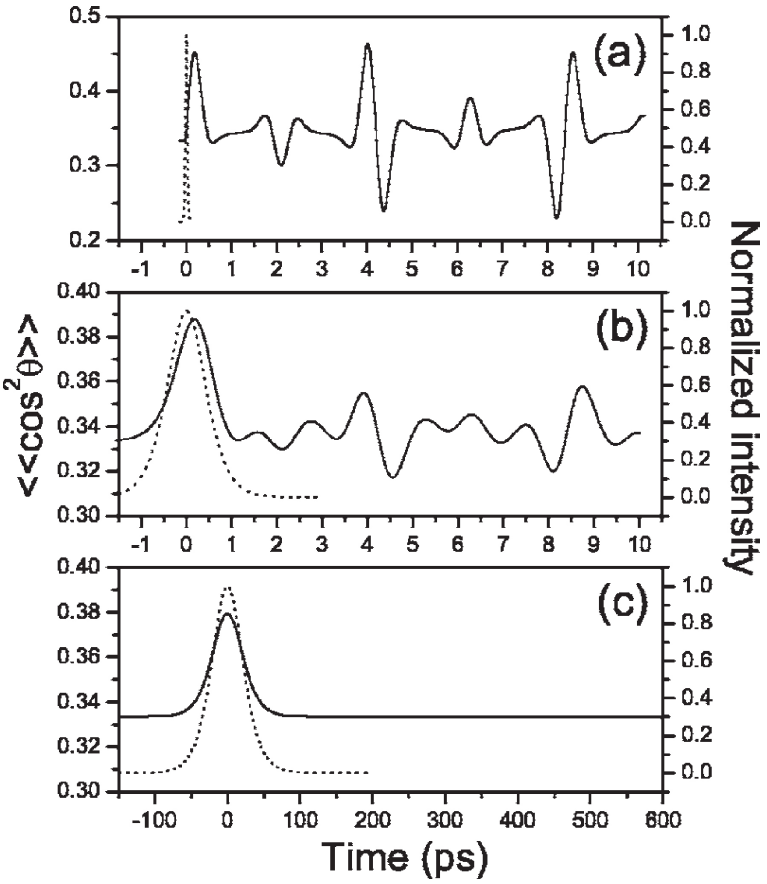

Figure 8.4: The transition from adiabatic to impulsive alignment in N_2. In each instance the time evolution of the $\cos^2\theta$ parameter is illustrated (full curve) alongside the pulse profile (dashed curve). Panel (a) shows alignment in the pure impulsive regime (τ=50 fs, I_0=2.5×10^{13} Wcm^{-2}). Panel (c) shows alignment in the pure adiabatic regime (τ=50 ps, I_0= 2.5×10^{12} Wcm^{-2}). While panel (b) shows an intermediate case. (τ=1 ps, I_0=2.5×10^{12} Wcm^{-2}). Reproduced from [Torres et al., 2005]. The natural rotational period of N_2 is T_{rot} = 8.38 ps.

Figure 8.4 illustrates this boundary between the two regimes using calculations on nitrogen molecules. Panel (a) shows the alignment produced in the impulsive or dynamic regime with the characteristic time evolution of the $\cos^2\theta$ parameter clearly visible. In the inter-

mediate case, panel (b), this field free evolution is still present, suggesting the mechanism responsible is mostly impulsive in nature. However the magnitude of the revival is suppressed in comparison to the pure impulsive case and the period of the initial alignment seems more characteristic of the adiabatic regime. When the duration of the laser pulse is larger than the natural rotation time of the molecule, as in panel (c), the adiabatic regime is reached. Here field free alignment does not occur, which restricts applications of this technique as discussed in section 8.2.1.

As the impulsive alignment regime is only reached when the laser pulse duration approaches the natural rotational period of the molecule development of the technique has been heavily dependent on the development of laser technology. The first impulsive alignment experiments were reported in the 1970s [Heritage et al., 1975]
[Zon and Katsnel'son, 1975] and concentrated on larger molecules with slower rotational periods for example CS_2; T_{rot}=76 ps. As laser pulse durations decreased, smaller systems with smaller T_{rot} could be studied [Seideman, 1999, Bandrauk and Ruel, 1999, Zon, 2000a] [Rosca-Pruna and Vrakking, 2001] culminating in studies on hydrogenic molecules by our group and others in the last few years. Truncated pulses [Villeneuve et al., 2002]
[Underwood et al., 2003] have also been used to achieve dynamic alignment as the *kick* effect can be replicated using relatively long pulses with steep rising and falling edges that lead to non-adiabatic evolution.

Applications of field free alignment are also growing, one of the most interesting being the development of molecular phase modulation as a means of generating near single-cycle laser pulses [Zhavoronkov and Korn, 2002].

8.3 Theoretical Treatment

The experimental results presented in this chapter are examined through comparison with theoretical models developed primarily by Ricardo Torres of Imperial College London. His method for modelling impulsive alignment [Torres et al., 2005] starts with the rigid rotor model for a diatomic molecule, which models the rotational *kick* received by the molecule from the aligning laser pulse and then extracts the resulting values of the $\cos^2(\theta)$ parameter for a given evolution time. This treatment is not unique and many of the ideas are consistent with the paper of Dooley et al [Dooley et al., 2003], which has also been very influential in this evaluation.

8.3.1 Rigid Rotator Model and the Time Dependent Schrödinger Equation (TDSE)

The rigid rotor model is a common method (see for example [Banwell, 1983]) of modelling the rotational dynamics of diatomic and diatomic like (i.e. near linear triatomics such as CO_2) molecules. Here, the constituent atoms of the molecule are treated as two point masses separated by a rigid mass-less rod (the intermolecular bond), as shown in figure 8.5; and the molecule is thought to rotate end-over-end about the systems centre of mass (CM).

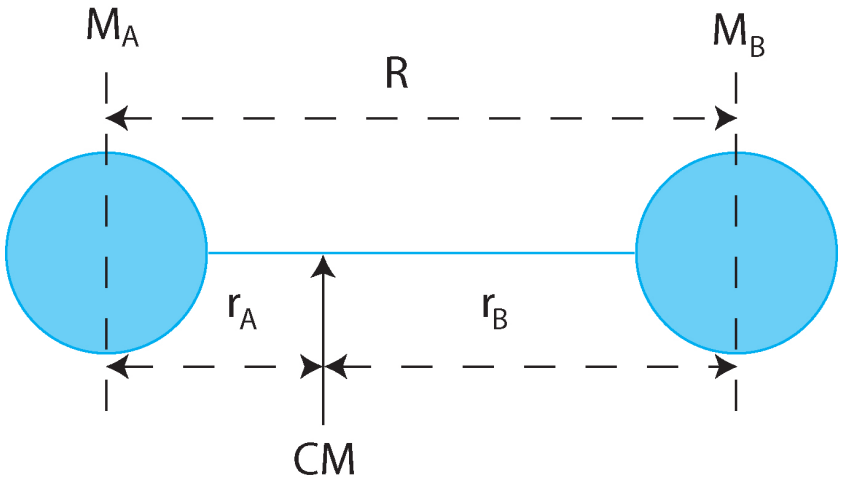

Figure 8.5: A diatomic molecule modelled as a rigid rotor. R is the internuclear separation of the two nuclei A and B. CM indicates the system's centre of mass around which the molecule rotates, and M_A and M_B, the masses of each nuclei, with r_A and r_B representing their displacement from the system's centre of mass. R=r_A+r_B.

Balancing the moments about the centre of mass, equation 8.10 can be used to relate the two atomic masses. Then by using the definition of the moment of inertia about the system's centre of mass, I, (equations 8.11 through to 8.13), inserting the reduced mass, μ, into the expression (equation 8.14) and by utilising the Schrödinger equation an expression for the rotational constant, B_0 can be found (equation 8.15), as well as the rotational energy of the system, E_J, (equation 8.16).

$$M_A r_A = M_B r_B \tag{8.10}$$

$$I = M_A r_A^2 + M_B r_B^2 \tag{8.11}$$

$$I = \left(\frac{M_A M_B}{M_A + M_B}\right) R^2 \tag{8.12}$$

$$I = \mu R^2 \tag{8.13}$$

$$\mu = \frac{M_A M_B}{M_A + M_B} \tag{8.14}$$

$$B_0 = \frac{h^2}{8\pi^2(\mu R^2)} = \frac{\hbar^2}{2(\mu R^2)} \tag{8.15}$$

$$E_J = B_0 J(J+1) \tag{8.16}$$

Using these equations, 8.10-8.16, the values in table 8.1 can be obtained and then used in the analysis of the rotational dynamics observed in the experiments.

Species	μ (a.u.)	R_0 (a.u.)	B_0 (cm^{-1})	$T_{J=1}$ (fs)
H_2	916.6	1.4	60.8530	274
$H_2{}^+$	916.6	2.0	30.210	552
D_2	1833.2	1.4	30.4436	547
$D_2{}^+$	1833.2	2.0	15.0160	1110
HD	1222.1	1.4	45.6550	365
HD^+	1222.1	2.0	22.4520	742

Table 8.1: Constants for hydrogenic molecular systems with regards to their rotational dynamics. The B_0 and R_0 values are obtained from the NIST atomic data base [Huber and Herzberg, 2001], whilst the remainder are calculated using a rigid rotor model described here.

The technicalities of the application of the Schrödinger equation are based on the work of Friedrich and Herschbach [Friedrich and Herschbach, 1995] and are expressed in detail in the publication by Torres et al [Torres et al., 2005]. The values of the polarisabilites, $\alpha_{\parallel}$ and $\alpha_{\perp}$, were sourced from Huber and Herzberg [Huber and Herzberg, 1979]. The laser pulse was considered to be monochromatic, with a pulse profile governed by f(t) as shown in equation 8.17.

$$f(t) = sech\left(\frac{2ln\left(\sqrt{2}\right)}{\tau}t\right) \tag{8.17}$$

$$\Psi(t) = \sum_J a_j \exp\left[-i\frac{E_J}{\hbar}t\right] \mid J, M\rangle \tag{8.18}$$

$$\Phi(t) = \Phi_J(0) - \frac{E_J t}{\hbar} \tag{8.19}$$

After the passing of the pulse, the resulting superposition of states, illustrated in equation 8.18 is free to evolve, with each constituent J-state phase, Φ_J, varying like that of a free rotor, equation 8.19.

8.3.2 Quantum Beats and Nuclear Spin Statistics

As in the case of the vibrational wavepackets, the subsequent dynamics of the system are governed by the quantum beats between the constituent states of the initial superposition of states. However, in this instance the picture is clouded further by the necessity to consider the nuclear spin statistics of the system in question. This problem arises due to the indistinguishable nuclei in hydrogen and deuterium and leads to the selection rule ΔJ=$\pm$2.

Nuclear spin statistics must be considered in the case of indistinguishable particles to satisfy the Pauli exclusion principle with regards to exchange. These considerations are summarised in table 8.2 where hydrogen molecules correspond to column 6 and deuterium to column 12 respectfully.

		Fermions					Bosons				
Electronic					g_{nuc}					g_{nuc}	
State	J	ψ_{rot}	ψ_{ns}	Ψ	I=1/2	I=3/2	ψ_{rot}	ψ_{ns}	Ψ	I=0	I=1
$\Sigma_g{}^+$	even	s	a	a	1	6	s	s	s	1	6
	odd	a	s	a	3	10	a	a	s	0	3

Table 8.2: Nuclear spin statistics: symmetries of the rotational ψ_{rot}, nuclear ψ_{ns}, and total Ψ wavefunctions and the statistical weights, g_{nuc}, for fermionic and bosonic nuclei reproduced from [Demtröder, 2006]. H_2 comprises of fermionic I=1/2 nuclei and D_2 I=1 bosonic nuclei. As the nuclei in the HD molecule are distinguishable spin statistics do not govern the J state population distribution.

Hydrogen nuclei (protons) have spin 1/2 and are fermions, whilst deuterium nuclei are bosons with a nuclear spin of unity, as the spins of the deuteron's neutron and proton sum to find the total. These values can then be used, as in table 8.2 to establish how the J-states of a given sample will be populated. Generally, for homonuclear diatomics with nuclear spin I, there are (2I+1)(I+1) ortho or symmetric states and (2I+1)I para or antisymmetric states. This leads to a ratio, N_{sym}/N_{asym}, between the nuclear statistical weights, g_{nuc}, of these states as shown in equation 8.20.

$$\frac{N_{sym}}{N_{asym}} = \frac{I+1}{I} \tag{8.20}$$

For fermions, in symmetric electronic states, such as H_2, this population ratio becomes equation 8.21, which means the even states in H_2 have a third of the statistical weight of the odd ones.

$$\frac{N(J=odd)}{N(J=even)} = \frac{I+1}{I} \tag{8.21}$$

And for bosons, in symmetric electronic states, such as D_2, this population ratio becomes equation 8.22. Subsequently, the even states in D_2 have twice the statistical weighting of the odd ones.

$$\frac{N(J=even)}{N(J=odd)} = \frac{I+1}{I} \tag{8.22}$$

For homonuclear (deuterium and hydrogen) molecules, the allowed Raman transitions dictate that $\Delta J=\pm 2$ [Banwell, 1983, Hollas, 2002], and consequently, the wavepacket dynamics are dominated by beats $\Delta\omega_{J,J+2}$. The duration of these beats can be found using equations 8.23-8.26 and are shown in table 8.3 rather than the fundamental periods of the J-states, ω_J, as described by equations 8.28 and 8.27, where ω_1 is equivalent to the frequency of the J=1 state.

$$\Delta\omega_{J,J+2} = \frac{(E_{J+2}-E_J)}{\hbar} \tag{8.23}$$

$$\Delta\omega_{J,J+2} = \frac{B_0}{\hbar}[(J+2)(J+3)-J(J+1)] \tag{8.24}$$

$$\Delta\omega_{J,J+2} = (4J+6)\frac{B_0}{\hbar} \tag{8.25}$$

$$\Delta\omega_{J,J+2} = (4J+6)\frac{\omega_1}{2} \tag{8.26}$$

J-states Beating	Beat Period (fs)	
	Deuterium	Hydrogen
0-2	183	92
1-3	110	55
2-4	78	39
3-5	61	31
4-6	50	25
5-7	42	21

Table 8.3: First order beat periods of the J-states ensemble in impulsively aligned deuterium and hydrogen. As deuterium hydride is a heteronuclear molecule, it is expected to have beats between adjacent J-states, $\Delta J=\pm 1$

$$\omega_1 = 4\pi B_0 c \tag{8.27}$$
$$\omega_J = \frac{1}{2} J(J+2)\omega_1 \tag{8.28}$$

In the case of heteronuclear molecules, such as HD, a dipole moment exists naturally. Therefore, ΔJ=$\pm$1 transitions are allowed and consequently the beating of the impulsively aligned HD molecules occurs between adjacent J-states as illustrated in equations 8.29-8.32 and table 8.4.

$$\Delta\omega_{J,J+1} = \frac{(E_{J+1} - E_J)}{\hbar} \tag{8.29}$$
$$\Delta\omega_{J,J+1} = \frac{B_0}{\hbar}[(J+1)(J+2) - J(J+1)] \tag{8.30}$$
$$\Delta\omega_{J,J+1} = (J+1)\frac{2B_0}{\hbar} \tag{8.31}$$
$$\Delta\omega_{J,J+1} = (J+1)\omega_1 \tag{8.32}$$

J-states Beating	Deuterium hydride Beat Periods (fs)
0-1	366
1-2	183
2-3	92
3-4	73
4-5	61
5-6	52
6-7	46

Table 8.4: First order beat periods of the J-states ensemble in impulsively aligned deuterium hydride.

As well as the nuclear spin statistics, the initial J-state populations must be considered, as it is these populations which govern the weightings of the individual beats and the subsequent shape of the wavepacket motion. A good estimation of these populations can be obtained from the Boltzmann distribution, equation 8.33, where N_J and N_0 are the number of molecules in a general J-state and the J=0 state respectively, and k and T are the Boltzmann constant and the temperature.

The degeneracy of the J-states also effects the populations, with 2J+1 degenerate states existing for each J level. This is incorporated in the calculation (equation 8.34) of the J-state populations, J_{pop}, and leads to the most populated J-state being greater than zero. The spin statistics may also be included by inputting g_{nuc} values that correspond to the

relevant weightings from nuclear spin considerations.

$$\frac{N_J}{N_0} = \exp\left[-\frac{E_J}{k_B T}\right] = \exp\left[-\frac{B_0 J(J+1)}{k_B T}\right] \tag{8.33}$$

$$J_{pop} \propto g_{nuc}(2J+1)\exp\left[-\frac{E_J}{k_B T}\right] \tag{8.34}$$

The results of such calculations are shown in figure 8.6 both without (a) and with (b), the inclusion of the effects of nuclear spin statistics. For higher B_0 values, lower J-states contain significant populations. All these calculations were conducted at 300 K. Reducing the temperature would reduce the number of populated states, whilst raising the ambient temperature would increase them. Meaning less or more states would be present in any superposition of rotational states excited by an aligning pulse.

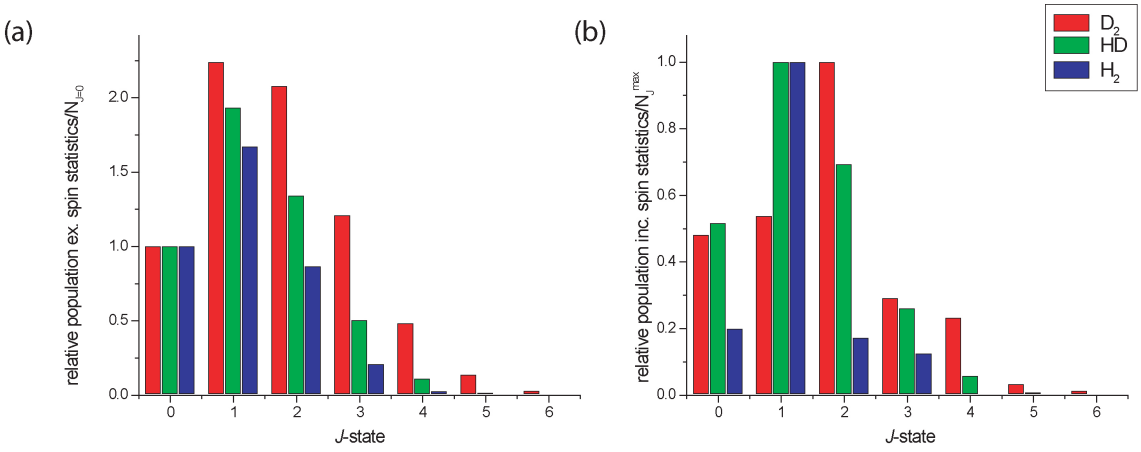

Figure 8.6: J-state populations for D_2, HD and H_2 at 300 K. Panel (a) shows the situation neglecting nuclear spin statistics, whereas (b) has the effects of the spin statistics, g_{nuc}, included. In the first instance, the populations are relative to the J=0 state, whereas in the latter they are normalised to the highest populated level.

8.4 Experimental Results

The experiments reported here are similar to those discussed in the vibrational wavepacket chapter, (chapter 7) and the connected publications [Bryan et al., 2007b] and [Mckenna et al., 2007]. The dynamics are initiated by a pump pulse and are imaged by a second probe pulse. Most of the analysis has been done on the work with deuterium, as this is the slowest (has the highest inertia) of the three molecules investigated, and subsequently is the system imaged with most clarity.

8.4.1 Experimental Details

The laser system used is as described in chapter 2 of this thesis and the experiments were conducted in TA1 of the Astra laser system. Using a Mach-Zehnder interferometer and a half wave plate, as discussed in section 3.3.2, alongside the hollow fibre chirped mirror compressor to produce collinear trains of pump and probe laser pulses. The intensity of these were of the order of 2×10^{14} Wcm^{-2} and the pulse duration, measured on a second harmonic intensity autocorrelator, was 12 fs per pulse for both pulse trains.

In the majority of the experiments, the polarisations of the two pulses are crossed with the pump pulse's polarisation set perpendicular to the detector's time-of-flight axis and the probe's fixed parallel. In the experiments to determine the angular dependence of the rotational wavepacket, the pump polarisation is rotated mapping out a series of alignment angles, θ. In all instances the first (pump) pulse is thought to create the rotational wavepacket and the second (probe) pulse is used to image the resulting dynamics. Between the two pulses the system is free to evolve naturaly.

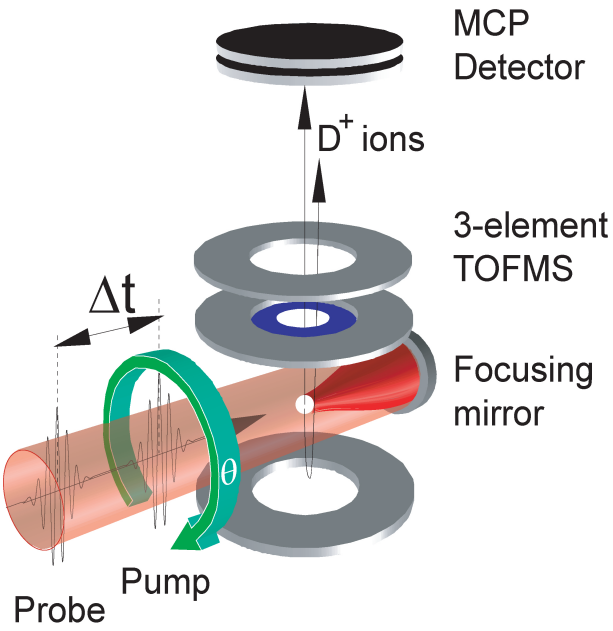

Figure 8.7: Experimental setup for studying rotational dynamics. The delay, Δt, between the pump (first) and probe (second) pulses is controlled with 1/3 fs resolution and the polarisation of the pump pulse can be varied using a half wave plate. The tight angular acceptance of the detector avoids spatial integration washing out the rotational dynamics. Figure reproduced from [Bryan et al., 2007a].

The detector used in the study, is shown in schematic in figure 8.7 and was described in detail in chapter 2 of this thesis. Before allowing the pulse trains to enter the detector, the system is filled with deuterium (hydrogen or deuterium hydride) gas to a pressure

of 2×10^{-7} mbar. The pulses are then allowed to enter the detector and are focussed using a f/5 broadband mirror. The unfocussed pulses pass through the interaction region before reaching the mirror, however, as their intensity ($\approx1\times10^{9}$ Wcm^{-2}) is many orders of magnitude lower than the focussed pulses, this interaction is neglected.

Typically, the rotational dynamics are seen clearest in the high energy (5-7 eV) Coulomb Explosion (CE), as this process is particularly strong along the bond axis. This energy range is also favoured, as the detector angular acceptance improves with energy. For example $\alpha\approx4^{o}$ for a 1e V deuteron compared to $\alpha\approx2^{o}$ for a 5.5 eV deuteron. Also, only forward ions are taken into account when comparing the experimental results to theory. This is due to higher signal strengths resulting in an improved signal to noise ratio when compared to the ion signal observed from the backward ions. As mentioned previously, the detector also contains a quarter of a millimetre aperture, so that only a *slice* of the focal volume is imaged by the spectrometer. This restricted acceptance avoids spatial averaging over the focus and reduces the range of intensities viewed. All of which improves resolution and adds to the clarity of the images obtained.

In order to build up a picture of how the dynamics change with evolution time, the delay between the two pulse trains is changed in 1fs steps, with time-of-flight spectra taken at each step, acting as *snap-shots* of the dynamics at a given instant. Combining these spectra then presents a full *picture* of the nuclear dynamics. Zero delay or evolution time corresponds to the situation where both pulses arrive at the interaction region of the spectrometer simultaneously, whereas a finite delay time corresponds to the pump pulse arriving at a delay time of zero and the probe following at a given time later on.

8.4.2 Deuterium

Figure 8.8 shows the time-resolved rotational dynamics in deuterium. In this instance the pump polarisation is set perpendicular to the probe and time-of-flight axis, which are both parallel to one another. Panel (a) is a plot of the integrated Coulomb explosion signal (black squares) against evolution time alongside the theoretical prediction (red curve). At first glance, the trace appears inverted when compared to figure 8.3. However, in this instance, the aligning pulse is perpendicular to the detection axis and imaging pulse. Therefore, troughs in the data correspond to alignment parallel to the pump, which corresponds to alignment perpendicular to the time-of-flight axis. Likewise peaks correlate to anti-alignment to the initial pulse and alignment along the time-of-flight axis.

Revivals of the wavepacket are observed at 560 fs (full revival) and 280 fs (half revival), as predicted.

The quantum revivals of the system are clearly observed in the raw data, but with additional smoothing (an 11-point adjacent averaging process) even the fractional revivals

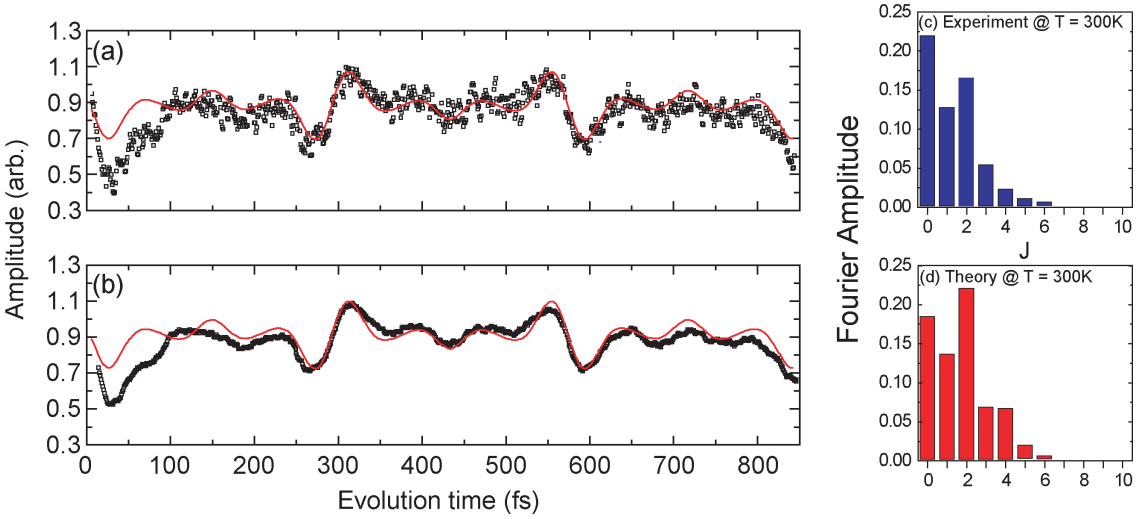

Figure 8.8: Impulsive alignment of D_2. Panel (a) shows the integrated Coulomb explosion yield (black points) as a function of pump probe delay (evolution time) alongside the theoretical prediction (red curve). Panel (b) is a reproduction of (a), but with an 11-point smoothing to the raw data (black curve), whereas panels (c) and (d), show the results of a FFT of both the theoretical (c) and the experimental data (d). The J-state designations are obtained from the lowest level in each of the dominant beats. I.e. the column J=0 corresponds to the amplitude of the beat between the levels J=2 and J=0. Figure adapted from [Bryan et al., 2007a]. Note the pump pulse polarisation is set perpendicular to the probe pulse, which is fixed parallel to the time-of-flight axis of the detector.

present in the prediction can be extracted from the experimental results; illustrated in panel (b). The deviation of experiment and theory at small evolution times occurs due to the interference between the pump and probe pulses when they overlap. Generally, this leads to a single multi-peaked pulse of mixed polarisation, with one or a mixture of elliptical, linear and circular polarisation.

Panels (c) and (d) of figure 8.8 show Fast Fourier Transforms (FFTs) of the curves displayed in panel (b). The experimental plot is not strictly a direct measure of the distribution of the J-state populations, but rather a measure of the J-states, ΔJ=2, beating in the superposition of states. However, it still offers a very good comparison, as this process is considerably more likely than any higher order transitions. As one would expect from panel (b), the two plots (panels (c) and (d)) are very similar to one another, and do not deviate much from those calculated in figure 8.6 with clear indication of the system's dependency upon the nuclear spin statistics discussed previously.

The angular dependence of deuterium's rotational dynamics has also been investigated, the results of which are summarised in figure 8.9. Experimentally, this is achieved by rotating the polarisation of the pump or aligning pulse while keeping the polarisation of the probe or imaging pulse fixed. To reduce the experimental observation time, only the

region about the wavepacket's half revival was selected for investigation and results were only taken for angles between θ=0 to θ=$\pi/2$ (with the remainder of those displayed in figure 8.9 (b) being achieved by repeated reflection of this data set).

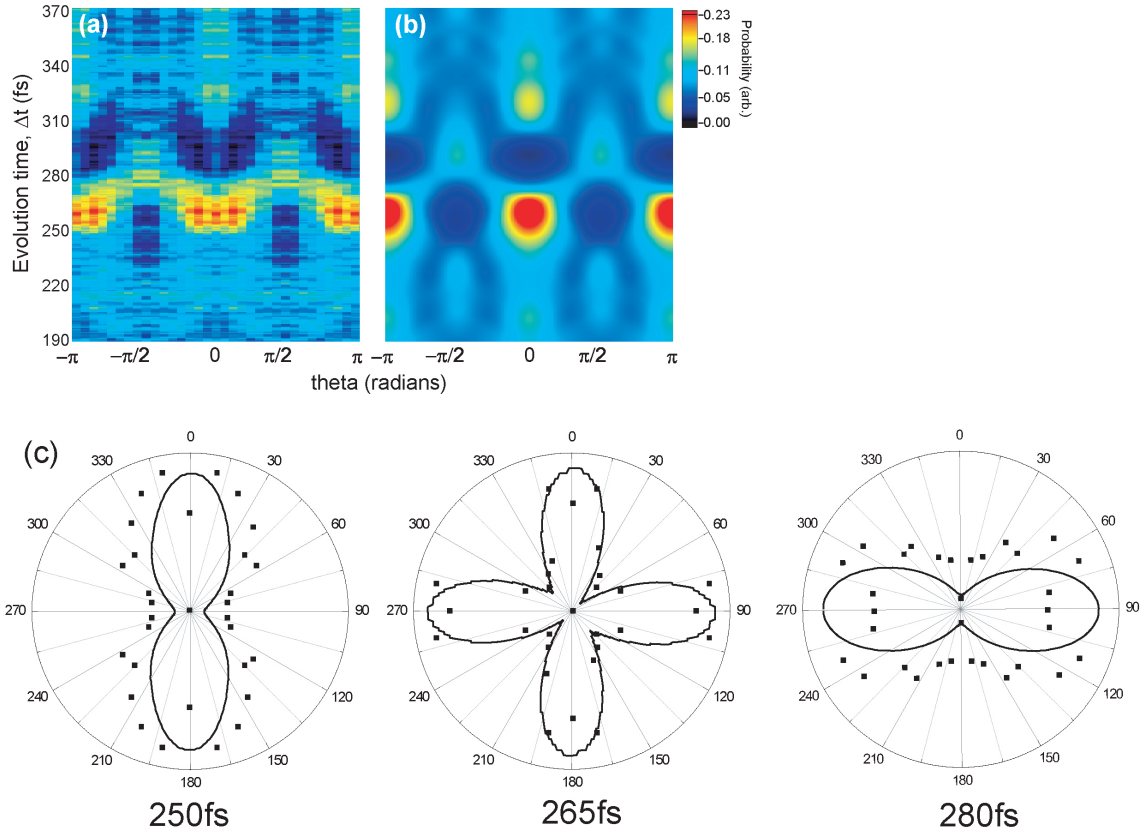

Figure 8.9: The angular dependence of the impulsive alignment of D_2. Panel (a) experiment and (b) theory show the so called *quantum carpet* around the half revival $\approx$ 270 fs. Panel (c) shows three cuts through the carpets displayed as polar plots, with the experimental data shown as black points and the theory as a black curve. Panels (a) and (b) are adapted from [Bryan et al., 2007a] and panel (c) from [English et al., 2006].

In figure 8.9(a) and (b) the alignment of the sample is displayed as a function of evolution time and polarisation angle. Red colours correspond to regions of strong alignment, and darker ones to anti-alignment. The agreement between experiment and theory is good, a fact further expressed in panel (c), within which cuts through panels (a) and (b) are presented. One interesting fact illustrated by the *quantum carpets* and polar plots is that the alignment does not go straight from maximal alignment to that of a random ensemble, but through states of intermediate and individually distinct alignment. This is illustrated more clearly in experiments on CS_2 reported by Torres et al [Torres et al., 2005], but also can be seen in the cross-shaped alignment observed in the central of the three polar plots.

One of the initial stumbling blocks in the analysis of the rotational dynamics was the

origin of the rotational signal. Was it from the D_2^+ population created by ionisation in the pump pulse or from D_2 molecules un-ionised by the first pulse, but which had been rotationaly excited?

As ionisation leads to an increase in the internuclear separation and a corresponding reduction in the rotational constant (see table 8.1), the time evolution of the $\cos^2(\theta)$ parameter would differ significantly between samples of D_2 and D_2^+. The difference however, is more apparent in the frequency domain. This is illustrated in figure 8.10.

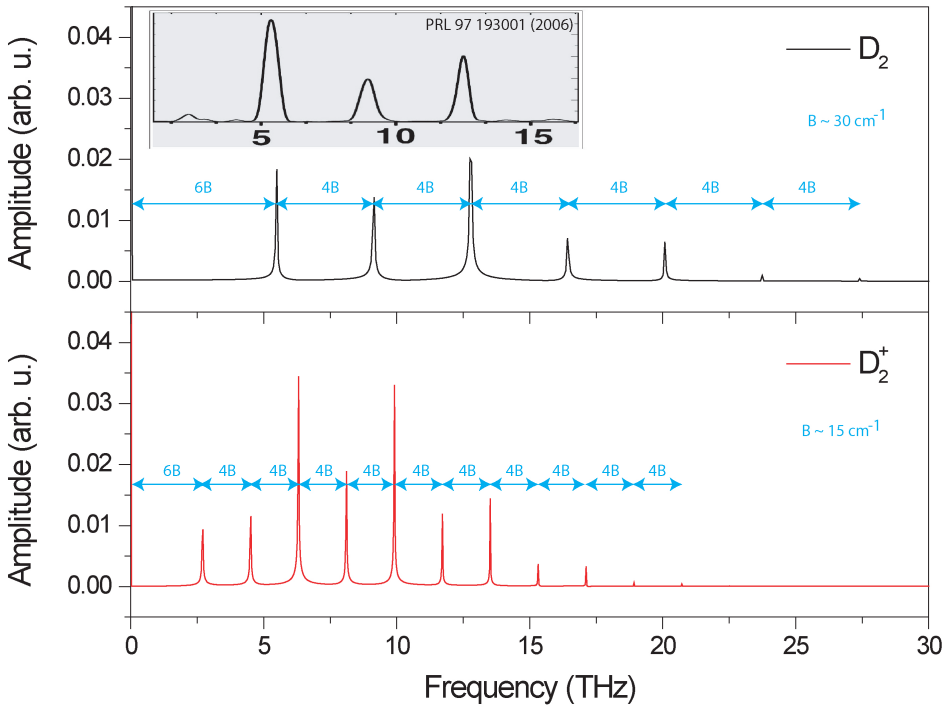

Figure 8.10: FFT of simulated D_2 and D_2^+ rotational wavepackets. Our study shows the rotaional dynamics observed are present only in the neutral, whereas Ergler et al [Ergler et al., 2006b], allthough observing the same spectrum (gray panel inset in the upper left of the figure), designated them to D_2^+ motion.

When expressed in terms of frequency the FFTs obtained from $\cos^2(\theta)$ versus evolution time plots can be used to extract the rotational constant of the system. This is fairly simple as the peaks in the FFTs differ in frequency in a manner described by equation 8.25. Consequently the first peak occurs at $6B_0$, with following peaks spaced by a further $4B_0$. Thus by measuring the peak separation the value of B_0 can be found. In our case the evidence was categorical in favour of the rotation being present in the neutral population only (hybrid systems were also analysed).

This point of view is now generally accepted [Bryan et al., 2007a, Bocharova et al., 2008], and private communication with the authors of [Ergler et al., 2006b] as the ionised population is thought to span too many vibrational levels for any rotational excitation to be

coherent. On the other hand, the neutral population can be considered to lie predominantly in the v=0 state. Initially, Ergler et al [Ergler et al., 2006b] had suggested that the rotational dynamics observed were in the ion. However, after discussion, they are now in agreement that the rotational signatures observed in both experiments are the results of a rotational wavepacket in the deuterium molecule.

The major results from this analysis were published in [Bryan et al., 2007a], as well the Central Laser Facility's Annual Review [McKenna et al., 2006, English et al., 2006].

8.4.3 Hydrogen

As well as experiments on deuterium, the hydrogen system was also investigated. As hydrogen is significantly lighter than deuterium, its resulting motion is faster, which effectively makes the laser pulses employed in the study longer. This results in a loss of clarity in the experimental images, and consequently the results of this study are not as clear as those obtained on the deuterium system. Correspondingly any conclusions made upon them cannot be made with the same degree of confidence.

A further fact inhibiting this study is the high rotational constant of hydrogen, which at ≈60 cm^{-1} leads to only a few J-states being populated at room temperature. Subsequently, any superposition of states that might be initiated by an aligning pulse could only comprise a few beating states, see figure 8.6 and Bocharova et al [Bocharova et al., 2008].

Figure 8.11 shows the results of the tests on hydrogen. Panel (a) is a false colour representation of the raw time-of-flight data with proton energy displayed against wavepacket evolution time, whilst panel (b) is the integrated Coulomb explosion signal chosen to best illustrate the rotation dynamics. The natural rotation period is illustrated.

Comparing these results to those of [Bocharova et al., 2008], the spacing of the peaks and troughs observed is similar (≈115 fs). Also, the comparison between the resolution achieved by Bocharova's deuterium and hydrogen studies and figures 8.11 and 8.9 is similar, even though, in the former instance, 8 fs pulses were used alongside COLTRIMS detection.

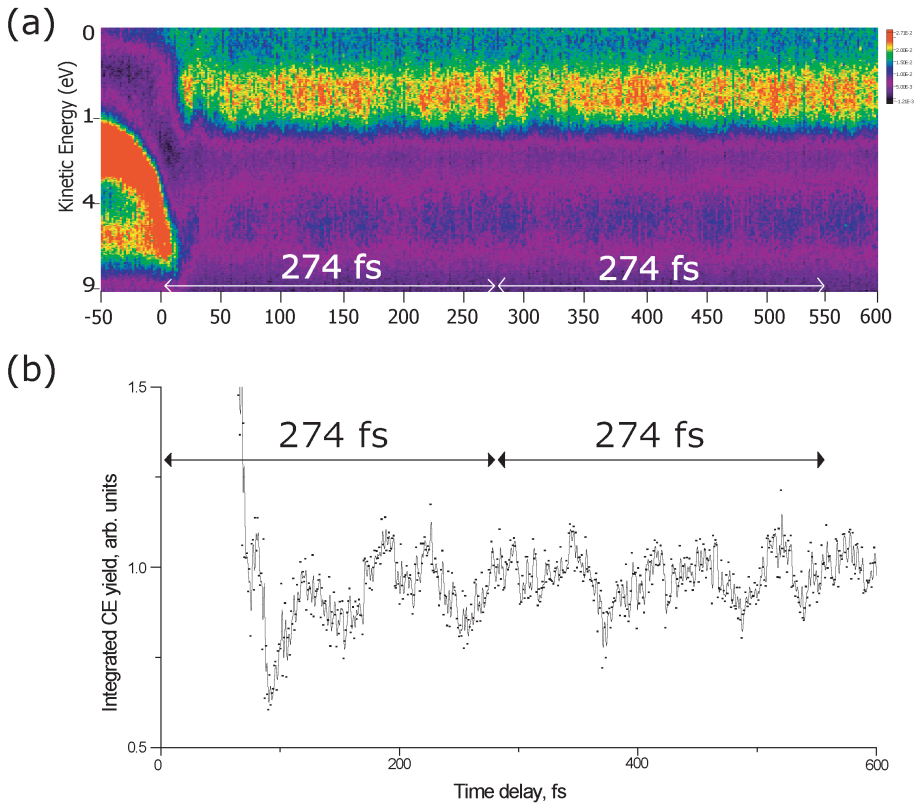

Figure 8.11: Rotational wavepackets in H_2. Panel (a) shows the raw experimental data with both the PD and CE channels clearly shown. As well as vibrational features, peaks and troughs due to H_2 rotational motion can be seen. Also indicated in the figure is the fundamental period of H_2. Panel (b), the integrated CE signal shows these features more clearly.

8.4.4 Deuterium Hydride

The last of the accessible isotopes of the family of hydrogen molecules was also studied. Like the hydrogen results, the results achieved can only be considered as preliminary, but distinct rotational structures were observed, as illustrated in figure 8.12.

The rotational signatures of the molecule can be seen as a series of distinct peaks in the ion yield (a) and integrated Coulomb explosion signal (b). The most distinct of which are the peak around 200 fs, the dip about 400 fs and the peak about 600 fs. These features are displaced somewhat from those predicted at 180 fs, 365 fs and 548 fs. However, the predicted values are those for onset of the features, rather than the position of their respective peaks (or troughs); subsequently, the mismatch is less than one might assume.

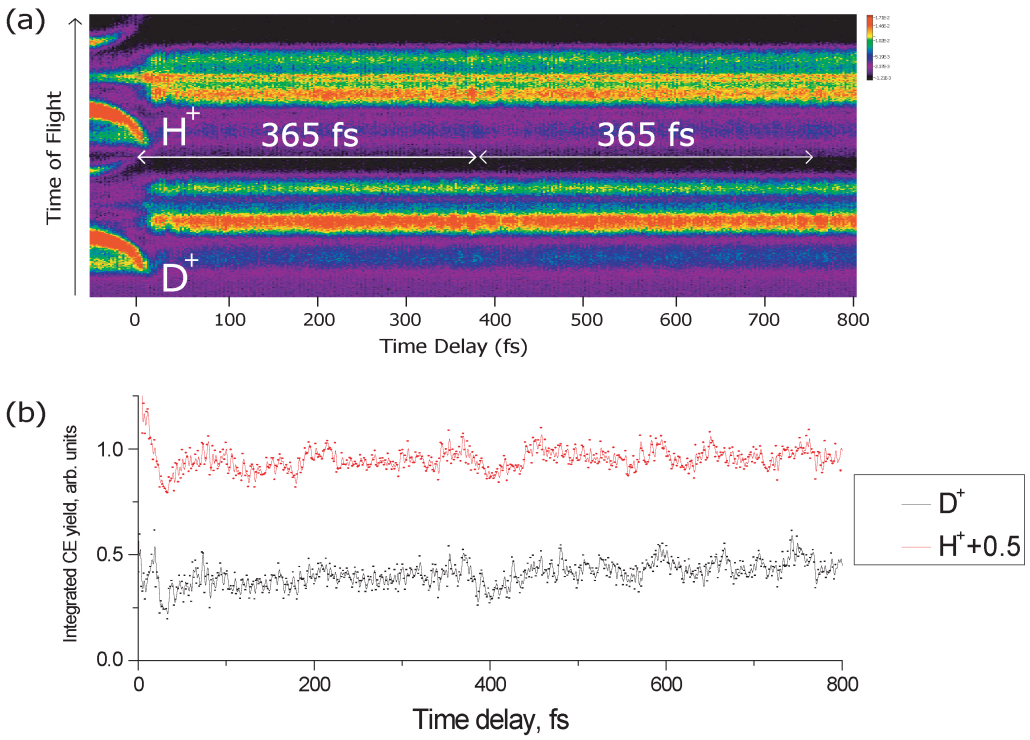

Figure 8.12: Rotational wavepackets in HD. Panel (a) shows the raw experimental data with both the PD and CE channels clearly shown. As the H^+ and D^+ ions are separated in the detector, two bands of peaks are observed. Like before, vibrational features are observed alongside the peaks and troughs, due to HD rotational motion. The fundamental period of HD rotation is also shown, alongside the data, to help isolate the repeating nature of the wavepacket's dynamics. Again, panel (b) shows the integrated CE signal, within which the rotational features can be more clearly observed.

8.4.5 Contemporary Studies

Prior to our publication on the impulsive alignment of D_2, only one peer review paper had been published on the topic, that of Lee et al [Lee et al., 2006]. In this study, 10 fs pump and probe pulses were used to first create (pump) and then image (probe) rotational wavepacket dynamics in neutral deuterium. The two sets of pulses where created using a core and annulus mirror method, which offered reduced time-delay control as compared to the Mach-Zehnder method utilised here. Also, the experimental results in this original paper are far fewer in number and subsequently have a larger separation between one another meaning that poor resolution of the smaller fraction revivals was achieved, see figure 8.13. The time evolution of the wavepacket motion was only followed until soon after the first half revival of the system, 350 fs.

Following the publication of our paper, Bocharova et al, published their paper [Bocharova et al., 2008] on impulsive alignment. Like us they employed a Mach-Zehnder

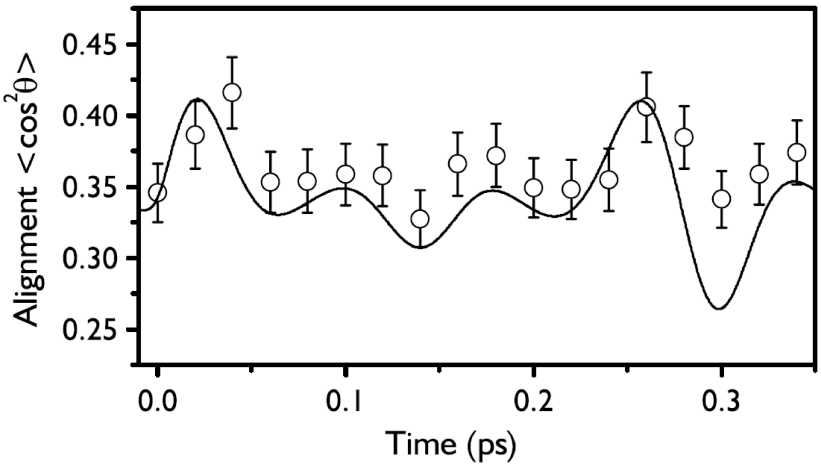

Figure 8.13: The impulsive alignment of D_2 as reported by Lee at al [Lee et al., 2006]. In this instance both the pump and probe pulses are parallel to the time-of-flight axis of the detector. The laser pulses used both have a duration of 10 fs and have intensities of 2×10^{14} Wcm^{-2} (pump) and 1×10^{15} Wcm^{-2} (probe), respectively. The smooth curve is the result of a numerical simulation and the data points, 20fs apart, are extracted from the experiment. Figure reproduced from [Lee et al., 2006]

interferometric method, but with the added advantage of COLTRIMS detector technology, rather than a simple time-of-flight detector employed here, and by Lee [Lee et al., 2006]. As mentioned earlier their experimental results, see figure 8.14, are consistent with those presented here.

In figure 8.14 results are shown for experiments with hydrogen, panels (a) and (c), and deuterium, panels (b) and (d). In both instances the laser pulses employed have the same pulse duration and peak intensity. As in the experiments reported here, the clarity of Bocharova et al's results on the deuterium system are clearer than their hydrogen results. In both instances the J-state populations involved in the beating waepacket where extracted, allowing the authors to show the underlying spin statistics of the two molecules.

8.5 Summary

In this chapter the impulsive alignment of deuterium has been fully characterised with both the time- and the angular- evolution of the rotational wavepacket dynamics being mapped out. Samples of hydrogen and deuterium hydride have also been investigated to

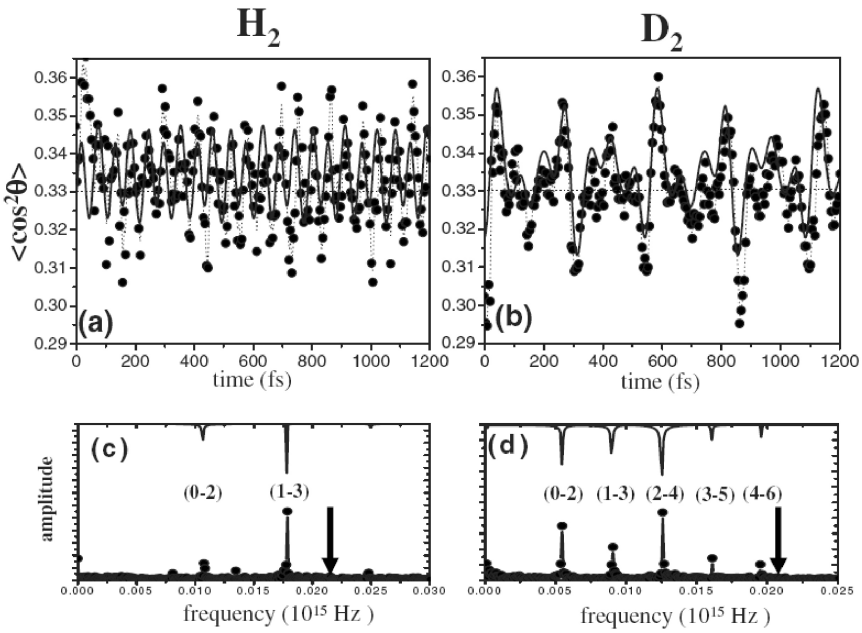

Figure 8.14: The impulsive alignment of H_2 (panel (a)) and D_2 (panel (b)) as reported by Bocharova at al. The measured results are shown as data points, and the theoretical prediction as the bold line. FFTs are also shown with panel (c) corresponding to H_2 and panel (d) to D_2. In the FFTs the experimental results are indicated by black circles and the theoretical by a black curve. The band width of the 8 fs aligning pulses is also indicated by a vertical arrow on each FFT plot. The laser pulses used in the experiment where 8 fs in duration and had intensities of 1×10^{14} Wcm^{-2}. Both the pump and probe pulses are parallel to the time-of-flight axis of the detector. In the simulations 10 fs, laser pulses were used and the initial temperature of the H_2 was considered to be 295 K and the D_2 sample 250 K, respectively. Figure reproduced from [Bocharova et al., 2008].

a lesser extent but preliminary findings suggest that these tests are consistent with the deuterium study and those of others published recently.

Chapter 9

Future Outlook

9.1 Introduction

In this thesis experimental results have been presented covering rotational and vibrational wavepacket dynamics in hydrogen molecular systems, multi electron tunnelling ionisation in atomic systems and recombination in metastable ions. In many instances the work has been, in some sense at least, pioneering and resulted in high profile publications in well respected peer reviewed journals.

As well as providing some insight into the physics of dilute media exposed to intense ultrafast laser pulses, this thesis leads one to consider the next generation of experiments that could be conducted in order to build on the foundations of this work and the exciting possibilities that might bring.

The possible continuations of this study can be split into three groups. The first concerns laser technology; the second detector technology and the third experimental techniques. Some of the possible extensions to the study will be briefly discussed below.

9.2 Laser Technology

One way in which this study could be enhanced would be to work with either shorter or more intense laser pulses. Our group has worked hard and has been fortunate to build a strong working relationship with the staff at the Central Laser Facility (CLF), which allows us the chance of using the world class facilities on offer there. Presently, this is particularly exciting as the facility is on the verge of two major upgrades coming on-line, for more details see
http://www.uknow.or.jp/be/science/events/HighEnergyDensity/John_Collier.pdf.

The first, Astra Gemini, will provide experimentalists with two laser beams each offering 0.5 PW beams capable of being focussed to a peak intensity of the order of 10^{22} Wcm^{-2}.

The second, Astra Artemis, will offer more new beam-lines and end-stations. The main laser will generate Carrier Envelope Phase (CEP) stabilised high power laser pulses 30 fs in duration at a central wavelength of 780 nm. Two repetition rates will be available (pulses with 14 mJ/pulse at 1kHz or 3.5 mJ/pulse at 3 kHz). The output energy of the main laser can then be split into one of the three available beam lines:

1. 1 mJ can be further compressed to 10fs, 0.5mJ/pulse.
2. 8 mJ can be used to pump an Infra Red (IR) Optical Parametric Amplification (OPA) system providing tune-able 40 fs pulses in the spectral range of 1.18 μm-15 μm with an output of up to 1.5 mJ/pulse.
3. The remaining energy can be used as synchronized pump-probe pulses.

A High Harmonic Generation (HHG) chamber with a kHz gas-jet and an eXtreme Ultra Violet (XUV) flat-field spectrometer (10 nm-40 nm spectral region) will be available alongside a monochromator to select a single XUV harmonic in the spectral range 10 eV-100 eV. Space for visiting end-stations (for example the TOFMS and ion beam apparatus employed in this study) will also be available.

At Artemis, experiments into attosecond physics could be conducted utilising the enhanced timing resolution availiable. This could offfer the opportunity for experimentalists, to directly image both electric fields [Goulielmakis et al., 2004] and bound electron dynamics [Drescher et al., 2002, Fohlisch et al., 2005]. While Gemini opens up the chance of studying the physics of systems exposed to even more extreme conditions, such as the production of monochromatic electron beams [Mangles et al., 2004] and HHG in the relativistic regime [Dromey et al., 2006].

9.3 Detector Technology

The Time of Flight Mass Spectrometer (TOFMS) used in this thesis is a compact device that offers good experimental resolution while being portable and hardwearing. However, the device does not record any of the information held within the electrons. This results in an incomplete picture of the interaction. A transfer towards a COLd Target Recoil Ion Momentum Spectroscopy (COLTRIMS)[Ullrich, 2004] style approach would lead to more kinematically complete experiments providing a more complete picture of the laser matter interaction. This increase in sophistication, however, would lead to more complicated procedures in the laboratory making the experiments more labour intensive. As an

interim measure, an electron time-of-flight spectrometer could be used alongside the existing TOFMS in order to access the information stored in the electron population. Such a device could either be constructed along the lines of a magnetic bottle spectrometer, such as that utilised in the study of Gibson et al [Gibson, 2004] or bought commercially.

Finally, approaches to observe the photons emitted from the laser matter interaction could be imaged with a device such as a flat field spectrometer. This approach would be particularly useful alongside HHG experiments (for an example, see the study by Baker et al [Baker et al., 2006] in which such techniques were used to image small hydrocarbon molecules).

9.4 Experimental Techniques

The final way in which these experiments can be enhanced would be to build on the existing methods. This approach requires least investment in equipment and consequently the time scale for implementation would be considerably shorter.

9.4.1 Recombination and Ion Beam Experiments

The most obvious way of enhancing the ion beam studies would be the development of a deconvolution method akin to that used in the TOFMS experiments [Bryan et al., 2006b]. As shown in the METI chapter of this thesis, this enables a more precise comparison of experiment and theory and would be useful in the recombination work.

A second extension to this work would be to study ions that are not so readily obtained from a neutral apparatus such as the TOFMS. For instance, a study could be conducted on open shell atomic ions such as, C^+,N^+ and O^+, thus enabling the study of how the addition of each valence electron affects the physics of the interaction of the atomic core with a laser field.

9.4.2 Multi Electron Tunnelling Ionisation (METI)

The METI work presented in this thesis was conducted with 50 fs laser pulses. The theory provided by Kornev at al [Kornev et al., 2003] also used 50 fs laser pulses, however, results for 5 fs pulses were also published, see figure 9.1. Hence a natural extension of our experiments would be to test these predictions. The study could also be extended to cover the remaining noble gas atoms and hopefully answer the questions raised about helium and neon in Kornev et al's second METI publication [Kornev et al., 2004].

The pump-probe technique used previously in the molecular studies could also be used

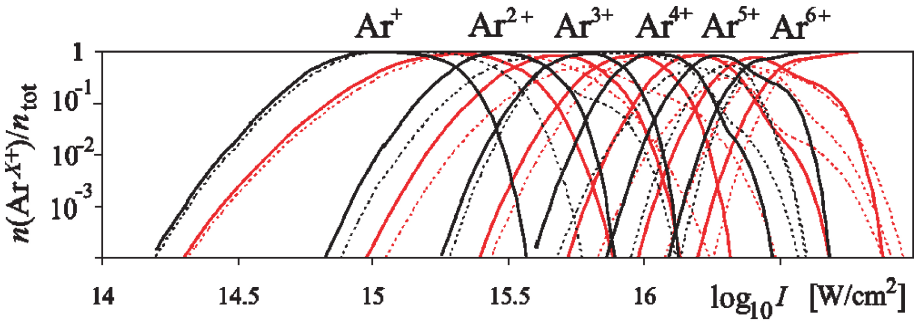

Figure 9.1: Concentration of multiply charged argon ions n(Ar^{X+}) up to X=6. Calculations are shown for both METI (bold curves) and ADK (dashed curves) predictions using circularly polarised laser pulses of 5 fs (red) and 50 fs (black) in duration. With the shorter pulse length the charge states move to higher intensity but the subtle effects of METI are still expected to be observable. Adapted from [Kornev et al., 2003].

here in order to time-resolve the excitation process. In experiments similar to those used to assess the at-focus pulse duration with xenon, Intensity Selective Scanning (ISS) experiments could be run at different delay steps and the states involved in the *shake-up* excitation process hopefully resolved.

9.4.3 Vibrational Wavepacket Dynamics

An extension to the vibrational wavepacket work would be the introduction of a control pulse. As before the wavepacket dynamics would be initiated by a pump pulse. This would be followed by a control laser pulse used to manipulate the evolving system, before the superposition of states is finally measured by a probe pulse. Such experiments have already been discussed [Niikura et al., 2003, Niikura et al., 2004, Murphy et al., 2007b] [Niederhausen and Thumm, 2008] however, only a single published experiment on the fastest systems has to date been published [Niikura et al., 2006]. In such schemes the control pulse is typically used to manipulate the v-state population of the wavepacket, either forcing the system into fewer states or a particular desired combination of v-states. Subsequently such ideas tend to evoke quantum control analogues and possible applications to the field of quantum computation [Gollub et al., 2006, Troppmann et al., 2006].

If shorter pulses were used, improved imaging resolutions could be achieved, as the Coulomb Explosion Imaging (CEI) technique used to image the motion would be more accurate. The use of shorter pulses would also open the possibility of studying the vibrational dynamics in the neutral molecule. This has already been done for deuterium where Ergler et al [Ergler et al., 2006a] used 7 fs laser pulses in a pump-probe configuration to image the neutral systems vibrational dynamics.

More massive systems could also be investigated, such as small bio-molecules, using this

time-resolved approach to image the fragmentation dynamics of specific bonds of the system.

Along with the ion beam apparatus a linear ion trap (see section 3.4.7) could be used to control the initial v-state population of the vibrational wavepackets [Orr et al., 2007]. Subsequent pump-probe experiments could then be used to see how this effects the dephasing and revival dynamics of the system.

9.4.4 Rotational Wavepacket Dynamics

Building on the work presented in chapter 8 one of the more fruitful approaches for further study would be to heat or cool the target gas. This would allow the experimenter to control the initial J-state population prior to the impulsive alignment taking place. This would effect the appearance of the rotational wavepacket revival and allow a more direct comparison to the most recently published data of Bocharova et al [Bocharova et al., 2008] to be conducted.

Applications towards Molecular Phase Modulation (MPM) [Zhavoronkov and Korn, 2002] could also be investigated as well as improving the fidelity of the interim data presented on H_2 and HD rotational dynamics.

9.5 Summary

This section has included a brief description of a few possible ways in which the work presented here could be furthered. Improvements in the experimental hardware have been discussed and new experiments suggested. Also possible applications of the work towards the fields of quantum computation and biological systems have been mentioned.

Appendix A

Time lag focussing in time of flight mass spectrometry

Two focussing geometries are described by Wiley and McLaren [Wiley and McLaren, 1955]; space and time-lag focusing. Space focusing is used to minimize peak broadening due to the spatial distribution of ions at the beginning of the time-of-flight measurement. While time-lag focusing enforces an effective time delay between the formation of ions and their (time delayed) extraction from the interaction region of the spectrometer to reduce the impact of the ions initial velocity distribution on the width of the detected peak.

These two regimes are best understood by considering the derivative of the time-of-flight, T, with respect to the ions' average initial position at the start of the time measurement, X_0. Equation A.1 shows the condition for spatial focussing. X_0 is defined by the target gas dynamics and the appropriate potential differences applied to the spectrometers extraction plates and acceleration grid.

$$\frac{dT}{dX_0} = 0 \tag{A.1}$$

In time-lag focussing, ions with velocities directed towards the detector have sufficient time to move to regions of lower potential energy. Conversely, ions travelling away from the detector reach regions of higher electrical potential. Under the optimum conditions, the change in potential energy can be made to compensate for the differences in the initial velocity, v_0.

As the ions travel a distance v_0t in time t the desired focusing conditions can be found (i.e. the situation when the change in flight time due to the delay compensates for the

differences in flight time expected from the various kinetic energies of the target molecules obtained) by ensuring equation A.2 is satisfied.

$$\left(\frac{dT}{dX_0}\right) v_0 t \quad = \quad -\frac{dT}{dv_0} \tag{A.2}$$

In the spectrometer employed here, time-lag focusing is used for the molecular experiments and space-focusing for the atomic work. This is achieved by changing the voltage applied to the acceleration grid of the spectrometer compared to the spectrometers top extraction plate. For time-lag or Wiley McLauren focussing this voltage is larger than that of the top plate. For the spatial geometry, the voltage applied to the acceleration grid is set equal to that of the top plate. Optimum values for these potentials were obtained by past students of the group [Thomas, 1999] and are summarised in tables A.1 and A.2.

Plate	Potential Difference (V)
Bottom Plate	+300
Top Plate	-300
Acceleration Grid	-300

Table A.1: Potential differences applied to the extraction plates and acceleration grid of the TOFMS used for experiments on noble gas targets.

Plate	Potential Difference (V)
Bottom Plate	+20
Top Plate	-20
Acceleration Grid	-60

Table A.2: Potential differences applied to the extraction plates and acceleration grid of the TOFMS used for experiments on hydrogen molecules.

Appendix B

Time of flight to energy Jacobian for the TOFMS

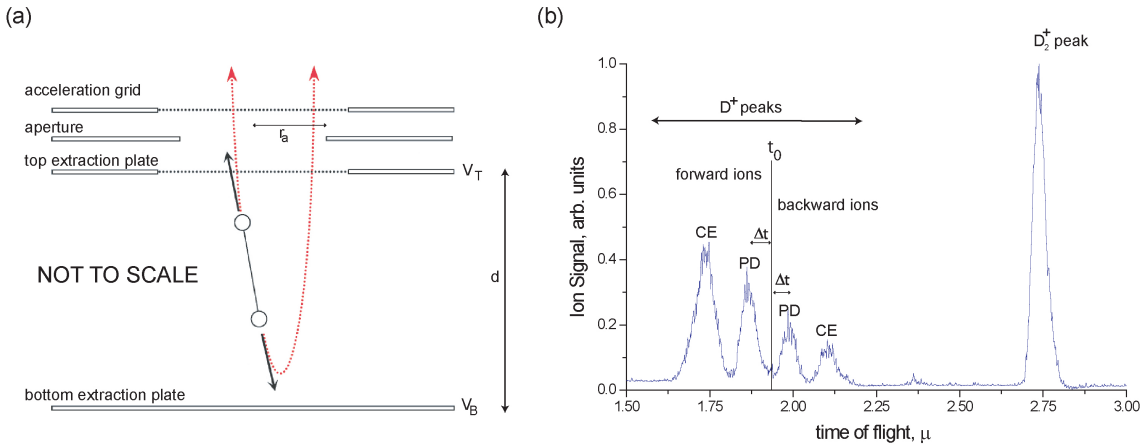

Figure B.1: Panel (a) shows geometry of the TOFMS interaction region. Panel (b) shows a typical time-of-flight spectrum following interaction of a D_2 target with an intense laser pulse

In order to establish the fragmentation energy of an ion resulting from the break-up of a molecular target, the difference in flight time between the forward and backward ion peaks, $2\Delta t$, must be evaluated (Δt = the flight time measured from the zero momentum time of flight, t_0). This difference in flight time occurs due to the backward ion having to be turned round in the extraction field before reaching the drift tube, see figure B.1. As the majority of the flight path for both forward and backward ions is identical, and the backward ions turn around is symmetric, Δt equates to the time required for the ion to be stopped, reach v=0, by the extraction field.

Starting from the force (**F**) on the ion, of mass(m) and charge (q), exerted by the extraction

field (**E**) the ions acceleration (**a**) can be obtained. The extraction field is balanced about the top and bottom plates with the applied volages equal in magnitude but with V_T negative and V_B positive.

$$\mathbf{F} = -q\mathbf{E} = m\mathbf{a} \tag{B.1}$$

$$\mathbf{a} = -\frac{\mathbf{E}q}{m} \tag{B.2}$$

Given the ions final velocity (v) is zero and the classical expression for kinetic energy (T), $T=1/2mu^2$, the ions initial velocity (u) can be obtained.

$$u = \sqrt{\frac{2T}{m}} \tag{B.3}$$

Then using the expression v = u + at and equations B.2 and B.4 an expression for Δt can be obtained.

$$\Delta t = \frac{m}{qE}\sqrt{\frac{2T}{m}} \tag{B.4}$$

This can be re-arranged to obtain an expression for the initial kinteic energy of the ion, as shown below.

$$T = \frac{1}{2m}(qE\Delta t)^2 \tag{B.5}$$

Now fragment energy, T, is not linear w.r.t. Δt and hence the signal, which is binned in equal steps of t, must be scaled accordingly. This is done using the simple kinematic equation, the equation for classical kinetic energy and the Jacobian below, see equations B.6-B.8.

$$u = \frac{d}{t} \tag{B.6}$$

$$t = \frac{1}{2}mu^2 \tag{B.7}$$

$$\int f(t)dt \quad = \quad \int f(T)dt \tag{B.8}$$

Which results in equation B.9 below, where t, is the flight time and d, the length of the TOFMS drift tube. All the other symbols are denied previously. (The Jacobian itself is actually comprised of two steps, with f(t) first being transformed to f(u) before f(T). Also after each step the background of the spectra needs renormalising to a linear base ([Brouillard and McGowan, 1983, Goodworth, 2002]).

$$f(T) \quad = \quad \frac{t^2}{dmu} f(t) \tag{B.9}$$

Appendix C

TOFMS Acceptance Angle

The angular acceptance of the Time of Flight Mass Spectrometer (TOFMS) is dependent upon the potentials applied to the extraction plates, V_B and V_T, the radius of the aperture, r_a, in the top extraction plate and the ion momentum, m**u**. Below is a simple treatment used to establish the acceptance angle of the TOFMS. In this instance the ion in question is considered to lie in the centre of the interaction region, between the two extraction plates, with an initial energy, T velocity **u** and an angle of incidence, α, defined with respect to the time-of-flight axis.

The ions are extracted by the electrostatic force, **F** exerted by the potential difference generated by the voltages on the extraction plates. Equating this to include the ions mass, using Newton's 2^{nd} law of motion, an expression for the acceleration experienced by the ion can be obtained, equation C.3.

$$\mathbf{F} = q\mathbf{E} = m\mathbf{a} \tag{C.1}$$

$$\mathbf{E} = \frac{V}{\mathbf{d}} = \frac{V_B - V_T}{\mathbf{d}} \tag{C.2}$$

$$\mathbf{a} = \frac{q}{m}\frac{(V_B - V_T)}{\mathbf{d}} \tag{C.3}$$

Now there is no force on the ions in the x-direction as the electric field is homogenous along this axis, hence it is comparably simple to breakdown the vector acceleration into its two orthogonal components, a_x and a_y.

$$a_x = 0 \tag{C.4}$$

$$a_y = \frac{q\mathbf{E}}{m} \tag{C.5}$$

Now in order to establish the ions' initial velocity, u, the classical expression for kinetic energy, T, is utilised.

$$T = \frac{1}{2}mu^2 \tag{C.6}$$

$$u = \sqrt{\frac{2T}{m}} \tag{C.7}$$

The magnitude of the total initial velocity can then be split into its components, using the ions' angle of incidence, α.

$$\mathbf{u} = \mathbf{u}\cos(\alpha) + \mathbf{u}\sin(\alpha) \tag{C.8}$$

$$\mathbf{u} = u_x\mathbf{i} + u_y\mathbf{j} \tag{C.9}$$

Now the ion only experiences an acceleration (feels a force) parallel to the y-axis, therefore the final velocity in the x-direction remains constant. The final velocity in the y-direction is obtained using one of the equations of motion for constant acceleration,
$v^2 = u^2+2as$, where s is the half the distance between the extraction plates, d.

$$v_x = u_x \tag{C.10}$$

$$v_y = \sqrt{u_y^2 + 2as} \tag{C.11}$$

Knowing this the time the ion takes to cross the radius of the aperture, $t^{(x)}$, in the top plate can be calculated; as well as the time for the ion to travel from the centre of the extraction region to the aperture, $t^{(y)}$. (Obtained using two other equations for constant acceleration, v = u+at and s = ut $+1/2at^2$)

$$t^{(x)} = \frac{r_a}{u_x} \tag{C.12}$$

$$t^{(y)} = \frac{(v_y - u_y)}{a} \tag{C.13}$$

Now for the ion to reach the detector $t^{(y)}$ must be smaller than $t^{(x)}$. Using these equations and the mass and charge of a deuteron ion, the energy dependence of the maximum acceptances angle (for forward ions) of the spectrometer has been plotted, see figure C.1.

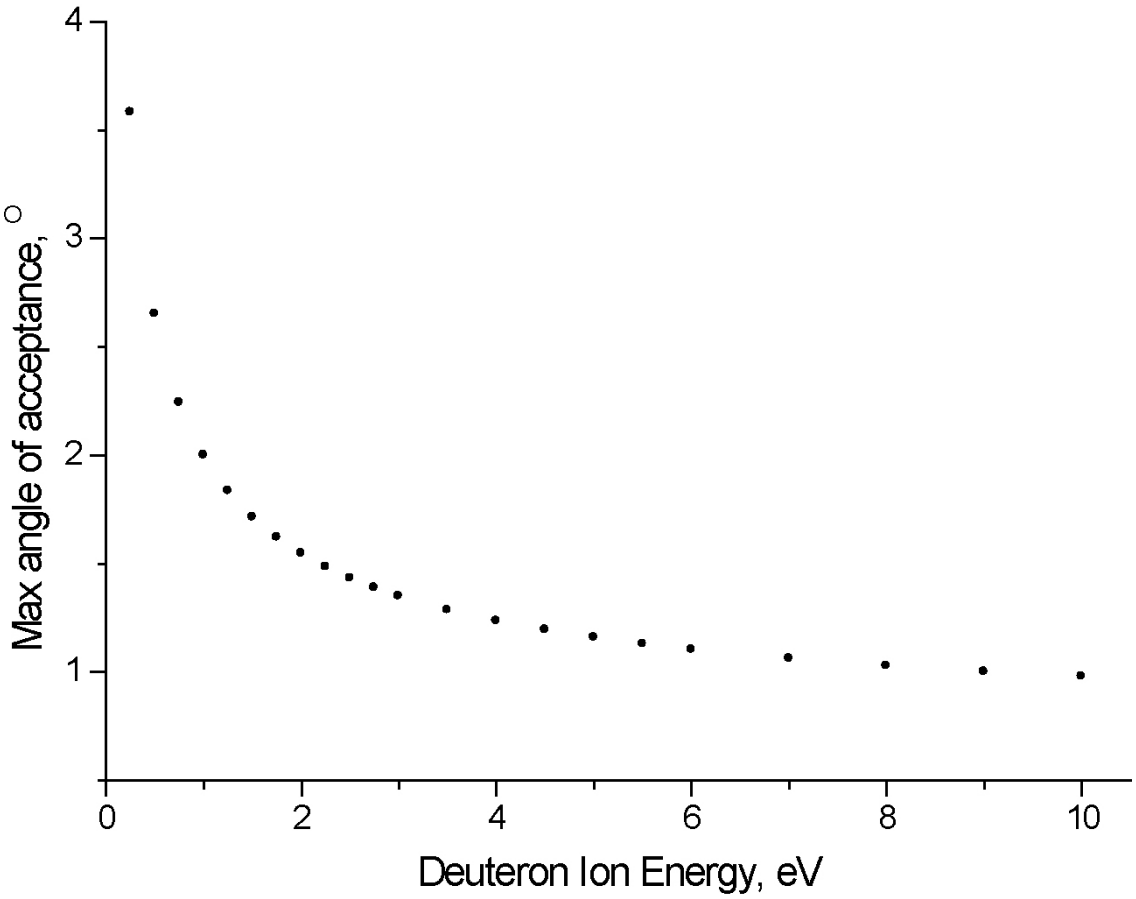

Figure C.1: The acceptance angle for deuteron ions in the time of flight mass spectrometer employed in this study.

Appendix D

Time of flight to energy Jacobian for the Ion Beam

As is the case with the TOFMS apparatus, time of flight must be converted into energy in order to fully analyse the resulting fragments detected from the ion laser interaction in the ion beam experiments. However, this is more complex as the ions cannot be considered as stationary upon interaction with the laser in the lab frame. Subsequently the fragmentation energy is first established in the lab frame, within which the measurements are conducted and then transferred into the desired inertial (or centre of mass) frame.

A further complication is that two separate approaches are required. One for the neutral channel, and a second for the charged ion channel. A very brief outline of the time-of-flight to energy conversion is shown here, for more details see [Goodworth, 2002] for the neutral channel and [McKenna, 2000] for the charged channel.

The energy of the beam, T, can be found in terms of the target ions mass, m, the zero momentum time-of-flight, t_0, and the distance from the interaction region to the neutral channel detector, d, as shown in equation D.1. Jacobians, $J_{v,E}$ and $J_{t,v}$, equivalent to those used in the analysis of the TOFMS spectra can then be used, see appendix B, to show the energy dependence with the time of flight spectra explicitly.

$$T = \frac{1}{2}m\left(\frac{d}{t_0}\right)^2 \tag{D.1}$$

$$f(E) = J_{v,E}J_{t,v}f(t) \tag{D.2}$$

Working these Jacobians through and making the appropriate transformations between the lab frame and the target frame, expressions for the forward ions (equation D.3) and

the backward ions (equation D.4) in the neutral channel can be obtained.

$$\Delta E_f = \frac{\mu}{m}\Delta E_{CM} + \sqrt{2\mu V_B^2 \Delta E_{CM}} \quad \text{(D.3)}$$

$$\Delta E_b = \frac{\mu}{m}\Delta E_{CM} - \sqrt{2\mu V_B^2 \Delta E_{CM}} \quad \text{(D.4)}$$

Where ΔE_f and ΔE_b are the differences in energy from the zero momentum time-of-flight energy, $E(t_0)$, in the lab frame for the forward and backward ions respectfully. μ is the reduced mass of the target ion and V_B is the initial beam velocity.

Solving equations D.3 and D.4 for ΔE_{CM}, the energy difference in the centre of mass frame, the energy of the fragmentation can be obtained, see equation D.5. ΔE represents either ΔE_f or ΔE_b used previously depending upon which ions are being analysed.

$$\Delta E_{CM} = \frac{(\Delta E m\mu + V_B^2 m^2 \mu) \pm \sqrt{2V_B^2 m^3 \mu^2 (\Delta E + \frac{1}{2}V_B^2 m)}}{\mu^2} \quad \text{(D.5)}$$

Note the values of ΔE_{CM} from both the forward and backward peaks in any spectra become degenerate upon transformation from time to energy, hence the fragmentation energy obtained is the same from both channels.

When observing the charged fragments, analysis is conducted using post interaction electrostatic deflection. The dependence of the fragmentation energy, E_i, upon the applied deflection field, ϵ, is given by equation D.6.

$$E_i = \frac{e^2 l^2}{4E_\parallel}\left(\frac{d_1 + l/2}{d_1 + d_2 + l}\right)^2 \epsilon^2 \quad \text{(D.6)}$$

Here l, is the length of the detector, d_1 is the distance from the interaction region to the start of the deflection region. d_2 is the distance from the end of the deflection region and the parallel plate analyser and $E_\parallel$ is the energy of the ion fragment calculated from the component of the ions velocity lying parallel to the time-of-flight axis in the laboratory frame.

Appendix E

Ion Rig B-Field selection

In the ion-beam apparatus an electromagnet is used to select only those ions of a specific mass to charge ratio (m/q) produced from the ion source to make the beam. This is done by applying the necessary current to ensure only the desired ions travel through the magnet's 2 mm exit aperture. Below is the derivation of the link between the current in the magnets coils and the selected ions m/q ratio.

The selection magnet produces a magnetic field of strength, **B**, which is perpendicular to the ions path. This exerts a force, **F**, on the ion (travelling at velocity, **v**) given by equation E.1, which given the perpendicular nature of the magnetic field to the ion's propagation, can be simplified to a scalar expression for the magnetic field strength, see equation E.2.

$$\mathbf{F} = q\mathbf{v} \times \mathbf{B} \tag{E.1}$$

$$F = qvB \tag{E.2}$$

Considering this interaction as centripetal motion, the ion maps out an arc of radius r, which can be related to the force exerted on the ion by the field by equation E.3

$$\mathbf{F} = \frac{mv^2}{r}\hat{\mathbf{r}} \tag{E.3}$$

Equating these two expressions (equations E.2 and E.3) and rearranging, an expression for the magnetic field strength can be obtained, equation E.5

$$qvB = \frac{mv^2}{r} \tag{E.4}$$

$$B = \frac{mv}{qr} \tag{E.5}$$

Now the ion's kinetic energy, T, can be written in terms of its mass and velocity or the voltage used to extract the ions from the ion source, V.

$$T = \frac{mv^2}{2} \tag{E.6}$$

$$T = qV \tag{E.7}$$

Equating these two expression (equation E.6 and E.7) an equation for the ion's velocity can be obtained, see equation E.9.

$$qV = \frac{mv^2}{2} \tag{E.8}$$

$$v = \sqrt{\frac{2qV}{m}} \tag{E.9}$$

Substituting this expression (equation E.9) for v into the expression for B (equation E.5) yields equation E.11.

$$B = \frac{m}{qr}\sqrt{\frac{2qV}{m}} \tag{E.10}$$

$$B = \sqrt{\frac{2mV}{qr^2}} \tag{E.11}$$

Now, the magnetic field strength exerted by the selection magnet is proportional to the current flowing through the magnet's coils (I). Using κ as a constant of proportionality this can be used to write equation E.12. Furthermore for a given beam energy, V and r as well as $\sqrt{2}$ can be considered constants too and can all be rolled into κ, to form a second constant, K. This results in a simplified equation relating the selected ions m/q ratio and the current applied to the selection magnet.

$$B = \kappa B = \frac{\kappa}{r}\sqrt{\frac{2mV}{q}} \tag{E.12}$$

$$I = K\sqrt{\frac{m}{q}} \tag{E.13}$$

Appendix F

Ionisation Potentials of Selected Noble Gases

Below, and continued over-page, is a table of the ionisation potentials of the noble gases employed in this thesis.

Species		Ionisation Potential	
Symbol	Spec. Notation	(eV)	(cm^{-1})
He	He I	24.587	198,312.0
He^{+}	He II	54.418	438,911.9
Ne	Ne I	21.565	173,930.9
Ne^{+}	Ne II	41.077	331,311.5
Ne^{2+}	Ne III	63.423	511,547.0
Ne^{3+}	Ne IV	97.117	783,305.3
Ne^{4+}	Ne V	126.247	1,018,257.0
Ne^{2+}	Ne VI	154.214	1,243,828.4
Ne^{3+}	Ne VII	207.271	1,671,761.8
Ne^{4+}	Ne VIII	239.097	1,928,460.0
Ar	Ar I	15.760	127,110.7
Ar^{+}	Ar II	27.630	222,849.7
Ar^{2+}	Ar III	40.735	328,552.2
Ar^{3+}	Ar IV	59.686	481,403.4
Ar^{4+}	Ar V	75.134	606,004.0
Ar^{2+}	Ar VI	91.000	733,969.6
Ar^{3+}	Ar VII	124.328	1,002,779.1
Ar^{4+}	Ar VIII	143.457	1,157,064.4

Table F.1: The ionisation potentials above were sourced from the National Institute of Standards and Technology (NIST) Atomic Spectra Database (version 3.1.5)[Online]. Available: http://physics.nist.gov/asd3 [2008, September 11]. The National Institute of Standards and Technology, Gaithersburg, Maryland, USA.

Below is the continuation of table F.1.

Species		Ionisation Potential	
Symbol	Spec. Notation	(eV)	(cm^{-1})
Kr	Kr I	14.000	112,915.2
Kr^{+}	Kr II	24.360	196,476.7
Kr^{2+}	Kr III	36.950	298,022.3
Kr^{3+}	Kr IV	52.495	423,402.9
Kr^{4+}	Kr V	64.695	521,804.0
Kr^{2+}	Kr VI	78.494	633,104.4
Kr^{3+}	Kr VII	111.003	895,305.8
Kr^{4+}	Kr VIII	125.802	1,014,671.8
Xe	Xe I	12.130	97,834.5
Xe^{+}	Xe II	21.983	177,306.1
Xe^{2+}	Xe III	31.046	250,401.4
Xe^{3+}	Xe IV	40.915	330,002.4
Xe^{4+}	Xe V	54.144	436,703.0
Xe^{2+}	Xe VI	66.703	537,999.7
Xe^{3+}	Xe VII	91.600	738,804.9
Xe^{4+}	Xe VIII	105.976	854,760.0

Table F.2: The ionisation potentials above were sourced from the National Institute of Standards and Technology (NIST) Atomic Spectra Database (version 3.1.5)[Online]. Available: http://physics.nist.gov/asd3 [2008, September 11]. The National Institute of Standards and Technology, Gaithersburg, Maryland, USA.

Appendix G

Simplified Potential Energy Diagram of the Hydrogen Molecular Ion

The Morse potential [Morse, 1929] is an empirical expression derived by Morse to fit anharmonic diatomic molecular potentials. Overleaf a version of the Morse potential for the $1s\sigma_g$ state (U_{Morse}) is plotted alongside the values obtained by Sharp [Sharp, 1971] used in this thesis. Also a double exponential fit of the excited $2p\sigma_u$ state (V_{fit}) is plotted. For the variables used in the plot see equations G.1 and G.2 and table G.1 (all values in atomic units).

$$U_{morse} = d(\exp[-2a(R-r_e)] - 2\exp[-a(R-r_e)]) + b \quad \text{(G.1)}$$

$$V_{fit} = A_1 \exp[-B_1 R] + A_2 \exp[-B_2 R] + A_3 \quad \text{(G.2)}$$

variable	value
b	0.664286
d	0.102606
a	0.7
r_e	2
A_1	8.664240
A_2	2.442410
A_3	0.664015
B_1	5.690550
B_2	0.996562

Table G.1:

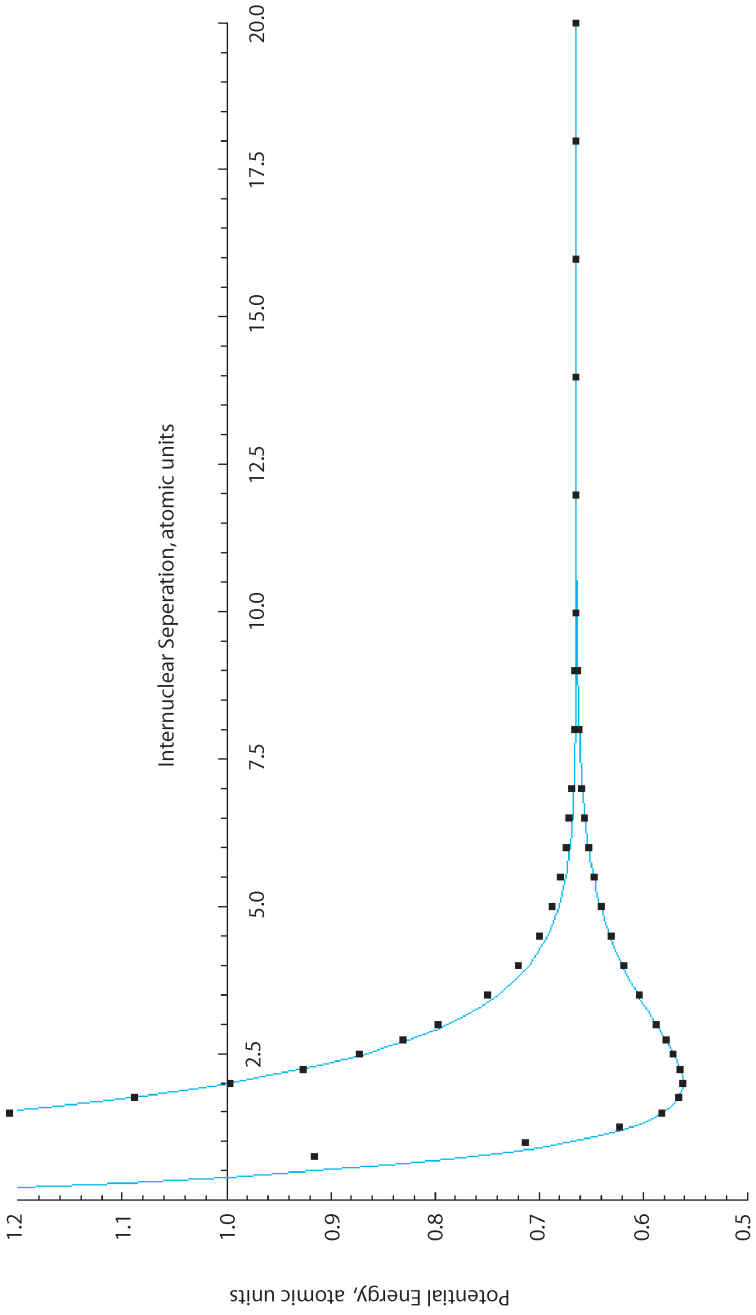

Figure G.1: The Morse potential (lower cyan curve) for the $1s\sigma_g$ and a double exponential fit (upper cyan curve) for the $2p\sigma_u$ levels of $H_2{}^+$ are plotted alongside the values obtained by Sharp (black squares).

Appendix H

Natural Abundances of the Stable Isotopes of Selected Noble Gases.

Atomic Symbol	Atomic Mass Number (% Abundance)
Ne	20 (90.48), 21 (0.27), 22(9.25)
Ar	36 (0.34), 38 (0.06), 40 (99.60)
Kr	78 (0.36), 80 (2.29), 82 (11.59), 83 (11.50), 84 (56.99), 86 (17.28)
Xe	124 (0.10), 126 (0.09), 128 (1.91), 129 (26.40), 130 (4.07), 131 (21.23), 132 (26.91), 134 (10.44), 136 (8.86)

Table H.1: Natural abundances of the stable isotopes of selected noble gases. Data taken from [de Laeter et al., 2003].

Appendix I

Energy Levels of the Vibrational States of H_2^+ and their Franck-Condon Factors

In table I.1 zero energy is the disosciation limit of the $1s\sigma_g$ electronic state of the H_2^+ ion. Data reproduced from [Suresh, 2005].

Vibrational Level	Energy (eV)	F-C population
0	-2.646	0.119
1	-2.375	0.190
2	-2.119	0.188
3	-1.878	0.152
4	-1.652	0.110
5	-1.441	0.077
6	-1.244	0.053
7	-1.060	0.036
8	-0.891	0.024
9	-0.735	0.016
10	-0.593	0.011
11	-0.465	0.008
12	-0.351	0.005
13	-0.252	0.004
14	-0.168	0.003
15	-0.100	0.002
16	-0.049	0.001

Table I.1: Vibrational Energies and Franck-Condon Factors of H_2^+.

Appendix J

Energy Levels of the Vibrational States of D_2^+ and their Franck-Condon Factors

In table J.1 zero energy is the disosciation limit of the $1s\sigma_g$ electronic state of the D_2^+ ion. Data reproduced from [Suresh, 2005].

Vibrational Level	Energy (eV)	F-C population
0	-2.646	0.119
1	-2.375	0.190
2	-2.119	0.188
3	-1.878	0.152
4	-1.652	0.110
5	-1.441	0.077
6	-1.244	0.053
7	-1.060	0.036
8	-0.891	0.024
9	-0.735	0.016
10	-0.593	0.011
11	-0.465	0.008
12	-0.351	0.005
13	-0.252	0.004
14	-0.168	0.003
15	-0.100	0.002
16	-0.049	0.001

Table J.1: Vibrational Energies and Franck-Condon Factors of D_2^+

Appendix K

Oral Presentations

1. Molecular wave packet revivals in fast quantum systems, Atomic, Molecular, Optical and Positron Physics Group Seminar, Department of Physics and Astronomy, University College London. 06/06/07

Appendix L

Poster Presentations

I have presented my research at the following international meetings, workshops and conferences.

1. Christmas Meeting of the High Power Laser Science Community, Abingdon-UK, December 2004.
2. Christmas Meeting of the High Power Laser Science Community, Abingdon-UK, December 2005.
3. Ultra-Fast Dynamic Imaging Workshop, London-UK, April 2006.
4. Lasers for Science Facility Users Meeting, Abingdon-UK, November 2005.
5. Christmas Meeting of the High Power Laser Science Community, Abingdon-UK, December 2006.
6. European Conference on Atoms Molecules and Photons (ECAMP 9), Crete-Greece, May 2007.
7. International Conference on Photonic, Electronic and Atomic Collisions (ICPEAC XXV), Freiburg-Germany, July 2007.
8. International Workshop on Attosecond Physics (ATTO 07), Dresden-Germany, August 2007.
9. Quantum, Atomic, Molecular and Plasma Physics Conference (QUAMP 2007), London-UK, September 2007.

Appendix M

Conference Proceedings

1. *Probing atomic ionization mechanisms in intense laser fields by calculating geometry and diffraction independent ionization probabilities* Ultra-Fast Dynamic Imaging Workshop, London-UK, April 2006.

2. *A two pulse experiment on xenon: A diagnostic for intense femtosecond laser pulses* Ultra-Fast Dynamic Imaging Workshop, London-UK, April 2006.

3. *Field-free dynamic alignment of deuterium with intense few cycle pulses* European Conference on Atoms Molecules and Photons (ECAMP 9), Crete-Greece, May 2007.

4. *Controlling dissociation pathways in the deuterium molecular ion with intense ultrashort pulses* European Conference on Atoms Molecules and Photons (ECAMP 9), Crete-Greece, May 2007.

5. *Optical generation of a rotational wavepacket in room temperature deuterium* International Conference on Photonic, Electronic and Atomic Collisions (ICPEAC XXV), Freiburg-Germany, July 2007.

6. *Mapping vibrational wavepackets in hydrogenic molecular ions with ultrashort laser pulses* International Conference on Photonic, Electronic and Atomic Collisions (ICPEAC XXV), Freiburg-Germany, July 2007.

7. *Optical generation of a rotational wavepacket in room temperature deuterium* International Workshop on Attosecond Physics (ATTO 07), Dresden-Germany, August 2007.

8. *Mapping vibrational wavepackets in hydrogenic molecular ions with ultrashort laser pulses* International Workshop on Attosecond Physics (ATTO 07), Dresden-Germany, August 2007.

9. *Mapping ultrafast rotational wavepacket dynamics with 12 fs laser pulses* Quantum, Atomic, Molecular and Plasma Physics Conference (QUAMP 2007), London-UK, September 2007.

10. *Imaging the vibrational motion of $D_2{}^+$ with ultrshort laser pulses* Quantum, Atomic, Molecular and Plasma Physics Conference (QUAMP 2007), London-UK, September 2007.

Appendix N

Peer Reviewed Publications

Here is a list of the Papers upon which I am a named author. All of the following are appended to this thesis after the bibliography.

1. W A Bryan, S L Stebbings, J McKenna, E M L English, M Suresh, J Wood, B Srigengan, I C E Turcu, J M Smith, E J Divall, C J Hooker, A J Langley, J L Collier, I D Williams and W R Newell, *Atomic excitation during recollision-free ultrafast multi-electron tunnel ionization*, Nature Physics 2, 379-383 (2006)

2. W A Bryan, S L Stebbings, J McKenna, E M L English, M Suresh, J Wood, B Srigengan, I C E Turcu, I D Williams and W R Newell, *On the recollision-free excitation of krypton during ultrafast multi-electron tunnel ionization*, Journal of Physics B: Atomic, Molecular and Optical Physics 39, (13) S349-S356 (2006)

3. J McKenna, W A Bryan, C R Calvert, E M L English, J Wood, D S Murphy, I C E Turcu, J M Smith, K G Ertel , O Chekhlov, E J Divall, J F Mccann, W R Newell and I D Williams, *Observing time-dependent vibrational quantum dynamics in deuterium hydride molecular ions*, Journal of Modern Optics 54, (7) 1127-1138 (2007)

4. D S Murphy, J McKenna, C R Calvert, W A Bryan, E M L English, J Wood, I C E Turcu, W R Newell, I D Williams and J F McCann, *Controlling dissociation processes in the D_2^+ molecular ion using high-intensity, ultrashort laser pulses*, Journal of Physics B: Atomic, Molecular and Optical Physics 40, (11) S359-S372 (2007)

5. J McKenna, M Suresh, D S Murphy, W A Bryan, L-Y Peng, S L Stebbings, E M L English, J Wood, B Srigengan, I C E Turcu, J L Collier, J F McCann, W R Newell and I D Williams, *Intense-field dissociation dynamics of D_2^+ molecular ions using ultrafast laser pulses*, Journal of Physics B: Atomic, Molecular and Optical Physics 40, (13) 2607-2619 (2007)

6. W A Bryan, E M L English, J McKenna, J Wood, C R Calvert, I C E Turcu, R Torres, J L Collier, I D Williams and W R Newell, *Mapping the evolution of optically generated rotational wave packets in a room-temperature ensemble of* D_2, Physical Review A 76, 023414 (2007)

7. I D Williams, J McKenna, J Wood, M Suresh, W A Bryan, S L Stebbings, E M L English, C R Calvert, B Srigengan, E J Divall, C J Hooker, A J Langley and W R Newell, *Excited ions in intense femtosecond laser pulses: Laser-induced recombination*, Physical Review Letters 99, 173002 (2007)

8. W A Bryan, J McKenna, E M L English, J Wood, C R Calvert, R Torres, D S Murphy, I C E Turcu, J L Collier, J F McCann, I D Williams and W R Newell, *Isolated vibrational wavepackets in* $D_2{}^+$*: Defining superposition conditions and wavepacket distinguishability*, Physical Review A 76, 053402 (2007)

9. J McKenna, C R Calvert, W A Bryan, E M L English, J Wood, D S Murphy, I C E Turcu, J M Smith, K G Ertel O Chekhlov, E J Divall, J F McCann, W R Newell and I D Williams, *Imaging quantum vibrations on an ultrashort timescale: the deuterium molecular ion*, Journal of Physics: Conference Series 58, 375-378 (2007)

10. C R Calvert, J McKenna, W A Bryan, J Wood, E M L English, I C E Turcu, J M Smith, K G Ertel O Chekhlov, E J Divall, W R Newell and I D Williams, *Dynamic imaging of a dissociative* $D_2{}^+$ *nuclear wavepacket in intense laser fields*, Journal of Physics: Conference Series 58, 379-382 (2007)

Bibliography

[Agostini et al., 1979] Agostini, P., Fabre, F., Mainfray, G., Petite, G., and Rahman, N. K. (1979). Free-free transitions following six-photon ionization of xenon atoms. *Physical Review Letters*, 42(17):1127–1130.

[Agrawal, 2007] Agrawal, G. P. (2007). *Nonlinear Fiber Optics*. Academic Press, San Diego, California, USA, Fourth edition.

[Alnaser et al., 2005] Alnaser, A. S., Ulrich, B., Tong, X. M., Litvinyuk, I. V., Maharjan, C. M., Ranitovic, P., Osipov, T., Ali, R., Ghimire, S., Chang, Z., Lin, C. D., and Cocke, C. L. (2005). Simultaneous real-time tracking of wave packets evolving on two different potential curves in $H_2{}^+$ and $D_2{}^+$. *Physical Review A (Atomic, Molecular, and Optical Physics)*, 72(3):030702.

[Altunata et al., 2002] Altunata, S. N., Cao, J., and Field, R. W. (2002). Semiclassical modeling of Rydberg wave-packet dynamics in diatomic molecules: Average decoupling theory. *Physical Review A*, 65(5):053415.

[Ammosov et al., 1986] Ammosov, M. V., Delone, N. B., and Krainov, V. P. (1986). Tunnel ionization of complex atoms and of atomic ions in an alternating electromagnetic field. *Soviet Physics JETP*, 64(6):1191–1194.

[Andersen and Bolko, 1990] Andersen, L. H. and Bolko, J. (1990). Radiative recombination measurements with H- and Li-like ions. *Journal of Physics B: Atomic, Molecular and Optical Physics*, 23(18):3167–3172.

[Andersen et al., 1990] Andersen, L. H., Bolko, J., and Kvistgaard, P. (1990). Radiative recombination between free electrons and bare carbon ions. *Physical Review Letters*, 64(7):729–732.

[Augst et al., 1991] Augst, S., Meyerhofer, D. D., Strickland, D., and Chin, S. L. (1991). Laser ionization of noble gases by Coulomb-barrier suppression. *Journal of the Optical Society of America B*, 8(4):858.

[Augst et al., 1989] Augst, S., Strickland, D., Meyerhofer, D. D., Chin, S. L., and Eberly, J. H. (1989). Tunneling ionization of noble gases in a high-intensity laser field. *Physical Review Letters*, 63(20):2212–2215.

[Auguste et al., 1992] Auguste, T., Monot, P., Lompre, L. A., Mainfray, G., and Manus, C. (1992). Multiply charged ions produced in noble gases by a 1 ps laser pulse at $\lambda =$ 1053 nm. *Journal of Physics B: Atomic, Molecular and Optical Physics*, 25(20):4181–4194.

[Averbukh and Perelman., 1989] Averbukh, I. S. and Perelman., N. F. (1989). Fractional revivals: Universality in the long-term evolution of quantum wave packets beyond the correspondence principle dynamics. *Physics Letters A*, 139(9):449–453.

[Baker et al., 2006] Baker, S., Robinson, J. S., Haworth, C. A., Teng, H., Smith, R. A., Chiril, C. C., Lein, M., Tisch, J. W. G., and Marangos, J. P. (2006). Probing proton dynamics in molecules on an attosecond time scale. *Science*, 312(5772):424 – 427.

[Bandrauk, 1993] Bandrauk, A. D. (1993). *Molecules in Laser Fields*. Marcel Dekker, New York, USA.

[Bandrauk and Ruel, 1999] Bandrauk, A. D. and Ruel, J. (1999). Charge-resonance-enhanced ionization of molecular ions in intense laser pulses: Geometric and orientation effects. *Physical Review A*, 59(3):2153–2162.

[Banerji and Ghosh, 2006] Banerji, J. and Ghosh, S. (2006). The role of ro-vibrational coupling in the revival dynamics of diatomic molecular wave packets. *Journal of Physics B: Atomic, Molecular and Optical Physics*, 39(5):1113–1123.

[Banwell, 1983] Banwell, C. N. (1983). *Fundamentals of molecular spectroscopy*. McGraw-Hill, London, UK, Third edition.

[Bardeen et al., 1997] Bardeen, C. J., Yakovlev, V. V., Wilson, K. R., Carpenter, S. D., Weber, P. M., and Warren, W. S. (1997). Feedback quantum control of molecular electronic population transfer. *Chemical Physics Letters*, 280(1-2):151–158.

[Bartels et al., 2000] Bartels, R., Backus, S., Zeek, E., Misogutl, L., Vdovin, G., Christov, I. P., Murnane, M. M., and Kapteyn, H. C. (2000). Shaped-pulse optimization of coherent emission of high-harmonic soft X-rays. *Nature*, 406:164–166.

[Bates, 1951] Bates, D. R. (1951). The oscillator strength of $H_2{}^+$, 1sσ-2pσ. *The Journal of Chemical Physics*, 19(9):1122–1124.

[Baumann and Bethge, 1974] Baumann, H. and Bethge, K. (1974). PIG ion-source with end extraction for multiply charged ions. *Nuclear Instruments and Methods*, 122(3):517–525.

[Becker and Faisal, 1999] Becker, A. and Faisal, F. H. M. (1999). S-matrix analysis of ionization yields of noble gas atoms at the focus of Ti:sapphire laser pulses. *Journal of Physics B: Atomic, Molecular and Optical Physics*, 32(14):L335–L343.

[Becker and Faisal, 2002] Becker, A. and Faisal, F. H. M. (2002). S-matrix analysis of coincident measurement of two-electron energy distribution for double ionization of He in an intense laser field. *Physical Review Letters*, 89(19):193003.

[Becker and Faisal, 2005] Becker, A. and Faisal, F. H. M. (2005). Intense-field many-body S-matrix theory. *Journal of Physics B: Atomic, Molecular and Optical Physics*, 38(3):R1–R56.

[Bethe and Salpeter, 1957] Bethe, H. A. and Salpeter, E. E. (1957). *Quantum mechanics of one- and two-electron atoms*. Springer-Verlag, Berlin, Germany.

[Bocharova et al., 2008] Bocharova, I. A., Mashiko, H., Magrakvelidze, M., Ray, D., Ranitovic, P., Cocke, C. L., and Litvinyuk, I. V. (2008). Direct Coulomb-explosion imaging of coherent nuclear dynamics induced by few-cycle laser pulses in light and heavy hydrogen. *Physical Review A (Atomic, Molecular, and Optical Physics)*, 77(5):053407.

[Brabec and Krausz, 2000] Brabec, T. and Krausz, F. (2000). Intense few-cycle laser fields: Frontiers of nonlinear optics. *Review of Modern Physics*, 72(2):545–591.

[Brichta et al., 2006] Brichta, J. P., Liu, W.-K., Zaidi, A. A., Trottier, A., and Sanderson, J. H. (2006). Comparison of ADK ionization rates as a diagnostic for selective vibrational level population measurement. *Journal of Physics B: Atomic, Molecular and Optical Physics*, 39(18):3769–3779.

[Brixner et al., 2003] Brixner, T., Damrauer, N. H., Krampert, G., Niklaus, P., and Gerber, G. (2003). Femtosecond learning control of quantum dynamics in gases and liquids: Technology and applications. *Journal of Modern Optics*, 50(3):539–560.

[Broetz et al., 2001] Broetz, F., Trassl, R., McCullough, R. W., Arnold, W., and Salzborn, E. (2001). Design of compact all-permanent magnet electron cyclotron resonance (ECR) ion sources for atomic physics experiments. *Physica Scripta*, T92:278–280.

[Brouillard and McGowan, 1983] Brouillard, F. and McGowan, J. W. (1983). *Physics of Ion-Ion and Electron-Ion Collisions, NATO Series B, Physics, Volume 83*. Plenum Publishers, New York, New York, USA.

[Bryan, 2001] Bryan, W. A. (2001). *Ultrafast processes in small molecules*. PhD thesis, University College London, Department of Physics and Astronomy, University College London, England.

[Bryan et al., 2007a] Bryan, W. A., English, E. M. L., McKenna, J., Wood, J., Calvert, C. R., Turcu, I. C. E., Torres, R., Collier, J. L., Williams, I. D., and Newell, W. R.

(2007a). Mapping the evolution of optically generated rotational wave packets in a room-temperature ensemble of D_2. *Physical Review A (Atomic, Molecular, and Optical Physics)*, 76(2):023414.

[Bryan et al., 2007b] Bryan, W. A., McKenna, J., English, E. M. L., Wood, J., Calvert, C. R., Torres, R., Murphy, D. S., Turcu, I. C. E., Collier, J. L., McCann, J. F., Williams, I. D., and Newell, W. R. (2007b). Isolated vibrational wavepackets in $D_2{}^+$: Defining superposition conditions and wavepacket distinguishability. *Physical Review A (Atomic, Molecular, and Optical Physics)*, 76(5):053402.

[Bryan et al., 2006a] Bryan, W. A., Newell, W. R., Sanderson, J. H., and Langley, A. J. (2006a). Observation of multiple ionization pathways for OCS in an intense laser field resolved by three-dimensional covariance mapping and visualized by hierarchical ionization topology. *Physical Review A (Atomic, Molecular, and Optical Physics)*, 74(5):053409.

[Bryan et al., 2000] Bryan, W. A., Sanderson, J. H., El-Zein, A., Newell, W. R., Taday, P. F., and Langley, A. J. (2000). Laser-induced Coulomb explosion, geometry modification and reorientation of carbon dioxide. *Journal of Physics B: Atomic, Molecular and Optical Physics*, 33(4):745–766.

[Bryan et al., 2006b] Bryan, W. A., Stebbings, S. L., English, E. M. L., Goodworth, T. R. J., Newell, W. R., McKenna, J., Suresh, M., Srigengan, B., Williams, I. D., Turcu, I. C. E., Smith, J. M., Divall, E. J., Hooker, C. J., and Langley, A. J. (2006b). Geometry- and diffraction-independent ionization probabilities in intense laser fields: Probing atomic ionization mechanisms with effective intensity matching. *Physical Review A (Atomic, Molecular, and Optical Physics)*, 73(1):013407.

[Bryan et al., 2006c] Bryan, W. A., Stebbings, S. L., McKenna, J., English, E. M. L., Suresh, M., Wood, J., Srigengan, B., Turcu, I. C. E., Smith, J. M., Divall, E. J., Hooker, C. J., Langley, A. J., Collier, J. L., Williams, I. D., and Newell, W. R. (2006c). Atomic excitation during recollision-free ultrafast multi-electron tunnel ionization. *Nature Physics*, 2(6):379–383.

[Bryan et al., 2006d] Bryan, W. A., Stebbings, S. L., McKenna, J., English, E. M. L., Suresh, M., Wood, J., Srigengan, B., Turcu, I. C. E., Williams, I. D., and Newell, W. R. (2006d). On the recollision-free excitation of krypton during ultrafast multi-electron tunnel ionization. *Journal of Physics B: Atomic, Molecular and Optical Physics*, 39(13):S349–S356.

[Bucksbaum, 2007] Bucksbaum, P. H. (2007). The future of attosecond spectroscopy. *Science*, 317(5839):766–769.

[Bucksbaum et al., 1990] Bucksbaum, P. H., Zavriyev, A., Muller, H. G., and Schumacher, D. W. (1990). Softening of the $H_2{}^+$ molecular bond in intense laser fields. *Physical Review Letters*, 64(16):1883–1886.

[Busch, 2004] Busch, K. L. (2004). Space charge in mass spectrometery. *Spectroscopy*, 19(6):35–38.

[Calvert, 2008] Calvert, C. R. (2008). *Time-resolved dynamics of ultrafast fundamental molecules in intense laser fields*. PhD thesis, Queen's University Belfast, School of Mathematics and Physics, Queen's University Belfast, Northern Ireland.

[Calvert and McKenna, 2006] Calvert, C. R. and McKenna, J. (2006). *Ion Beam Apparatus Manual*. Queen's University Belfast, Belfast, United Kingdom.

[Calvert et al., 2007] Calvert, C. R., McKenna, J., Bryan, W. A., Wood, J., English, E. M. L., Turcu, I. C. E., Smith, J. M., Ertel, K. G., Cheklov, O., Divall, E. J., Newell, W. R., and Williams, I. D. (2007). Dynamic imaging of a dissociative D_2^+ nuclear wavepacket in intense laser fields. *Journal of Physics: Conference Series*, 58:379–382.

[Carlson, 1967] Carlson, T. A. (1967). Double electron ejection resulting from photoionization in the outermost shell of He, Ne, and Ar, and its relationship to electron correlation. *Physical Review*, 156(1):142–149.

[Carlson et al., 1968] Carlson, T. A., Nestor, C. W., Tucker, T. C., and Malik, F. B. (1968). Calculation of electron shake-off for elements from Z=2 to 92 with the use of self-consistent-field wave functions. *Physical Review*, 169(1):27–36.

[Chaloupka et al., 2003] Chaloupka, J. L., Rudati, J., Lafon, R., Agostini, P., Kulander, K. C., and DiMauro, L. F. (2003). Observation of a transition in the dynamics of strong-field double ionization. *Physical Review Letters*, 90(3):033002.

[Charalambidis et al., 1997] Charalambidis, D., Xenakis, D., Uiterwaal, C. J. G. J., Maragakis, P., Zhang, J., Schrder, H., Faucher, O., and Lambropoulos, P. (1997). Multiphoton ionization saturation intensities and generalized cross sections from ATI spectra. *Journal of Physics B: Atomic, Molecular and Optical Physics*, 30(6):1467–1480.

[Chen et al., 2007] Chen, Y.-H., Varma, S., York, A., and Milchberg, H. M. (2007). Single-shot, space- and time-resolved measurement of rotational wavepacket revivals in H_2, D_2, N_2, O_2, and N_2O. *Optics Express*, 15(18):11341–11357.

[Chilla and Martinez, 1991] Chilla, J. L. A. and Martinez, O. E. (1991). Direct determination of the amplitude and the phase of femtosecond light pulses. *Optics Letters*, 16(1):39–41.

[Chu, 1981] Chu, S.-I. (1981). Floquet theory and complex quasivibrational energy formalism for intense field molecular photodissociation. *The Journal of Chemical Physics*, 75(5):2215–2221.

[Codling and Frasinski, 1993] Codling, K. and Frasinski, L. J. (1993). Dissociative ionization of small molecules in intense laser fields. *Journal of Physics B: Atomic, Molecular and Optical Physics*, 26(5):783–809.

[Codling et al., 1988] Codling, K., Frasinski, L. J., and Hatherly, P. A. (1988). Multiphoton ionisation of H_2 and D_2 using an intense sub-picosecond laser. *Journal of Physics B: Atomic, Molecular and Optical Physics*, 21(15):L433–L438.

[Continetti, 2001] Continetti, R. E. (2001). Coincidence spectroscopy. *Annual Review of Physical Chemistry*, 52(1):165–192.

[Corkum, 1993] Corkum, P. B. (1993). Plasma perspective on strong field multiphoton ionization. *Physical Review Letters*, 71(13):1994–1997.

[Corkum et al., 1989] Corkum, P. B., Burnett, N. H., and Brunel, F. (1989). Above-threshold ionization in the long-wavelength limit. *Physical Review Letters*, 62(11):1259–1262.

[Cornaggia et al., 1990] Cornaggia, C., Lavancier, J., Normand, D., Morellec, J., and Liu, H. X. (1990). Intensity dependence of the multielectron dissociative ionization of N_2 at 305 and 610 nm. *Physical Review A*, 42(9):5464–5472.

[Dahan et al., 1998] Dahan, M., Fishman, R., Heber, O., Rappaport, M., Altstein, N., Zajfman, D., and van der Zande, W. J. (1998). A new type of electrostatic ion trap for storage of fast ion beams. *Review of Scientific Instruments*, 69(1):76–83.

[Danby and Eland, 1972] Danby, C. J. and Eland, J. H. D. (1972). Photoelectron-photoion coincidence spectroscopy. II design and performance of a practical instrument. *International Journal of Mass Spectrometry and Ion Processes*, 8:153–161.

[Davies et al., 1999] Davies, J. A., LeClaire, J. E., Continetti, R. E., and Hayden, C. C. (1999). Femtosecond time-resolved photoelectron–photoion coincidence imaging studies of dissociation dynamics. *The Journal of Chemical Physics*, 111(1):1–4.

[de Laeter et al., 2003] de Laeter, J. R., Bhlke, J. K., Bivre, P. D., Hidaka, H., Peiser, H. S., Rosman, K. J. R., and Taylor, P. D. P. (2003). Atomic weights of the elements. review 2000 (IUPAC technical report). *Pure and Applied Chemistry*, 75(6):4746–4753.

[Delone and Krainov, 1998] Delone, N. B. and Krainov, V. P. (1998). Tunneling and barrier-suppression ionization of atoms and ions in a laser radiation field. *Physics-Uspekhi*, 41(5):469–485.

[Delone and Krainov, 2000] Delone, N. B. and Krainov, V. P. (2000). *Multiphoton Processes in Atoms*. Springer-Verlag, Berlin, Germany, Second edition.

[DeLong et al., 1994] DeLong, K. W., Trebino, R., Hunter, J., and White, W. E. (1994). Frequency-resolved optical gating with the use of second-harmonic generation. *Journal of the Optical Society of America B*, 11(11):2206.

[Demtröder, 2006] Demtröder, W. (2006). *Atoms, Molecules and Photons*. Springer, Berlin, Germany.

[Dendy, 1996] Dendy, R. (1996). *Plasma Physics: An Introductory Course*. Cambridge University Press, Cambridge, UK.

[DeWitt et al., 1994] DeWitt, D. R., Schuch, R., Quinteros, T., Gao, H., Zong, W., Danared, H., Pajek, M., and Badnell, N. R. (1994). Absolute dielectronic recombination cross sections of hydrogenlike helium. *Physical Review A*, 50(2):1257–1264.

[DiMauro, 2002] DiMauro, L. F. (2002). Atomic photography. *Nature*, 419:789–790.

[Dooley et al., 2003] Dooley, P. W., Litvinyuk, I. V., Lee, K. F., Rayner, D. M., Spanner, M., Villeneuve, D. M., and Corkum, P. B. (2003). Direct imaging of rotational wavepacket dynamics of diatomic molecules. *Physical Review A*, 68(2):023406.

[Dörner et al., 1994] Dörner, R., Mergel, V., Ali, R., Buck, U., Cocke, C. L., Froschauer, K., Jagutzki, O., Lencinas, S., Meyerhof, W. E., Nüttgens, S., Olson, R. E., Schmidt-Böcking, H., Spielberger, L., Tökesi, K., Ullrich, J., Unverzagt, M., and Wu, W. (1994). Electron-electron interaction in projectile ionization investigated by high resolution recoil ion momentum spectroscopy. *Physical Review Letters*, 72(20):3166–3169.

[Dörner et al., 2000] Dörner, R., Mergel, V., Jagutzki, O., Spielberger, L., Ullrich, J., Moshammer, R., and Schmidt-Böcking, H. (2000). Cold target recoil ion momentum spectroscopy: A momentum microscope to view atomic collision dynamics. *Physics Reports*, 330(2-3):95–192.

[Dörner et al., 1997] Dörner, R., Mergel, V., Spielberger, L., Achler, M., Khayyat, K., Vogt, T., Brauning, H., Jagutzki, O., Weber, T., Ullrich, J., Moshammer, R., Unverzagt, M., Schmitt, W., Khemliche, H., Prior, M. H., Cocke, C. L., Feagin, J., Olson, R. E., and Schmidt-Bocking, H. (1997). Kinematically complete experiments using cold target recoil ion momentum spectroscopy. *Nuclear Instruments and Methods in Physics Research Section B: Beam Interactions with Materials and Atoms*, 124(2-3):225–231.

[Dörner et al., 2002] Dörner, R., Weber, T., Weckenbrock, M., Staudte, A., Hattass, M., Moshammer, R., Ullrich, J., and Schmidt-Böcking, H. (2002). Reconstruction of atomic ionization probabilities in intense laser fields. *Advances in Atomic and Molecular Physics*, 48(1):3083–3089.

[Drescher et al., 2002] Drescher, M., Hentschel, M., Kienberger, R., Uiberacker, M., Yakovlev, V., Scrinzi, A., Westerwalbesloh, T., Kleineberg, U., Heinzmann, U., and Krausz, F. (2002). Time-resolved atomic inner-shell spectroscopy. *Nature*, 419(6909):803–807.

[Dromey et al., 2006] Dromey, B., Zepf, M., Gopal, A., Lancaster, K., Wei, M. S., Krushelnick, K., Tatarakis, M., Vakakis, N., Moustaizis, S., Kodama, R., Tampo, M., Stoeckl, C., Clarke, R., Habara, H., Neely, D., Karsch, S., and Norreys, P. (2006). High harmonic generation in the relativistic limit. *Nature Physics*, 2(7):456–459.

[Dyson and Williams, 1997] Dyson, J. and Williams, D. (1997). *The Physics of the Interstellar Medium (Graduate Series in Astronomy)*. Institute of Physics, Bristol, UK, Second edition.

[Eberly and Sleeper, 1968] Eberly, J. H. and Sleeper, A. (1968). Trajectory and mass shift of a classical electron in a radiation pulse. *Physical Review*, 176(5):1570–1573.

[Eden, 2004] Eden, J. G. (2004). High-order harmonic generation and other intense optical fieldmatter interactions: Review of recent experimental and theoretical advances. *Progress in Quantum Electronics*, 28(3-4):197–246.

[Eichmann et al., 2000] Eichmann, U., Dörr, M., Maeda, H., Becker, W., and Sandner, W. (2000). Collective multielectron tunneling ionization in strong fields. *Physical Review Letters*, 84(16):3550–3553.

[El-Zein, 2001] El-Zein, A. A. A. (2001). *Electron and photon interactions with molecules*. PhD thesis, University College London, Department of Physics and Astronomy, University College London, England.

[El-Zein et al., 2001] El-Zein, A. A. A., McKenna, P., Bryan, W. A., Johnston, I. M. G., Goodworth, T. R. J., Sanderson, J. H., Williams, I. D., Newell, W. R., Taday, P. F., Divall, E. J., and Langley, A. J. (2001). A detailed study of multiply charged ion production within a high intensity laser focus. *Physica Scripta*, T92:119–121.

[Eland, 1979] Eland, J. H. D. (1979). Angular distributions, energy disposal, and branching studied by photoelectron–photoion coincidence spectroscopy: O_2^+, NO^+, ICl^+, IBr^+, and I_2^+ fragmentation. *The Journal of Chemical Physics*, 70(6):2926–2933.

[Eland and Pearson, 1990] Eland, J. H. D. and Pearson, A. H. (1990). Simple radial position-sensitive detector with short deadtime for time-of-flight and coincidence experiments. *Measurement Science and Technology*, 1(1):36–40.

[Ellert and Corkum, 1999] Ellert, C. and Corkum, P. B. (1999). Role of electron localization in intense-field molecular ionization. *Physical Review A*, 59(5):R3170–R3174.

[English, 2007] English, E. M. L. (2007). *Laser Induced Ultrafast Dynamics in Atoms and Molecules*. PhD thesis, University College London, Department of Physics and Astronomy, University College London, England.

[English et al., 2006] English, E. M. L., Wood, J., Newell, W. R., McKenna, J., Calvert, C. R., Williams, I. D., Bryan, W. A., Turcu, I. C. E., Smith, J. M., Ertel, K. G., Divall, E. J., Chekhlov, O., and Torres, R. (2006). Revival of a rotational wavepacket initiated by ultrafast impulsive alignment. In *Central Laser Facility Annual Report 2005-2006, RAL-TR-2006-025*, pages 77–79. Council for the Central Laboratory of the Research Councils.

[Eppink and Parker, 1997] Eppink, A. T. J. B. and Parker, D. H. (1997). Velocity map imaging of ions and electrons using electrostatic lenses: Application in photoelectron and photofragment ion imaging of molecular oxygen. *Review of Scientific Instruments*, 68(9):3477–3484.

[Ergler et al., 2006a] Ergler, T., Feuerstein, B., Rudenko, A., Zrost, K., Schroter, C. D., Moshammer, R., and Ullrich, J. (2006a). Quantum-phase resolved mapping of ground-state vibrational D_2 wave packets via selective depletion in intense laser pulses. *Physical Review Letters*, 97(10):103004.

[Ergler et al., 2005] Ergler, T., Rudenko, A., Feuerstein, B., Zrost, K., Schroter, C. D., Moshammer, R., and Ullrich, J. (2005). Time-resolved imaging and manipulation of H_2 fragmentation in intense laser fields. *Physical Review Letters*, 95(9):093001.

[Ergler et al., 2006b] Ergler, T., Rudenko, A., Feuerstein, B., Zrost, K., Schroter, C. D., Moshammer, R., and Ullrich, J. (2006b). Spatiotemporal imaging of ultrafast molecular motion: Collapse and revival of the $D_2{}^+$ nuclear wave packet. *Physical Review Letters*, 97(19):193001.

[Ergler et al., 2006c] Ergler, T., Rudenko, A., Feuerstein, B., Zrost, K., Schroter, C. D., Moshammer, R., and Ullrich, J. (2006c). Ultrafast mapping of $H_2{}^+$ ($D_2{}^+$) nuclear wave packets using time-resolved Coulomb explosion imaging. *Journal of Physics B: Atomic, Molecular and Optical Physics*, 39(13):S493–S501.

[Fabian et al., 2003] Fabian, C., Kitzler, M., Milosevic, N., and Brabec, T. (2003). Multi-electron strong field theory. *Journal of Modern Optics*, 50(3-4):589–595.

[Ferray et al., 1988] Ferray, M., L'Huillier, A., Li, X. F., Lompre, L. A., Mainfray, G., and Manus, C. (1988). Multiple-harmonic conversion of 1064 nm radiation in rare gases. *Journal of Physics B: Atomic, Molecular and Optical Physics*, 21(3):L31–L35.

[Feuerstein et al., 2007] Feuerstein, B., Ergler, T., Rudenko, A., Zrost, K., Schroter, C. D., Moshammer, R., Ullrich, J., Niederhausen, T., and Thumm, U. (2007). Complete characterization of molecular dynamics in ultrashort laser fields. *Physical Review Letters*, 99(15):153002.

[Feuerstein and Thumm, 2003] Feuerstein, B. and Thumm, U. (2003). Mapping of coherent and decohering nuclear wave-packet dynamics in $D_2{}^+$ with ultrashort laser pulses. *Physical Review A*, 67(6):063408.

[Fielding, 2005] Fielding, H. H. (2005). Rydberg wavepackets in molecules: From observation to control. *Annual Review of Physical Chemistry*, 56:91–117.

[Fittinghoff et al., 1992] Fittinghoff, D. N., Bolton, P. R., Chang, B., and Kulander, K. C. (1992). Observation of nonsequential double ionization of helium with optical tunneling. *Physical Review Letters*, 69(18):2642–2645.

[Fittinghoff et al., 1994] Fittinghoff, D. N., Bolton, P. R., Chang, B., and Kulander, K. C. (1994). Polarization dependence of tunneling ionization of helium and neon by 120-fs pulses at 614 nm. *Physical Review A*, 49(3):2174–2177.

[Flechard et al., 2001] Flechard, X., Nguyen, H., Wells, E., Ben-Itzhak, I., and DePaola, B. D. (2001). Kinematically complete charge exchange experiment in the Cs^++Rb collision system using a MOT target. *Physical Review Letters*, 87(12):123203.

[Fohlisch et al., 2005] Fohlisch, A., Feulner, P., Hennies, F., Fink, A., Menzel, D., Sanchez-Portal, D., Echenique, P. M., and Wurth, W. (2005). Direct observation of electron dynamics in the attosecond domain. *Nature*, 436(7049):373–376.

[Fork and Martinez, 1984] Fork, R. L. and Martinez, O. E. (1984). Negative dispersion using pairs of prisms. *Optics Letters*, 9(5):150.

[Fransinski et al., 1989] Fransinski, L. J., Codling, K., and Hatherly, P. A. (1989). Multiphonon multiple ionisation of N_2 probed by covariance mapping. *Physics Letters A*, 142(8-9):499–503.

[Frasinski et al., 1987] Frasinski, L. J., Codling, K., Hatherly, P., Barr, J., Ross, I. N., and Toner, W. T. (1987). Femtosecond dynamics of multielectron dissociative ionization by use of a picosecond laser. *Physical Review Letters*, 58(23):2424–2427.

[Frasinski et al., 1989] Frasinski, L. J., Codling, K., and Hatherly, P. A. (1989). Covariance mapping: A correlation method applied to multiphoton multiple ionization. *Science*, 246(4933):1029–1031.

[Frasinski et al., 1994] Frasinski, L. J., Hatherly, P. A., Codling, K., Larsson, M., Persson, A., and Wahlstrom, C. G. (1994). Multielectron dissociative ionization of CO_2 in intense laser fields. *Journal of Physics B: Atomic, Molecular and Optical Physics*, 27(6):L109–L114.

[Frasinski et al., 2001] Frasinski, L. J., Plumridge, J., Posthumus, J. H., Codling, K., Taday, P. F., Divall, E. J., and Langley, A. J. (2001). Counterintuitive alignment of $H_2{}^+$ in intense femtosecond laser fields. *Physical Review Letters*, 86(12):2541–2544.

[Frasinski et al., 1999] Frasinski, L. J., Posthumus, J. H., Plumridge, J., Codling, K., Taday, P. F., and Langley, A. J. (1999). Manipulation of bond hardening in $H_2{}^+$ by chirping of intense femtosecond laser pulses. *Physical Review Letters*, 83(18):3625–3628.

[Frasinski et al., 1992] Frasinski, L. J., Stankiewicz, M., Hatherly, P. A., Cross, G. M., Codling, K., Langley, A. J., and Shaikh, W. (1992). Molecular H_2 in intense laser fields probed by electron-electron, electron-ion and ion-ion covariance techniques. *Physical Review A*, 46(11):R6789–R6792.

[Friedrich and Herschbach, 1995] Friedrich, B. and Herschbach, D. (1995). Alignment and trapping of molecules in intense laser fields. *Physical Review Letters*, 74(23):4623–4626.

[Friedrich and Herschbach, 1999] Friedrich, B. and Herschbach, D. (1999). Manipulating molecules via combined static and laser fields. *Journal of Physical Chemistry A*, 103(49):10280–10288.

[Gaire et al., 2007] Gaire, B., Sayler, A. M., Wang, P. Q., Johnson, N. G., Leonard, M., Parke, E., Carnes, K. D., and Ben-Itzhak, I. (2007). Determining the absolute efficiency of a delay line microchannel-plate detector using molecular dissociation. *Review of Scientific Instruments*, 78(2):024503.

[Garcia et al., 2005] Garcia, G. A., Nahon, L., Harding, C. J., Mikajlo, E. A., and Powis, I. (2005). A refocusing modified velocity map imaging electron/ion spectrometer adapted to synchrotron radiation studies. *Review of Scientific Instruments*, 76(5):053302.

[Gibson, 2004] Gibson, E. A. (2004). *Quasi-Phase Matching of Soft X-ray Light from High-Order Harmonic Generation using Waveguide Structures*. PhD thesis, University of Colorado, Department of Physics, University of Colorado, Colorado, USA.

[Giusti-Suzor et al., 1990] Giusti-Suzor, A., He, X., Atabek, O., and Mies, F. H. (1990). Above-threshold dissociation of H_2^+ in intense laser fields. *Physical Review Letters*, 64(5):515–518.

[Giusti-Suzor and Mies, 1992] Giusti-Suzor, A. and Mies, F. H. (1992). Vibrational trapping and suppression of dissociation in intense laser fields. *Physical Review Letters*, 68(26):3869–3872.

[Giusti-Suzor et al., 1995] Giusti-Suzor, A., Mies, F. H., DiMauro, L. F., Charron, E., and Yang, B. (1995). Dynamics of H_2^+ in intense laser fields. *Journal of Physics B: Atomic, Molecular and Optical Physics*, 28(3):309–339.

[Gollub et al., 2006] Gollub, C., Troppmann, U., and de Vivie-Riedle, R. (2006). The role of anharmonicity and coupling in quantum computing based on vibrational qubits. *New Journal of Physics*, 8(4):48.

[Goodworth, 2002] Goodworth, T. R. J. (2002). *Dynamics of atoms, molecules and ions in intense laser fields*. PhD thesis, University College London, Department of Physics and Astronomy, University College London, England.

[Goodworth et al., 2005] Goodworth, T. R. J., Bryan, W. A., Williams, I. D., and Newell, W. R. (2005). Reconstruction of atomic ionization probabilities in intense laser fields. *Journal of Physics B: Atomic, Molecular and Optical Physics*, 38(17):3083–3089.

[Goulielmakis et al., 2004] Goulielmakis, E., Uiberacker, M., Kienberger, R., Baltuska, A., Yakovlev, V., Scrinzi, A., Westerwalbesloh, T., Kleineberg, U., Heinzmann, U., Drescher, M., and Krausz, F. (2004). Direct measurement of light waves. *Science*, 305(5688):1267–1269.

[Greenwood et al., 2002] Greenwood, J. B., Johnston, I. M. G., McKenna, P., Williams, I. D., Goodworth, T. R. J., Sanderson, J. H., Bryan, W. A., El-Zein, A. A. A., Newell, W. R., Langley, A. J., and Divall, E. J. (2002). Suppression of multiple ionization of atomic ions in intense ultrafast laser pulses. *Physical Review Letters*, 88(23):233001.

[Griffin, 1989] Griffin, D. C. (1989). A review of radiative and dielectronic recombination for C and O ions. *Physica Scripta*, T28:17–24.

[Gubbini et al., 2006] Gubbini, E., Eichmann, U., Kalashnikov, M., and Sandner, W. (2006). Multiple ionization of Kr in an intense circularly polarized laser field. *Journal of Physics B: Atomic, Molecular and Optical Physics*, 39(13):S381–S387.

[Guo et al., 1998] Guo, C., Li, M., Nibarger, J. P., and Gibson, G. N. (1998). Single and double ionization of diatomic molecules in strong laser fields. *Physical Review A*, 58(6):R4271–R4274.

[Gyuzalian et al., 1979] Gyuzalian, R. N., Sogomonian, S. B., and Horvath, Z. G. (1979). Background-free measurement of time behaviour of an individual picosecond laser pulse. *Optics Communications*, 29(2):239–242.

[Hagstrum, 1956] Hagstrum, H. D. (1956). Metastable ions of the noble gases. *Physical Review*, 104(2):309–316.

[Hahn, 1997] Hahn, Y. (1997). Electron - Ion recombination processes - An overview. *Reports on Progress in Physics*, 60(7):691–759.

[Halbach, 1980] Halbach, K. (1980). Design of permanent multipole magnets with oriented rare earth colbalt materials. *Nuclear Instruments and Methods*, 196:1–10.

[Hankin et al., 2000] Hankin, S. M., Villeneuve, D. M., Corkum, P. B., and Rayner, D. M. (2000). Nonlinear ionization of organic molecules in high intensity laser fields. *Physical Review Letters*, 84(22):5082–5085.

[Hansch et al., 1996] Hansch, P., Walker, M. A., and Woerkom, L. D. V. (1996). Spatially dependent multiphoton multiple ionization. *Physical Review A*, 54(4):R2559–R2562.

[Hansch and Woerkom, 1996] Hansch, P. and Woerkom, L. D. V. (1996). High-precision intensity-selective observation of multiphoton ionization: A new method of photoelectron spectroscopy. *Optics Letters*, 21(16):1286.

[Hasegawa et al., 2001] Hasegawa, H., Hishikawa, A., and Yamanouchi, K. (2001). Coincidence imaging of Coulomb explosion of CS_2 in intense laser fields. *Chemical Physics Letters*, 36(1-2):57–63.

[Hatherly et al., 1994] Hatherly, P. A., Stankiewicz, M., Codling, K., Frasinski, L. J., and Cross, G. M. (1994). The multielectron dissociative ionization of molecular iodine in intense laser fields. *Journal of Physics B: Atomic, Molecular and Optical Physics*, 27(14):2993–3003.

[Hauri et al., 2004] Hauri, C., Kornelis, W., Helbing, F., Heinrich, A., Couairon, A., Mysyrowicz, A., Biegert, J., and Keller, U. (2004). Generation of intense, carrier-envelope phase-locked few-cycle laser pulses through filamentation. *Journal Applied Physics B: Lasers and Optics*, 79(6):673–677.

[Hecht, 1998] Hecht, E. (1998). *Optics*. Addison-Wesley, Reading, Massachusetts, USA, 3^{rd} edition.

[Heerlein et al., 2003] Heerlein, C., Zwicknagel, G., and Toepffer, C. (2003). Scaling law for recombination in electron coolers. *Nuclear Instruments and Methods in Physics Research Section B: Beam Interactions with Materials and Atoms*, 205:395–398.

[Hentsche et al., 2000] Hentsche, M., Cheng, Z., Krausz, F., and Spielmann, C. (2000). Generation of 0.1-TW optical pulses with a single-stage Ti:sapphire amplifier at a 1-kHz repetition rate. *Applied Physics B Lasers and Optics*, 70(sup. 1):S161–S164.

[Heritage et al., 1975] Heritage, J. P., Gustafson, T. K., and Lin, C. H. (1975). Observation of coherent transient birefringence in CS_2 vapor. *Physical Review Letters*, 34(21):1299–1302.

[Hillegas et al., 1994] Hillegas, C. W., Tull, J. X., Goswami, D., Strickland, D., and Warren, W. S. (1994). Femtosecond laser pulse shaping by use of microsecond radio-frequency pulses. *Optics Letters*, 19(10):737.

[Hishikawa et al., 1998a] Hishikawa, A., Iwamae, A., Hoshina, K., Kono, M., and Yamanouchi, K. (1998a). Coulomb explosion dynamics of N_2 in intense laser field by mass-resolved momentum imaging. *Chemical Physics*, 231(2-3):315–329.

[Hishikawa et al., 1998b] Hishikawa, A., Iwamae, A., Hoshina, K., Kono, M., and Yamanouchi, K. (1998b). Mass-resolved two-dimensional momentum imaging of the Coulomb explosion of N_2 and SO_2 in an intense laser field. *Chemical Physics Letters*, 282(3-4):283–291.

[Hishikawa et al., 1999] Hishikawa, A., Iwamae, A., and Yamanouchi, K. (1999). Ultrafast deformation of the geometrical structure of CO_2 induced in intense laser fields. *Physical Review Letters*, 83(6):1127–1130.

[Hishikawa et al., 2001] Hishikawa, A., Liu, S., Iwasaki, A., and Yamanouchi, K. (2001). Light-induced multiple electronic-state coupling of $O_2{}^+$ in intense laser fields. *The Journal of Chemical Physics*, 114(22):9856–9862.

[Hishikawa et al., 2006] Hishikawa, A., Takahashi, E. J., and Matsuda, A. (2006). Electronic and nuclear responses of fixed-in-space H_2S to ultrashort intense laser fields. *Physical Review Letters*, 97(24):243002.

[Hollas, 2002] Hollas, J. M. (2002). *Basic Atomic and Molecular Spectroscopy (Basic Concepts In Chemistry)*. Royal Society of Chemistry, Cambridge, UK, Fourth edition.

[Huber and Herzberg, 1979] Huber, K. P. and Herzberg, G. (1979). *Molecular spectra and molecular structure IV: Constants and diatomic molecules*. Van Nostrand Reinhold, New York, New York, USA.

[Huber and Herzberg, 2001] Huber, K. P. and Herzberg, G. (2001). *NIST Chemistry WebBook*. National Insitute of Standards and Technology, Gaithersburg, Maryland, USA.

[Iaconis and Walmsley, 1998] Iaconis, C. and Walmsley, I. (1998). Spectral phase interferometry for direct electric-field reconstruction of ultrashort optical pulses. *Optics Letters*, 23(10):792–794.

[Iaconis and Walmsley, 1999] Iaconis, C. and Walmsley, I. (1999). Self-referencing spectral interferometry for measuring ultrashort optical pulses. *IEEE Journal of Quantum Electronics*, 35(4):501–509.

[Ilkov et al., 1992] Ilkov, F. A., Decker, J. E., and Chin, S. L. (1992). Ionization of atoms in the tunnelling regime with experimental evidence using Hg atoms. *Journal of Physics B: Atomic, Molecular and Optical Physics*, 25(19):4005–4020.

[Itatani et al., 2005] Itatani, J., Zeidler, D., Levesque, J., Spanner, M., Villeneuve, D. M., and Corkum, P. B. (2005). Controlling high harmonic generation with molecular wave packets. *Physical Review Letters*, 94(12):123902.

[Janszky et al., 1977] Janszky, J., Corradi, G., and Gyuzalian, R. N. (1977). On a possibility of analysing the temporal characteristics of short light pulses. *Optics Communications*, 23(3):293–298.

[Johnsson et al., 2007] Johnsson, P., Siu, W., Gijsbertsen, A., Meijer, A. S., der Zande, W. J. V., Verhoeven, J., and Vrakking, M. J. J. (2007). Single-shot harmonic content measurements and velocity map imaging at the FLASH free electron laser. In *HASYLAB Annual Report 2007 - PART I*, pages 445–446. HASSYLAB.

[Judson and Rabitz, 1992] Judson, R. S. and Rabitz, H. (1992). Teaching lasers to control molecules. *Physical Review Letters*, 68(10):1500–1503.

[Kajumba, 2007] Kajumba, N. D. (2007). *Angular dependence of high harmonic generation from impulsively aligned molecules*. PhD thesis, Imperial College London, Blackett laboratory Laser Consortium, Imperial College London, England.

[Kane and Trebino, 1993a] Kane, D. J. and Trebino, R. (1993a). Characterization of arbitrary femtosecond pulses using frequency-resolved optical gating. *IEEE Journal of Quantum Electronics*, 29(2):571–579.

[Kane and Trebino, 1993b] Kane, D. J. and Trebino, R. (1993b). Single-shot measurement of the intensity and phase of an arbitrary ultrashort pulse by using frequency-resolved optical gating. *Optics Letters*, 18(10):823.

[Kane and Squier, 1997] Kane, S. and Squier, J. (1997). Grism-pair stretcher–compressor system for simultaneous second- and third-order dispersion compensation in chirped-pulse amplification. *Journal of the Optical Society of America B*, 14(3):661–665.

[Kärtner et al., 1997] Kärtner, F. X., Matuschek, N., Schibli, T., Keller, U., Haus, H. A., Heine, C., Morf, R., Scheuer, V., Tilsch, M., and Tschudi, T. (1997). Design and fabrication of double-chirped mirrors. *Optics Letters*, 22(11):831–833.

[Kato, 1950] Kato, T. (1950). On the adiabatic theorem of quantum mechanics. *Journal of the Physical Society of Japan*, 5(6):435–439.

[Keitel and Knight, 1995] Keitel, C. H. and Knight, P. L. (1995). Monte carlo classical simulations of ionization and harmonic generation in the relativistic domain. *Physical Review A*, 51(2):1420–1430.

[Keldysh, 1965] Keldysh, L. V. (1965). Ionization in the field of a strong electromagnetic wave. *Soviet Physics JETP*, 20(4):1307–1314.

[Kim and Pratt, 1983] Kim, Y. S. and Pratt, R. H. (1983). Direct radiative recombination of electrons with atomic ions: Cross sections and rate coefficients. *Physical Review A*, 27(6):2913–2924.

[Kling and Vrakking, 2008] Kling, M. F. and Vrakking, M. J. J. (2008). Attosecond electron dynamics. *Annual Review of Physical Chemistry*, 59:463–492.

[Kolmeder et al., 1979] Kolmeder, C., Zinth, W., and Kaiser, W. (1979). Second harmonic beam analysis, a sensitive technique to determine the duration of single ultrashort laser pulses. *Optics Communications*, 30(3):453–457.

[Kornev et al., 2003] Kornev, A. S., Tulenko, E. B., and Zon, B. A. (2003). Kinetics of multiple ionization of rare-gas atoms in a circularly polarized laser field. *Physical Reveiw A*, 68(4):043414.

[Kornev et al., 2004] Kornev, A. S., Tulenko, E. B., and Zon, B. A. (2004). Ne^{+} and Ne^{2+} ion formation in circularly polarized laser fields: Comparison between theory and experiment. *Physical Review A (Atomic, Molecular, and Optical Physics)*, 69(6):065401.

[Kramers, 1923] Kramers, H. A. (1923). On the theory of x-ray absorption and of the continuous x-ray spectrum. *Philosophical Magazine*, 46:836–871.

[Krause et al., 1992] Krause, J. L., Schafer, K., and Kulander, K. C. (1992). High-order harmonic generation from atoms and ions in the high intensity regime. *Physical Review Letters*, 68(24):3535–3538.

[Krausz et al., 1986] Krausz, F., Juhasz, T., Bakos, J. S., and Kuti, C. (1986). Microprocessor-based system for measurement of the characteristics of ultra-short laser pulses. *Journal of Physics E: Scientific Instruments*, 19(12):1027–1030.

[Kulander et al., 1995] Kulander, K. C., Cooper, J., and Schafer, K. J. (1995). Laser-assisted inelastic rescattering during above-threshold ionization. *Physical Review A*, 51(1):561–568.

[Kulander et al., 1991] Kulander, K. C., Schafer, K. J., and Krause, J. L. (1991). Single-active electron calculation of multiphoton process in krypton. *International Journal of Quantum Chemistry*, 40(S25):415–429.

[Kumarappan et al., 2008] Kumarappan, V., Holmegaard, L., Martiny, C., Madsen, C. B., Kjeldsen, T. K., Viftrup, S. S., Madsen, L. B., and Stapelfeldt, H. (2008). Multiphoton electron angular distributions from laser-aligned CS_2 molecules. *Physical Review Letters*, 100(9):093006.

[Lafon et al., 2001] Lafon, R., Chaloupka, J. L., Sheehy, B., Paul, P. M., Agostini, P., Kulander, K. C., and DiMauro, L. F. (2001). Electron energy spectra from intense laser double ionization of helium. *Physical Review Letters*, 86(13):2762–2765.

[Landau and Lifshitz, 1977] Landau, L. D. and Lifshitz, E. M. (1977). *Quantum Mechanics: Non-Relativistic Theory*. Pergamon Press, Oxford, UK.

[Laporte and Meggers, 1925] Laporte, O. and Meggers, W. F. (1925). Some rules of spectral structure. *Journal of the Optical Society of America*, 11(5):459.

[Larochelle et al., 1998] Larochelle, S., Talebpour, A., and Chin, S. L. (1998). Non-sequential multiple ionization of rare gas atoms in a Ti:sapphire laser field. *Journal of Physics B: Atomic, Molecular and Optical Physics*, 31(6):1201–1214.

[Larsen et al., 2000] Larsen, J. J., Hald, K., Bjerre, N., Stapelfeldt, H., and Seideman, T. (2000). Three dimensional alignment of molecules using elliptically polarized laser fields. *Physical Review Letters*, 85(12):2470–2473.

[Larsen et al., 1999] Larsen, J. J., Sakai, H., Safvan, C. P., Wendt-Larsen, I., and Stapelfeldt, H. (1999). Aligning molecules with intense nonresonant laser fields. *The Journal of Chemical Physics*, 111(17):7774–7781.

[Larsson, 1995] Larsson, M. (1995). Atomic and molecular physics with ion storage rings. *Reports on Progress in Physics*, 58(10):1267–1319.

[L'Huillier et al., 1983] L'Huillier, A., Lompre, L. A., Mainfray, G., and Manus, C. (1983). Multiply charged ions induced by multiphoton absorption in rare gases at 0.53 μm. *Physical Review A*, 27(5):2503–2512.

[Lee et al., 2006] Lee, K. F., Légaré, F., Villeneuve, D. M., and Corkum, P. B. (2006). Measured field-free alignment of deuterium by few-cycle pulses. *Journal of Physics B: Atomic, Molecular and Optical Physics*, 39(20):4081–4086.

[Lee et al., 2004] Lee, K. F., Villeneuve, D. M., Corkum, P. B., and Shapiro, E. A. (2004). Phase control of rotational wave packets and quantum information. *Physical Review Letters*, 93(23):233601.

[Légaré et al., 2005] Légaré, F., Lee, K. F., Litvinyuk, I. V., Dooley, P. W., Bandrauk, A. D., Villeneuve, D. M., and Corkum, P. B. (2005). Imaging the time-dependent structure of a molecule as it undergoes dynamics. *Physical Review A (Atomic, Molecular, and Optical Physics)*, 72(5):052717.

[Lewenstein et al., 1994] Lewenstein, M., Balcou, P., Ivanov, M. Y., L'Huillier, A., and Corkum, P. B. (1994). Theory of high-harmonic generation by low-frequency laser fields. *Physical Review A*, 49(3):2117–2132.

[Litvinyuk et al., 2003] Litvinyuk, I. V., Lee, K. F., Dooley, P. W., Rayner, D. M., Villeneuve, D. M., and Corkum, P. B. (2003). Alignment-dependent strong field ionization of molecules. *Physical Review Letters*, 90(23):233003.

[Litvinyuk et al., 2005] Litvinyuk, I. V., Légaré, F., Dooley, P. W., Villeneuve, D. M., Corkum, P. B., Zanghellini, J. ., Pegarkov, A., Fabian, C., and Brabec, T. (2005). Shakeup excitation during optical tunnel ionization. *Physical Review Letters*, 94(3):033003.

[Loch et al., 2002] Loch, S. D., Pindzola, M. S., Ballance, C. P., Griffin, D. C., Mitnik, D. M., Badnell, N. R., O'Mullane, M. G., Summers, H. P., and Whiteford, A. D. (2002). Electron-impact ionization of all ionization stages of krypton. *Physical Review A*, 66(5):052708.

[Lompre et al., 1977] Lompre, L. A., Mainfray, G., Manus, C., and Thebault, J. (1977). Multiphoton ionization of rare gases by a tunable-wavelength 30-psec laser pulse at 1.06 μm. *Physical Review A*, 15(4):1604–1612.

[Maine et al., 1988] Maine, P., Strickland, D., Bado, P., Pessot, M., and G.Mourou (1988). Generation of ultrahigh peak power pulses by chirped pulseamplification. *IEEE Journal of Quantum Electronics*, 24(2):398–403.

[Man et al., 1987] Man, K. F., Smith, A. C. H., and Harrison, M. F. A. (1987). A measurement of the cross section for electron impact ionisation of Ne^+, Ar^+, Kr^+ and Xe^+. *Journal of Physics B: Atomic and Molecular Physics*, 20(21):5865–5880.

[Man et al., 1993] Man, K. F., Smith, A. C. H., and Harrison, M. F. A. (1993). A measurement of the cross section for electron impact ionization of Ar^{2+}, Kr^{2+} and Xe^{2+}. *Journal of Physics B: Atomic, Molecular and Optical Physics*, 26(7):1365–1378.

[Mangles et al., 2004] Mangles, S. P. D., Murphy, C. D., Najmudin, Z., Thomas, A. G. R., Collier, J. L., Dangor, A. E., Divall, E. J., Foster, P. S., Gallacher, J. G., Hooker, C. J., Jaroszynski, D. A., Langley, A. J., Mori, W. B., Norreys, P. A., Tsung, F. S., Viskup,

R., Walton, B. R., and Krushelnick, K. (2004). Monoenergetic beams of relativistic electrons from intense laser-plasma interactions. *Nature*, 431(7008):535–538.

[Marangos, 2006] Marangos, J. P. (2006). Attophysics: Tunnel vision. *Nature*, 446(7136):619–621.

[Marcatili and Schmeltzer, 1964] Marcatili, E. A. and Schmeltzer, R. A. (1964). Hollow metallic and dielectric waveguides for long distance optical transmission and lasers. *Bell Systems Technology Journal*, 43:1783–1809.

[Matuschek, 1998] Matuschek, Y. (1998). Theory of double chirped mirrors. *IEEE Journal of Selected Topics in Quantum Electronics*, 4(2):197–208.

[Matuschek et al., 1999] Matuschek, Y., Kärtner, F. X., and Keller, U. (1999). Analytical design of double-chirped mirrors with custom-tailored dispersion characteristics. *IEEE Journal of Quantum Electronics*, 35(2):129–137.

[Mauritsson, 2003] Mauritsson, J. (2003). *Temporal aspects of high intensity laser-matter interactions*. PhD thesis, Lund University, Lund Institute of Technology, Lund University, Lund, Sweeden.

[McDaniel et al., 1993] McDaniel, E. W., Mitchell, J. B. A., and Rudd, M. E. (1993). *Atomic Collisions*. John Wiley and Sons Inc., New York, New York, USA.

[McKenna, 2006] McKenna, J. (2006). *Probing atomic and molecular dynamics with intense femtosecond laser pulses*. PhD thesis, Queen's University Belfast, School of Mathematics and Physics, Queen's University Belfast, Northern Ireland.

[Mckenna et al., 2007] Mckenna, J., Bryan, W. A., Calvert, C. R., English, E. M. L., Wood, J., Murphy, D. S., Turcu, I. C. E., Smith, J. M., Ertel, K. G., Chekhlov, O., Divall, E. J., Mccann, J. F., Newell, W. R., and Williams, I. D. (2007). Observing time-dependent vibrational quantum dynamics in deuterium hydride molecular ions. *Journal of Modern Optics*, 54(7):1127–1138.

[McKenna et al., 2006] McKenna, J., Calvert, C. R., Murphy, D. S., McCann, J. F., Williams, I. D., Wood, J., English, E. M. L., Newell, W. R., Bryan, W. A., Turcu, I. C. E., Chekhlov, O., Ertel, K., Smith, J. M., Divall, E. J., and Torres, R. (2006). Observing time-dependent rotational and vibrational quantum dynamics in deuterium. In *Central Laser Facility Annual Report 2005-2006, RAL-TR-2006-025*, pages 84–87. Council for the Central Laboratory of the Research Councils.

[McKenna et al., 2005] McKenna, J., Suresh, M., Srigengan, B., Williams, I. D., Wood, J., English, E. M. L., Stebbings, S. L., Bryan, W. A., Newell, W. R., and Turcu, I. C. E. (2005). Intense field dynamics of H_2 and D_2 with few-cycle pulses. In *Central Laser Facility Annual Report 2004-2005, RAL-TR-2005-025*, pages 53–56. Council for the Central Laboratory of the Research Councils.

[McKenna, 2000] McKenna, P. (2000). *Electron and laser interactions with positive ions*. PhD thesis, Queen's University Belfast, School of Mathematics and Physics, Queen's University Belfast, Northern Ireland.

[McLaughlin and Hahn, 1991] McLaughlin, D. J. and Hahn, Y. (1991). Scaling behavior of radiative recombination cross sections and rate coefficients. *Physical Review A*, 43(3):1313–1323.

[McPherson et al., 1987] McPherson, A., Gibson, G., Jara, H., Johann, U., Luk, T. S., McIntyre, I. A., Boyer, K., and Rhodes, C. K. (1987). Studies of multiphoton production of vacuum-ultraviolet radiation in the rare gases. *Journal of the Optical Society of America B*, 4(4):595.

[Meacher et al., 1991] Meacher, D. R., Meyler, P. E., Hughes, I. G., and Ewart, P. (1991). Observations of the collapse and fractional revival of a Rydberg wavepacket in atomic rubidium. *Journal of Physics B: Atomic, Molecular and Optical Physics*, 24(3):L63–L69.

[Mergel et al., 1995] Mergel, V., Dörner, R., Ullrich, J., Jagutzki, O., Lencinas, S., Nüttgens, S., Spielberger, L., Unverzagt, M., Cocke, C. L., Olson, R. E., Schulz, M., Buck, U., Zanger, E., Theisinger, W., Isser, M., Geis, S., and Schmidt-Böcking, H. (1995). State selective scattering angle dependent capture cross sections measured by cold target recoil ion momentum spectroscopy. *Physical Review Letters*, 74(12):2200–2203.

[Merzbacher, 1998] Merzbacher, E. (1998). *Quantum Mechanics*. Wiley, London, UK, third edition.

[Minns et al., 2003] Minns, R. S., Patel, R., Verlet, J. R. R., and Fielding, H. H. (2003). Optical control of the rotational angular momentum of a molecular Rydberg wave packet. *Physical Review Letters*, 91(24):243601.

[Moreno et al., 1995] Moreno, P., Plaja, L., Malyshev, V., and Roso, L. (1995). Influence of barrier suppression in high-order harmonic generation. *Physical Review A*, 51(6):4746–4753.

[Morse, 1929] Morse, P. M. (1929). Diatomic molecules according to the wave mechanics. II vibrational levels. *Physical Review*, 34(1):57–64.

[Moshammer et al., 2000] Moshammer, R., Feuerstein, B., Schmitt, W., Dorn, A., Schröter, C. D., Ullrich, J., Rottke, H., Trump, C., Wittmann, M., Korn, G., Hoffmann, K., and Sandner, W. (2000). Momentum distributions of Ne^{n+} ions created by an intense ultrashort laser pulse. *Physical Review Letters*, 84(3):447–450.

[Moshammer et al., 1994] Moshammer, R., Ullrich, J., Unverzagt, M., Schmidt, W., Jardin, P., Olson, R. E., Mann, R., Dörner, R., Mergel, V., Buck, U., and Schmidt-Böcking, H. (1994). Low-energy electrons and their dynamical correlation with recoil

ions for single ionization of helium by fast, heavy-ion impact. *Physical Review Letters*, 73(25):3371–3374.

[Moshammer et al., 1996] Moshammer, R., Ullrich, J., Unverzagt, M., Schmitt, W., and Schmidt-Bocking, B. (1996). A 4π recoil-ion electron momentum analyzer: A high-resolution microscope for the investigation of the dynamics of atomic, molecular and nuclear reactions. *Nuclear Instruments and Methods in Physics Research Section B: Beam Interactions with Materials and Atoms*, 108(4):425–445.

[Moulton, 1986] Moulton, P. F. (1986). Spectroscopic and laser characteristics of Ti:Al_2O_3. *Journal of the Optical Society of America B*, 3(1):125–133.

[Mourou et al., 2006] Mourou, G. A., Tajima, T., and Bulanov, S. V. (2006). Optics in the relativistic regime. *Reviews of Modern Physics*, 78(2):309.

[Mulliken, 1939] Mulliken, R. S. (1939). Intensities of electronic transitions in molecular spectra II. charge-transfer spectra. *The Journal of Chemical Physics*, 7(1):20–34.

[Murphy et al., 2007a] Murphy, D. S., McKenna, J., Calvert, C. R., Bryan, W. A., English, E. M. L., Wood, J., Turcu, I. C. E., Newell, W. R., Williams, I. D., and McCann, J. F. (2007a). Controlling dissociation processes in the $D^+{}_2$ molecular ion using high-intensity, ultrashort laser pulses. *Journal of Physics B: Atomic, Molecular and Optical Physics*, 40(11):S359–S372.

[Murphy et al., 2007b] Murphy, D. S., McKenna, J., Calvert, C. R., Williams, I. D., and McCann, J. F. (2007b). Ultrafast coherent control and quantum encoding of molecular vibrations in $D_2{}^+$ using intense laser pulses. *New Journal of Physics*, 9(8):260.

[Newell et al., 2003] Newell, W. R., Bryan, W. A., and Williams, I. D. (2003). Atomic and molecular ions in intense ultra-fast laser fields. *The European Physical Journal D*, 26:99–104.

[Ni, 2006] Ni, Y. (2006). *From strong field ionization to the generation of attosecond laser pulses*. PhD thesis, FOM Institute for Atomic and Molecular Physics (AMOLF), FOM Institute for Atomic and Molecular Physics, Amsterdam, The Netherlands.

[Niederhausen and Thumm, 2008] Niederhausen, T. and Thumm, U. (2008). Controlled vibrational quenching of nuclear wave packets in $D_2{}^+$. *Physical Review A (Atomic, Molecular, and Optical Physics)*, 77(1):013407.

[Niikura et al., 2003] Niikura, H., Corkum, P. B., and Villeneuve, D. M. (2003). Controlling vibrational wave packet motion with intense modulated laser fields. *Physical Review Letters*, 90(20):203601.

[Niikura et al., 2004] Niikura, H., Villeneuve, D. M., and Corkum, P. B. (2004). Stopping a vibrational wave packet with laser-induced dipole forces. *Physical Review Letters*, 92(13):133002.

[Niikura et al., 2006] Niikura, H., Villeneuve, D. M., and Corkum, P. B. (2006). Controlling vibrational wave packets with intense, few-cycle laser pulses. *Physical Review A (Atomic, Molecular, and Optical Physics)*, 73(2):021402.

[Nisoli et al., 1996] Nisoli, M., Silvestri, S. D., and Svelto, O. (1996). Generation of high energy 10 fs pulses by a new pulse compression technique. *Applied Physics Letters*, 68(20):2793–2795.

[Nisoli et al., 1997] Nisoli, M., Silvestri, S. D., Svelto, O., Szipocs, R., Ferencz, K., Spielmann, C., Sartania, S., and Krausz, F. (1997). Compression of high-energy laser pulses below 5fs. *Optics Letters*, 22(8):522–524.

[Orr et al., 2007] Orr, P. A., Williams, I. D., Greenwood, J. B., Turcu, I. C. E., Bryan, W. A., Pedregosa-Gutierrez, J., and Walter, C. W. (2007). Above threshold dissociation of vibrationally cold HD^+ molecules. *Physical Review Letters*, 98(16):163001.

[Ortigoso et al., 1999] Ortigoso, J., Rodríguez, M., Gupta, M., and Friedrich, B. (1999). Time evolution of pendular states created by the interaction of molecular polarizability with a pulsed nonresonant laser field. *The Journal of Chemical Physics*, 110(8):3870–3875.

[O'Shea et al., 2000] O'Shea, P., Kimmel, M., Gu, X., and Trebino, R. (2000). Increased-bandwidth in ultrashort-pulse measurement using an angle-dithered nonlinear-optical crystal. *Optics Express*, 7(10):342–349.

[O'Shea et al., 2001] O'Shea, P., Kimmel, M., Gu, X., and Trebino, R. (2001). Highly simplified device for ultrashort-pulse measurement. *Optics Letters*, 26(12):932–934.

[Pavičić, 2004] Pavičić, D. (2004). *Coulomb Explosion and Intense-Field Photodissociation of Ion-Beam H_2^+ and D_2^+*. PhD thesis, Ludwig-Maximilians-Universität, Ludwig-Maximilians-Universität, München, Germany.

[Pavičić et al., 2005] Pavičić, D., Kiess, A., Hänsch, T. W., and Figger, H. (2005). Intense-laser-field ionization of the hydrogen molecular ions H_2^+ and D_2^+ at critical internuclear distances. *Physical Review Letters*, 94(16):163002.

[Pavičić et al., 2007] Pavičić, D., Lee, K. F., Rayner, D. M., Corkum, P. B., and Villeneuve, D. M. (2007). Direct measurement of the angular dependence of ionization for N_2, O_2, and CO_2 in intense laser fields. *Physical Review Letters*, 98(24):243001.

[Peng et al., 2003] Peng, L.-Y., Dundas, D., McCann, J. F., Taylor, K. T., and Williams, I. D. (2003). Dynamic tunnelling ionization of H_2^+ in intense fields. *Journal of Physics B: Atomic, Molecular and Optical Physics*, 36(18):L295–L302.

[Perelomov et al., 1966] Perelomov, A. M., Popov, V. S., and Terent'ev, M. V. (1966). Ionization of atoms in an alternating electric field. *Soviet Physics JETP*, 23(5):924–934.

[Peterson and Bucksbaum, 2001] Peterson, E. R. and Bucksbaum, P. H. (2001). Above-threshold double-ionization spectroscopy of argon. *Physical Review A*, 64(5):053405.

[Pfeifer et al., 2006] Pfeifer, T., Spielmann, C., and Gerber, G. (2006). Femtosecond x-ray science. *Reports on Progress in Physics*, 69(2):443–505.

[Plummer and McCann, 1997] Plummer, M. and McCann, J. F. (1997). Orientation dependence of field ionization of the hydrogen molecular ion. *Journal of Physics B: Atomic, Molecular and Optical Physics*, 30(11):L401–L411.

[Popov, 1999] Popov, V. S. (1999). On the history of developing the theory of tunneling ionization in atoms and ions. *Physics-Uspekhi*, 42(7):733–734.

[Popov, 2004] Popov, V. S. (2004). Tunnel and multiphoton ionization of atoms and ions in a strong laser field (Keldysh theory). *Physics-Uspekhi*, 47(9):855–885.

[Posthumus, 2001] Posthumus, J., editor (2001). *Molecules and Clusters in Intense Laser Fields*. Cambridge University Press, Cambridge, UK.

[Posthumus, 2004] Posthumus, J. H. (2004). The dynamics of small molecules in intense laser fields. *Reports on Progress in Physics*, 67(5):623–665.

[Posthumus et al., 1995] Posthumus, J. H., Frasinski, L. J., Giles, A. J., and Codling, K. (1995). Dissociative ionization of molecules in intense laser fields: a method of predicting ion kinetic energies and appearance intensities. *Journal of Physics B: Atomic, Molecular and Optical Physics*, 28(10):L349–L353.

[Posthumus et al., 1996] Posthumus, J. H., Giles, A. J., Thompson, M. R., and Codling, K. (1996). Field-ionization, Coulomb explosion of diatomic molecules in intense laser fields. *Journal of Physics B: Atomic, Molecular and Optical Physics*, 29(23):5811–5829.

[Posthumus et al., 2000] Posthumus, J. H., Plumridge, J., Frasinski, L. J., Codling, K., Divall, E. J., Langley, A. J., and Taday, P. F. (2000). Slow protons as a signature of zero-photon dissociation of $H_2{}^+$ in intense laser fields. *Journal of Physics B: Atomic, Molecular and Optical Physics*, 33(16):L563–L569.

[Posthumus et al., 1999] Posthumus, J. H., Plumridge, J., Taday, P. F., Sanderson, J. H., Langley, A. J., Codling, K., and Bryan, W. A. (1999). Sub-pulselength time resolution of bond softening and coulomb explosion using polarization control of laser-induced alignment. *Journal of Physics B: Atomic, Molecular and Optical Physics*, 32(5):L93–L101.

[Powis, 1993] Powis, I. (1993). Photoelectron–photofragment ion recoil vector correlations in the dissociative photoionization of PF_3 at He I and Ne I ionizing wavelengths. *The Journal of Chemical Physics*, 99(5):3436–3443.

[Proctor and Wise, 1992] Proctor, B. and Wise, F. W. (1992). Quartz prism sequence for reduction of cubic phase in a mode-locked Ti:Al_2O_3 laser. *Optics Letters*, 17(18):1295.

[Protopapas et al., 1996] Protopapas, M., Keitel, C. H., and Knight, P. L. (1996). Relativistic mass shift effects in adiabatic intense laser field stabilization of atoms. *Journal of Physics B: Atomic, Molecular and Optical Physics*, 29(16):L591–L598.

[Protopapas et al., 1997] Protopapas, M., Keitel, C. H., and Knight, P. L. (1997). Atomic physics with super-high intensity lasers. *Reports on Progress in Physics*, 60(4):389–486.

[Raab et al., 1987] Raab, E. L., Prentiss, M., Cable, A., Chu, S., and Pritchard, D. E. (1987). Trapping of neutral sodium atoms with radiation pressure. *Physical Review Letters*, 59(23):2631–2634.

[Rivière et al., 2008] Rivière, P., Ruiz, C., and Rost, J.-M. (2008). Attosecond light-pulse-induced photoassociation. *Physical Review A (Atomic, Molecular, and Optical Physics)*, 77(3):033421.

[Robinett, 2004] Robinett, R. W. (2004). Quantum wave packet revivals. *Physics Reports*, 392(1-2):1–119.

[Robinson et al., 2006] Robinson, J. S., Haworth, C. A., Teng, H., Marangos, J. P., and Tisch, J. W. G. (2006). The generation of intense, transform-limited laser pulses with tunable duration from 6 to 30fs in a differentially pumped hollow fibre. *Applied Physics B Lasers and Optics*, 85(8):525–529.

[Rolland and Corkum, 1988] Rolland, C. and Corkum, P. B. (1988). Compression of high-power optical pulses. *Journal of the Optical Society of America B*, 5(3):641.

[Rolles et al., 2005] Rolles, D., Pesic, Z. D., Perri, M., Bilodeau, R. C., Ackerman, G. D., Rude, B. S., Kilcoyne, A. L. D., Bozek, J. D., and Berrah, N. (2005). A velocity map imaging spectrometer for electron-ion and ion-ion coincidence experiments with synchrotron radiation. *Nuclear Instruments and Methods in Physics Research Section B: Beam Interactions with Materials and Atoms*, 261(1-2):170–174.

[Rosca-Pruna et al., 2001] Rosca-Pruna, F., Springate, E., Offerhaus, H. L., Krishnamurthy, M., Farid, N., Nicole, C., and Vrakking, M. J. J. (2001). Spatial alignment of diatomic molecules in intense laser fields: I. Experimental results. *Journal of Physics B: Atomic, Molecular and Optical Physics*, 34(23):4919–4938.

[Rosca-Pruna and Vrakking, 2001] Rosca-Pruna, F. and Vrakking, M. J. J. (2001). Experimental observation of revival structures in picosecond laser-induced alignment of I_2. *Physical Review Letters*, 87(15):153902.

[Rudenko et al., 2005] Rudenko, A., Feuerstein, B., Zrost, K., de Jesus, V. L. B., Ergler, T., Dimopoulou, C., Schröter, C. D., Moshammer, R., and Ullrich, J. (2005). Frag-

mentation dynamics of molecular hydrogen in strong ultrashort laser pulses. *Journal of Physics B: Atomic, Molecular and Optical Physics*, 38(5):487–501.

[Rudenko et al., 2004] Rudenko, A., Zrost, K., Feuerstein, B., de Jesus, V. L. B., Schröter, C. D., Moshammer, R., and Ullrich, J. (2004). Correlated multielectron dynamics in ultrafast laser pulse interactions with atoms. *Physical Review Letters*, 93(25):253001.

[Rulliere, 1998] Rulliere, C. (1998). *Femtosecond Laser Pulses Principles and Experiments*. Springer Verlag, Heidelberg, Germany.

[Saito and Kobayashi, 2002] Saito, T. and Kobayashi, T. (2002). Conformational change in azobenzene in photoisomerization process studied with chirp-controlled sub-10-fs pulses. *Journal of Physical Chemistry A*, 106(41):9436–9441.

[Saloman, 2007] Saloman, E. B. (2007). Energy levels and observed spectral lines of krypton, Kr I through Kr XXXVI. *Journal of Physical and Chemical Reference Data*, 36(1):215–386.

[Sanderson et al., 2001] Sanderson, J. H., Goodworth, T. R. J., Bryan, W. A., El-Zein, A., Taday, P. F., Dival, E. J., and Langley, A. J. (2001). Ion momentum imaging of carbonyl sulphide in high intensity femtosecond laser pulses. In *Central Laser Facility Annual Report 2000-2001, RAL-TR-2001-025*, pages 63–64. Council for the Central Laboratory of the Research Councils.

[Sändig et al., 2000] Sändig, K., Figger, H., and Hänsch, T. W. (2000). Dissociation dynamics of $H_2{}^+$ in intense laser fields: Investigation of photofragments from single vibrational levels. *Physical Review Letters*, 85(23):4876–4879.

[Schafer et al., 1993] Schafer, K. J., Yang, B., DiMauro, L. F., and Kulander, K. C. (1993). Above threshold ionization beyond the high harmonic cutoff. *Physical Review Letters*, 70(11):1599–1602.

[Schiff, 1955] Schiff, L. I. (1955). *Quantum Mechanics*. McGraw-Hill, New York, New York, USA, Second edition.

[Schmidt et al., 1994] Schmidt, M., Normand, D., and Cornaggia, C. (1994). Laser-induced trapping of chlorine molecules with pico- and femtosecond pulses. *Physical Review A*, 50(6):5037–5045.

[Scrinzi et al., 1999] Scrinzi, A., Geissler, M., and Brabec, T. (1999). Ionization above the Coulomb barrier. *Physical Review Letters*, 83(4):706–709.

[Scrinzi et al., 2006] Scrinzi, A., Ivanov, M. Y., Kienberger, R., and Villeneuve, D. M. (2006). Attosecond physics. *Journal of Physics B: Atomic, Molecular and Optical Physics*, 39(1):R1–R37.

[Seideman, 1999] Seideman, T. (1999). Revival structure of aligned rotational wave packets. *Physical Review Letters*, 83(24):4971–4974.

[Seideman, 2001] Seideman, T. (2001). On the dynamics of rotationally broad, spatially aligned wave packets. *The Journal of Chemical Physics*, 115(13):5965–5973.

[Seideman et al., 1995] Seideman, T., Ivanov, M. Y., and Corkum, P. B. (1995). Role of electron localization in intense-field molecular ionization. *Physical Review Letters*, 75(15):2819–2822.

[Shapiro et al., 2003] Shapiro, E. A., Spanner, M., and Ivanov, M. Y. (2003). Quantum logic approach to wave packet control. *Physical Review Letters*, 91(23):237901.

[Sharan and Goswami, 2002] Sharan, A. and Goswami, D. (2002). Atomic photography. *Current Science*, 82(1):30–37.

[Sharp, 1971] Sharp, T. E. (1971). Potential-energy curves for molecular hydrogen and its ions. *Atomic Data*, 2:119–169.

[Sherriff, 1998] Sherriff, R. E. (1998). Analytic expressions for group-delay dispersion and cubic dispersion in arbitrary prism sequences. *Journal of the Optical Society of America B*, 15(3):1224–1230.

[Shirley, 1965] Shirley, J. H. (1965). Solution of the Schrödinger equation with a hamiltonian periodic in time. *Physical Review*, 138(4B):B979–B987.

[Shuman et al., 1999] Shuman, T., Walmsley, I. A., Waxer, L., Anderson, M., Iaconis, C., and Bromage, J. (1999). Real-time SPIDER: ultrashort pulse characterization at 20 Hz. *Optics Express*, 5(6):134–143.

[Siegman, 1986] Siegman, A. E. (1986). *Lasers*. University Science Books, Sausalito, California, USA.

[Springate et al., 2001] Springate, E., Rosca-Pruna, F., Offerhaus, H. L., Krishnamurthy, M., and Vrakking, M. J. J. (2001). Spatial alignment of diatomic molecules in intense laser fields: II. Numerical modelling. *Journal of Physics B: Atomic, Molecular and Optical Physics*, 34(23):4939–4956.

[Stapelfeldt, 2003] Stapelfeldt, H. (2003). Alignment of molecules by strong laser pulses. *The European Physical Journal D - Atomic, Molecular, Optical and Plasma Physics*, 26(1):15–19.

[Stapelfeldt, 2004] Stapelfeldt, H. (2004). Laser aligned molecules: Applications in physics and chemistry. *Physica Scripta*, T110:132–136.

[Stapelfeldt et al., 1995] Stapelfeldt, H., Constant, E., and Corkum, P. B. (1995). Wave packet structure and dynamics measured by Coulomb explosion. *Physical Review Letters*, 74(19):3780–3783.

[Stapelfeldt et al., 1998] Stapelfeldt, H., Constant, E., Sakai, H., and Corkum, P. B. (1998). Time-resolved Coulomb explosion imaging: A method to measure structure and dynamics of molecular nuclear wave packets. *Physical Review A*, 58(1):426–433.

[Stapelfeldt and Seideman, 2003] Stapelfeldt, H. and Seideman, T. (2003). Colloquium: Aligning molecules with strong laser pulses. *Reviews of Modern Physics*, 75(2):543–557.

[Stavros et al., 1999] Stavros, V. G., Ramswell, J. A., Smith, R. A. L., Verlet, J. R. R., Lei, J., and Fielding, H. H. (1999). Vibrationally autoionizing rydberg wave packets in NO. *Physical Review Letters*, 83(13):2552–2555.

[Steinmeyer, 2003] Steinmeyer, G. (2003). A review of ultrafast optics and optoelectronics. *Journal of Optics A: Pure and Applied Optics*, 5(1):R1–R15.

[Stephens, 1946] Stephens, W. E. (1946). Proceedings of the american physical society, j1 - a pulsed mass spectrometer with time dispersion. *Physical Review*, 69(11-12):674.

[Stingl et al., 1995] Stingl, A., Lenzner, M., Spielmann, C., Krausz, F., and Szipocs, R. (1995). Sub-10f-fs mirror-dispersion-controlled Ti:sapphire laser. *Optics Letters*, 20(6):602–604.

[Stobrawa et al., 2001] Stobrawa, G., Hacker, M., Feurer, T., Zeidler, D., Motzkus, M., and Reichel, F. (2001). A new high-resolution femtosecond pulse shaper. *Applied Physics B: Lasers and Optics*, 72(5):627–630.

[Stolen and Lin, 1978] Stolen, R. H. and Lin, C. (1978). Self-phase-modulation in silica optical fibers. *Physical Review A*, 17(4):1448–1453.

[Strickland and Mourou, 1985] Strickland, D. and Mourou, G. (1985). Compression of amplified chirped optical pulses. *Optics Communications*, 56(3):219–221.

[Suda et al., 2005] Suda, A., Hatayama, M., Nagasaka, K., and Midorikawa, K. (2005). Generation of sub-10-fs, 5-mJ-optical pulses using a hollow fiber with a pressure gradient. *Applied Physics Letters*, 86(11):111116.

[Suresh, 2005] Suresh, M. (2005). *Neutral and ionic atoms and molecules in femtosecond laser pulses*. PhD thesis, Queen's University Belfast, Faculty of Science and Agriculture, Queen's University Belfast, Northern Ireland.

[Suresh et al., 2005] Suresh, M., McKenna, J., Srigengan, B., Williams, I., English, E., Stebbings, S., Bryan, W., Newell, W., Divall, E., Hooker, C., and Langley, A. (2005). Multiple ionization of ions and atoms by intense ultrafast laser pulses. *Nuclear Instruments and Methods in Physics Research Section B: Beam Interactions with Materials and Atoms*, 235(1-4):216–220.

[Szipocs et al., 1994] Szipocs, R., Ferencz, K., Spielmann, C., and Krausz, F. (1994). Chirped multilayer coatings for broadband dispersion control in femtosecond lasers. *Optics Letters*, 19(3):201–203.

[Takeda et al., 1982] Takeda, M., Ina, H., and Kobayashi, S. (1982). Fourier-transform method of fringe-pattern analysis for computer-based topography and interferometry. *Journal of the Optical Society of America*, 72(1):156.

[Talebpour et al., 1997] Talebpour, A., Chien, C.-Y., Liang, Y., Larochelle, S., and Chin, S. L. (1997). Non-sequential ionization of Xe and Kr in an intense femtosecond Ti:sapphire laser pulse. *Journal of Physics B: Atomic, Molecular and Optical Physics*, 30(7):1721–1730.

[ten Wolde et al., 1988] ten Wolde, A., Noordam, L. D., Lagendijk, A., and van Linden van den Heuvell, H. B. (1988). Observation of radially localized atomic electron wave packets. *Physical Review Letters*, 61(18):2099–2101.

[Texier and Jungen, 1998] Texier, F. and Jungen, C. (1998). Nuclear-electronic wave-packet dynamics in perturbed Rydberg states of molecular hydrogen. *Physical Review Letters*, 81(20):4329–4332.

[Thomas, 1999] Thomas, R. V. (1999). *Short pulse, high intensity laser interactions with molecules*. PhD thesis, University College London, Department of Physics and Astronomy, University College London, England.

[Thompson et al., 1997] Thompson, M. R., Thomas, M. K., Taday, P. F., Posthumus, J. H., Langley, A. J., Frasinski, L. J., and Codling, K. (1997). One and two-colour studies of the dissociative ionization and coulomb explosion of H_2 with intense Ti:sapphire laser pulses. *Journal of Physics B: Atomic, Molecular and Optical Physics*, 30(24):5755–5772.

[Tisch et al., 2005] Tisch, J. W. G., Robinson, J. S., Haworth, C. A., and Gregory, A. (2005). *Hollow Fibre Pulse Compression System User's Guide*. Imperial College London, London, United Kingdom.

[Tong et al., 2002] Tong, X. M., Zhao, Z. X., and Lin, C. D. (2002). Theory of molecular tunneling ionization. *Physical Review A*, 66(3):033402.

[Torres et al., 2005] Torres, R., de Nalda, R., and Marangos, J. P. (2005). Dynamics of laser-induced molecular alignment in the impulsive and adiabatic regimes: A direct comparison. *Physical Review A (Atomic, Molecular, and Optical Physics)*, 72(2):023420.

[Tournois, 1997] Tournois, P. (1997). Acousto-optic programmable dispersive filter for adaptive compensation of group delay time dispersion in laser systems. *Optics Communications*, 140:245–249.

[Treacy, 1971] Treacy, E. B. (1971). Measurement and interpretation of dynamic spectrograms of picosecond light pulses. *Journal of Applied Physics*, 42(10):3848–3858.

[Trebino and Kane, 1993] Trebino, R. and Kane, D. J. (1993). Using phase retrieval to measure the intensity and phase of ultrashort pulses: frequency-resolved optical gating. *Journal of the Optical Society of America A*, 10(5):1101.

[Trebino et al., 2001] Trebino, R., O'Shea, P., Kimmel, M., and Gu, X. (2001). Measuring ultrashort laser pulses just got a lot easier! *Optics and Photonics News*, 12(6):22–25.

[Trebino and Walmsley, 1996] Trebino, R. and Walmsley, I. A. (1996). Measuring fast pulses with slow detectors. *Optics and Photonics News*, 7(3):23–32.

[Troppmann et al., 2006] Troppmann, U., Gollub, C., and de Vivie-Riedle, R. (2006). The role of phases and their interplay in molecular vibrational quantum computing with multiple qubits. *New Journal of Physics*, 8(6):100.

[Trump et al., 1999] Trump, C., Rottke, H., and Sandner, W. (1999). Multiphoton ionization of dissociating $D_2{}^+$ molecules. *Physical Review A*, 59(4):2858–2863.

[Turkstra et al., 2001] Turkstra, J. W., Hoekstra, R., Knoop, S., Meyer, D., Morgenstern, R., and Olson, R. E. (2001). Recoil momentum spectroscopy of highly charged ion collisions on magneto-optically trapped Na. *Physical Review Letters*, 87(12):123202.

[Ullrich, 2004] Ullrich, J., editor (2004). *Ten Years of COLTRIMS and Reaction Microscopes*. Max-Planck-Institut fur Kernpysik Heidelberg, Heidelberg, Germany.

[Ullrich et al., 1994] Ullrich, J., Dörner, R., Mergel, V., Jagutzki, O., Schmitt, L. S. W., and Schmidt-Bocking, H. (1994). Cold-target recoil-ion momentum spectroscopy: First results and future perspectives of a novel high resolution technique for the investigation of collision-induced many-particle reactions. *Comments on Atomic and Molecular Physics*, 30(5):285–304.

[Ullrich et al., 2003] Ullrich, J., Moshammer, R., A. Dorn, R. D., Schmidt, L. P. H., and Schmidt-Böcking, H. (2003). Recoil-ion and electron momentum spectroscopy: reaction-microscopes. *Reports on Progress in Physics*, 66(9):1463–1545.

[Ullrich et al., 1997] Ullrich, J., Moshammer, R., Dörner, R., Jagutzki, O., Mergel, V., Schmidt-Böcking, H., and Spielberger, L. (1997). Recoil-ion momentum spectroscopy. *Journal of Physics B: Atomic, Molecular and Optical Physics*, 30(13):2917–2974.

[Underwood et al., 2003] Underwood, J. G., Spanner, M., Ivanov, M. Y., Mottershead, J., Sussman, B. J., and Stolow, A. (2003). Switched wave packets: A route to nonperturbative quantum control. *Physical Review Letters*, 90(22):223001.

[Vallance, 2004] Vallance, C. (2004). Molecular photography: Velocity-map imaging of chemical events. *Philosophical Transactions of the Royal Society A*, 362(1825):2591–2609.

[Vallerga et al., 1989] Vallerga, J. V., Kaplan, G. C., Siegmund, O. H. W., Lampton, M., and Malina, R. F. (1989). Imaging characteristics of the extreme ultraviolet explorermicrochannel plate detectors. *IEEE Transactions on Nuclear Science*, 36(1-1):881–886.

[van der Poel et al., 2001] van der Poel, M., Nielsen, C. V., Gearba, M.-A., and Andersen, N. (2001). Fraunhofer diffraction of atomic matter waves: Electron transfer studies with a laser cooled target. *Physical Review Letters*, 87(12):123201.

[Varga and Winter, 1978] Varga, P. and Winter, H. (1978). Determination of metastable fractions in noble-gas-ion beams. *Physical Review A*, 18(6):2453–2458.

[Vdovin, 1995] Vdovin, G. (1995). Spatial light modulator based on the control of the wavefront curvature. *Optics Communications*, 115(1-2):170–178.

[Verluise et al., 2000] Verluise, F., Laude, V., Cheng, Z., Spielmann, C., and Tournois, P. (2000). Amplitude and phase control of ultrashort pulses by use of an acousto-optic programmable dispersive filter: pulse compression and shaping. *Optics Letters*, 25(8):575–577.

[Villeneuve, 2007] Villeneuve, D. M. (2007). Attophysics: At a glance. *Nature*, 449(7165):997–999.

[Villeneuve et al., 2002] Villeneuve, D. M., Aseyev1, S. A., Avery1, A., and Corkum, P. B. (2002). Using frequency-domain manipulation of stretched femtosecond laser pulses to create fast rise and fall times on picosecond pulses. *Journal of Applied Physics B: Lasers and Optics*, 74(1):S157–S161.

[Vogt et al., 2006] Vogt, G., Nuernberger, P., Brixner, T., and Gerber, G. (2006). Femtosecond pump-shaped-dump quantum control of retinal isomerization in bacteriorhodopsin. *Chemical Physics Letters*, 433(1-3):211–215.

[von Busch and Dunn, 1972] von Busch, F. and Dunn, G. H. (1972). Photodissociation of H_2^+ and D_2^+: Experiment. *Physical Review A*, 5(4):1726–1743.

[Vrakking, 2001] Vrakking, M. J. J. (2001). An iterative procedure for the inversion of two-dimensional ion/photoelectron imaging experiments. *Review of Scientific Instruments*, 72(11):4084–4089.

[Vrakking et al., 1996] Vrakking, M. J. J., Villeneuve, D. M., and Stolow, A. (1996). Observation of fractional revivals of a molecular wave packet. *Physical Review A*, 54(1):R37–R40.

[Wagner et al., 2007] Wagner, N., Zhou, X., Lock, R., Li, W., Wüest, A., Murnane, M., and Kapteyn, H. (2007). Extracting the phase of high-order harmonic emission from a molecule using transient alignment in mixed samples. *Physical Review A (Atomic, Molecular, and Optical Physics)*, 76(6):061403.

[Walker et al., 1994] Walker, B., Sheehy, B., DiMauro, L. F., Agostini, P., Schafer, K. J., and Kulander, K. C. (1994). Precision measurement of strong field double ionization of helium. *Physical Review Letters*, 73(9):1227–1230.

[Walker et al., 1998] Walker, M. A., Hansch, P., and Van Woerkom, L. D. (1998). Intensity-resolved multiphoton ionization: Circumventing spatial averaging. *Physical Review A*, 57(2):R701–R704.

[Walsh et al., 1997] Walsh, T. D. G., Ilkov, F. A., and Chin, S. L. (1997). The dynamical behaviour of H_2 and D_2 in a strong, femtosecond, titanium:sapphire laser field. *Journal of Physics B: Atomic, Molecular and Optical Physics*, 30(9):2167–2175.

[Wang et al., 2005] Wang, P. Q., Sayler, A. M., Carnes, K. D., Esry, B. D., and Ben-Itzhak, I. (2005). Disentangling the volume effect through intensity-difference spectra: application to laser-induced dissociation of $H_2{}^+$. *Optics Letters*, 30(6):664–666.

[Wang et al., 2006] Wang, P. Q., Sayler, A. M., Carnes, K. D., Xia, J. F., Smith, M. A., Esry, B. D., and Ben-Itzhak, I. (2006). Dissociation of $H_2{}^+$ in intense femtosecond laser fields studied by coincidence three-dimensional momentum imaging. *Physical Review A (Atomic, Molecular, and Optical Physics)*, 74(4):043411.

[Watson, 2005] Watson, S. (2005). *Femtosecond laser interactions with dilute matter*. PhD thesis, University College London, Department of Physics and Astronomy, University College London, England.

[Weber, 1967] Weber, H. P. (1967). Method for pulsewidth measurement of ultrashort light pulses generated by phase-locked lasers using nonlinear optics. *Journal of Applied Physics*, 38(5):2231–2234.

[Weiner, 2000] Weiner, A. M. (2000). Femtosecond pulse shaping using spatial light modulators. *Review of Scientific Instruments*, 71(5):1929–1960.

[Weiner et al., 1988] Weiner, A. M., Heritage, J. P., and Kirschner, E. M. (1988). High-resolution femtosecond pulse shaping. *Journal of the Optical Society of America B*, 5(8):1563.

[Weiner et al., 1992] Weiner, A. M., Leaird, D. E., Patel, J. S., R., J., and Wullert (1992). Programmable shaping of femtosecond optical pulses by use of 128-element liquid crystal phase modulator. *IEEE Journal of Quantum Electronics*, 28(4):908–920.

[Whaling et al., 1995] Whaling, W., Anderson, W. H. C., Carle, M. T., Brault, J. W., and Zarem, H. A. (1995). Argon ion linelist and level energies in the hollow-cathode discharge. *Journal of Quantitative Spectroscopy and Radiative Transfer*, 53(1):53–75.

[Wiley and McLaren, 1955] Wiley, W. C. and McLaren, I. H. (1955). Time-of-flight mass spectrometer with improved resolution. *Review of Scientific Instruments*, 26(12):1150–1157.

[Williams et al., 2007] Williams, I. D., McKenna, J., Wood, J., Suresh, M., Bryan, W. A., Stebbings, S. L., English, E. M. L., Calvert, C. R., Srigengan, B., Divall, E. J., Hooker,

C. J., Langley, A. J., and Newell, W. R. (2007). Excited ions in intense femtosecond laser pulses: Laser-induced recombination. *Physical Review Letters*, 99(17):173002.

[Winterfeldt et al., 2008] Winterfeldt, C., Spielmann, C., and Gerber, G. (2008). Colloquium: Optimal control of high-harmonic generation. *Reviews of Modern Physics*, 80(1):117.

[Witzel et al., 2000] Witzel, B., Papadogiannis, N. A., and Charalambidis, D. (2000). Charge-state resolved above threshold ionization. *Physical Review Letters*, 85(11):2268–2271.

[Wolff and Stephens, 1953] Wolff, M. M. and Stephens, W. E. (1953). A pulsed mass spectrometer with time dispersion. *Review of Scientific Instruments*, 24(8):616–617.

[Wood et al., 2006] Wood, J., English, E. M. L., Newell, W. R., Calvert, C. R., McKenna, J., Williams, I. D., Bryan, W. A., Turcu, I. C. E., Ertel, K. G., Smith, J. M., Divall, E. J., and Chekhlov, O. (2006). Defining the coherence and controlling the motion of a nuclear wavepacket. In *Central Laser Facility Annual Report 2005-2006, RAL-TR-2006-025*, pages 88–90. Council for the Central Laboratory of the Research Councils.

[Wood et al., 2005] Wood, J., English, E. M. L., Stebbings, S. L., Bryan, W. A., Newell, W. R., McKenna, J., Suresh, M., Srigengan, B., Williams, I. D., Turcu, I. C. E., Smith, J. M., Ertel, K. G., Divall, E. J., Hooker, C. J., and Langley, A. J. (2005). Probing atomic ionization mechanisms in intense laser fields by calculating geometry and diffraction independent ionization probabilities. In *Central Laser Facility Annual Report 2004-2005, RAL-TR-2005-025*, pages 51–52. Council for the Central Laboratory of the Research Councils.

[Wu et al., 1995] Wu, W., Wong, K. L., Cocke, C. L., Giese, J. P., and Montenegro, E. C. (1995). Recoil longitudinal momentum and Q-value measurements in electron-capture processes of fast multiply charged ions colliding with he. *Physical Review A*, 51(5):3718–3725.

[Yamakawa et al., 2004] Yamakawa, K., Akahane, Y., Fukuda, Y., Aoyama, M., Inoue, N., Ueda, H., and Utsumi, T. (2004). Many-electron dynamics of a Xe atom in strong and superstrong laser fields. *Physical Review Letters*, 92(12):123001.

[Yeazell et al., 1990] Yeazell, J. A., Mallalieu, M., and Stroud, C. R. (1990). Observation of the collapse and revival of a Rydberg electronic wave packet. *Physical Review Letters*, 64(17):2007–2010.

[Yu et al., 1998] Yu, H., Zuo, T., and Bandrauk, A. D. (1998). Intense field ionization of molecules with ultra-short laser pulses - enhanced ionization and barrier-suppression effects. *Journal of Physics B: Atomic, Molecular and Optical Physics*, 31(7):1533–1551.

[Zajfman et al., 1997] Zajfman, D., Heber, O., Vejby-Christensen, L., Ben-Itzhak, I., Rappaport, M., Fishman, R., and Dahan, M. (1997). Electrostatic bottle for long-time storage of fast ion beams. *Physical Review A*, 55(3):R1577–R1580.

[Zeek et al., 2000] Zeek, E., Bartels, R., Murnane, M. M., Kapteyn, H. C., Backus, S., and Vdovin, G. (2000). Adaptive pulse compression for transform-limited 15-fs high-energy pulse generation. *Optics Letters*, 25(8):587–589.

[Zerrad and Hahn, 1998] Zerrad, E. and Hahn, Y. (1998). Radiative recombination at low energies. *Journal of Quantitative Spectroscopy and Radiative Transfer*, 59(6):637–651.

[Zettili, 2006] Zettili, N. (2006). *Quantum Mechanics: Concepts and Applications*. John Wiley and Sons Ltd, Chichester, UK, Third edition.

[Zewail, 1988] Zewail, A. H. (1988). Laser femtochemistry. *Science*, 242:1645–1653.

[Zewail, 2000] Zewail, A. H. (2000). Femtochemistry. past, present and future. *Pure and Applied Chemistry*, 72(12):2219–2231.

[Zhavoronkov and Korn, 2002] Zhavoronkov, N. and Korn, G. (2002). Generation of single intense short optical pulses by ultrafast molecular phase modulation. *Physical Review Letters*, 88(20):203901.

[Zheltikov, 2002] Zheltikov, A. M. (2002). Ultrashort light pulses in hollow waveguides. *Physcis-Uspekhi*, 45(7):687–718.

[Zon, 1999] Zon, B. A. (1999). Many-electron tunneling in atoms. *Soviet Physics JETP*, 89(2):219–222.

[Zon, 2000a] Zon, B. A. (2000a). Classical theory of the molecule alignment in a laser field. *The European Physical Journal D - Atomic, Molecular, Optical and Plasma Physics*, 8(3):377–384.

[Zon, 2000b] Zon, B. A. (2000b). Tunneling ionization of atoms with excitation of the core. *Soviet Physics JETP*, 91(5):899–904.

[Zon and Katsnel'son, 1975] Zon, B. A. and Katsnel'son, B. G. (1975). Nonresonant scattering of intense light by a molecule. *Soviet Physics - JETP*, 42(4):595–601.

[Zrost et al., 2006] Zrost, K., Rudenko, A., Ergler, T., Feuerstein, B., de Jesus, V. L. B., Schröter, C. D., Moshammer, R., and Ullrich, J. (2006). Multiple ionization of Ne and Ar by intense 25 fs laser pulses: Few-electron dynamics studied with ion momentum spectroscopy. *Journal of Physics B: Atomic, Molecular and Optical Physics*, 39(13):S371–S380.

[Zuo and Bandrauk, 1995] Zuo, T. and Bandrauk, A. D. (1995). Charge-resonance-enhanced ionization of diatomic molecular ions by intense lasers. *Physical Review A*, 52(4):R2511–R2514.

[Zuo et al., 1993] Zuo, T., Chelkowski, S., and Bandrauk, A. D. (1993). Harmonic generation by the $H_2{}^+$ molecular ion in intense laser fields. *Physical Review A*, 48(5):3837–3844.